CHEMICAL INTERACTIONS AT ZINC OXIDE SURFACES

by

IMANTS RUDOLF LAUKS

A thesis submitted in partial fulfilment of the

requirements for the degree of Doctor of Philosophy

in the University of London, Imperial College

1977

Department of Electrical Engineering

ACKNOWLEDGEMENTS

I would like to thank my supervisor, Dr. Mino Green for his helpful guidance throughout the course of this work.

I would like to thank Professor J.C. Anderson for provision of laboratory facilities, Professor G. Heiland for providing zinc oxide single crystals and Professor M.W. Roberts for kindly making available the E.S.C.A. facilities at the University of Bradford.

I am grateful to Ms. Cynthia Collins for the speedy typing of this thesis.

I wish to acknowledge the award of an S.R.C. studentship.

ABSTRACT

The purpose of this study was to investigate the interaction of the ZnO surfaces with oxygen and nitrous oxide and to obtain data which were amenable to theoretical analysis. It was, therefore, necessary to examine a single, well defined, crystal plane of ZnO. With this in mind the $10\bar{1}0$ prism planes of ZnO single needles were investigated (the $10\bar{1}0$ plane consisting of 99.99% of the exposed surface).

Clean ZnO surfaces were obtained by heating the crystals in oxygen (as shown by ESCA and mass-spectrometric studies).

Gas-solid interactions were followed in controlled flow-rate vacuum system (of UHV quality cleanliness). Gas flows were monitored using a mass-spectrometer and facilities were available for imposing pressure and temperature transients on the gas-solid system.

There is presented in this thesis a kinetic study of the decomposition of the zinc oxide single crystal $10\bar{1}0$ surface lattice layer. A mechanism has been formulated, based on experimental findings, which involves the high temperature formation of positively charged surface oxygen vacancies when molecular oxygen is evolved from the surface lattice layer. A parallel zinc loss reaction destroys the surface oxygen vacancies and produces oxygen atoms at step sites. This mechanism shows that the surface concentration of oxygen vacancies and step sites can be controllably varied, from zero to 0.04 of a monolayer for vacancies and from 0 to 0.2 for step sites, by appropriate pre-treatment. Isotopic oxygen exchange has been used to investigate further the nature of these surface defects. The kinetics of the catalytic decomposition of nitrous oxide has been investigated. A mechanism for the catalytic decomposition of nitrous oxide has been formulated, involving the interaction of the gas with surface defects on the now controllably defined zinc oxide surface.

CONTENTS

List of Figures

Page

Page

Page

Fig. 4.19:

Theoretical variation of $A_{O^{16}O^{18}}/A_{O_2^{18}}$ with gas phase fraction of O^{18} atoms for 'grouped states' model, 219

(a) using histogram distribution of states

(b) using two state model

(c) using single state model

compared with experimental values reproduced from fig. (3.13)

Fig. 4.20:

Arrhenius plot of the log of the rate of $O^{16}O^{18}$ incorporation normalised to constant O^{16} O^{18} pressure, versus 1/T 222

Fig. 4.21:

Log of the amount of O^{16} O^{18} incorporated in a fixed time and constant pressure, versus 1/T 224

Fig. 22:

Nitrous oxide pressure divided by the rate of decomposition plotted against nitrous oxide pressure for the steady-state decomposition of nitrous oxide 233

Fig. 23:

Reciprocal of the rate of decomposition plotted against the reciprocal of the nitrous oxide pressure for the steady-state decomposition of nitrous oxide 234

Page

List of Plates

1. INTRODUCTION

It is the current view that, in the adsorption and catalysis reactions on ionic semiconductor surfaces, the adsorption mechanism involves charge transfer, and that in many cases the adsorption site is exclusively over a surface defect.

An exposition of the energetics of the charge transfer adsorption process are found in an article by Green and Lee (1969), a simplified version of which is as follows. When the adsorption of a molecule or atom gives rise to localised energy levels in the band gap at the surface of a semiconductor, charge may flow between adsorbent and adsorbate. Consider the energy level diagram of a semiconductor taken, for simplicity, in the flat band approximation with no surface states and corresponding band bending. When a neutral gas atom, X, is brought up to the semiconductor surface, charge is transferred. If, for example, the charge transferred is an electron from the solid to X, there results a depleted semiconductor surface, shown by the bands bending up, and a filled surface state of X^-. The energy required to remove an electron from the semiconductor to infinity is its work function, $\Delta\Phi$, and the energy gained when this electron is put into an upper empty energy level of the gas atom, is its electron affinity, $\Delta\eta$. On this elementary model, the difference in energy between the Fermi level and the surface state energy level of X^-, is postulated to equal $\Delta\Phi - \Delta\eta$ and is the energy of charge transfer.

Using a more complete description of the energy balance,(fig. 1.1), the steps in the formation of an acceptor surface complex from the neutral species, X, are as follows. There is the removal of an electron from the semiconductor to infinity, i.e. the work function, $\Delta\Phi$, and its attachment to the atom X, the energy of this process given by the electron affinity,

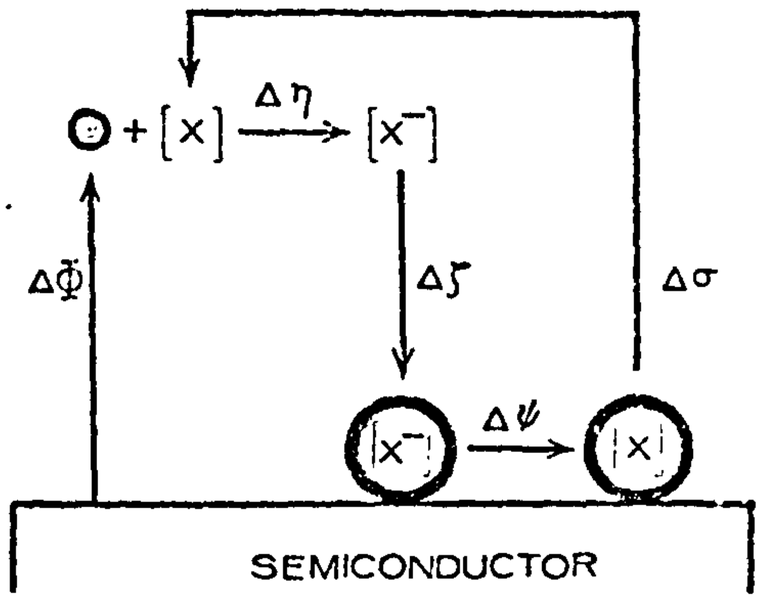

Fig.1.1. Energy cycle for the formation of a negative, acceptor, surface complex.

$\Delta\eta$. When the ion X^- is brought up to the semiconductor surface there is an electrostatic interaction, whose energy is given by $\Delta\zeta$. The total energy of adsorption of X^- , ΔE_{X^-} , is then given by

$$\Delta E_{X^-} = \Delta\bar{\Phi} + \Delta\eta + \Delta\zeta$$

Green and Lee (1969) found, when quantifying the terms on the right-hand side of the above equation, that, for many gases, adsorption was not an energetically very favourable process on a perfect semiconductor surface. However, if there is a local positive charge centre on the semiconductor surface (e.g. a trivalent dopant defect in a II-VI semiconductor surface) and a gas atom, X, adsorbs over such a site, the resulting increase in the attractive Coulomb interaction energy between the X^- and the positive surface centre now makes the adsorption energetically very favourable. Adsorption would therefore be highly preferential over such a surface defect.

The experimental evidence for the validity of the charge transfer model is extensive, but in most cases of a rather qualitative nature (Vol'Kenshtein 1963, and Many et al. 1965), in order to test the model the nitrous oxide catalytic decomposition reaction was chosen to be studied. Zinc oxide was the chosen ionic semiconductor for these experiments, since it is a solid readily obtainable in single crystal form and with high purity, with a well known bulk and surface solid state chemistry (Kröger 1964, and Heiland et al. 1959). The $10\bar{1}0$ surface was the chosen adsorbent surface of the zinc oxide single crystal sample, since it is more stable than the polar surfaces, with a more clearly defined surface structure (see later).

The problems involved in performing qualitative adsorption and catalysis studies on zinc oxide can be summed up as follows. Firstly, there is the problem of obtaining a suitably defined crystal surface on which the reaction is to take place. This requires research on single crystal samples where the surface crystallography has been determined. Secondly, there is the problem of how to obtain a reproducibly defined crystal surface with respect to the solid state defect configuration, of both intrinsic and dopant defects. Thirdly, there is the problem of surface cleanliness, that is, how to obtain an uncontaminated surface, and, if contaminants are present, how do they interact with the surface and the adsorbing species. Many experimental studies are contained in the past literature where some of these problems are attacked, but with varying degrees of success: these will be referred to in the appropriate section of this introduction.

Recognising the importance of a quantitative knowledge of the surface defect configuration in the catalytic reaction, a series of experiments were performed on the interaction between oxygen and the $10\bar{1}0$ zinc oxide surface in order to obtain such a quantitative estimate.

It is of current concern whether or not oxygen adsorbs on a clean $10\bar{1}0$ zinc oxide surface. There are, in the recent literature, conflicting reports on this issue (Shapira et al. 1976, Göpel , 1976), and reference is made to the presence of surface contaminants in this adsorption process (Shapira et al., 1976). In this thesis we have attempted to ascertain the nature of the surface contamination and define its role in the oxygen adsorption process.

1.1 Crystallography

Zinc oxide, ZnO, crystallises in the hexagonal wurtzite lattice (fig 1.2a) in which the oxygen atoms are arranged in closest hexagonal packing with the zinc atoms in half of the tetrahedral holes and having the same relative spatial arrangement as the oxygen atoms. The zinc oxygen bond is partly ionic, partly covalent with an effective charge on each ion estimated as about one electronic charge (Heiland and Kunstmann, 1969). The crystals are non-centrosymmetric and exhibit a polar C-axis. The wurtzite structure can be thought of as a series of stacked double layers where the distance between oxygen and zinc atoms from the next nearest double layers is 1.96×10^{-8} cm measured parallel to the C-axis, and the nearest neighbour zinc-oxygen atom distance within the double layers is 1.98×10^{-8} cm (0.65×10^{-8} cm measured parallel to the C-axis). The series is terminated at either end of the crystal by two different surfaces, one, the 0001 surface, consisting of zinc atoms, the other, the $000\bar{1}$ surface, consisting of oxygen atoms. The two polar surfaces can be distinguished by suitable etching (Heiland et al., 1963 and Klein, 1965), or X-ray procedures (Mariano and Hanneman, 1963).

The unit cell lattice constants, fig (1.2a), are $c = 5.207 \times 10^{-8}$ cm and $a = 3.250 \times 10^{-8}$ cm with a unit cell volume of 47.62×10^{-24} cm^3 (as in Abrahams and Bernstein, 1968).

The prism surfaces, figs (1.2b) and (1.2c) are parallel to the C-axis and contain an equal number of cations and anions, with atomic arrangements in the $10\bar{1}0$ and $11\bar{2}0$ planes as indicated. Fig. (1.2b) shows the $10\bar{1}0$ plane revealing an approximately square mesh of oxygen atoms (and zinc atoms) with a density of 5.99×10^{14} atoms cm^{-2}. In the $11\bar{2}0$ plane (fig. 1.2c) there are 6.92×10^{14} oxygen atoms cm^{-2}.

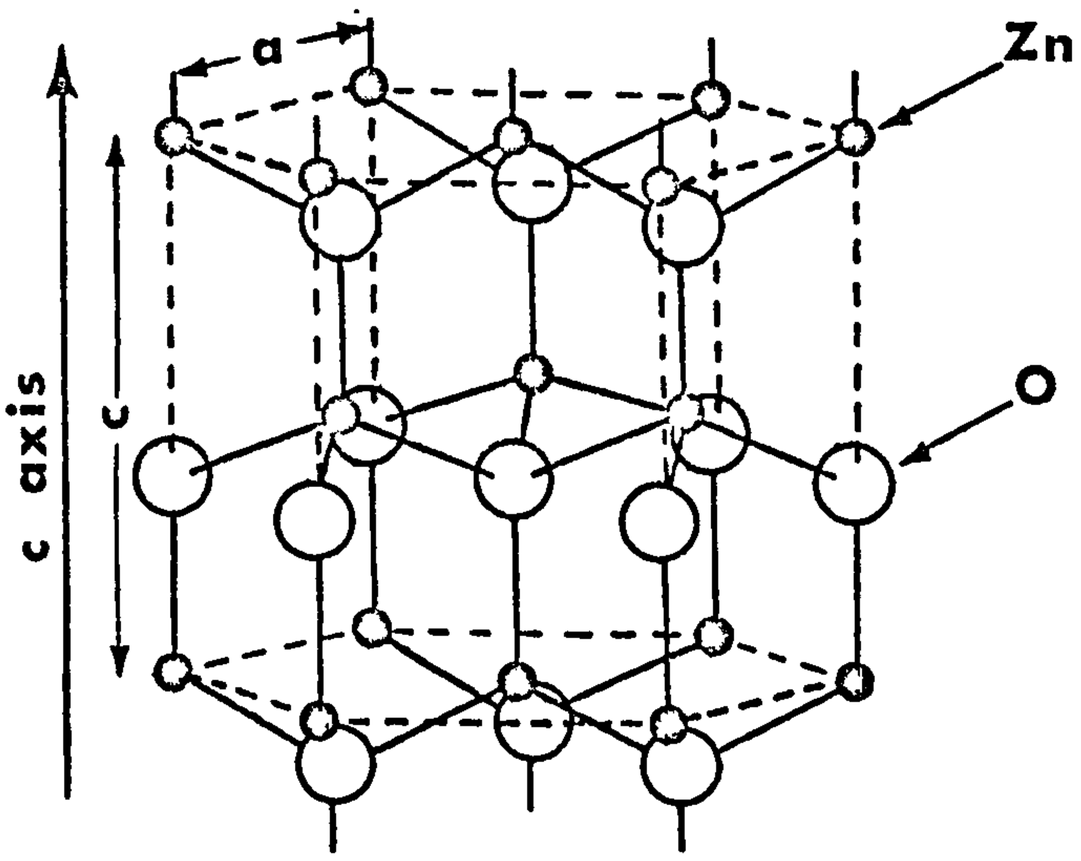

(a)

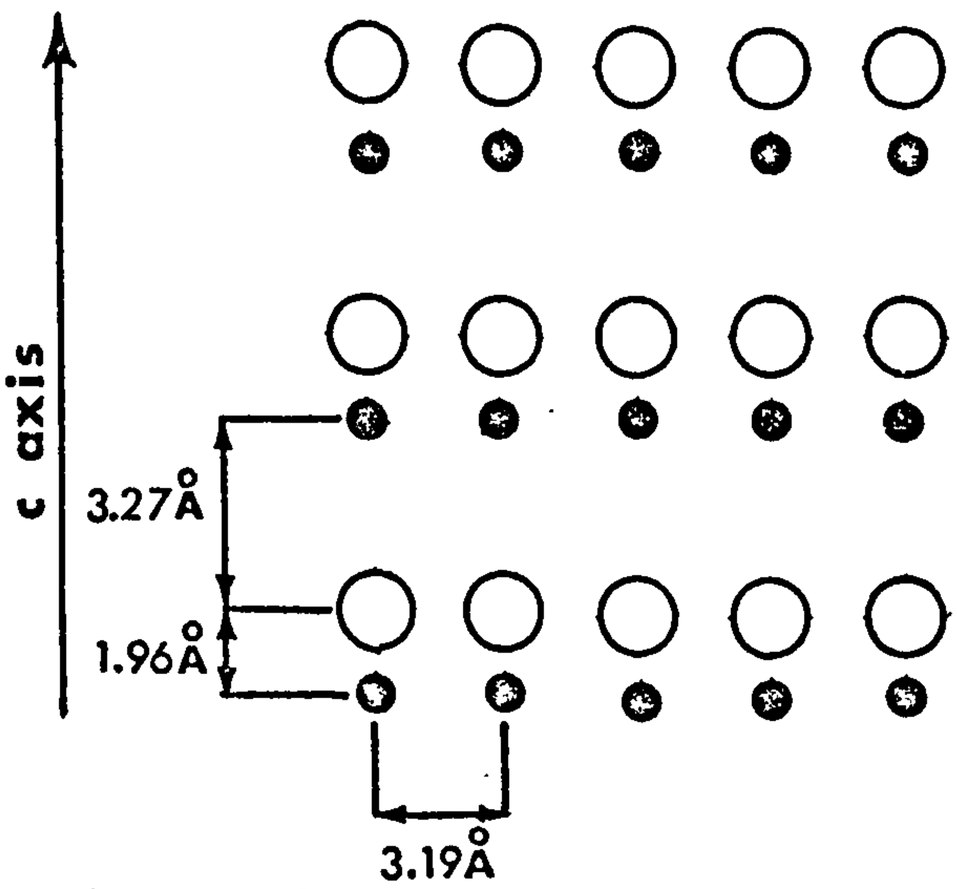

(b)

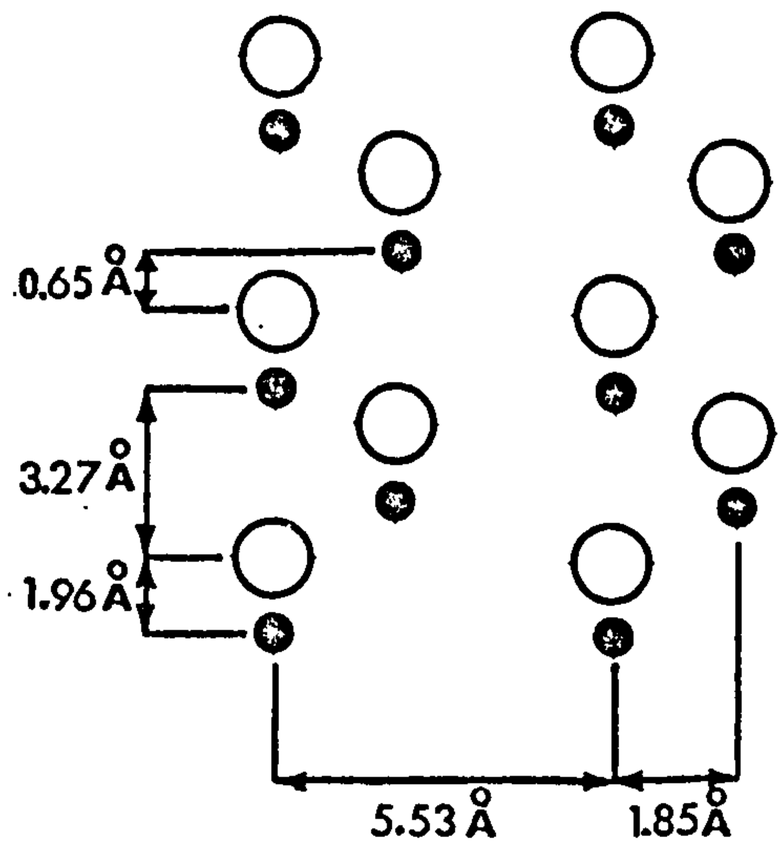

(c)

Fig. 1.2:

(a) the zinc oxide wurtzite lattice structure

(b) atom arrangement in the $10\bar{1}0$ surface plane

(c) atom arrangement in the $11\bar{2}0$ surface plane

This thesis reports adsorption and catalysis experiments on both zinc oxide powder, assumed to reveal all four types of surface, and zinc oxide single crystal prisms showing almost exclusively the $10\bar{1}0$ surface plane. (For a review of single crystal growth techniques and our sample characterisation see chapter 2). The prism surface of zinc oxide was chosen in preference to the polar surfaces for our single crystal experimental work, for the following reasons. The polar surfaces are highly unstable, potential gradients exist that are limited to the surface region (Nosker et al., 1970). Reconstruction of the polar surfaces was observed by Chung and Farnsworth, 1970, after ion bombardment and annealing using L.E.E.D., and, Margoninski and Kirby, 1975, found that the 0001 surface reconstructed by heating above 600°C and observed faceting on the $000\bar{1}$ surface. The prism surfaces, on the other hand, are highly stable and do not reconstruct (Levine et al., 1972, and, Chang and Mark, 1974). Since the prism planes contain equal numbers of cations and anions no potential gradients exist in the surface region and hence charge transfer effects due to adsorption on these surfaces are much simplified.

1.2 Defect chemistry

1.2.1 Native defects

There exists in the past literature extensive work on the native defect structure of the zinc oxide bulk, reviewed by Kroger in 1964 and Boltaks in 1963. Zinc oxide has hitherto only been known to have n-type conductivity. This conductivity is explained by a zinc excess which can be realised in two ways: excess zinc as zinc interstitial or oxygen vacancy defects. Some authors (Hutson 1957, Mohanty and Azaroff 1961, and, Hoffmann and Hahn 1974) have assumed that interstitial zinc as Zn_i^+

or Zn_i° is the effective donor, whilst others (Bogner 1961, Hausmann 1970, and Lal 1971) conclude that the excess zinc arises from oxygen vacancies, V_o^{++}. These V_o^{++} centres containing one or two electrons act as the donors. More recently, Hausmann and Utsch (1975), using their reported Hall effect and conductivity data on undoped single crystals (Utsch and Hausmann 1975), argue that the sole donor defects are oxygen vacancies. Hagemark (1976), on the other hand, using low temperature electrical transport measurements on zinc doped single crystals (Hagemark and Chacka 1975), argues the presence of both zinc interstitials and oxygen vacancies. Whilst the situation is by no means clear, the weight of the recent evidence would suggest that the predominant bulk native defect in zinc oxide is the oxygen vacancy. Further evidence to support this claim is afforded by e.s.r. data. Hausmann (1970), interpreted the signals at g = 1.96 to be due to oxygen vacancies occupied by an electron. This was confirmed by Hoffmann and Hahn, 1974,.Born et al. in 1971 published e.s.r. measurements on zinc oxide powder and determined the oxygen vacancy electron trap depth of 0.52eV below the conduction band, whilst Mookherji, 1972, found the oxygen vacancy electron trap depth to be 0.31 $\pm$ 0.02eV below the conduction band.

1.2.2 Dopant defects

It has become accepted that surface defects affect the kinetics of charge transfer adsorption and catalysis. There are numerous literature examples of published data where a dopant has been introduced into the zinc oxide lattice to create such surface defects, and its effect on adsorption and catalysis kinetics measured. (For a review of the data on the decomposition of nitrous oxide and oxygen adsorption on zinc oxide published before 1972, see Roussel and Teichner, 1972. For more recent

literature see the next section.) However, some remarks are entered here to suggest some of the dangers involved when using this approach.

Firstly, in order to quantify the energetics of the charge transfer adsorption mechanism it would be desirable that the dopant centres were immobile in the surface lattice. The diffusion of defects in zinc oxide is summarised in fig. (1.3). At a typical temperature where catalytic decomposition of nitrous oxide on zinc oxide takes place, say 700°C, fig. (1.3) indicates that many of the dopant species are relatively mobile (except cobalt and manganese, but their complicated electronic configurations make them unlikely candidates for testing the theory). Indium, for example, has a diffusion coefficient at 700°C of 10^{-14} cm^2 s^{-1} , which means that in the period of a typical experiment, say, 100 secs, the indium atom will have moved a characteristic distance given by $l=(Dt)^{\frac{1}{2}}$ of 100 Å. This extent of movement of defect centres would undoubtedly complicate the reaction kinetics. Secondly, a knowledge of the true surface concentration of dopant atoms is required. In the past, the bulk dopant concentration was measured and correlated with surface reaction kinetics. However, a bulk dopant concentration is by no means a reliable indication of the surface concentration, since fractionation of the dopant between the surface and the bulk is an extremely likely occurrence. This claim is substantiated by our own ESCA experiments on indium doped zinc oxide single crystals (chapter 2), where a large surface excess of indium is indicated. Thirdly, the surface evaporation of dopant atoms (as volatile oxides, e.g. of indium and lithium) is another factor that would influence the dopant surface concentration.

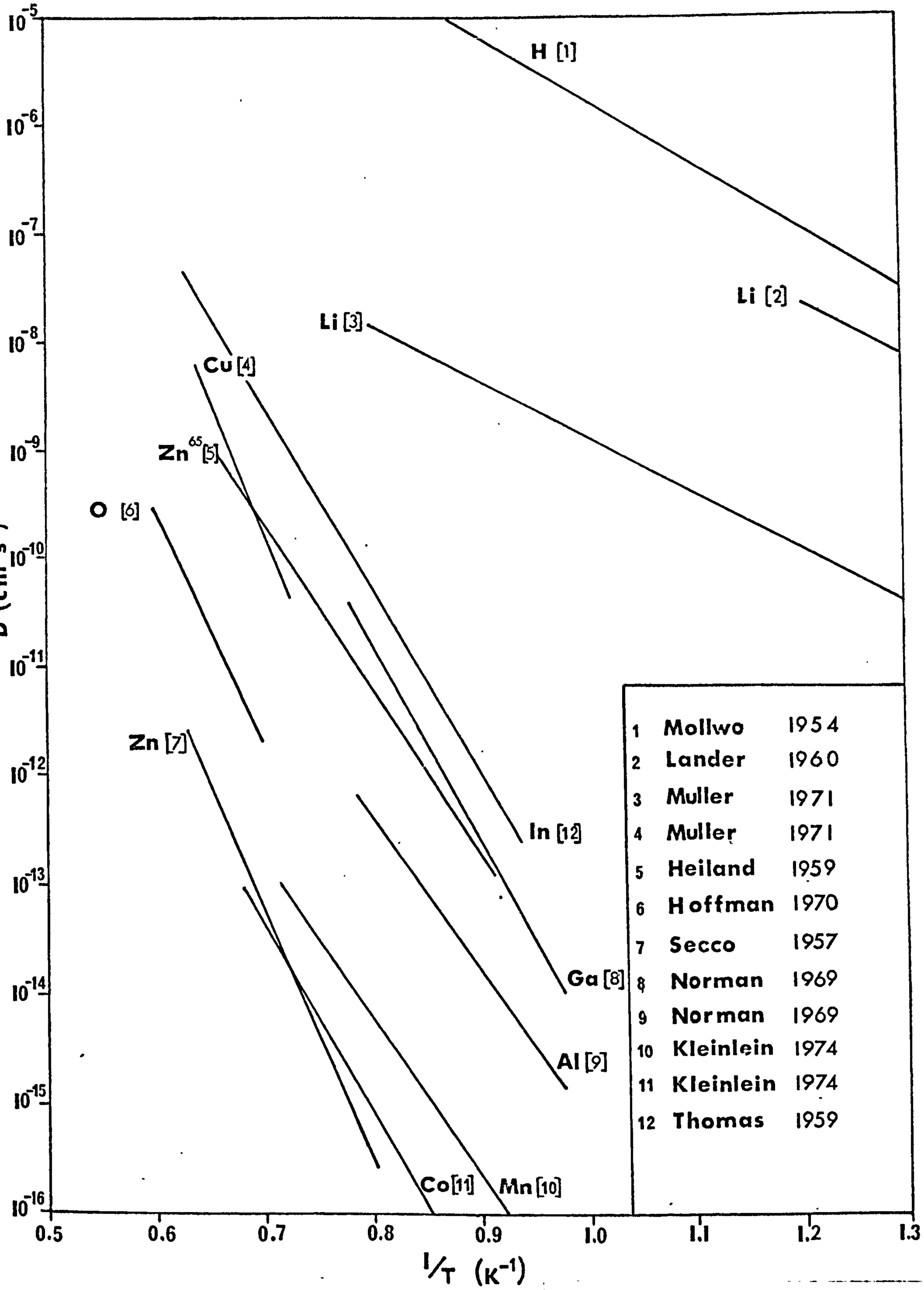

Fig. 1.3:

The diffusion of defects in zinc oxide : the diffusion coefficient, D, versus 1/T

In conclusion, since the surface configuration of dopant atoms is time varying and ill-defined - at typical reaction temperatures, we did not proceed with surface studies using doped zinc oxide.

1.3 Surface chemistry

1.3.1 Surface contamination

There have been many recent investigations, using A.E.S. and X.P.S., of the surface contamination of zinc oxide. These studies yield overwhelming evidence that both the prism and the polar surfaces of zinc oxide are grossly contaminated with carbon, regardless of the pre-vacuum treatment, when first examined by A.E.S. or X.P.S. It is also clear that this carbon contamination can be entirely removed by heating alone (Hopkins et al. 1975).

Four sources of contamination of the zinc oxide surface can be identified. There is the original surface contamination of the as grown crystal (normally gross carbon contamination). There is the contamination from the chemical etch if one is used. For the vacuum mounted crystal there is comtamination by surface diffusion from the sample holder and by out-diffusion of impurities from the crystal bulk. In all investigations to date, the zinc oxide crystals have received chemical etch pre-treatments prior to A.E.S. or X.P.S. examination. Hopkins et al., 1975, using A.E.S., observed C, S, P, Ca, Cl and K surface impurities on both prism and polar surfaces etched in HCl and H_3PO_4 and heated in vacuum at 750K for one hour. They found that all except Ca could be removed by heating to 1100K. Margoninsky and Kirby, 1975, observed only C and Cl polar surface contaminants using HCl etch, whilst Fiermans et al., 1973, found C, S, Cl , P and Ca using A.E.S. and X.P.S. on the HCl and H_3PO_4 treated 0001 polar surface. They

observe that Cl and S remain after heating. It has, then, not been made entirely clear what is the source of these surface impurities. In this thesis X.P.S. experiments on as grown, unetched crystals (chapter 2.4) are reported. Gross carbon contamination on the as grown samples is found, and Na, K, Cl peaks appear after bakeout in vacuum (or 10^{-2} torr O_2). We are confident that these impurities arise by out-diffusion from the bulk, and it has been shown that they can be removed by heating to 900°C.

Whether or not a zinc oxide $10\bar{1}0$ surface can be cleaned entirely by heating depends upon the nature of the impurities. It would appear that unetched samples are more easily heat cleaned, since, in the case of the etched samples, the etchant itself very probably introduces considerable contamination. When, on heating, all contaminants that come to the surface (by out-diffusion from the bulk - in our case of Na, K, Cl, or surface diffusion of contaminants from the crystal holder - in our case probably carbon, see chapter 2.4) are volatile, they will be removed into the gas phase and the surface can be said to be clean. If, however, involatile surface contaminants are present (e.g. Ca found by Hopkins et al., 1975), these cannot be removed by heating.

1.3.2 Oxygen adsorption

The recent literature provides overwhelming evidence for oxygen adsorbing on zinc at low temperatures (room temperature up to 500°C). The e.s.r. evidence of the interaction of oxygen with zinc oxide powder has not, as yet, led to a conclusive adsorption model; however, many authors (Setaka et al., 1970, and references therein) have attributed the signals at $g \doteqdot 2.0$ to oxygen adsorbed species. More recently, Cope and Campbell (1973) examined the e.s.r. of the oxygen chemisorption at 20°C and postulated O_2^- and O^- surface adsorbed species at sites neighbouring oxygen ion vacancies. We

have found no literature data on the e.s.r. of the oxygen interaction with single crystal zinc oxide.

That oxygen adsorbs on zinc oxide is well established by gas adsorption measurements, and that this occurs with charge transfer is established by correlating the adsorption data with electrical measurements on the zinc oxide adsorbent (e.g. surface conductivity and work function change) - for references see reviews by Roussel and Teichner (1972), and, Scott and Reed (1975). Two criticisms can be made of such experiments. Firstly, since uncharacterised zinc oxide powder surfaces have been studied, only generalised statements concerning the adsorption mechanism can be made, and little insight is gained about the detailed nature of the reaction or the adsorption site. Secondly, there was no direct evidence (using, for example, photodesorption thermally programmed desorption (T.P.D.) or electron stimulated desorption techniques) of the chemical nature of the oxygen in the chemisorbed phase.

In the more recent literature, working on zinc oxide single crystal surfaces, several authors have observed differing oxygen adsorption behaviour. Shapira et al. (1975 and 1976) have studied oxygen chemisorption on zinc oxide powder and $000\bar{1}$ single crystal surfaces. Their single crystals were polished and etched in HCl, but received no vacuum pre-treatment. They observed, using A.E.S., significant C, S and Cl surface contaminants. Photodesorption of oxygen chemisorbed on such "real" zinc oxide surface showed CO_2 as the only desorbed product. They concluded that oxygen adsorbs with charge transfer (they found a similar correlation between surface conductivity change with amount adsorbed to that obtained by previous authors) only at preferred sites of carbon contamination, and suggest that earlier work on "real" surfaces can be described similarly.

This is supported by the data of Many (1974) and Eger et al. (1975), whose study of oxygen chemisorption on single crystal zinc oxide (prism and polar surfaces) shows adsorption kinetics explained by charge transfer across a buffer layer (presumed to be carbon) present between the zinc oxide surface proper and the adsorbing species.

Göpel (1976), on the other hand, working on clean (LEED, A.E.S.) $10\bar{1}0$ zinc oxide surfaces, finds that oxygen reversibly chemisorbs as O_2^- in the temperature range 300K to 600K with a desorption activation energy of 1.14eV. By correlating the amount adsorbed with conductivity and work function changes, charge transfer adsorption was shown quantitatively. Using oxygen T.P.D. Gopel obtained typically 6×10^{11} molecules cm^{-2} adsorbed (for a pre-treatment at 300K for 20 minutes in 10^{-6} torr oxygen). This is a fractional coverage of 10^{-3}. For such small extents of adsorption it appears to us highly dangerous to discuss this in terms of a "clean" surface. Any contamination less than ca. 1% surface coverage, which is typically the limit of sensitivity using LEED or A.E.S., would not show up using these techniques, but could quite easily be a preferred adsorption site for oxygen, were it present.

Steinbach and Harboth (1973 and 1974) observed thermodesorption of molecular oxygen at temperatures of 400-450°C. Their zinc oxide single crystals were previously etched in phosphoric acid and vacuum outgassed at 550°C. We have shown that at this temperature there is considerable out-diffusion of bulk impurities (several monolayers). It is therefore very likely that their surface is similarly grossly contaminated.

1.3.3 Nitrous oxide decomposition

The use of the nitrous oxide decomposition reaction in evaluating the effects of electronic properties of solids in catalysis is well known. Nitrous oxide decomposition on metal oxides has been studied extensively, (Winter, 1970). Read (1973) and Winter (1969) have studied the decomposition reaction on rare-earth oxides, whilst Cimino and his school have examined the effect on catalytic activity of metal ions in a host oxide lattice (for example Cimino et al., 1973, and references therein). Kobayashi and Kobayashi studied the nitrous oxide decomposition on manganese dioxide using a transient response technique (for a review of this work see Kobayashi and Kobayashi, 1974).

More specifically, on zinc oxide the decomposition of nitrous oxide has been reviewed by Roussel and Teichner, (1972).

Tanaka and Blyholder (1971) found the decomposition kinetics to be first order with rate determining decomposition of N_2O in the adsorbed phase. They suggest that the N_2O surface complex formation does not involve charge transfer. Shulz and Scheve (1969), measuring the decomposition on lithium and gallium doped zinc oxide, propose rate determining formation of an activated N_2O^- charge transfer adsorbed complex. Results from e.s.r. on nitrous oxide adsorption on zinc oxide (Iyengar et al., 1969) show charge transfer adsorption at surface oxygen vacancy sites (reduction of the $g \doteqdot 1.96$ signal upon treatment with N_2O).

All past literature data is for the decomposition reaction on zinc oxide powder samples. In this thesis we have attempted to clarify the decomposition reaction mechanism on the $10\bar{1}0$ zinc oxide single crystal surface, in particular with respect to the formation or otherwise of a charge transfer adsorbed complex.

Chapter 1 : References

Abrahams, S.C. and Bernstein, J.L., Acta. Cryst., B25, 1233, (1969)

Bogner, G., J. Phys. Chem. Sol., 19, 235, (1961)

Boltaks, B.I., "Diffusion in Semiconductors", ed. H.J. Goldsmid, Infosearch Ltd., London, (1963)

Born, G.K., Hofstaetter, A.B., Scharmann, A.O., Arnett, G.M., Kroes, R.L. and Wegner, U.E., Phys. Stat. Sol. (a), 4, 675, (1971)

Chang, S.C. and Mark, P., Surface Sci., 45, 721, (1974)

Chung, M.F. and Farnsworth, H.E., Surface Sci., 22, 93, (1970)

Cimino, A., Indovina, V., Pepe, F. and Stone, F.S., Gazz. Chim. Ital., 103, 935, (1973)

Cope, J.O. and Campbell, I.D., J.C.S. Faraday Trans., 69, 1, (1973)

Eger, D., Goldstein, Y. and Many, A., R.C.A. Review, 36, 508, (1975)

Fiermans, L.,Arijs, E., Vennik, J. and Maenhout-Van Der Vorst, W., Surface Sci., 39, 357, (1973)

Göpel, W., Ber. Bun. Ges., 80, 481, (1976)

Green, M., Lee, M.J., "Solid State Surface Science", ed. Green, M., Marcel Dekker, New York, 1, 133 (1969)

Hagemark, K.I., J. Sol. State Chem., 16, 293, (1976)

Hagemark, K.I. and Chacka, L.C., J. Sol. State Chem., 15, 261, (1975)

Hausmann, A., Z. Physik, 237, 86, (1970)

Hausmann, A. and Utsch, B., Z. Physik, B21, 217, (1975)

Heiland, G. and Kunstmann, P., Surface Sci., 13, 72, (1969)

Heiland, G., Kunstmann, P. and Pfister, H., Z. Physik, 176, 485 (1963)

Heiland, G., Mollwo , E. and Stöckmann, F., "Solid State Physics", eds. Seitz F. and Turnbull D., Academic Press, New York, 8, 193, (1959)

Hoffman, J.W. and Lauder, I., Trans. Faraday Soc., 66, no. 573, 2346,(1970)

Hoffmann, K. and Hahn, D., Phys. Stat. Sol. (a), 24, 637, (1974)

Hopkins, B.J., Leysen, R. and Taylor, P.A., Surface Sci., 48, 486, (1975)

Hutson, A.R., Phys. Rev., 108, 222, (1957)

Iyengar, R.D., Subba Rao, V.V. and Zettlemoyer, A.C., Surface Sci., 13, 251 (1969)

Klein, A., Z. Physik, 188, 352, (1965)

Kleinlein, F.W. and Helbig, R., Z. Physik, 266, 201, (1974)

Kobayashi, H. and Kobayashi, M., Catalysis Rev., 10, 139, (1974)

Kröger, F.A., "The Chemistry of Imperfect Crystals", North-Holland Amsterdam, (1964)

Lal, R.B., Phys. Stat. Sol. (a), 5, K19, (1971)

Lauder, J.J., J. Phys. Chem. Sol., 15, 324, (1960)

Levine, J.D., Willis, A., Bottoms, W.R. and Mark, P., Surface Sci., 29, 144, (1972)

Many, A., Crit. Rev. Sol. Sta. Sci., 4, 515, (1974)

Many, A., Goldstein, Y. and Grover, N.B., "Semiconduction Surfaces", North-Holland Amsterdam, (1965)

Margoninski, Y. and Kirby, R.E., J. Phys. C., 8, 1516, (1975)

Mariano, A.N. and Hanneman, R.E., J. Appl. Phys., 34, 384, (1963)

Mohanty, G.P. and Azaroff, L.V., J. Chem. Phys., 35, 1268, (1961)

Mollwo , E., Z. Physik, 138, S478, (1954)

Mookherji, T., Phys. Stat. Sol. (a), 13, 293, (1972)

Müller, G. and Helbig, R., J. Phys. Chem. Sol., 32, 1971, (1971)

Nosker, R., Mark, P. and Levine, J., Surface Sci., 19, 291, (1970)

Norman, V.J., Aust. J. Chem., 22, 235, (1969)

Read, J.F., J. Catalysis, 28, 428, (1973)

Roussel, P. and Teichner, S.J., Catalysis Rev., 6, 133, (1972)

Schulz, W.D. and Scheve, J., Z. Anorg. Allge. Chemie, 366, 231, (1969)

Scott, C.G. and Reed, C.E., "Surface Physics of Phosphors and Semiconductors", eds. Scott, C.G. and Reed, C.E., Academic Press, London, 411, (1975)

Secco, E.A. and Moore, W.J., J. Chem. Phys. 26, 942, (1957)

Setaka, M., Sancier, K.M. and Kwan, T., J. Catalysis, 16, 44, (1970)

Shapira, Y., Cox, S.M. and Lichtman, D., Surface Sci., 50, 503, (1975)

Shapira, Y., Cox, S.M. and Lichtman, D., Surface Sci., 54, 43, (1976)

Steinbach, F. and Harboth, R., Faraday Disc., 58, 143, (1974)

Steinbach, F. and Harboth, R., Ber. Bunsenges, Phys. Chem., 77, 1024, (1973)

Tanaka, K. and Blyholder, G., J. Phys. Chem., 75, 1037, (1971)

Thomas, G.D., Phys. Chem., Sol., 9, 31, (1959)

Utsch, B. and Hausmann, A., Z. Physik, B21, 27, (1975)

Vol'Kenshtein, F.F., "The Electronic Theory of Catalysis on Semiconductors", Pergamon Press, Oxford, (1963)

Winter, E.R.S., J. Catalysis, 15, 144, (1969)

Winter, E.R.S., J. Catalysis, 19, 32, (1970)

2. MATERIALS PREPARATION AND CHARACTERISATION

In the work described in this thesis both single crystal and powder zinc oxide samples were used. The powdered zinc oxide, obtained from Johnson Matthey Chemicals Limited, is "Puratronic Grade", with a batch analysis quoted by the makers as shown below.

Iron		3 p.p.m.
Cadmium		2 p.p.m.
Magnesium		2 p.p.m.
Silicon		1 p.p.m.
Calcium, Copper, Manganese, Sodium	each less than	1 p.p.m.

The preparation of the zinc oxide single crystal samples undertaken in this study, together with a review of other available crystal growth techniques is described below.

2.1 Zinc Oxide Crystal Growth

Four different types of crystal growth techniques are described in the literature, these are: growth from a flux, hydrothermal growth, the method of vapour phase reaction in an open flow system and chemical vapour transport (C.V.T.) in a sealed tube.

Zinc oxide single crystals can be prepared by a flux method by growing the crystals from the melt with a PbF_2 (Nielsen and Dearborn, 1960, Timofeeva, 1965) or, with a mixed V_2O_5 and P_2O_5 flux (Wanklyn 1970). Growth

from the melt yields predominantly platelet crystals.

Hydrothermal growth of zinc oxide single crystals has been studied extensively, (see, for example, Laudise and Hutson 1967, Kolb and Laudise 1966, 1965). Both platelet and needle single crystals have been grown using this technique.

The vapour phase reaction method, first published by Scharowsky (1953), and reviewed by Heiland et al. (1959), involves the oxidation of zinc vapour. This method was subsequently improved to obtain larger crystals, by Nielsen (1968) and Helbig (1972). Fischer (1976) describes the oxidation of zinc vapour by atmospheric oxygen in an open flow system. Matsushita et al. (1974) report the growth of single crystals by the oxidation of zinc vapour produced in the reduction of zinc oxide by carbon. Zinc oxide single crystals have also been produced by a vapour phase method involving the oxidation of ZnI_2 (Hirose and Kubo 1969, Hirose and Furuya 1970, Hirose 1971), ZnS, ZnSe (Park and Reynolds 1967) or Zn Br_2 (Hirose et al. 1970); and, by the vapour phase hydrolysis of ZnF_2 (Kubo 1961), Zn Cl_2 (Weaver 1967, and Takahasi et al.1966), Zn Br_2 (Hirose et al. 1970) or ZnI_2 (Hirose 1971).

The sealed tube C.V.T. method has been reported by Emmenegger and Petermann (1968) using Cl_2 and HCl as transport agents; by Piekarczyk et al. (1972) using Br_2 and Cl_2 ; and, by Shiloh and Gutman (1971) using the transport agents NH_4Cl, H_2 , Cl_2 and Hg Cl_2 .

The zinc oxide single crystal samples used in the experiments described in this thesis are from two sources. Both large (5 mm diameter: 2 cm length) and small (ca. 10μ - 500μ diameter: 1 cm length) undoped hexagonal single crystal needles, grown by the oxidation of zinc vapour, were obtained from Professor Heiland. Small single crystal needles (ca. 10μ - 500μ diameter: 1 cm lenth), both undoped and indium doped,

were grown in this laboratory by the oxidation of ZnI_2 vapour; single crystal zinc oxide (5 mm diameter: 5 mm length) was also grown in this laboratory using the sealed tube C.V.T. method with NH_4Cl as the transport agent.

The technique of zinc iodide oxidation involves the sublimation at 420°C of zinc iodide in the silica combustion tube, fig. (2.1a), and its transport by dry nitrogen to the growth zone which is at 1200°C. Oxygen, flowing parallel to the zinc iodide vapour, reacts with it at the end of the silica tube, where single crystal needles and whiskers of zinc oxide are formed. Of the many methods available, this was chosen for two main reasons. Firstly, the zinc oxide single crystal product is in the form of long thin needles and whiskers, with an axial ratio, typically, c:a = 200 : 1. So, for a typical needle, whose dimensions are 50μ diameter and 1 cm length, the ratio of the area of the prism faces to the area of the polar faces is ca 2000:1. This means that, in subsequent surface studies, the single crystal surface can be effectively taken to consist entirely of the prism type surface. Secondly, the temperature of single crystal growth, namely 1200°C is lower than the growth temperature for the other vapour phase oxidation techniques (all of which yield predominantly single crystal needles), where the growth temperature is above ca. 1300°C. Silica combustion tubes, providing a very clean growth surface, can be safely used at temperatures up to ca. 1250°C, but not at the higher temperatures of the other methods. Both the gas flow rates and the physical dimensions of the combustion tubes were found to be critical parameters in the growth process. For example, too high a nitrogen transport gas flow rate relative to the oxygen gas flow rate

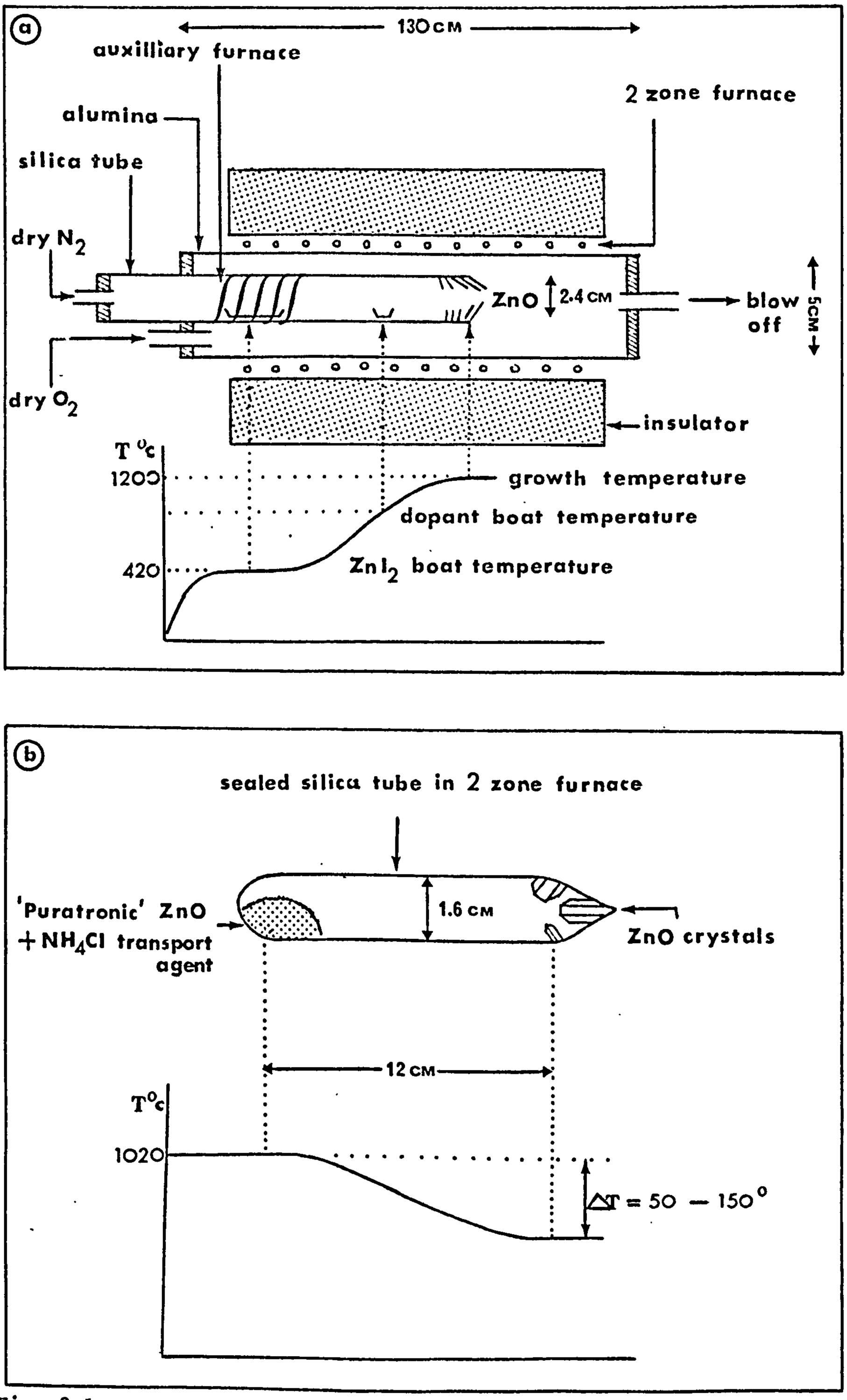

Fig. 2.1:

(a) open-flow apparatus for the growth of zinc oxide single crystals by the vapour phase oxidation of zinc iodide

(b) sealed tube method for growing zinc oxide single crystals

means that a lot of ZnI_2 is transported unreacted through the growth region. When both gas flow rates are high, crystal growth is fast, but crystal quality suffers due to the unstable flow conditions: when gas flow rates are low, crystal growth is slow. Using a growth tube with a diameter of 2.4 cm produced longer and better formed crystals than when using a 4 cm diameter growth tube. Hirose (1971) found that crystal growth occurred only when the reactant and carrier gas flows were parallel. For the apparatus dimensions indicated in fig. (2.1a) optimum growth occurred when the nitrogen flow rate was set at 700 $cm^3 min^{-1}$ and the oxygen flow rate at 150 $cm^3 min^{-1}$. In general, where the detailed mechanism of the growth process is not known, as in this case, it is vital to give all relevant details of the apparatus dimensions etc. It is our experience that past literature often contains insufficient data to follow a "recipe" with success.

Plate 1 shows a photograph of a typical run, after 20 hours. Long single crystal needles were found to grow radially inwards from the edges of the silica combustion tube. Very fine whiskers grew further down the tube.

Indium doping was achieved by placing a boat of indium oxide in the combustion tube, the extent of doping being dependent on the temperature of the indium oxide (500°C to 900°C). The highly doped samples (In_2O_3 boat at 900°C) with a resistivity of ca 10^{-2} Ω cm (giving an estimated bulk indium conc. of 10^{19} cm^{-3} , see next section) were generally of poorer quality than the undoped samples (see plate 2b), the dopant seemingly affecting the crystal growth.

Zinc oxide single crystals were also grown using the sealed tube C.V.T. method, with NH_4Cl as the transport agent, fig. (2.1b). With

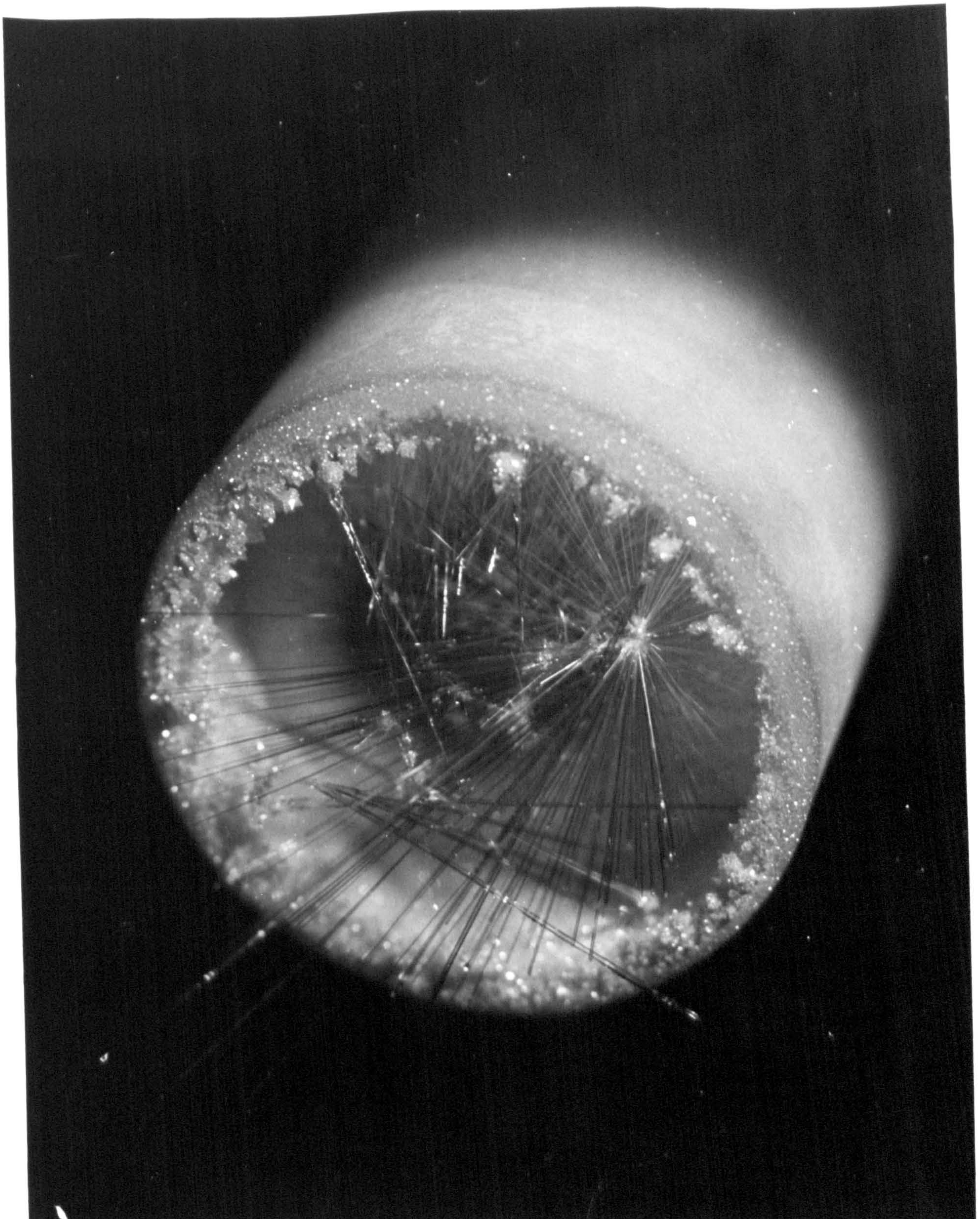

Plate 1:

Zinc oxide crystals grown by the vapour phase oxidation of zinc iodide; photograph of the growth tube after a 20 hour run

this technique single crystals of up to 5 mm diameter and 1 cm length were obtained, but, since the axial ratio for crystals grown by this method was, typically, c : a = 1 : 1, with approximately equal areas of prism and polar faces, they were unsuitable for our surface studies. This method was therefore subsequently abandoned.

2.2 Zinc oxide bulk characterisation

2.2.1 Resistivity measurement

The accurate measurement of the bulk resistivity of small (10μ to 500μ diameter : 1 cm length) zinc oxide needles presents an appreciable problem. The four-point probe technique requires making two electrical contacts to the needle along its length. Such small crystals are very brittle, tending to cleave perpendicular to the long c-axis, when any mechanical strain is applied. It was therefore necessary to design an apparatus to overcome this problem. The four-point probe apparatus that we used is shown in fig. (2.2). The small zinc oxide needle is placed across two metal plates being supported at either end by them. Good electrical contact is ensured by applying silver-dag. The middle two contacts were made by raising two columns of mercury,beneath the crystal, until they just make contact with the needle. These mercury contacts apply minimal strain to the crystal.

In the four-point probe technique a measured current is passed through the sample. The voltage across the middle two probes (measured on a high impedance voltmeter so that no current is drawn) is then a measure of the sample resistance. Using this method, the problem of contact resistance (notoriously high for zinc oxide) can be overcome.

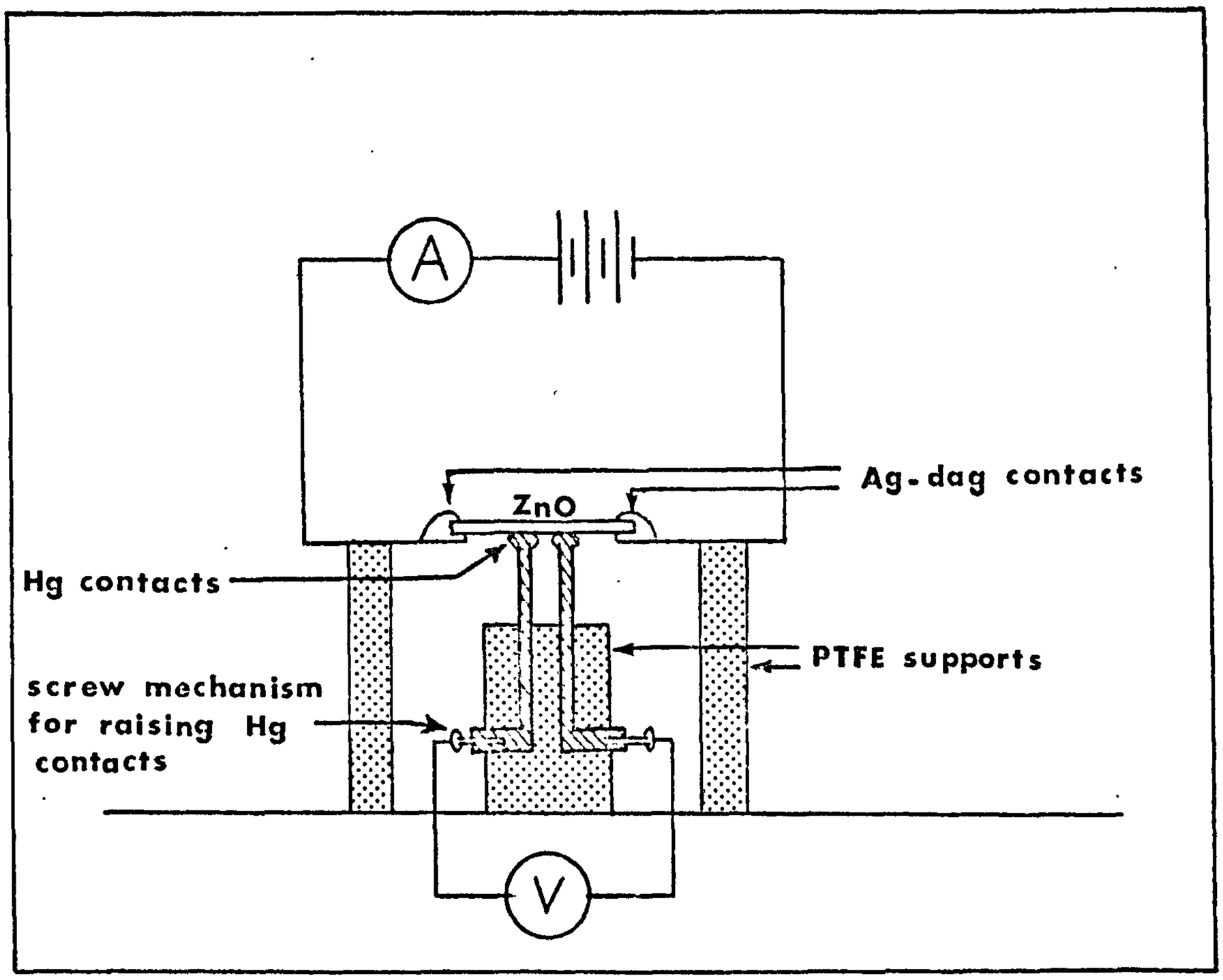

Fig. 2.2:

Four point probe apparatus for measuring zinc oxide crystal resistivity

The sample resistivity ρ is then given by

$$\rho = Va/Al \quad \Omega\,cm.$$

Where A (amps) is the measured current, a (cm^2) is the cross-sectional area of the crystal sample (A/a, the current density is assumed uniform across the middle two probes); V (volts) is the voltage across the middle two probles and l (cm) is the distance between them. The conductivity, σ $(\Omega\ cm)^{-1}$, is then simply given by $1/\rho$. From the measured conductivity the carrier density can be calculated using the relation

$$\sigma = ne\mu$$

where n is the carrier density (cm^{-3}), e is the electronic charge (1.6×10^{-19} Coulombs) and μ the bulk mobility (cm^2/Vs). The value of the room temperature bulk mobility of undoped single crystal zinc oxide varies between 150 and 200 cm^2/Vs (Utsch and Hausmann 1975, by measuring the Hall effect mobility). For indium doped single crystals, the bulk mobility is lower, with values between 40 and 130 cm^2/Vs (Hausamnn and Teuerle 1972, by measuring the Hall effect mobility).

The undoped single crystals grown by the oxidation of zinc vapour gave values for their room temperature resistivity of 10-20 Ωcm. This corresponds to a carrier density of $(2.4 \pm 0.6) \times 10^{15}$ carriers per cm^3 (using an average value of μ = 175 $cm^2/V.s$), typical for zinc oxide samples of high purity. The undoped zinc oxide crystals grown by the oxidation of zinc iodide showed resistivity values varying from run to run, and with their position in the growth tube. The resistivities were in the range 2 - 100 Ωcm, corresponding to carrier densities between 3.6×10^{14} and 1.8×10^{16} carriers per cm^3. In general, those crystals at the end of the growth tube, (see section 2.1) situated in a good supply of oxygen, were of higher resistivity. Those crystals

growing further down the growth tube, where there is less oxygen, are slightly coloured yellow and have a lower resistivity, excess zinc probably accounting for the higher conductivity values. The low carrier concentrations overall, indicate crystals of high purity.

Indium doped single crystal needles were in general coloured light green. The value of the resistivity depended on the extent of doping (dependent on the position in the growth tube of the indium oxide boat - see section 2.1) and was in the range $\rho = 1\ \Omega$ cm to $\rho = 10^{-2}\ \Omega$ cm. Using an average value of the bulk mobility for indium doped crystals of ca. 80 cm^2/Vs these resistivities corresponded to carrier concentrations in the range ca. 8×10^{16} per cm^3 and ca. 8×10^{18} per cm^3. Assuming that each indium dopant atom provides one electron to the conduction band, then the above carrier densities are a measure of the bulk indium concentration. The highly doped samples (ca. 8×10^{18} carriers per cm^3) have an indium concentration of up to 200 p.p.m.

2.2.2 Bulk analysis

The bulk impurity analysis for zinc oxide 'puratronic' powder is shown at the beginning of this chapter.

The bulk impurity analysis of undoped zinc oxide single crystal needles (obtained from Professor Heiland) using the technique of emission spectroscopic micro analysis is as follows:

Copper	1 p.p.m.
Iron	0.5 p.p.m.
Magnesium	0.4 p.p.m.
Silicon	5 p.p.m.
Aluminium	1.5 p.p.m.

2.3 Zinc oxide surface characterisation

2.3.1 Scanning electron microscopy (S.E.M.)

Scanning electron micrographs of small (ca. 10μ to 500μ diameter : 1 cm length) zinc oxide single crystal needles are shown in plates 2 and 3.

The scanning electron micrographs of as-grown undoped crystals in general reveal little discernible structure (down to 250$\mathring{A}$, the claimed resolution of the instrument) showing crystals of good quality. The S.E.M. of the undoped needle grown by the oxidation of zinc vapour (plate 2.3, showing a ca. 200μ diameter needle) shows no surface structure, but occasionally the undoped needles grown by the oxidation of zinc iodide vapour revealed steps on the prism faces perpendicular to the c-axis, (plate 2.4, showing a ca. 400μ diameter needle with a few microns high steps occurring every 10-100μ) particularly the larger (ca. 500μ diameter) crystals. The small (10μ - 100μ diameter) undoped needles, grown by zinc iodide oxidation, were of good quality. In general where steps appeared on the prism faces, they were perpendicular to the c-axis, however, very rarely, crystals were observed with steps parallel to the c-axis (plate 2.1, showing a ca. 500μ diameter needle).

Indium doped small (10μ to 500μ diameter : 1 cm length) needles, grown by the oxidation of zinc iodide vapour, were generally of poorer quality, with the heavily doped samples showing very unstable growth and multi-facetting (plate 3.1). The prism faces of such crystals (plate 2.2, showing a ca. 500μ diameter indium doped needle, with a bulk resistivity ρ = (1.5 ± 0.5) x 10^{-2} Ω cm corresponding to an indium doping concentration of ca. 5 x 10^{18} per cm^3) show platelet-like growth in the $\langle 10\bar{1}0 \rangle$ directions.

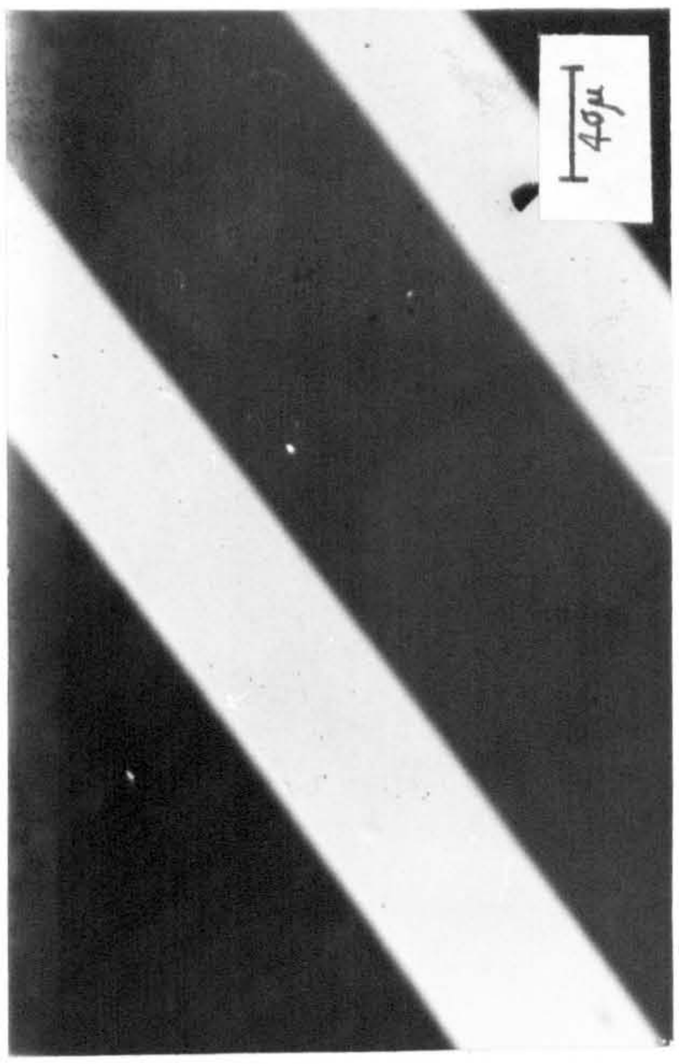

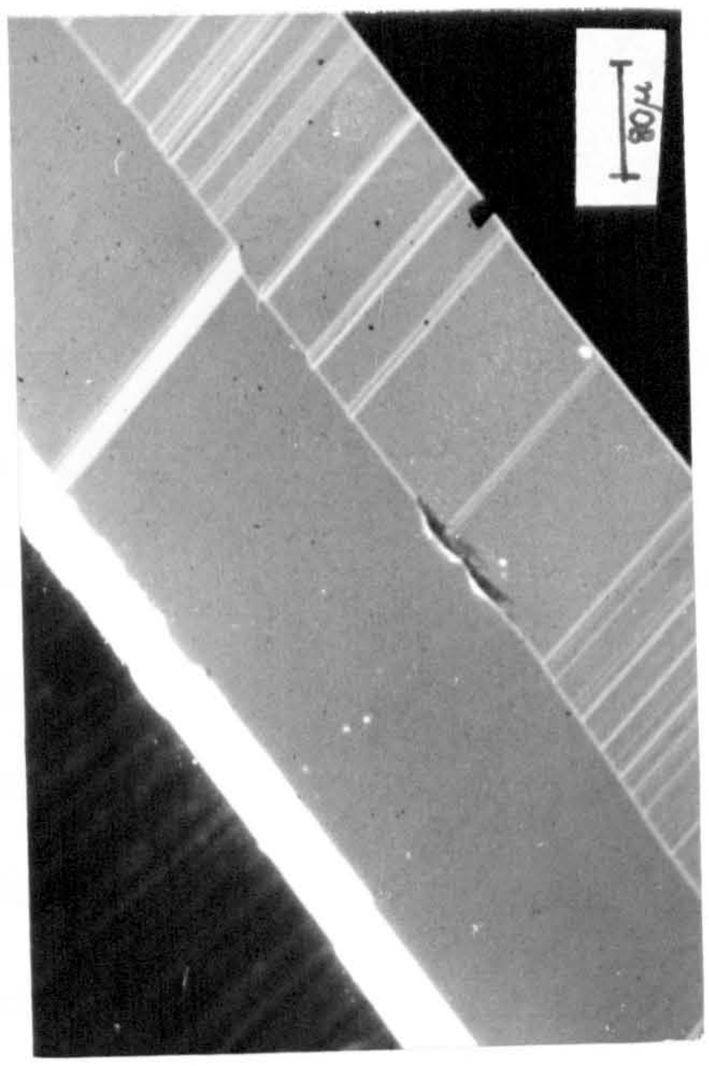

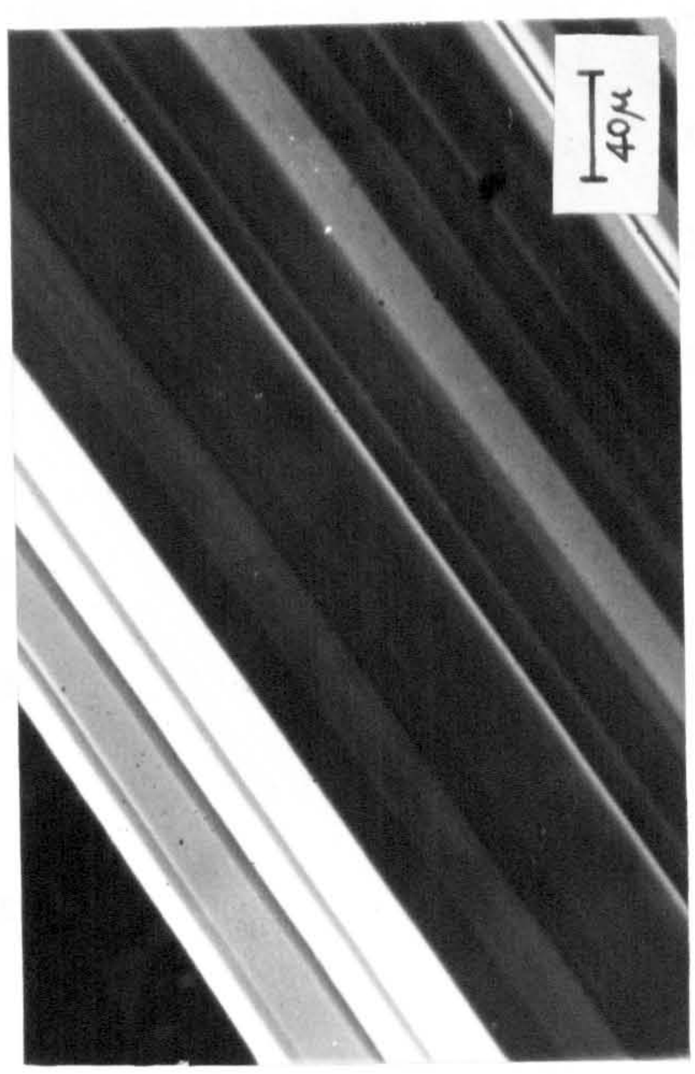

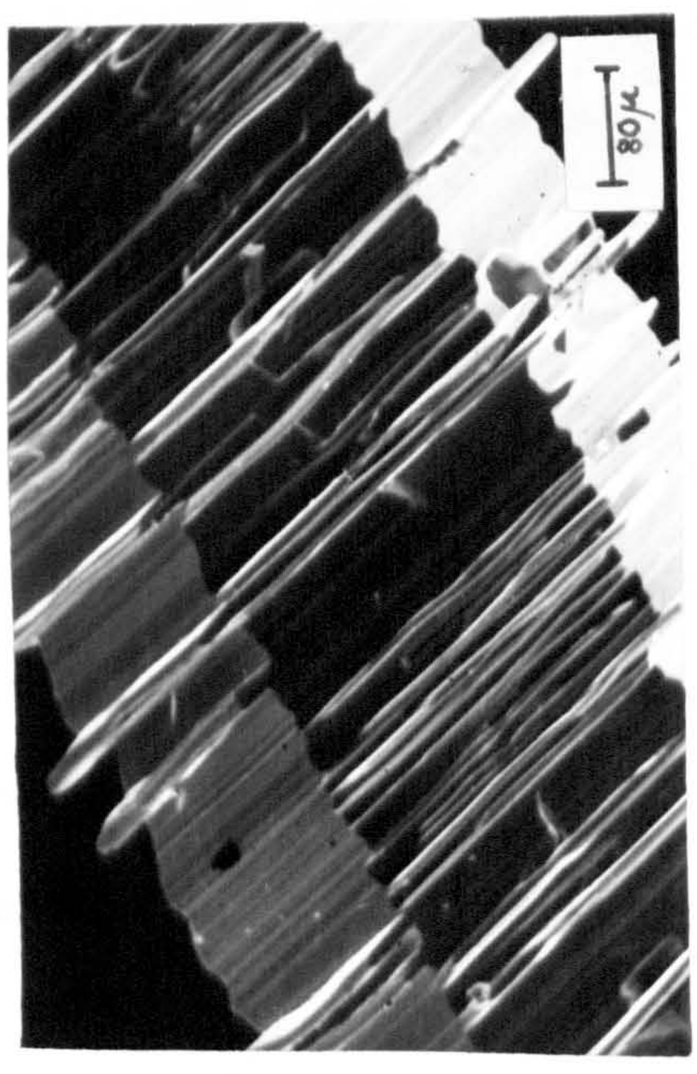

Plate 2:

Scanning electron micrographs of 'as grown' zinc oxide single crystal needles

The S.E.M.'s of etched (5 minutes in 6% hydrochloric acid) crystals are shown in plate 3 (2 to 6). Plate 3.1 shows the terminating polar plane in an 'as grown', indium doped (ρ = (1.5 ± 0.5) x 10^{-2} Ω cm corresponding to 5 x 10^{18} indium atoms per cm^3) 500μ diameter needle. Here, little structure is observed on the polar plane. After etching, such a polar plane can reveal etch patterns as shown in plate 3.2 (500μ diameter indium doped needle). This is the typical etching behaviour of the polar surfaces of a twinned crystal. (Leysen and van Hove 1972, Heiland and Kunstmann 1969.) Such a twinned crystal is terminated by a polar face containing both zinc type 0001 and oxygen type $000\bar{1}$ surfaces, where the etch pattern reveals the different etching behaviour of the two types of surface. The dark area is the 0001 oriented zinc surface which is not attacked by the etchant, the light area shows the etch-pitted $000\bar{1}$ oxygen surface. The characteristic triangular etch pits on the prism faces of zinc oxide needles are shown in plates 3.3 and 3.4 (500μ diameter, undoped needle grown by vapour phase oxidation of zinc). These have been shown (Heiland et al. 1963, Klein 1965) to point in the $\langle 0001 \rangle$ direction. The prism faces shown sub-micron etch-pitting whereas the $000\bar{1}$ oxygen polar face shows large (several microns) etch pits. Plate 3.5 (indium doped 100μ diameter needle) shows how a good quality 'as grown' indium doped needle reveals steps on the prism faces after etching (0.2μ high steps every 2μ).

Plate 3.6 (100μ diameter, undoped needle) shows that the growth of small (less than 100μ) whiskers occurs with a resulting axial hole. The growth mechanism of such hollow whiskers has been explained (Sharma, 1970) by the movement of multiple axial dislocations.

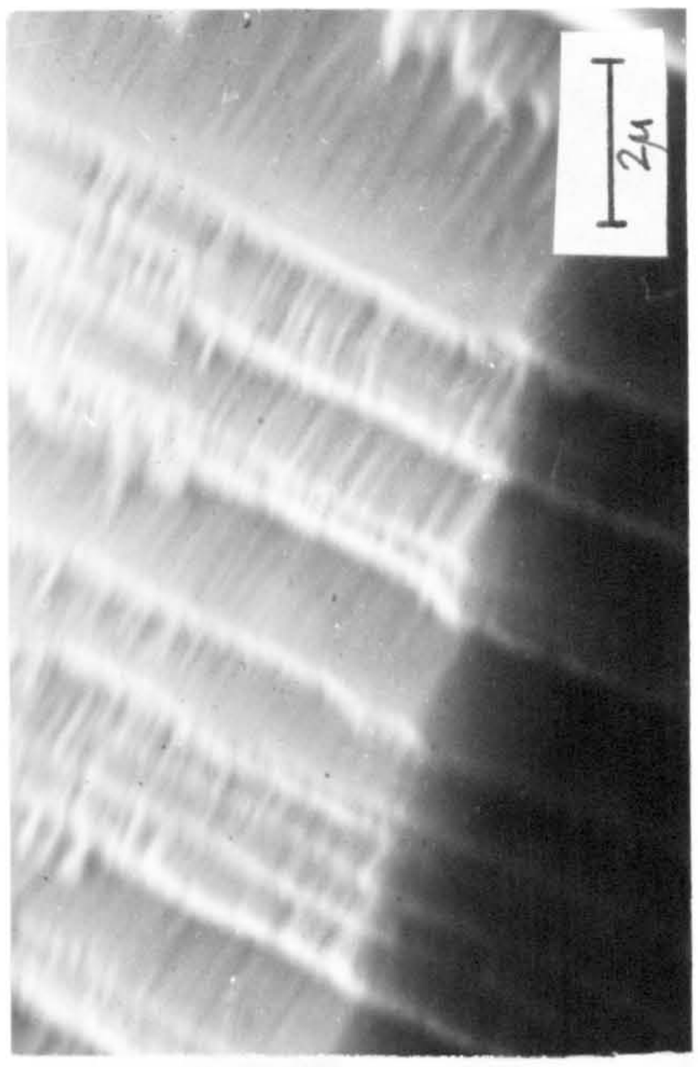

5

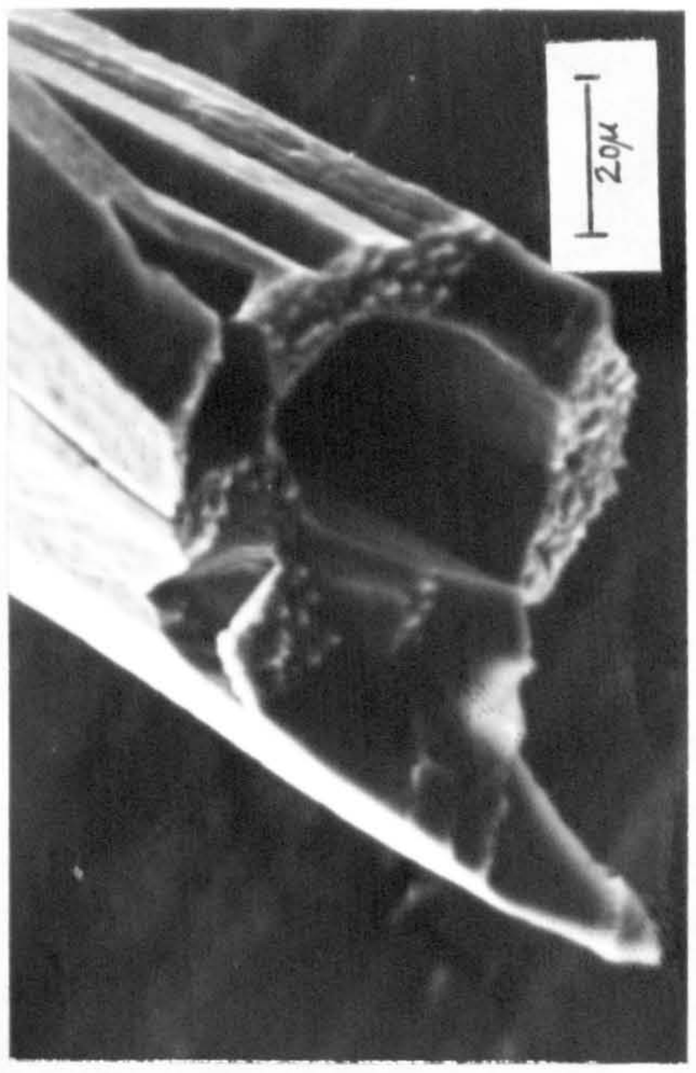

6

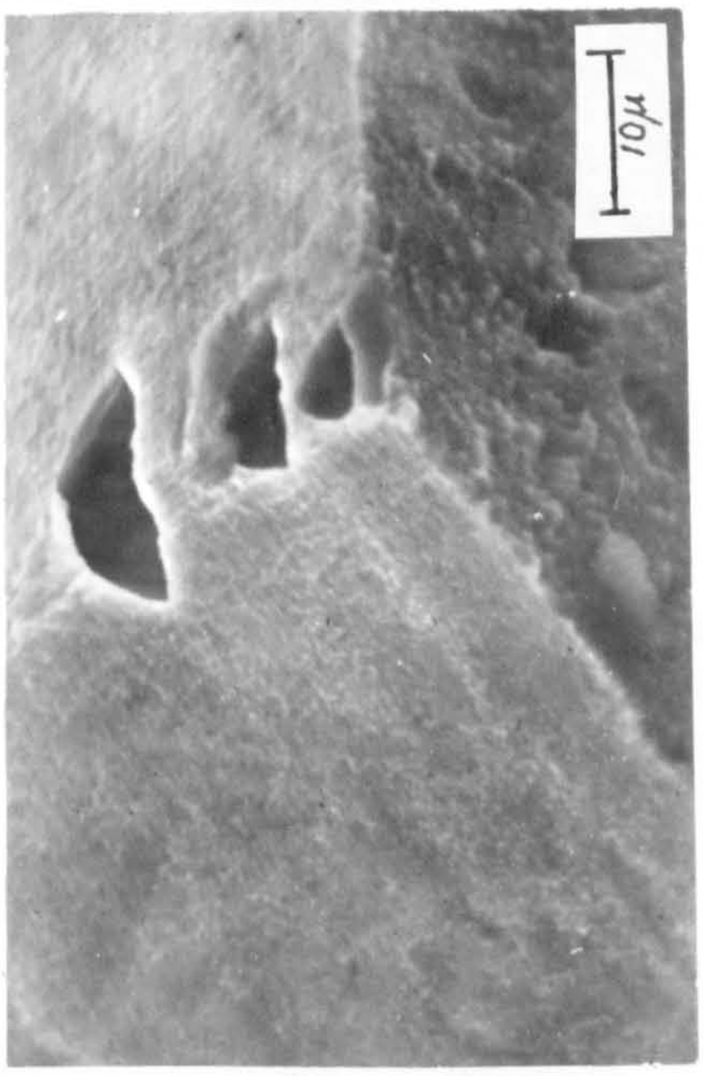

3

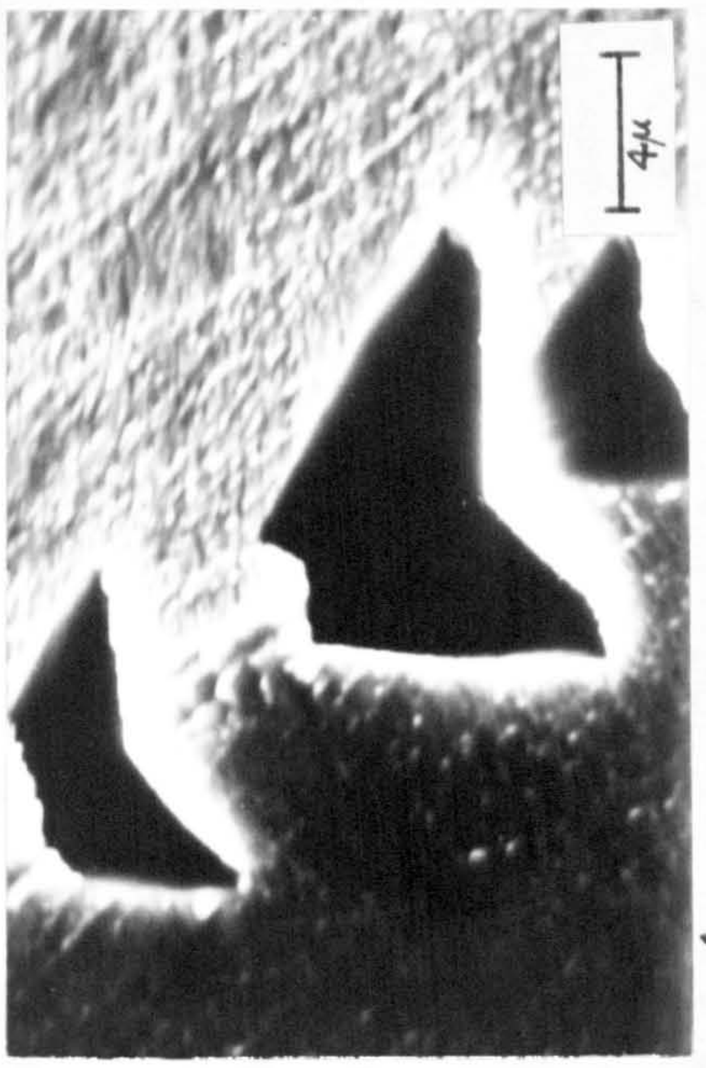

4

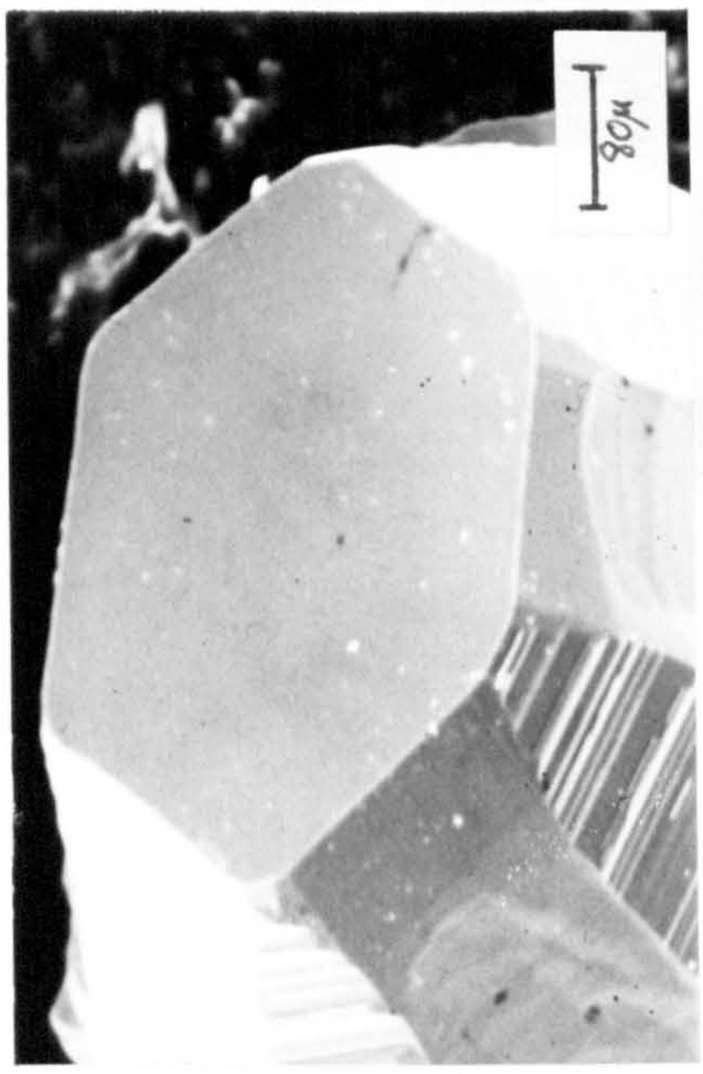

1

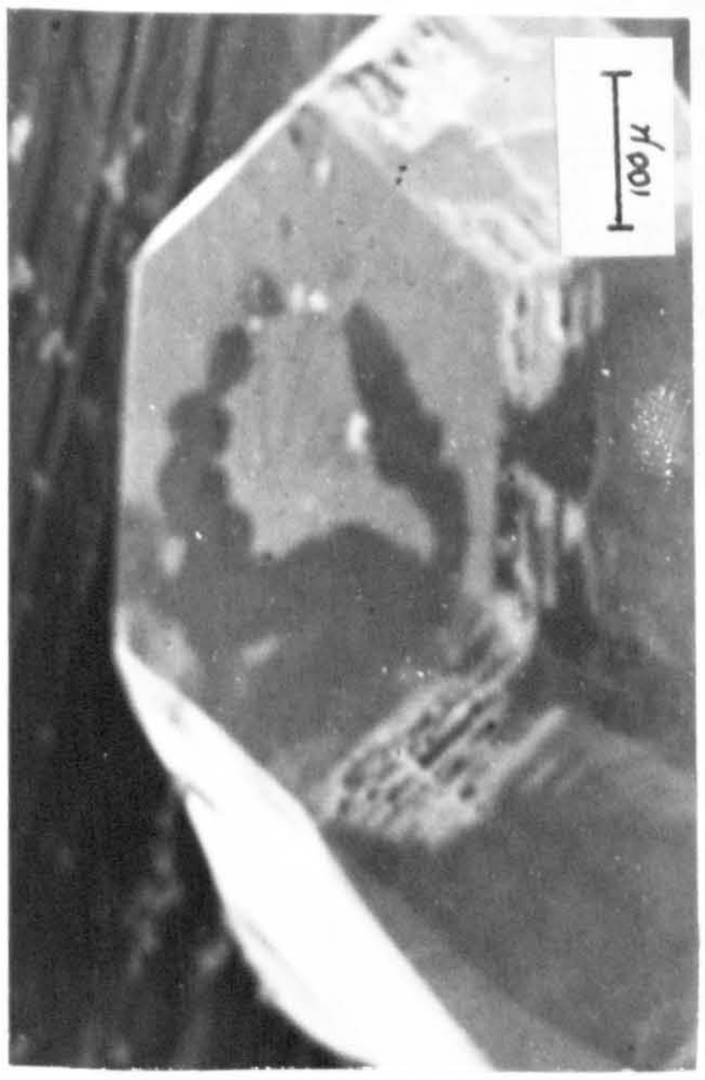

2

Plate 3:

Scanning electron micrographs of etched (5 minutes in 6% HCl) zinc oxide single crystal needles

Plate 4:

Scanning electron micrograph of zinc oxide 'puratronic' powder

The S.E.M. of zinc oxide 'puratronic' powder is shown in plate 4. This is for the zinc oxide powder sample taken out of the reaction tube after our series of oxygen adsorption experiments (see chapter 3), that is, after repeated cycles of heating up to 600°C. The micrograph shows that appreciable sintering has occurred at this temperature. The average particle size by surface area measurement (see section 2.3.3) of ca. 3μ diameter (specific surface area 3500 cm^2/g) agrees well with typical particle size of a few microns shown on the micrograph.

2.3.2 X-ray oscillation photographs

The X-ray oscillation camera used in these experiments was the Unicam Instruments Ltd. S.25 single crystal goniometer. Zinc oxide single crystal needles were mounted on the goniometer head with their long, c-axis vertical. X-rays (Cu-Kα , nickel filtered, at electron energy 40 kV and 20 mA) impinged on the single crystal needle perpendicular to the c-axis, and the needle was oriented so that X-rays impinged normal to one of the prism faces. The crystal was set to oscillate, $\pm 7\frac{1}{2}^{\circ}$ about the normal position. Reflected X-ray beams were recorded on a photographic plate mounted concentrically around the single crystal needle.

The zinc oxide prism face can be either of the $10\bar{1}0$ type or of the $11\bar{2}0$ type. When the crystal is oriented with its prism face (say, for example, $10\bar{1}0$) normal to the incident X-rays, and allowed to oscillate by $\pm 7\frac{1}{2}^{\circ}$ about that normal, only reflections from that prism face (and some from other planes) will be observed : reflections from the other type of prism plane (say, for example $11\bar{2}0$, which is at 30° to the $10\bar{1}0$ plane) will be absent.

By measuring the horizontal distance, x, between the back reflected spots and the zero order back reflection on the X-ray photograph, and

knowing the radius of the camera, r, the Bragg angle θ can be calculated, where 2θ, the angle between the reflected beam and the zero order beam is given by

$$2\theta = 360x/2\pi r$$

where r in our case is 3 cm. Using the Bragg relation, namely

$$n\lambda = 2d\sin\theta$$

where n is the order of the reflection, λ the wavelength of the X-radiation (λ for Cu-Kα_1 x-rays is 1.54×10^{-8} cm), and d is the inter-planar spacing, and the measured value of θ, d/n can be calculated. For all crystals examined a value of $d = (2.83 \pm 0.04) \times 10^{-8}$ cm for the first order reflection (n = 1) was obtained.

The hexagonal unit cell perpendicular to the c-axis for zinc oxide is shown below.

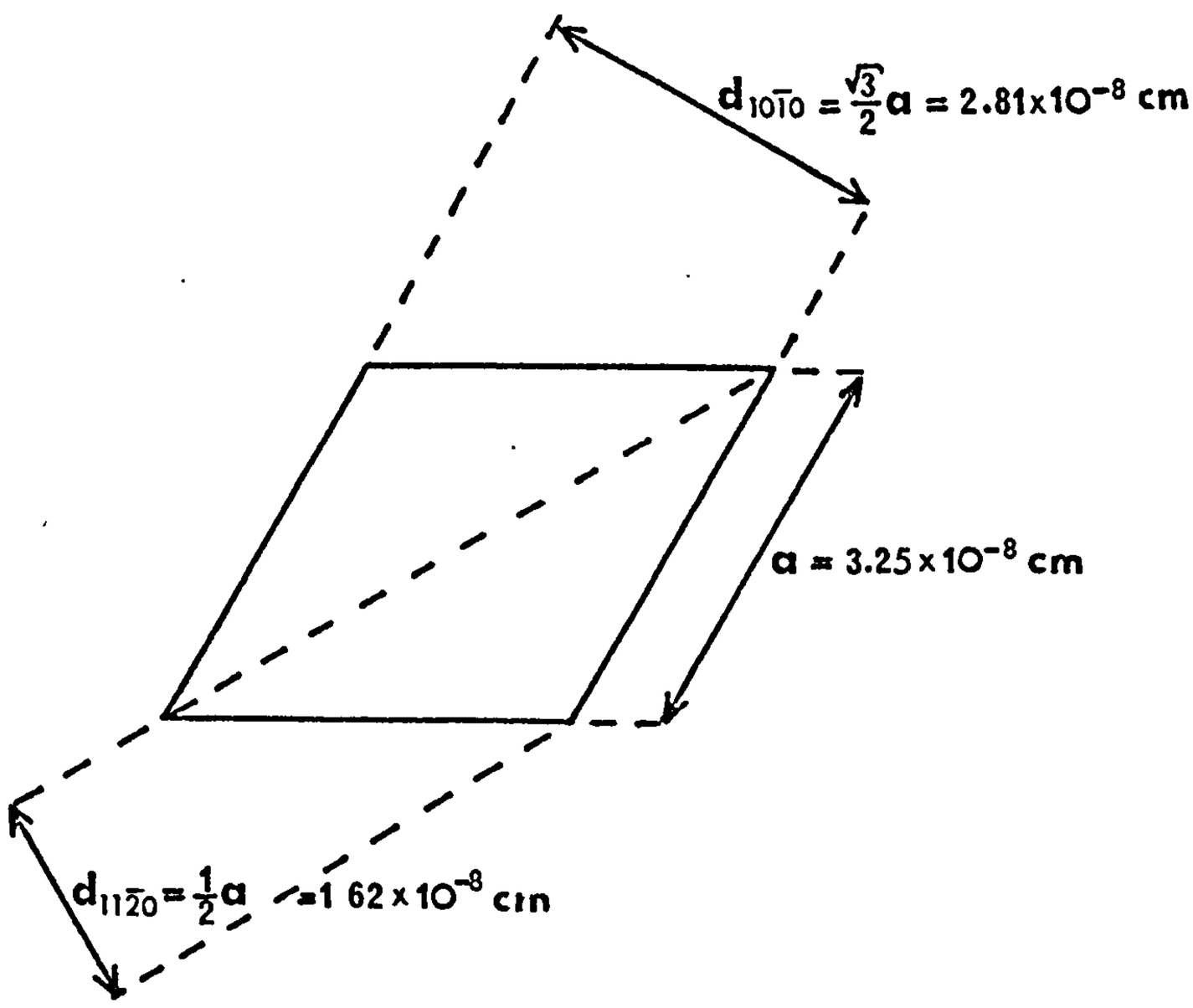

Here the unit cell dimension is a = 3.25 x 10^{-8} cm, the $10\bar{1}0$ inter-planar distance is 2.81 x 10^{-8} cm, and the $11\bar{2}0$ inter-planar distance is 1.62 x 10^{-8} cm, as shown. Clearly then, the value of d = (2.83 ± 0.04) x 10^{-8} cm is for reflections from the $10\bar{1}0$ face.

The crystals examined by this technique were: large undoped needles ca. 5 mm daimeter : 2 cm length) and small undoped needles (ca. 10μ - 500μ diameter : 1 cm length), grown by the oxidation of zinc vapour, and, small (ca. 10μ- 500μ diameter : 1 cm length) undoped and indium doped needles grown by oxidation of zinc iodide vapour. In all cases (20 crystals examined in all) the prism face was of the $10\bar{1}0$ type.

2.3.3 Surface area measurement

Surface areas of zinc oxide were found by measuring the Krypton adsorption isotherm at liquid nitrogen temperature (77.4 K). The apparatus is a standard B.E.T. apparatus but with a thermistor pressure gauge and stainless steel shut off valves, both with a small dead space volume, essential when measuring low surface areas.

The B.E.T. equation describing the liquid nitrogen Krypton adsorption isotherm is

$$\frac{P}{N(P_0-P)} = \frac{(C-1)}{N_M C}\cdot\frac{P}{P_0} + \frac{1}{N_M C}$$

which relates the number of molecules adsorbed, N, to the pressure P, where P_0 is the saturated vapour pressure of Krypton at liquid nitrogen temperaturee (2.75 torr), N_M is the number of molecules forming a monolayer and C is a constant relating the heat of adsorption of Krypton in the first layer, E_1, to the heat of adsorption in subsequent layers, which is the heat of liquefaction, E_L, by

$$C = \exp -\left(\frac{E_1-E_L}{kT}\right)$$

So, a plot of P/P_0 against $P/N(P_0-P)$ should yield a straight line of slope $(C-1)/N_MC$ and intercept $1/N_MC$. $1/N_M$ is then found by summing the slope and the intercept. N_M , which is the number of molecules forming a monolayer then gives the surface area, when σ, the effective cross-sectional area per molecule is known, by

$$\sigma N_M = \text{surface area.}$$

For Krypton, reported values of σ are in the range 19.5 to 22.6 x 10^{-16} cm^2 . We used a value of 20 x 10^{-16} cm^2 throughout.

Surface areas measured were in the range 200-500 cm^2 for zinc oxide single crystal needles and 3000 cm^2 for powdered zinc oxide. The results are reported later in this chapter.

2.4 Surface cleanliness

2.4.1 ESCA Studies

ESCA studies (electron spectroscopy for chemical analysis) were performed on several zinc oxide single crystal samples on the ESCA-3 machines (Vacuum Generators Ltd.) at the University of Bradford and at Imperial College, London. These experiments employed the technique of X.P.S. (X-ray Photoelectron Spectroscopy) using aluminium Kα radiation (8 kV, 50 mA) throughout. The spectra recorded on the University of Bradford machine were taken directly onto a chart recorder, whilst those at London were taken from a computer output,where the signals are summed over several scans. Results for three different samples, namely: large (ca. 0.3 cm diameter by 1 cm long) undoped single crystals; small (ca. 200μ - 500μ diameter by 1 cm long) undoped single crystals, and; small indium doped needles, are shown separately and discussed below.

(i) *Large undoped single crystal zinc oxide:* The spectra shown in fig. (2.3) are for the surface of large undoped single crystal zinc oxide needles at various stages of pre-treatment. The crystals were mounted in a gold holder attached to the ESCA probe (which was capable of being heated to 500^{o}C). Spectrum A shows the as-grown needles with photo-electron signals due to zinc and oxygen of the substrate crystal plus carbon contamination. After 15 minutes of heating at 520 K in vacuum (ca. 10^{-7} torr) Spectrum B shows a reduced carbon 1s photoelectron peak together with an increased zinc signal. Further heating at 620 K in oxygen at a pressure of 0.03 torr for 15 hours showed a further decrease in the carbon 1s signal, increased substrate peaks, and now new peaks attributed to sodium, potassium and chlorine contaminants as indicated in Spectrum C, Still further heating at 770 K in 0.03 torr oxygen for 45 minutes revealed a further reduced carbon peak whilst all other signals became proportionately stronger : Spectrum D.

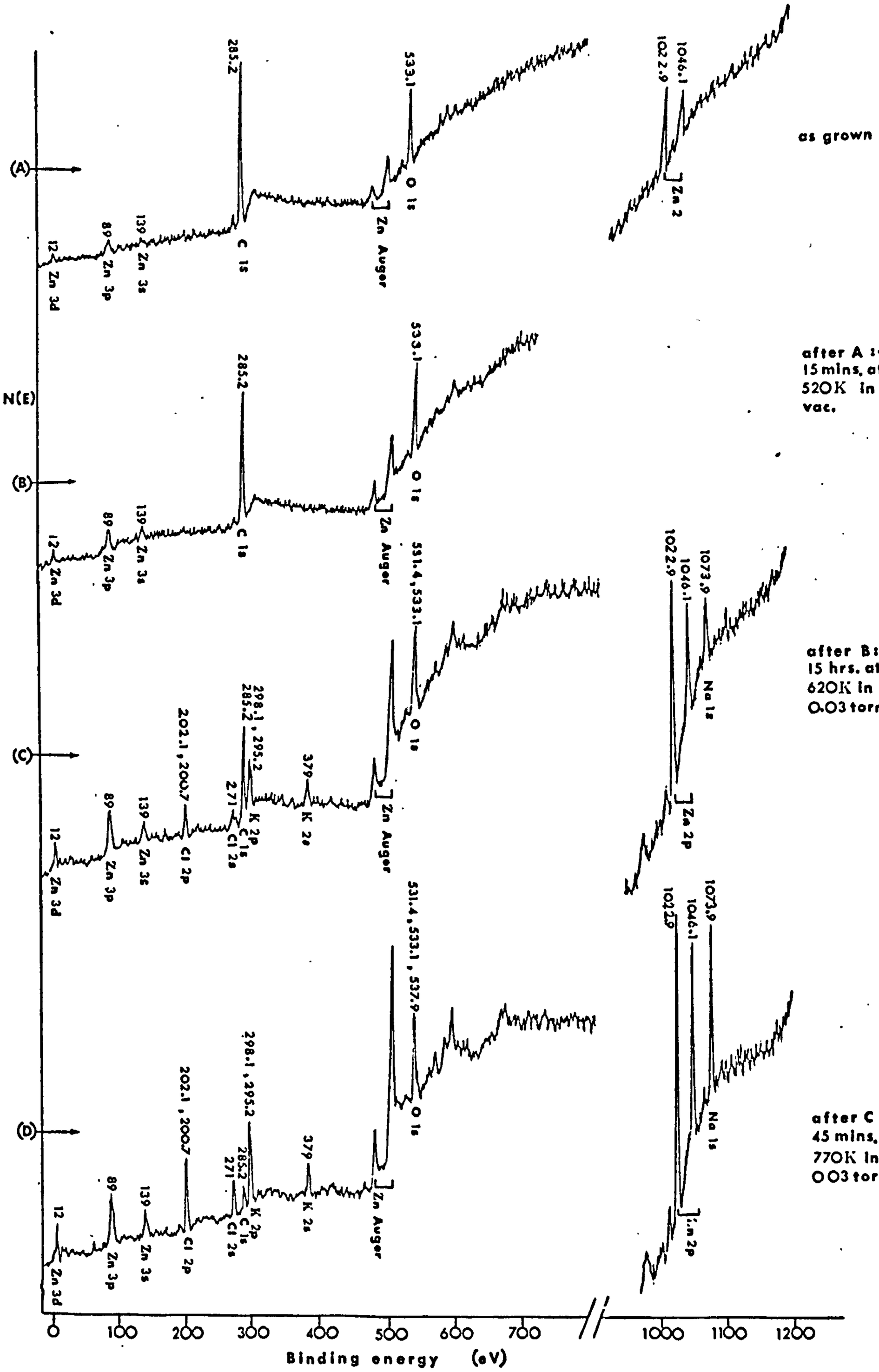

Fig. 2.3:

X.P.S. spectra of large undoped zinc oxide needles for various pre-treatments

For the as-grown crystals - Spectrum A, it is quite reasonable to suggest a model in which the zinc oxide surface is covered with a layer of carbon contaminant (whether this be elemental carbon or carbon containing hydrocarbons is discussed later). The further contamination of the crystal surface by potassium, sodium and chlorine, after heating to 620 K in 0.03 torr of oxygen for 15 hours - Spectrum C, is postulated to occur by out-diffusion of these impurities from the bulk of the zinc oxide; contamination of the crystal surface via the gold holder is rejected since these impurities do not occur in our gold. Therefore, it is suggested that these elements come to the surface and form a separate surface phase, in this case a mixed sodium, potassium chloride phase, intruded between the zinc oxide surface proper and the carbon overlayer. An alternative model in which these impurities come to the surface but remain within the zinc oxide lattice forming a highly doped zinc oxide surface layer is rejected since the total extent of such segregation would require inordinately high solubilities of these impurity elements in the zinc oxide - see later.

A quantitative estimate of the extent of the surface contamination, based on the model proposed above can be made by comparing the total photoelectron yield of the substrate crystal (in this case the total zinc atom photoelectron yield) with the photoelectron yield due to the overlayers.

Using the formalism developed by Henke (1972), Madey et al. (1973) have shown that the total no-energy-loss photoelectron yield from a bulk element of infinite thickness is given by

$$Y = K I_x \mu \rho \lambda \qquad [2.1]$$

where K is a constant dependent on the instrument geometry, I_x is the incident X-ray flux, μ is the mass X-ray absorption coefficient ($cm^2\ g^{-1}$), ρ is the sample density ($g\ cm^{-3}$), and λ, which is here assumed independent of photoelectron kinetic energy, is the photoelectron mean free path (cm). Now, the total no-energy-loss photoelectron yield from a solid of thickness, d, is given by Madey et al. (1973) as

$$Y = \frac{KI_x \mu \rho}{\cos\theta} \int_0^d \exp-\left[\frac{z(1+\mu\rho\lambda)}{\lambda \cos\theta}\right] dz \qquad [2.2]$$

where θ is the electron take-off angle (assumed to equal 45^o). This gives, assuming $\mu\rho\lambda \ll 1$, which in our case is always satisfied,

$$Y = K I_x \mu \rho \lambda \left(1 - \exp-\{d/\lambda\cos\theta\}\right) \qquad [2.3]$$

For an overlayer of thickness, d, the total photoelectron yield is then given by

$$Y_0 = K I_x \mu_o \rho_o \lambda_o^o \left(1 - \exp-\{d/\lambda_o^o \cos\theta\}\right) \qquad [2.4]$$

where subscripts 'O' refer to the overlayer and λ_o^o is the mean free path of the overlayer electrons through the overlayer. The photoelectron yield from the substrate, Y_s, is given by the total photoelectron yield of the clean substrate, $Y_{s,\infty}$, corrected for the attenuation of the signal through the overlayer, i.e.

$$Y_s = Y_{s,\infty} \exp-\{d/\lambda_s^o \cos\theta\} \qquad [2.5]$$

where λ_s^o is the mean free path of substrate photoelectrons through the overlayer. The photoelectron yield of the clean substrate is given by

equation [2.1], whence

$$Y_{s,\infty} = K I_x \mu_s \rho_s \lambda_s^s \qquad [2.6]$$

where all subscripts 's' refer to the substrate and λ_s^s is the mean free path of substrate electrons through the substrate. Combining equations [2.4], [2.5], [2.6] gives then, for the total relative photoyield

$$\frac{Y_0}{Y_s} = \frac{\mu_0 \rho_0 \lambda_0^0 \left(1 - \exp-\{d/\lambda_0^0 \cos\theta\}\right)}{\mu_s \rho_s \lambda_s^s \exp-\{d/\lambda_s^s \cos\theta\}} \qquad [2.7]$$

and when $d > \lambda_0^0 \cos\theta$ and $d > \lambda_s^0 \cos\theta$ (i.e. for thick overlayers where $d \geqslant 15\text{Å}$ for λ_0^0 and $\lambda_s^0 \doteqdot 15\text{Å}$ and $\theta = 45^\circ$ - see later) this becomes

$$\frac{Y_0}{Y_s} = \frac{\mu_0 \rho_0 \lambda_0^0}{\mu_s \rho_s \lambda_s^s} \exp-\{d/\lambda_s^0 \cos\theta\} \qquad [2.8]$$

All experimental photoyields are expressed, in arbitrary units, as the total area under the photoelectron peak normalised to 100eV analyser energy, and 1500eV electron kinetic energy, allowing for the $(\text{K.E.})^{-1}$ dependence of the sensitivity of detection of ESCA-3.

Spectrum A of fig. (2.3) for the as grown crystal sample gives photoelectron yields (in arbitrary units) for zinc 1.56, for carbon 5.76 and for oxygen 1.96. In all cases photoyields are measured by taking the area under the main line peaks which for the above case are the zinc 2 , carbon 1s and oxygen 1s peaks. This is a good approximation, since nearly all of the photoyields occur for these elements at their main line peaks. The oxygen 1s signal occurring at 533.1eV binding energy (where the binding energy in eV relative to the Fermi level (B.E.)

is given by B.E. = $h\nu - E - \Phi$ where $h\nu$ is the X-ray photon energy, E is the electron kinetic energy and Φ is the sample work function) is shown later to be due to a surface adsorbed species and not to the zinc oxide substrate oxygen. It is supposed that this oxygen is in an adsorbed layer over the carbon contaminant layer. To estimate the carbon overlayer thickness equation [2.8] is used, since in this case $d > \lambda \cos\theta$ - see later. When comparing the carbon and zinc signals it is assumed that they are equally attenuated through the oxygen overlayer and in any event the attenuation is small since the oxygen overlayer is only of the order of 1 monolayer, (see later). Values of μ and ρ in equation [2.8] are for zinc, μ_{Zn} is 5.02 x 10^3 cm^2 g^{-1} (Henke and Ebisu, 1974) and ρ_{Zn}, the density of zinc in zinc oxide, is 4.5 g cm^{-3} and for carbon μ_c is 7.18 x 10^2 cm^2 g^{-1} (Henke and Ebisu, 1974) and ρ_c, the density of carbon, is ca.2 for amorphous carbon. θ is taken as 45°. Values of λ are generally not well known. Brundle (1974) lists some mean free path lengths, and for many materials a value of $\lambda = 15 \pm 5\text{Å}$ is a good estimate. So, as a first approximation all λ values are taken to be 15Å. This gives, using equation [2.8] a carbon overlayer 38Å thick.

When there are several overlayers on a substrate, and the thickness of the topmost layer is d, then the photoelectron intensity due to the topmost layer, Y_o, relative to the substrate photoelectron intensity, Y_s, is given by

$$\frac{Y_o}{Y_s} = \frac{\mu_o \rho_o \lambda_o^o (1 - \exp-\{d/\lambda_o^o \cos\theta\})}{\mu_s \rho_s \lambda_s^s \exp-\{d_T/\lambda_s^o \cos\theta\}} \qquad [2.9]$$

where d_T is the total thickness of all the overlayers and exp - $(d_T/\lambda_s^o \cos\theta)$ is the extent to which the substrate signal is attenuated through these overlayers. If now for the topmost layer $d < \lambda_o^o \cos\theta$, then

equation [2.9] becomes

$$\frac{Y_0}{Y_s} = \frac{\mu_0 \rho_0 d}{\mu_s \rho_s \lambda_s^s \cos\theta} \exp\{d_T / \lambda_s^o \cos\theta\} \qquad [2.10]$$

and, using the relation

$$\rho_0 d = \sigma M / N \qquad [2.11]$$

where σ is the coverage per cm^2, M is the mass number of the overlayer atoms and N is 6.023×10^{23} $mole^{-1}$, then equation [2.10] becomes

$$\frac{Y_0}{Y_s} = \frac{\sigma \mu_0 M}{N \mu_s \rho_s \lambda_s^s \cos\theta} \exp\{d_T / \lambda_s^o \cos\theta\} \qquad [2.12]$$

So, for the topmost oxygen containing layer, putting $Y_0 = 1.96$ and $Y_s = 1.56$, together with appropriate values for the other parameters, into equation [2.12] namely, μ_0 for oxygen is 1.6×10^3 (Henke and Ebisu, 1974), M = 16, λ_s^s and λ_s^o are taken as 15Å and d_T, the total overlayer thickness, is taken to be approximately equal to the carbon layer thickness which is 38Å (since the oxygen overlayer is very much less than the carbon layer thickness), gives for the total oxygen overlayer coverage, $\sigma = 1.56 \times 10^{15}$ atoms cm^{-2}.

Spectrum B of fig. (2.3) shows photoyields for zinc of 2.6, oxygen 2.34 and carbon 4.3 in arbitrary units. This gives, using the above procedure a carbon overlayer 28Å thick and an oxygen overlayer coverage of 2.9×10^{15} atoms cm^{-2}.

Spectrum C indicates peaks for sodium, potassium, chlorine, carbon and oxygen contaminants. Photoyields expressed in arbitrary units are for sodium 0.64, potassium 2.40, chlorine 1.68, carbon 3.04, oxygen 2.04

and for the zinc of the substrate 4.20. The oxygen photoyield is the total area under the 533.1eV binding energy peak - see later. Using the model where it is postulated that the sodium, potassium and chlorine are contained in a surface layer of (Na, K) Cl intruded between the substrate and carbon overlayer, equation [2.12] is used when comparing the photoelectron signal of the individual constituents of the (Na, K) Cl phase, Y_0 , relative to the substrate signal, Y_S , given that d_T is the total thickness of the (Na, K) Cl phase. The effect of the carbon and oxygen layers over this (Na, K) Cl phase is to attenuate the photoelectron signal from that phase, but, it is assumed that the substrate photoelectron signal is equally attenuated through these layers, and when comparing the yield of the (Na, K) Cl photoelectrons relative to the substrate photoelectron yield, the presence of the carbon and oxygen overlayers can be ignored, (the $\lambda \propto (K.E.)^{1/2}$ relationship shows that the mean free path and hence the extent of attenuation of photoelectrons through the carbon and oxygen overlayers will depend upon the kinetic energy of the photoelectron signals. The error introduced in assuming equal attenuations of the (Na, K) Cl and zinc signals will be less than the uncertainty of calculated thicknesses accepting that the value for λ of 15Å is, in the first place, only an estimate). Using values of μ_{Na} for sodium of 3.36×10^3 cm^2 g^{-1} , for potassium 1.48×10^3 cm^2 g^{-1} and for chlorine 1.02×10^3 cm^2 g^{-1} (Henke and Ebisu, 1974), together with the photoyields obtained from Spectrum C, gives in equation [2.12] values for atomic coverage for sodium, $\sigma_{Na} = 5 \times 10^{14}$ atoms cm^{-2} , for potassium $\sigma_K = 2.5 \times 10^{15}$, and for chlorine $\sigma_{Cl} = 2.8 \times 10^{15}$, where all other parameters are as before. This is consistent with a (Na, K) Cl phase ca. 17Å thick where the atom ratio Na : K is 1:5. Using the alternative model of a homogeneous

Zn, O, K, Na, Cl surface region the photoelectron signals for these species, together with relative sensitivity values for potassium of 0.85, sodium 2.09, chlorine 0.46 and zinc 4.24 (Wagner, 1972) gives a surface composition approximately ZnO $K_{2.8}$ $Na_{0.31}$ $Cl_{3.6}$ which appears non-sensible. It is of interest to note that, using the published relative sensitivity data, gives values for the relative numbers of potassium sodium and chlorine atoms very similar to those obtained using the overlayer model and consistent with a potassium rich (Na, K) Cl phase. Using equation [2.10] where d is the thickness of the carbon layer and d_T the total surface film thickness (thickness of (Na, K) Cl phase plus carbon overlayer thickness) gives a thickness for the carbon overlayer of 9Å. Using equation [2.12] putting d_T equals 26Å (9Å + 17Å) and other parameters as before, gives for the total oxygen coverage, 1.7×10^{15} atoms cm^{-2} .

Spectrum D of fig. (2.3) gives peaks whose photoyields expressed in arbitrary units are:- zinc 8.07, carbon 0.9, oxygen 0.2, potassium 4,54, chlorine 3.38 and sodium 2.08. Using the procedure outlined above gives a surface with a 17Å thick (Na, K) Cl layer containing 2.4×10^{15} potassium atoms cm^{-2} , 0.8×10^{15} sodium atoms cm^{-2} and 2.8×10^{15} chlorine atoms cm^{-2} , covered by a 2.3Å thick carbon layer and 1.9×10^{14} oxygen atoms cm^{-2} .

The oxygen 1s signals for each of the four spectra shown in fig. (2.3) were observed in detail by scanning around the 530eV binding energy region. Spectra A to D of fig. (2.4) correspond to A to D of fig. (2.3). After heating the as grown crystal for 15 hours at 620 K in 0.03 torr oxygen the peak at 533.1eV binding energy has fallen in height and another peak at 531.4eV has appeared (cf. Spectrum C, fig. (2.4)). Further heating at 770 K for 45 minutes in 0.03 torr oxygen results in a further

Fig. 2.4:

Oxygen 1s photoelectron signal of large undoped zinc oxide needles for various pre-treatments

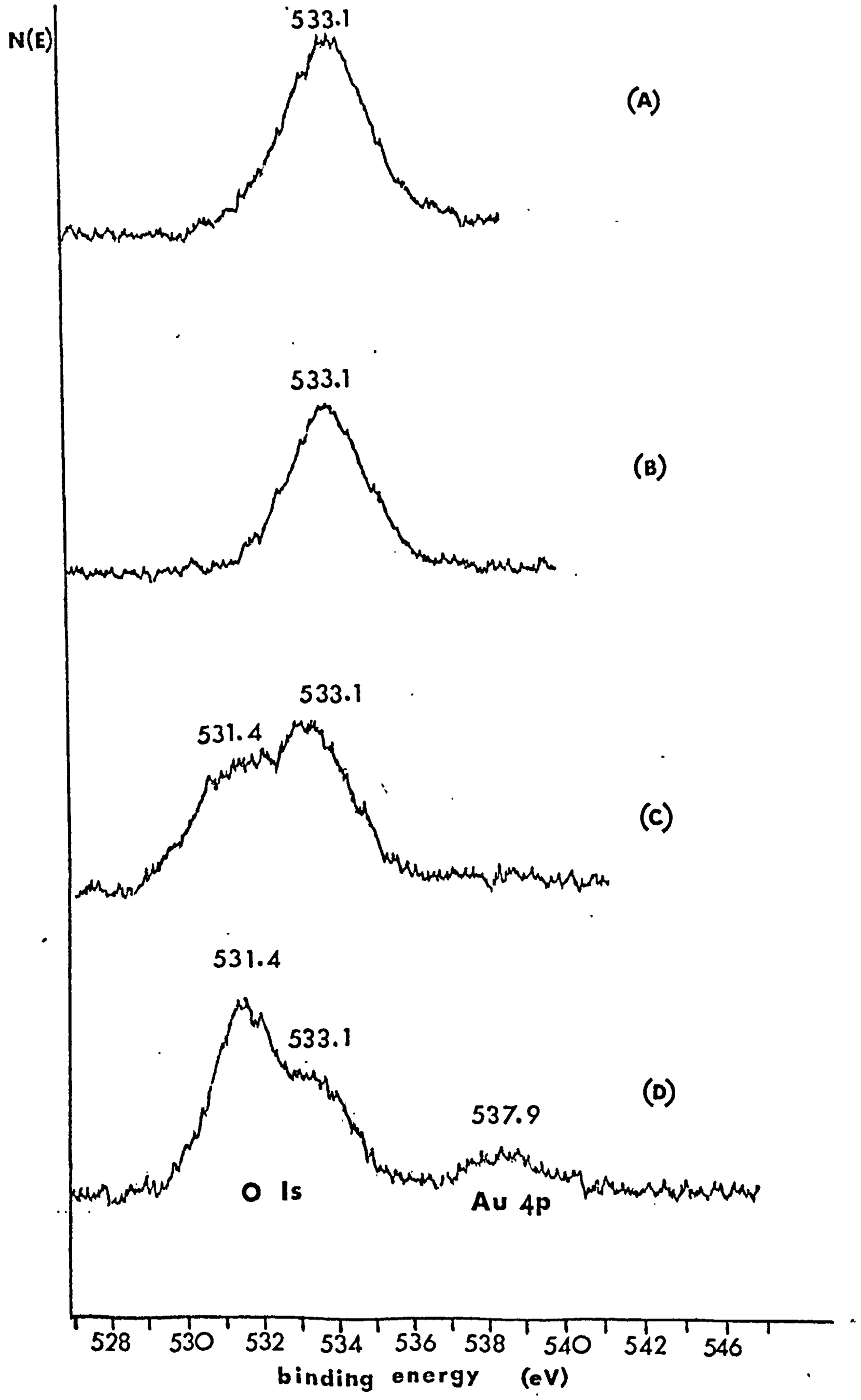

drop in the 533.1eV signal together with a rise in the 531.4eV signal and the appearance of a new peak at 537.9eV (cf. Spectrum D of fig.(2.4). It is felt that the increase in the 531.4eV peak is consistent with an increasing oxygen 1s signal from the oxygen of the zinc oxide lattice, as the surface overlayer thickness is progressively reduced. The signal at 533.1eV is thought to be due to a surface adsorbed species, possibly water. The signal at 537.9eV is thought to be the gold 4p peak due to the gold holder.

(ii) *Small undoped single crystal zinc oxide:* Fig. (2.5), Spectrum A shows the X.P.S. spectrum of as grown small (200μ - 500μ diameter by 1 cm long) undoped zinc oxide needles. Peaks occurring at 83.7eV and 336eV, 353eV are due to the gold 4f and 4d doublets of the gold holder. An unidentified doublet occurs at 405 and 412eV. The major contaminant is carbon. The total photoyield of carbon relative to zinc of the zinc oxide substrate is 1.84:6.75 (the total zinc photoyield was assessed by measuring the 991eV electron energy zinc Auger peak area and observing that for all the spectra taken the area of this peak relative to the zinc 2_p peak area is 1:1.70). Using the procedure adopted for the large crystals this gives, for the carbon overlayer, a thickness of 10Å. The coverage of the adsorbed oxygen species was not calculated since the detailed structure of the oxygen 1s signal was not recorded, however a coverage of 1 to 2 monolayers, as for the large crystals, seems a reasonable estimate. After heating at 790 K for 25 minutes in 0.03 torr oxygen, Spectrum B of fig. (2.5) shows a decreased carbon 1s signal, increased substrate signals and new peaks due to potassium and sodium. Since no chlorine is detected it is postulated that the surface phase formed by out-diffusion of these elements is a mixed sodium, potassium oxide. The measured photoyields of Spectrum B of zinc 11.0, potassium 0.5

Fig. 2.5:

X.P.S. spectra of small undoped zinc oxide needles for various pre-treatments

A : as grown

B : after A, 25 mins at 790K
in 0.03 torr O_2

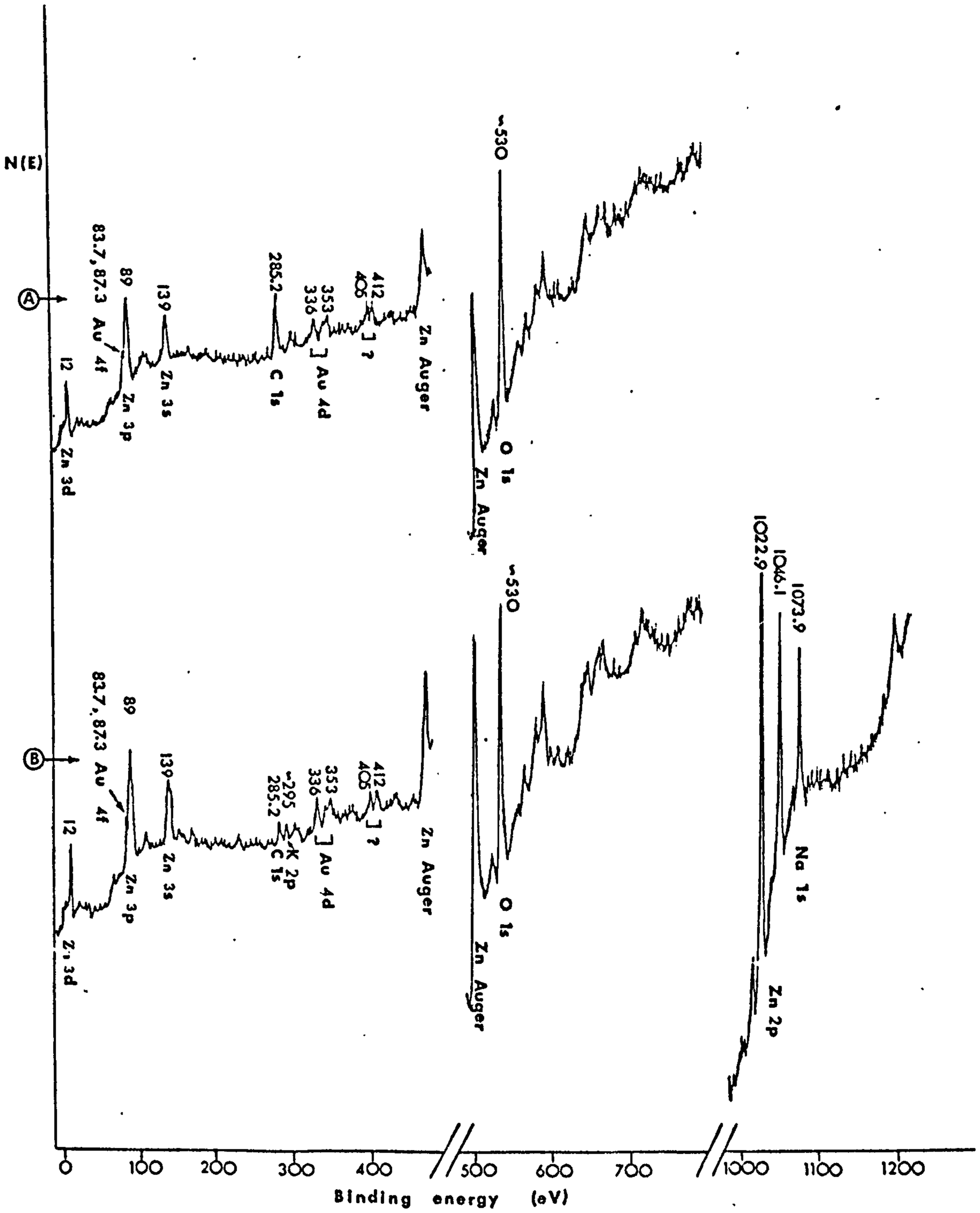

and sodium 1.37 give a 4.5Å thick phase containing 6.7×10^{14} potassium atoms and 1.4×10^{15} sodium atoms cm^{-2}. (Using a model where the out-diffused material forms a metallic phase gives a 7.6Å thick phase containing 1×10^{15} sodium atoms cm^{-2} and 5×10^{14} potassium atoms cm^{-2}.) The total carbon photoyield of 0.64 gives an overlayer thickness of 4Å.

Fig. (2.6) shows the X.P.S. scan taken on the ESCA-3 machine at Imperial College. The spectra are computer summed electron counts for 40 repeated scans. Spectrum A of fig.(2.6)is for an as grown crystal treated at 1170 K for 24 hours in 1 atmosphere of oxygen. Peaks due to potassium at 298.1 and 295.2eV, and sodium at 1073.9eV binding energy are shown to be entirely absent. This is consistent with the evaporation from the surface of the oxides of these elements. The sodium and potassium oxides produced by out-diffusion of the elements from the bulk are volatile at 1170 K and evaporate from the surface. The remnant carbon contamination is thought likely to occur mostly on the gold holder - see later.

Further heating in vacuum for 1 hour at 870 K shows that the surface has not been re-contaminated by sodium or potassium and that no new impurities have out-diffused onto the surface at this higher temperature - Spectrum B, fig. (2.6). After this treatment it can be observed that the carbon signal has increased. In addition the gold 4d photoelectron intensity has fallen whilst the zinc 2p signal has risen. This would suggest that the increased carbon signal is due to contamination at the gold holder arising from the surface diffusion of carbon along the probe support. That the carbon contamination of the zinc oxide single crystal surface can be entirely removed by heating in oxygen is shown later.

Fig. 2.61 X.P.S. spectra of small undoped zinc oxide needles for various pre-treatments

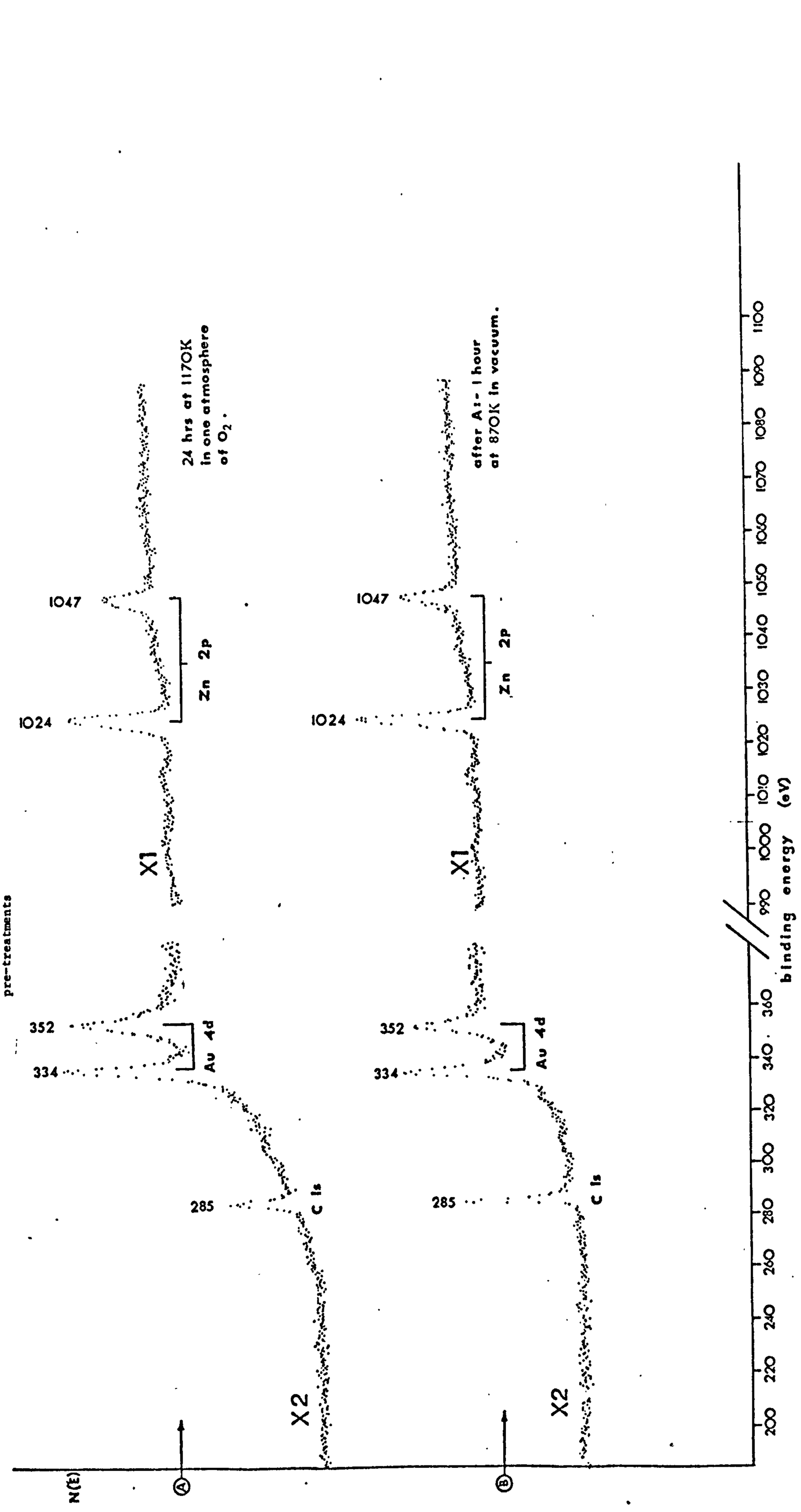

The following may be concluded from the above XPS experiments on undoped zinc oxide single crystals.

(a) When the small crystals are heated to 790 K only sodium and potassium are identified as out-diffusing from the bulk (where an estimated total of 2×10^{15} impurity atoms cm^{-2} have out-diffused). This surface contamination by these elements is shown to be removed by heating in oxygen to 1170 K, that no other contaminants out-diffuse at this temperature and that subsequent heating to 870 K in vacuum shows no further re-contamination by out-diffusion.

(b) When the large crystals are heated to 620 K in oxygen, sodium potassium and chlorine out-diffuse from the bulk. The surface phase thus formed is of a mixed sodium potassium chloride resulting from the out-diffusion of a total of 5.8×10^{15} impurity atoms cm^{-2} . The chlorides of sodium and potassium are appreciably volatile at ca. 1100 K and it is expected that these too should be removed by heating at this temperature.

(c) Non-volatile surface out-diffused contaminants, for example calcium shown by other workers (Fiermans et al., 1973, and Hopkins et al. 1975) have been shown not to be present. It must be stressed here that a crystal containing any significant amount of such bulk impurity will on heating lose this impurity to the surface and that the subsequent involatile surface layer cannot be cleaned by heating alone. For our crystals all impurities that do out-diffuse on heating are shown to be removable (i.e. volatile).

(d) The total relative amount of out-diffused material of the large crystals compared to the small in general shows the different surface to volume ratios of the two crystals, i.e. for large crystals where the surface to volume ratio is low, for a given bulk impurity concentration, the surface concentration of these impurities when they out-diffuse should

be higher than for small crystals where the surface to volume ratio is high. For the large crystals the total surface impurity concentration (5.8×10^{15} atoms cm^{-2}) is about three times that of the small (ca. 2×10^{15} atoms cm^{-2}), although the bulk Na impurity concentration appears higher in the small crystals .

(e) The total extent of carbon contamination for the as grown large crystals (ca. 40Å) is about four times that for the small (ca. 10Å). That this can be removed by heating in oxygen is shown by X.P.S. and it will be shown later that the surface can be entirely cleaned of this contaminant.

(f) The error in the value of all surface impurity concentrations which may amount to several tens percent, due to the uncertainty of mean free path values sheds doubt on the accuracy of the absolute magnitude of these impurity concentrations. Nevertheless, this does not invalidate comparison between different crystal samples of the different extents of surface contamination, and the way the level of contamination changes with treatment conditions.

(iii) *Small indium-doped single crystal zinc oxide:* Small (ca. 200μ - 500μ diameter by one cm long) indium-doped zinc oxice sinple crystals grown by the oxidation of zinc iodide, with a bulk resistivity of 2×10^{-2} Ω cm, were used for these X.P.S. experiments. The aim, here, was to measure the extent of surface segregation of indium on the as grown single crystals by taking the X.P.S. spectrum, calaculating the surface indium concentration and progressively sputtering away this surface layer whilst monitoring the corresponding change in indium concentration. The results of these experiments are shown in fig. (2.7). Peaks at 446eV and 454eV binding energy are due to indium 3d photoelectrons. The 401eV peak is possibly assigned to nitrogen 1s. The total surface concentration of indium is

Fig. 2.7:

X.P.S. indium 3d and zinc Auger signals for various argon ion bombardment pre-treatments

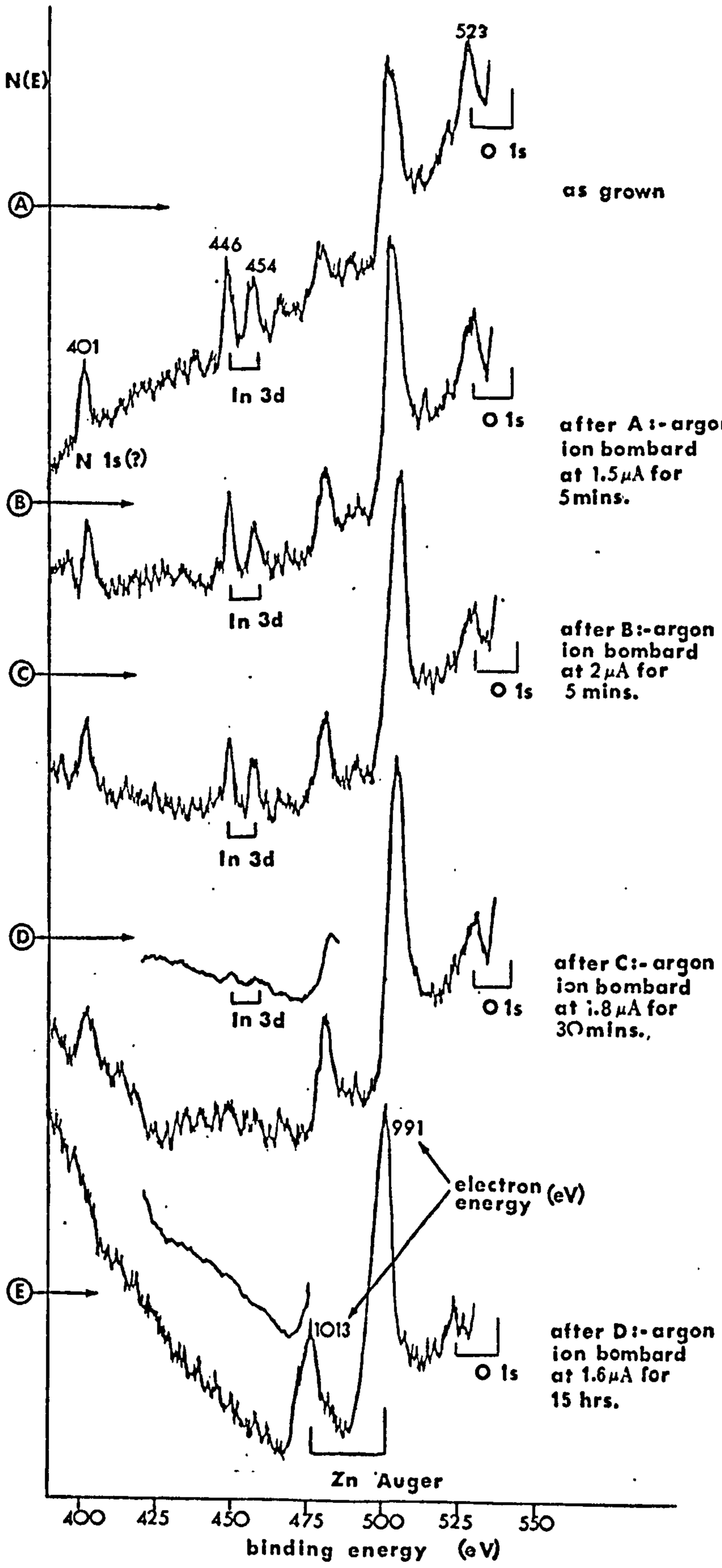

analysed using an overlayer model where an indium oxide (In_2O_3) phase overlays the zinc oxide substrate. Using the model of a homogeneous indium-doped zinc oxide surface phase gives inordinately high indium doping concentrations, vastly exceeding published saturation solubilities, and this model is rejected. Using a value of the indium relative sensitivity of 4.0 (Jorgensen and Berthou, 1972) gives a homogeneous surface phase of composition $ZnO\ In_{0.3}$.

The total surface indium coverage is estimated by comparing the indium photoyield (area of the indium 3d peaks) with the zinc photoyield (by comparing with the 991eV K.E. zinc Auger peak and observing that the zinc 2p photoyield is 1.7 times the zinc Auger peak area). This gives for the as grown crystals a relative photoyield Y_{In}/Y_{Zn} that equals 0.34 - Spectrum A. Using equation [2.12] with $\mu_{In} = 3.17 \times 10^3$ cm^2 g^{-1} (Henke and Ebisu, 1974) and M = 115, and all other parameters as before, this gives an indium oxide phase ca. 3Å thick containing 9.34×10^{14} indium atoms per cm^2. After 5 minutes argon ion bombardment at 5 μA current the relative photoyield has dropped to 0.19. This corresponds to a 1.9Å thick indium oxide layer containing 5.84×10^{14} indium atoms cm^{-2} - Spectrum B fig. (2.7). After a further 5 minutes bombardment at 2 μA the relative photoyield has decreased to 0.13, corresponding to a 1.4Å phase with 4.21×10^{14} indium atoms cm^{-2}. Bombarding for 30 more minutes at 1.8 μA shows only a very small indium photoyield that can only be detected above the noise level by altering the time constant of the noise filter and scanning across the energy range more slowly (time constant changed from 10 seconds to 33 seconds and scan speed 3 times smaller) - fig. (2.7), Spectrum D. The relative photoyield is estimated at 0.020 giving a 0.24Å thick indium oxide surface layer containing 7.3×10^{13} indium atoms cm^{-2}. An indium free zinc oxide surface is revealed after 15 hours bombardment at 1.6 μA - Spectrum E.

2.4.2 Extent of surface carbon contamination using mass spectrometer

Small undoped single crystal needles and whiskers of zinc oxide (ca. 50μ diameter by 1 cm long) were used in these experiments. The zinc oxide samples were from two sources,namely those grown by oxidation of zinc iodide and those grown by oxidation of zinc.

The zinc oxide sample, as grown,are introduced into a silica reaction chamber into which was passed oxygen at ca. 0.08 torr at a known flow rate. The flow rate of gases exiting from the reaction chamber was measured on a mass spectrometer. A full description of apparatus and experimental technique follows in the next chapter.

Fig. (2.8) shows the change in flow rate, in molecules s^{-1} of oxygen, water, carbon monoxide and carbon dioxide as the sample temperature was increased at a linear heating rate. The sample was zinc oxide grown by oxidation of zinc iodide vapour, and had a total surface area of 450 cm^2 . As the temperature increases the oxygen flow rate decreases, above ca. 200^{o}C, due to the oxidation of surface carbon contaminants, and eventually goes to zero showing that all the oxygen gas is being used up in the oxidation reaction. The water flow rate goes up with increasing temperature and peaks at ca. 350^{o}C. Both CO and CO_2 flow rates progressively increase with increasing temperature showing an increasing rate of carbon oxidation with increasing temperature. At ca. 550^{o}C (ca. 920 K) a pronounced extra increase in the CO and CO_2 flow rates is followed by a peak at ca. 620^{o}C (ca. 1100 K). This temperature is very close to the temperature at which oxygen is shown to come out of the surface lattice - see later. It is, therefore, very reasonable to suggest that, at this temperature, surface carbon is reacting with oxygen in the surface lattice of zinc oxide. The total area under these peaks of enhanced flow rate, at around about

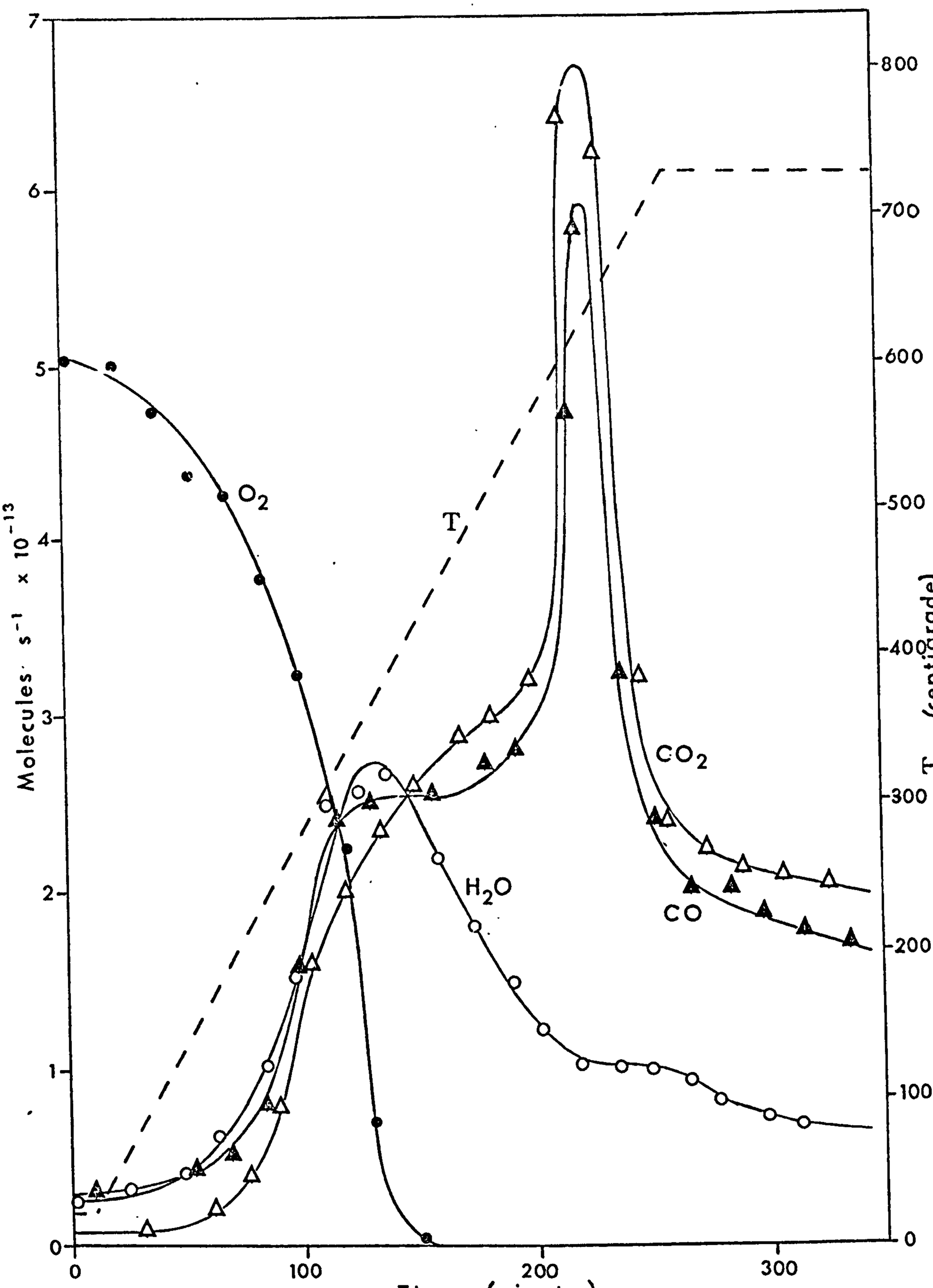

Fig. 2.8:

Analysis of the gas phase during the oxidation of surface impurities on 'as grown' small undoped zinc oxide needles

620°C, gives the total number of lattice oxygen atoms removed as 4×10^{14} cm^{-2}. This represents ca. 2/3 of a lattice layer. This extent of damage of the surface lattice is not tolerable and would require that the zinc oxide sample is heated below 550°C until all carbon contamination is removed. The high proportion of carbon monoxide resulting from the surface carbon oxidation reaction is consistent with the oxidation of carbon in an insufficient supply of oxygen: and, indeed the oxygen flow rate falls to zero at ca. 400°C.

The total area under all flow curves gives the total number of molecules produced. When normalised to unit surface area, this gives 1.05×10^{15} molecules of carbon dioxide cm^{-2}, 9.4×10^{14} molecules of carbon monoxide cm^{-2} and 5.2×10^{14} water molecules per cm^{-2}. This then gives a total carbon contamination of ca. 2×10^{15} carbon atoms cm^{-2}. Now, since the total amount of water evolved from the surface is only one quarter of the total number of carbon atoms it is presumed that the majority of the surface carbon contamination is due to elemental carbon, and that even if the carbon contamination was due to fully unsaturated hydrocarbon, the reaction $2(CH)_x + 2O_2 \longrightarrow CO + CO_2 + H_2O$ would give equal amounts of all three product gases and the water flow curve would follow those of carbon monoxide and carbon dioxide. This is not observed. The water is assumed to arise from a surface adsorbed layer on top of the carbon contaminant layer (cf. X.P.S. work). This run was discontinued after about 350 minutes when the zinc oxide was at 720°C.

A second run, fig. (2.9), showed the oxygen flow rate decreasing as the temperature increased, with corresponding increases in the carbon dioxide, carbon monoxide and water peaks. After heating to ca. 600°C

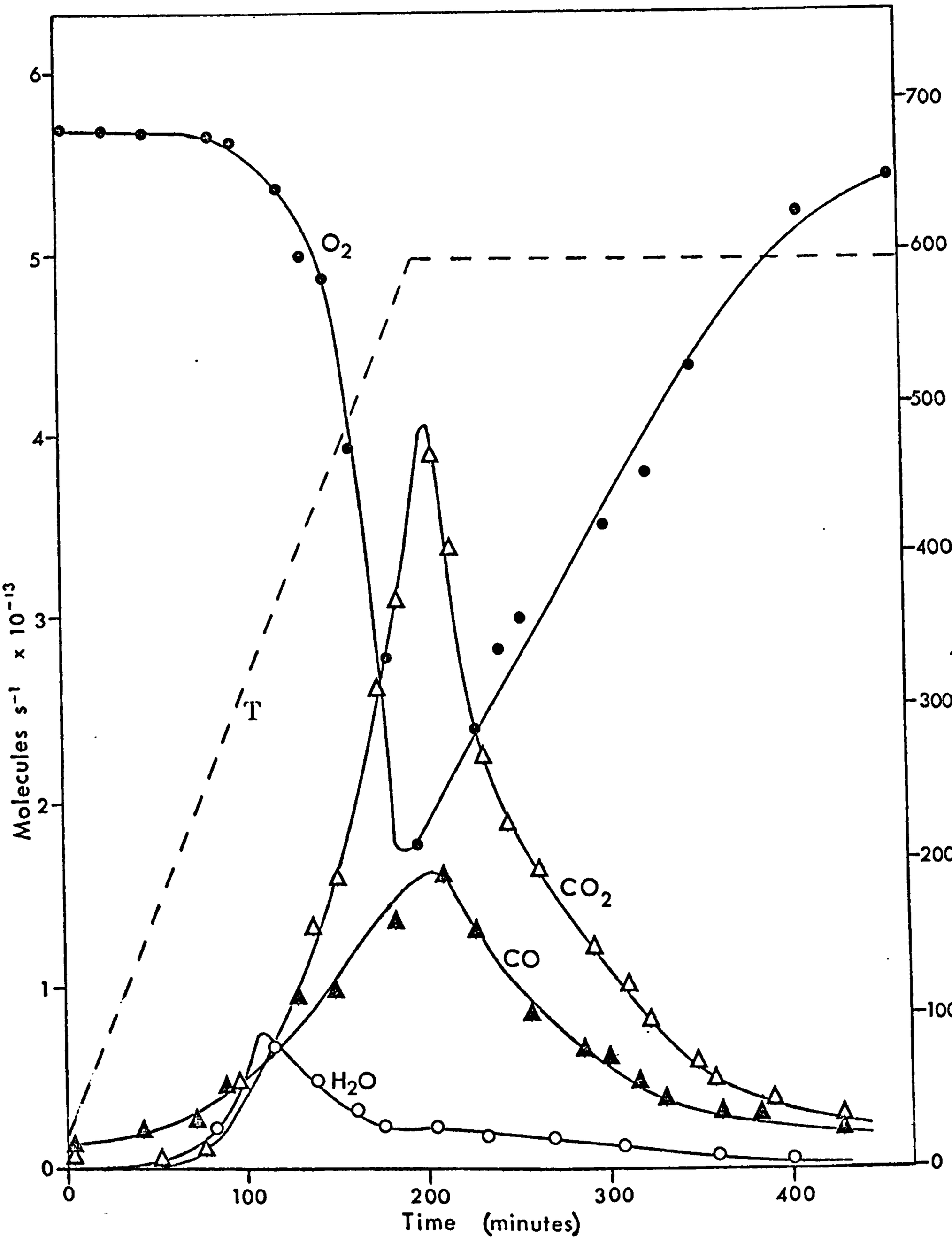

Fig. 2.9:

Analysis of the gas phase during the second cycle of oxidation of surface impurities on small undoped zinc oxide needles

and leaving at this temperature, the oxygen flow rate reached a minimum and then increased, finally to return to its original flow rate. This indicates that all the surface carbon contamination had been oxidised away, and indeed, the carbon monoxide and carbon dioxide flow rates return to their background value, which is close to zero. Total areas under the flow curves give 6.7×10^{14} molecules of carbon dioxide evolved, 3.9×10^{14} molecules of carbon monoxide and 1.16×10^{14} water molecules. Notice that now there is a sufficient oxygen supply and the oxidation products show twice as much carbon dioxide as carbon monoxide.

The total surface carbon contamination, which is given by the sum of those obtained in the two runs, is 3.1×10^{15} carbon atoms per cm^2 .

A similar experiment performed on the undoped small zinc oxide single crystals grown by the oxidation of zinc vapour showed a total surface carbon contamination that is very similar to the above, namely 3.2×10^{15} carbon atoms per cm^{-2}.

2.5 Summary

The zinc oxide samples used in our adsorption and catalysis experiments, described in the remainder of this thesis, are listed below.

(i) *Zinc oxide 'puratronic' powder:* 1g of this powder was used, with a total surface area by Krypton B.E.T. of 3500 ± 300 cm^2 , corresponding to an average particle diameter of 3μ .

(ii) *Zinc oxide single crystal needles - Sample 1:* Zinc oxide single crystal needles, grown by the vapour phase oxidation of zinc, with crystal dimensions typically 10μ - 500μ diameter : 1 cm length. These crystals were undoped, with a room temperature bulk resistivity of 10 ± 5 Ω cm and a bulk analysis given in section 2.2.2 . They are of

good crystallographic quality showing predominantly the $10\bar{1}0$ face.

Surface area by Krypton B.E.T. is 250 ± 30 cm^2 .

(iii) *Zinc oxide single crystal needles - Sample 2:* Zinc oxide single crystal needles, grown by the vapour phase oxidation of zinc iodide, with crystal dimensions typically 10μ - 500μ diameter : 1 cm length. These crystals were undoped, with a room temperature resistivity of 2 Ω cm - 100 Ω cm. They are of good crystallographic quality showing predominantly the $10\bar{1}0$ face. Surface area by Krypton B.E.T. is 450 ± 50 cm^2 .

Chapter 2 : References

Brundle, C.R., J. Vac. Sci. Technol., 11, 212, (1974)

Emmenegger, F. and Petermann, A.,
J. Crystal Growth, 2, 33, (1968)

Fiermans, L., Arijs, E., Vennik, J. and Maenhout-van Der Vorst, W.,
Surface Sci., 39, 357, (1973)

Fischer, K.J., J. Crystal Growth, 34, 139, (1976)

Hausmann, A. and Teuerle, W., Z. Physik, 257, 299, (1972)

Heiland, G. and Kunstmann, P., Surface Sci., 13, 72, (1969)

Heiland, G., Kunstmann, P. and Pfister, H., Z. Physik, 176, 485, (1963)

Heiland, G., Mollwo, E. and Stockmann, F., "Solid State Physics",
eds. Seitz, F. and Turnbull, D., Academic Press, New York, 8,
193, (1959)

Helbig, R., J. Crystal Growth, 15, 25, (1972)

Henke, B.L., Proc. of Intern. Conf. on Inner Shell Ionization Phenomena,
Atlanta, Georgia (1972)

Henke, B.L. and Ebisu, E.S., Adv. X-ray Anal.,17, 150, (1974)

Hirose, M., Jap. J. Appl. Phys., 10, 401, (1971)

Hirose, M. and Furuya, Y., Jap. J. Appl. Phys., 9, 423, (1970)

Hirose, M., Furuya, Y. and Kubo, I., Jap. J. Appl. Phys., 9, 726, (1970)

Hirose, M. and Kubo, I., Jap. J. Appl. Phys., 8, 402, (1969)

Hopkins, B., Leysen, R. and Taylor, P.A., Surface Sci., 48, 486, (1975)

Jorgensen, C.K. and Berthou, H., Faraday Disc., 54, 269, (1972)

Klein, A., Z. Physik., 188, 352, (1965)

Kolb, E.D. and Laudise, R.A., J. Amer. Ceram. Soc., 48, 342, (1965)

Kolb, E.D. and Laudise, R.A., J. Amer. Ceram. Soc., 49, 302, (1966)

Kubo, I., J. Phys. Soc. Jap., 16, 2358, (1961)

Laudise, R.A., Hutson, A.R. et al., Mater. Res. Bull., 2, 1099, (1967)

Leysen, R. and van Hove, H., "Current Problems in Electrophotography", New York, p.81, (1972)

Madey, T.E., Yates, J.T. and Erickson, N.E., Chem. Phys. Lett., 19, 487, (1973)

Matsushita, T., Kodaira, K., Saito, J. and Yoshida, R., J. Crystal Growth, 26, 147, (1974)

Nielsen, J. W. and Dearborn, E.F., J. Phys. Chem., 64, 1972, (1960)

Nielsen, K.F., J. Crystal Growth, 3,4, 141, (1968)

Park, Y.S. and Reynolds, D.C., J. Appl. Phys., 38,756, (1967)

Piekarczyk, W., Gazda, S. and Niemyski, T., J. Crystal Growth, 12, 272, (1972)

Scharowsky, E., Z. Physik, 135, 318, (1953)

Sharma, R.B., J. Appl. Phys., 41, 1866, (1970)

Shiloh, M. and Gutman, J., J. Crystal Growth, 11, 105, (1971)

Takahasi, T., Ebina, A. and Kamigawa, A., Jap. J. Appl. Phys., 5, 560, (1966)

Timofeeva, V.A., Rost. Kristallov (Crystal Growth), 6, 86, (1965)

Utsch, B. and Hausmann, A., Z. Physik, B21, 27, (1975)

Wagner, C.D., Anal. Chem., 44, 1051, (1972)

Wanklyn, B.M., J. Crystal Growth, 7, 107, (1970)

Weaver, E.A., J. Crystal Growth, 1, 320, (1967)

3. EXPERIMENTAL AND RESULTS

3.1 Gas phase analysis using the mass spectrometer

The system used in the experiments described later in this chapter is shown schematically in fig. (3.1). In essence it consists of a standard gas handling apparatus to the right of leak valve 1 where gas can be admitted into the source chamber, previously pumped out to better than 10^{-6} torr, at a pressure of ca. 1 torr measured on the thermistor pressure gauge. Since the total amount of material removed through leak valve 1 is small compared with the amount in the source chamber, there is a constant pressure in the source chamber for the duration of many experiments, and hence a constant leak rate into the reaction chamber set by leak valve 1. The gas flowing into the reaction chamber passes over the zinc oxide (whose temperature can be varied controllably - see later) at a pressure determined by the setting of leak valve 2. The gas exiting through leak valve 2 passes into the all stainless steel analysis chamber, consisting of mass spectrometer and ion pump, where its flow rate and composition are measured.

3.1.1 System calibration

(a) Thermistor pressure gauges

With these 'thermal conductivity' gauges the temperature of the element is governed by the difference between heat input and heat loss, the latter being primarily by thermal conduction through the gas. Since the thermal conductivity and gas pressure are directly related, then the thermistor temperature (and resistance) is a measure of gas pressure. So, the voltage across the thermistor element for a constant current, obtained from a balanced bridge source, is a measure of pressure. For accurate

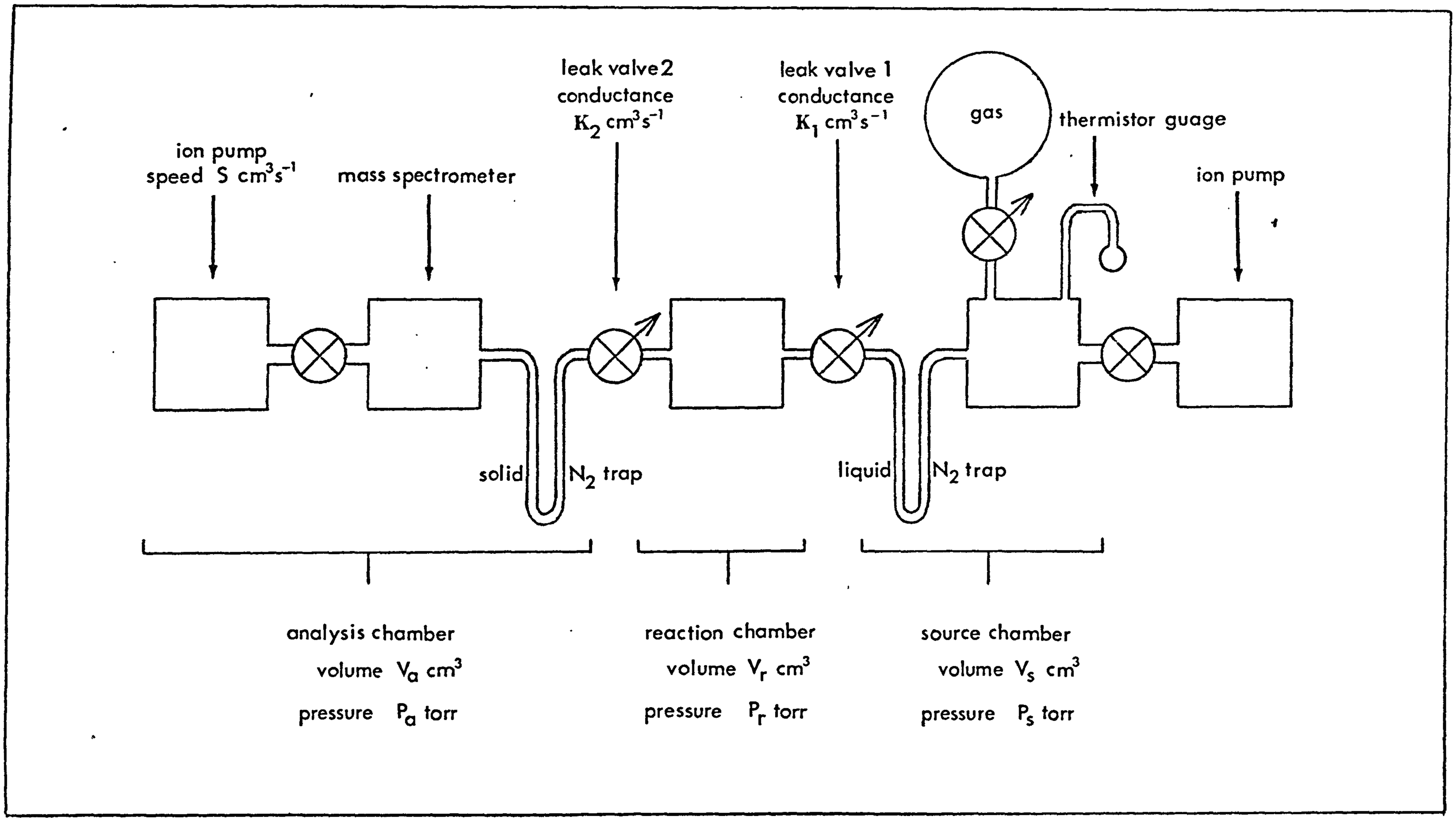

Fig. 3.1:

Schematic diagram of the apparatus

readings the gauge must be kept at constant temperature, in this case by immersion in melting ice.

Two types of thermistor gauge were constructed. One, to work in the pressure range 10^{-2} - 10^{-4} torr, was made by mounting the thermistor bead in a stainless steel canister. All the usual thermal conductivity gauges become insensitive to pressure changes below ca.10^{-3} torr, when radiation becomes the major heat loss mechanism. Having the element surrounded by metal of high reflectivity keeps the radiation loss to a minimum and hence increases the sensitivity to thermal conductivity change. When calibrated against a McLeod gauge, for both nitrous oxide and oxygen, good sensitivity was obtained down to 10^{-4} torr, with an estimated error of ±5%, and indeed, by careful measurement, the range could be extended to 10^{-5} torr. The second type, to work at pressures between 0.1 and 2 torr, was mounted in a stainless steel canister filled with powder (carborundum, mesh 100). The upper pressure limit of the standard gauge, which is about 0.5 torr, occurs when the distance between the thermistor bead and the walls of the gauge is roughly 10 times the mean free path of the gas particles. The presence of the powder modifies the heat loss mechanism and allows the pressure range to be extended, (Green and Lee, 1966). The gauge was calibrated up to a pressure of 2 torr (the upper limit of our McLeod gauge) for both nitrous oxide and air, with an estimated accuracy of ±5%.

(b) Leak valve 1:

This, the MV -2S -XL valve manufactured by Vacuum Accessories Corporation of America, is a stainless steel leak valve, metering being accomplished by a bellows mounted micro-grooved pin. Calibration was achieved, for both nitrous oxide and oxygen, by leaking the gas from a source at a

pressure of ca. 1 torr into a previously evacuated ($<10^{-6}$ torr) glass bulb of known volume. The pressure rise (measured on the low pressure thermistor gauge) versus time, gave the leak rate accurately.

The total conductance, K_1 in $cm^3\ s^{-1}$, against the number of turns open was measured in the range 10^{-5} to 10^{-1} $cm^3\ s^{-1}$ from 6 to 20 turns open, and obtained using the equation

$$K_1 (P_s - P_g) = F_{LV1} \quad \text{torr cm}^{-3}\ \text{s}^{-1}$$

and, since P_s, the source pressure of ca.1 torr, is much greater than the pressure in the glass bulb, P_g (10^{-2} torr maximum), then,

$$K_1 = F_{LV1} / P_s \quad \text{cm}^3\ \text{s}^{-1} \qquad [3.1]$$

whence the conductance K_1, is given by the measured flow, F_{LV1}, divided by the source pressure. This equation, which is strictly true only for the molecular flow pressure regime ($P_s < 10^{-2}$ torr), was found to hold at these higher source pressures, the error being within that of the thermistor gauge readings. Measured conductances are accurate to ±5% at the high conductance values, and, ±10% for low conductances, (below 10^{-5} $cm^3\ s^{-1}$ metering became erratic).

(c) Leak valve 2:

This, the SS-2SX valve manufactured by Nupro Company, is a stainless steel needle valve. Calibration was achieved, in situ on the main system (fig. 3.1), with a thermistor gauge (10^{-2} - 10^{-4} torr range) attached to the reaction chamber. Gas from the source chamber was admitted through leak valve 1 at a known flow rate, $K_1 P_s$. Leak valve 2 was set at conductance K_2, whence the total flow of gas out of the reaction chamber is $K_2 P_r$ (see equation [3.3]). At steady state these flows are equal, whence

$$K_2 = K_1 P_s / P_r$$

Measuring P_r on the thermistor gauge for different settings of leak valve 2 gave a calibration of conductance against number of turns open. The scatter of this calibration curve is consistent with the error of the thermistor gauge reading, i.e. ±5%.

(d) Ion pump

The ion pump (Ferranti FJAD8) speed, S, nominally 8 litres per second, was calibrated for both oxygen and nitrogen (nitrous oxide being pumped at the solid nitrogen trap - see later). By admitting gas from the source chamber through leak valve 1 and measuring the ultimate steady state analysis chamber pressure, the relation

$$S P_a = K_1 P_s$$

gives the pump speed when all the other terms are shown. The flow rate through leak valve 1, $K_1 P_s$, was checked by isolating the ion pump (closing the shut-off valve between the ion pump and mass spectrometer), leaking gas through leak valve 1, and monitoring the change in pressure with time, whence

$$(dP_a/dt)(V_a - V_p) = K_1 P_s$$

where P_a is the pressure measured at the mass spectrometer, V_a is the analysis chamber volume, (1100 ± 50 cm^3), and V_p the ion pump volume (250 ± 20 cm^3). The measured pump speed was found for both oxygen, S_{O_2}, and nitrogen, S_{N_2}, to be

$$S_{O_2} = (1.25 \pm 0.05) \times 10^3 \quad cm^3 \; s^{-1}$$

and

$$S_{N_2} = (1.50 \pm 0.05) \times 10^3 \quad cm^3 \; s^{-1}$$

The pump characteristics, as quoted by the makers, indicate a pump speed varying with pumping pressure. However, for pressures less than 10^{-6} torr, (experimental analysis chamber working pressure, P_a , being 10^{-6} torr $> P_a > 10^{-8}$ torr), the pump speed is constant to $\pm 7\%$.

(e) Mass spectrometer

The mass spectrometer (A.E.I., M.S.10) sensitivity to various gases was checked against a McLeod gauge on a separate vacuum system. The measured sensitivities were found to agree closely to those quoted by the makers, namely 48μA/torr for nitrogen, and 28μA/torr for oxygen. These values were used throughout.

An ion gauge (C.V.C., GIC - 028) was incorporated into the main vacuum system to measure the overall analysis chamber pressure and provide a constant check on the mass spectrometer calibration.

The background residual gas spectrum of the analysis chamber is shown in fig. (3.2). Immediately after bakeout, fig. (3.2b), an ultimate pressure of better than 10^{-8} torr was achieved. For several hours after bakeout the chamber walls have an appreciable pumping speed, therefore, all valid experimental data were taken well after bakeout, when the working background spectrum is as shown in fig. (3.2a). The spectrum taken with leak valve 2 closed, when subtracted from the spectrum taken at the working background pressure, gives the 'inferred' background in the reaction chamber which is shown in fig. (3.2c).

A second mass spectrometer (A.E.I., Minimass), was incorporated onto the system at the source chamber, where the working background pressure was 10^{-6} torr.. The residual gas spectrum at this pressure is shown in fig. (3.3a).

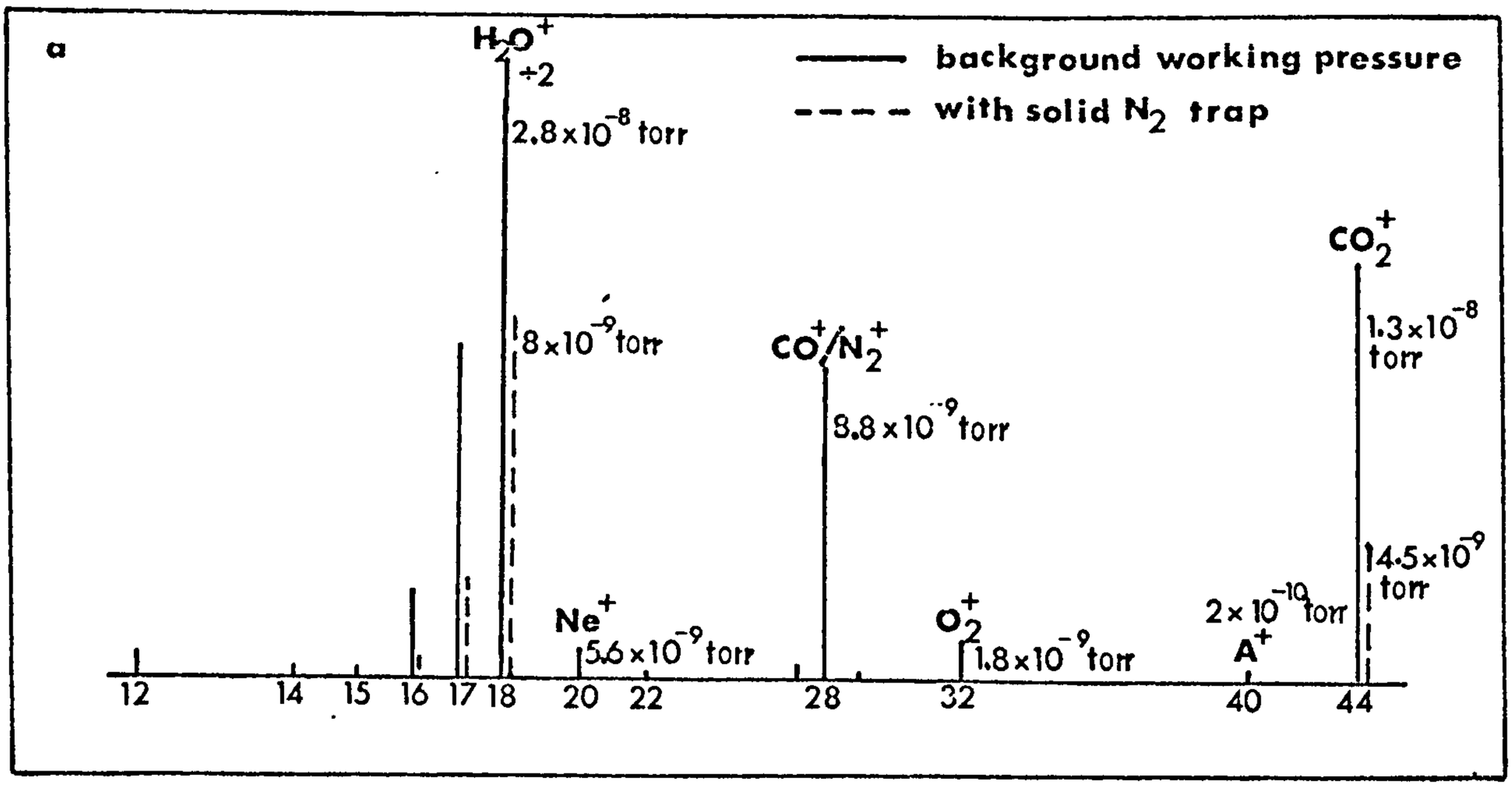

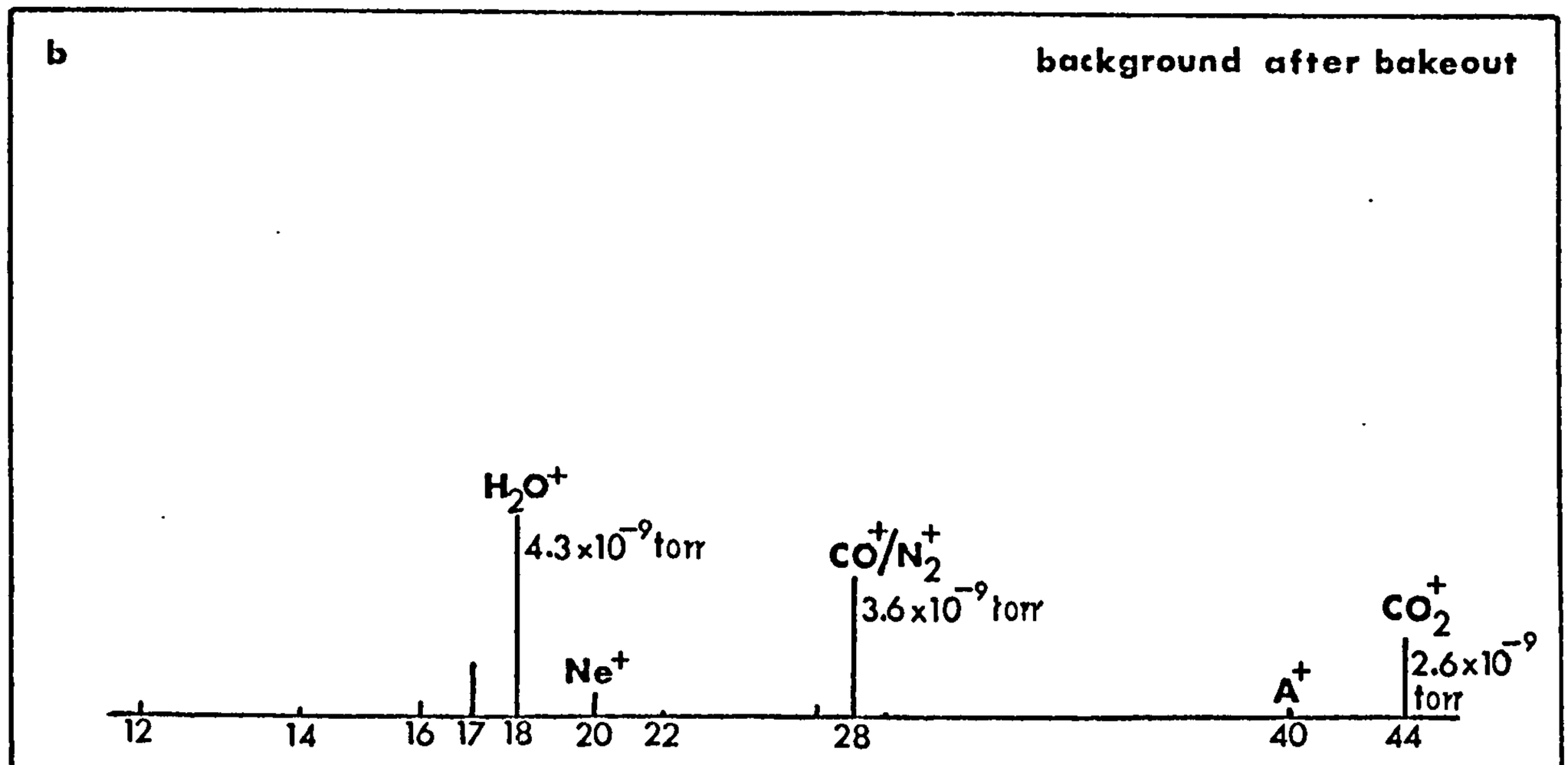

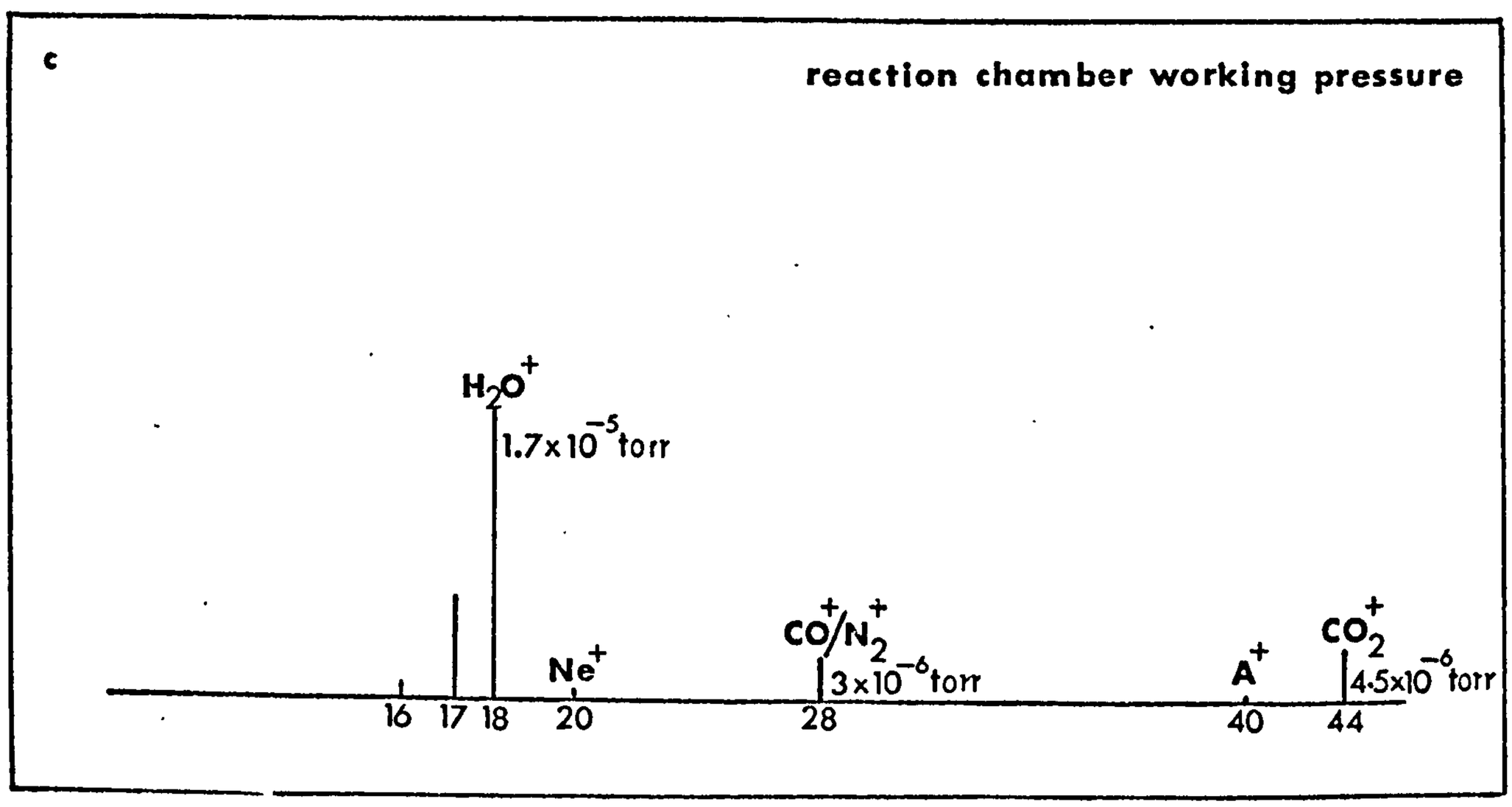

Fig. 3.2: Mass spectra of:-

(a) analysis chamber background working pressure

(b) analysis chamber background after bakeout

(c) reaction chamber working pressure

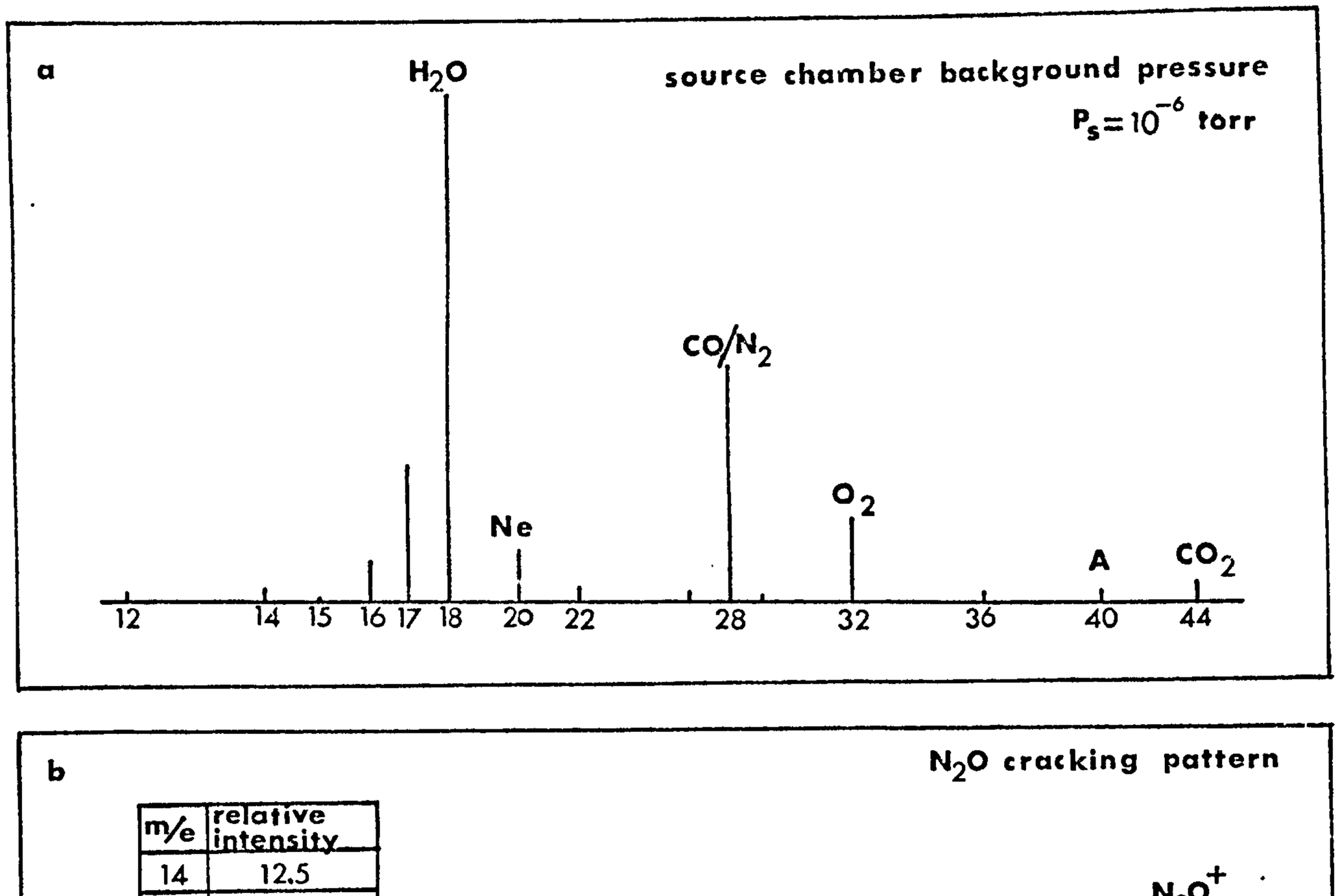

b

N_2O cracking pattern

m/e	relative intensity
14	12.5
16	4.6
28	55.3
30	27.1
32	5.2
44	100.0

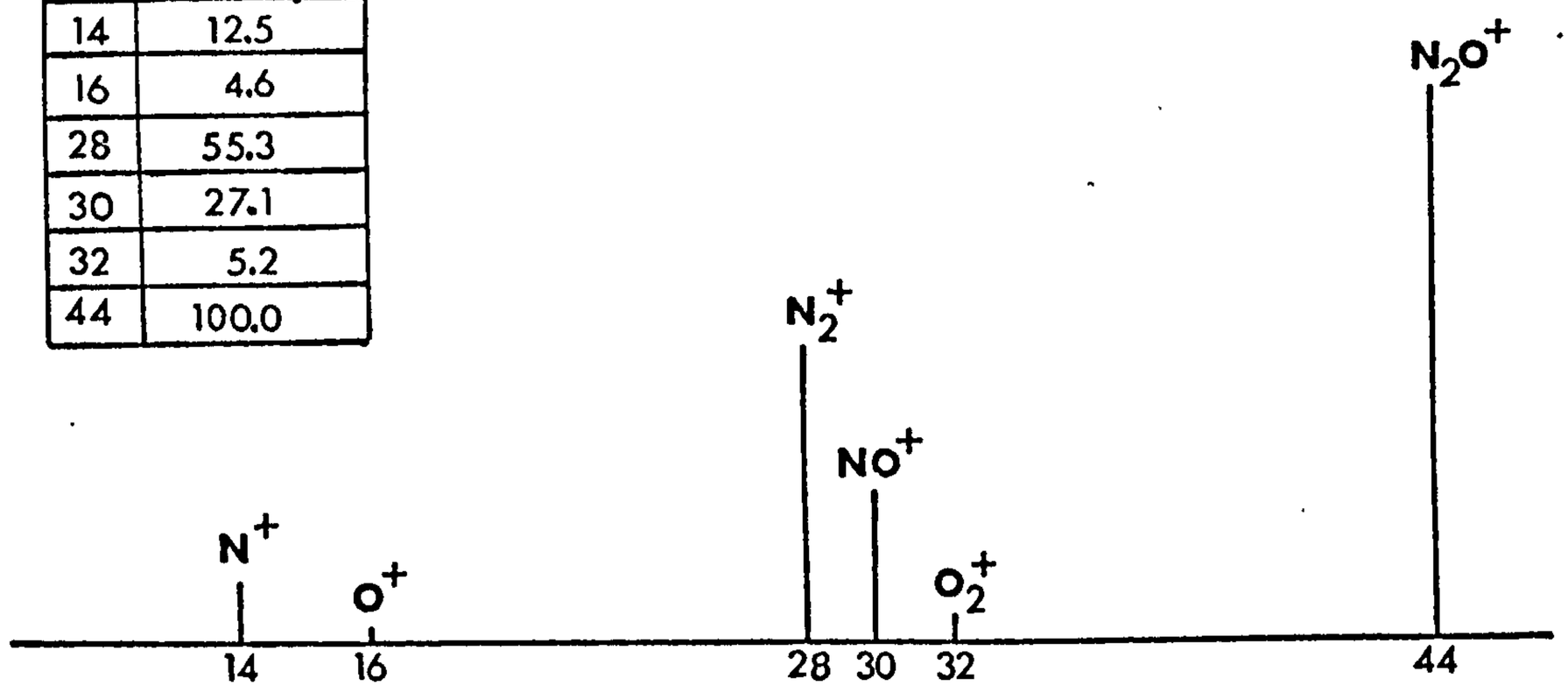

Fig. 3.3:

Mass spectra of:-

(a) source chamber background working pressure

(b) nitrous oxide cracking pattern

The cracking pattern for nitrous oxide, as obtained on the M.S.10, is shown in fig.(3.3b). This will be referred to later, (see section 3.2.3).

(f) Reaction chamber

The all-silica reaction chamber, shown diagramatically in fig. (3.4), has a total volume, V_r , of 5.80 cm^3 (including the dead space volume of the leak valves). Zinc oxide can be introduced into, or removed from the chamber, via the top opening, when the Viton o-ring union is removed. This o-ring coupling allows a thermocouple holder to be inserted into the reaction vessel, where thermocouple 1 (marked t/c1 on fig. 3.4) measures the temperature in the body of the catalyst. Heating is effected by a wire wound tube furnace which can be moved readily onto or off the reaction chamber. The furnace was constructed with a three zone heating assembly in order to achieve a flat temperature profile ($\pm$ 2K at furnace temperatures from 300 K to 1100 K) over the length of the zinc oxide in the reaction vessel, and is powered by a temperature programmer (Stanton Redcroft, model no. LT682) capable of linear heating or cooling rates over a range of 0.017 to 1.7 Ks^{-1}, or isothermal up to 1300 K. The thermocouple sensor for the temperature programmer (t/c 3 on fig. (3.4)) is located between the furnace windings and the surrounding thermal insulator, where the response time is shortest (when the programmer is set in the temperature transient mode). The temperature measured at thermocouple 2 (t/c 2 on fig. (3.4)), which is placed between the reaction vessel and the furnace, when compared with the temperature measured at t/c 1, indicates the temperature profile along the radius of the reaction chamber during temperature transient measurements. For a typically fast heating rate of 0.4 Ks^{-1} this temperature difference (T_1 versus T_2 on fig. (3.4)) is about 5 K. Good thermal contact between thermocouple 1 and its silica

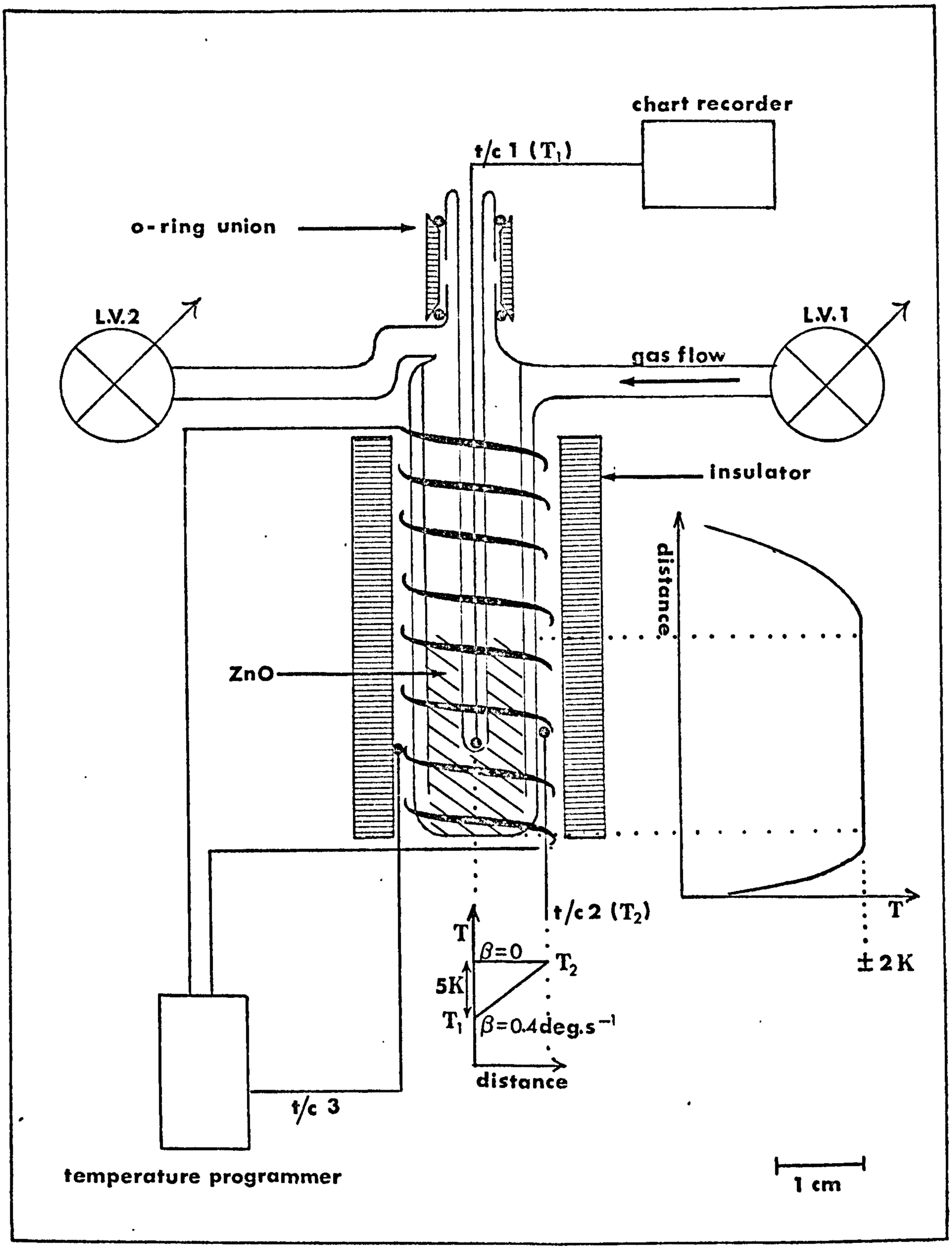

Fig. 3.4:

Schematic diagram of the reaction chamber

holder was ensured by placing silver-dag around the contact region. It is therefore very likely that most of the 5 K temperature lag occurs between the outer two walls of the reaction vessel, where the only mode of transfer is by radiation (and some by conduction through the low pressure gas). So, an arbitrary, but pessimistic, assessment of the radial temperature gradient across the zinc oxide mass would be 3 K. This is not much different from the longitudinal temperature uncertainty of ±2 K. At higher heating rates the temperature lag increases, but even at a heating rate of 1.7 Ks^{-1} the measured catalyst temperature (T_1) has a maximum 8 K uncertainty. At heating rates below 0.4 Ks^{-1} the catalyst temperature is $T_1 \pm 2$ K.

3.1.2 Pressure-time response of system under flow conditions

In any transient experiment where the pressure of gas over the adsorbent is changing with time, either as a result of changing K values or due to the adsorbent, it is required to know the time response of the system to this change. In other words, if a net flow of gas into the reaction chamber is changing with time, $F_1(t)$, what will be the corresponding rate of change of gas flow measured at the mass spectrometer. In the apparatus shown in fig. (3.1) only two factors affecting the response time need be considered, namely, the conductance of leak valve 2, K_2, and the pump speed S. Between the zinc oxide in the reaction tube and the mass spectrometer there is an extensive length of tubing of assorted diameter, but, since the conductance K_2 is so much smaller than any of these conductances, only it need be considered.

Consider first gas flow into and out of the reaction chamber (cf. fig. (3.1)). The total effective gas flow into the reaction chamber is the sum of that entering through leak valve 1, F_{LV1}, where according to equation [3.1]

$$F_{LV1} = K_1 P_s$$

plus or minus an amount flowing onto or off the zinc oxide surface, F_{ZnO} ; so,

$$F_1(t) = K_1 P_s \pm F_{ZnO}(t) \qquad [3.2]$$

Now, the total flow out of the reaction chamber through leak valve 2, F_{LV2} , is, according to the equation for molecular flow,

$$F_{LV2} = K_2 (P_r - P_a)$$

and since the reaction chamber working pressure, (P_r equals ca. 10^{-2} torr), is much greater than the analysis chamber pressure, (P_a is less than 10^{-6} torr) we can write

$$F_{LV2} = K_2 P_r \qquad [3.3]$$

so that the rate of change of reaction chamber pressure with time, which is given by

$$V_r (dP_r/dt) = F_1(t) - F_{LV2}$$

can be written

$$V_r (dP_r/dt) = F_1(t) - K_2 P_r \qquad [3.4]$$

Now, in a transient experiment, $F_1(t)$ is a function of time, as indicated. Consider $F_1(t)$ changing at a constant rate with time, for $t \geqslant 0$, so

$$F_1(t) = F_1(0) + gt \qquad [3.5]$$

where g is the constant rate of change, $(dF_1(t)/dt)$, and $F_1(0)$ is the constant value of $F_1(t)$ at $t \leqslant 0$. Then putting equation [3.5] into [3.4] and rearranging gives,

$$(dP_r/dt) + (K_2/V_r)P_r = \left[\frac{F_1(0) + gt}{V_r}\right] \qquad [3.6]$$

This differential equation, when solved, gives

$$P_r e^{K_2 t/V_r} = (1/V_r)\int (F_1(0) + gt)\, e^{K_2 t/V_r}\, dt$$

which on integration gives

$$P_r e^{K_2 t/V_r} = (F_1(0)/K_2)e^{K_2 t/V_r} + (gV_r/K_2^2)(K_2 t/V_r - 1)e^{K_2 t/V_r} + C$$

or, dividing through by $((1/K_2)e^{K_2 t/V_r})$ gives

$$K_2 P_r = F_1(0) + gt - gV_r/K_2 + Ce^{-K_2 t/V_r} \qquad [3.6a]$$

where C is the constant of integration. Now, assuming flow conditions at t = 0 such that K_2P_r (t = 0), the flow out through leak valve 2 equals $F_1(0)$, the flow into the reaction chamber, minus a constant, "a", i.e.

$$K_2 P_r(t = 0) = F_1(0) - a$$

This is a non-steady initial flow condition which is our most generalised case, so at t = 0, equation [3.6a] gives

$$C = gV_r/K_2 - a$$

whence, at time t,

$$K_2 P_r = F_1(0) + gt - (gV_r/K_2)(1 - e^{-K_2 t/V_r}) - a e^{-K_2 t/V_r} \qquad [3.7]$$

Considering now the time response in the pump, there is the relationship

$$V_a\,(dP_a/dt) = F_{Lv2} - S P_a \qquad [3.8]$$

where the net flux of gas into the pump is the pump speed multiplied by the pump pressure, which is the analysis chamber pressure, P_a , there being effectively no pressure gradients throughout the analysis chamber, since all parts are connected by high conductance tubing. Now, the flow of gas into the analysis chamber is that which comes through leak valve 2, F_{Lv2} . Using the transient value obtained for this in equation [3.7] and substituting into [3.8], this gives, after rearranging,

$$dP_a/dt + SP_a/V_a = F_i(0)/V_a + gt/V_a - gV_r/K_2V_a \qquad [3.9]$$
$$+ \left[(gV_r/K_2 - a)/V_a\right] e^{-K_2 t/V_r}$$

Solving this differential equation gives

$$P_a e^{St/V_a} = (F_i(0)/V_a - gV_r/K_2V_a) \int e^{St/V_a}\,dt + (g/V_a)\int t\, e^{St/V_a}\,dt$$
$$+ \left[(gV_r/K_2 - a)/V_a\right] \int e^{-(S/V_a - K_2/V_r)t}\,dt$$

and evaluating this integral gives

$$P_a e^{St/V_a} = (1/S)(F_i(0) - gV_r/K_2)\, e^{St/V_a} + (gV_a/S^2)(St/V_a - 1)\; e^{St/V_a}$$
$$+ \left[V_r(gV_r/K_2 - a)/(SV_r - K_2V_a)\right] e^{St/V_a}\, e^{-K_2 t/V_r} + D$$

which is after rearrangement

$$SP_a = F_i(0) + gt - g(V_r/K_2 + V_a/S)$$
$$+ \left[SV_r(gV_r/K_2 - a)/(SV_r - K_2V_a)\right] e^{-K_2 t/V_r} + D e^{-St/V_a}$$

where D is the constant of integration. Now, at t = 0 the flow conditions are that $SP_a(t = 0)$ equals $F_1(0)$ -a, hence,

$$D = g(V_r/K_2 + V_a/S) - \left[SV_r(gV_r/K_2 - a)/(SV_r - K_2V_a)\right] - a$$

whence, at time t,

$$F_M(t) = SP_a = F_1(0) + gt - g(V_r/K_2 + V_a/S)(1 - e^{-St/V_a}) - a e^{-St/V_a}$$

$$+ \left[SV_r(gV_r/K_2 - a)/(SV_r - K_2V_a)\right](e^{-K_2t/V_r} - e^{-St/V_a}) \quad [3.10]$$

This equation gives the relationship between the actual flow rate at the zinc oxide adsorbent at time t, given by $F_1(t) = F_1(0) + gt$, and the measured flow rate, $F_M(t)$, where V_r, K_2, V_a and S are all known parameters.

Using this equation the response time to various kinds of flow variation can be calculated.

(a) Time response for linearly varying flow

Two types of flow variation with time, corresponding to those obtained in the transient experiments to be described later, are to be considered. Firstly a linearly increasing or decreasing F_1 with time, beginning at steady state flow conditions for $t \leqslant 0$. In equation [3.10], then, "a" equals zero, and the other parameters are as follows

V_r = 5.8 cm^3

V_a = 1100 cm^3

S = 1250 $cm^3\ s^{-1}$ (for oxygen)

The maximum difference between measured and actual flow rate occurs at large t (typically about 30 seconds) when both $e^{-K_2 t/V_r}$ and e^{-St/V_2} approach zero; then equation [3.10], with the above parameters, becomes

$$F_M(t) = F_i(t) - g(5.8/K_2 + 0.88) \qquad [3.11]$$

The total measured flow, when compared with the actual flow at the adsorbent, is shown in the diagram of fig. (3.5a).

Fig. (3.5a), as well as equation [3.11], shows that the maximum time lag, τ, does not depend upon the rate of flow change, g, but solely on the system parameters, τ is given by

$$\tau = 5.8/K_2 + 0.88 \text{ sec.} \qquad [3.12]$$

and depends upon the conductance of leak valve 2. Various τ values corresponding to different settings of this conductance are tabulated in fig. (3.5b). These will be referred to in the appropriate section.

(b) Time response for a peak in the flow rate

The experimental peaks obtained in the thermally programmed desorption (TPD) of oxygen, (see later), can be closely approximated by a triangular peak, as shown in fig. (3.6a), where the gradient of the positive slope is half the gradient of the negative slope (the ratio of the areas before and after the peak is 2:1; experimentally this ratio is 1.83 : 1). The intervals between t = 0 to $t = t_1$ and $t = t_1$ to $t = t_2$ must be considered separately. From t = 0 to $t = t_1$ the flow increases linearly from steady state at t = 0, and the total time lag at $t = t_1$ is given by equation [3.12], i.e.

(a)

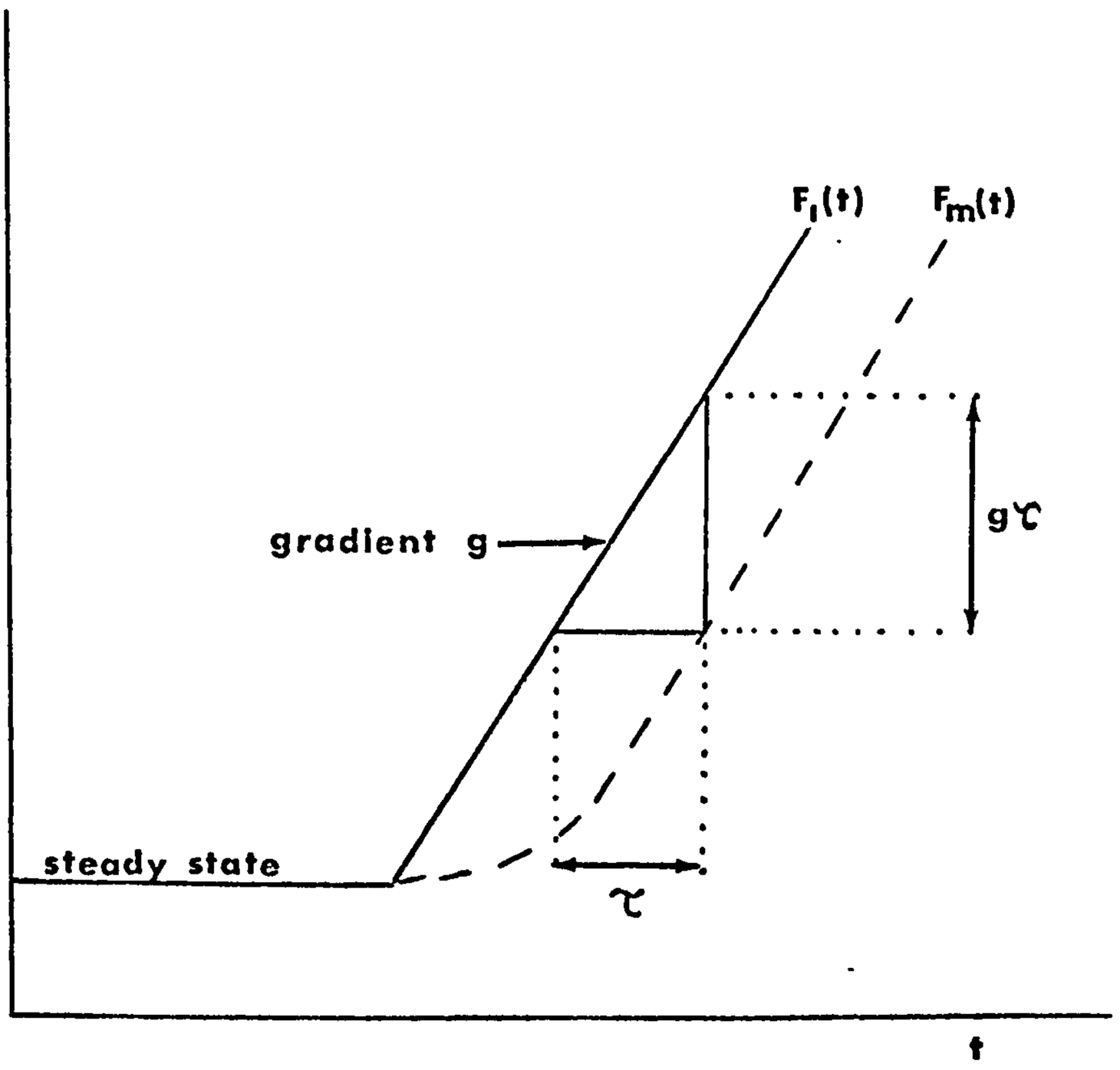

(b)

No. of turns open	K_2 ($cm^3\ s^{-1}$)	τ (s)
1	1.5×10^{-2}	387.6
2	3.0×10^{-2}	194.2
3	5.0×10^{-2}	116.9
4	7.6×10^{-2}	77.2
5	1.0×10^{-1}	58.9
6	1.5×10^{-1}	39.6
7	2.0×10^{-1}	29.9
8	2.5×10^{-1}	24.1
9	3.3×10^{-1}	18.5
Open	4.5×10^{-1}	13.8

Fig. 3.5:

(a) Time response curve for a linearly increasing flow rate

(b) values of the time lag, τ , for different settings of the conductance of leak valve 2

$$\tau(t_1) = 5.8/0.15 + 0.88 = 11.4 \text{ sec.}$$

where K_2 is 0.15 $cm^3\ s^{-1}$ (leak valve 2 is fully open in all T.P.D's).

From t_1 to t_2 equation [3.10] is used putting "a" equal to $11.4g^+$, where g+ is the gradient of the positive slope. Therefore equation [3.10] becomes

$$F_M(t) = F_1(t_1) + g^-(t-11.4) + 1.09\,g^-(10.55 - 11.4g^+/g^-)\,e^{-0.095t}$$

where the term e^{-St/V_a} is taken as zero, since it becomes very small after a few seconds. Since $2g^+ = g^-$, where g- is the gradient of the negative slope, then

$$F_M(t) = F_1(t_1) - 2g^+(t - 11.4 + 17.7\,e^{-0.095t}) \qquad [3.13]$$

where t is measured from t_1. This shows a maximum in the response curve occurring Δt_p = 5.5 seconds after the peak in $F_1(t)$ curve, that is independent of g. The height difference, Δh, equals 9.2g+. Now, this value of Δh can be expressed in terms of easily measurable quantities, namely, the peak height, h, and the peak width at half height, $\Delta t_{1/2}$, by observing that, for the theoretical triangular peak,

$$\Delta t_{1/2_1} = h_1/2g^+ + h_1/2g^- = 3h_1/4g^+$$

where the subscript 1 refers to the theoretical peak, (cf. fig. 3.6a), hence

$$\Delta h/h = 6.9/\Delta t_{1/2_1} \qquad [3.14]$$

(a)

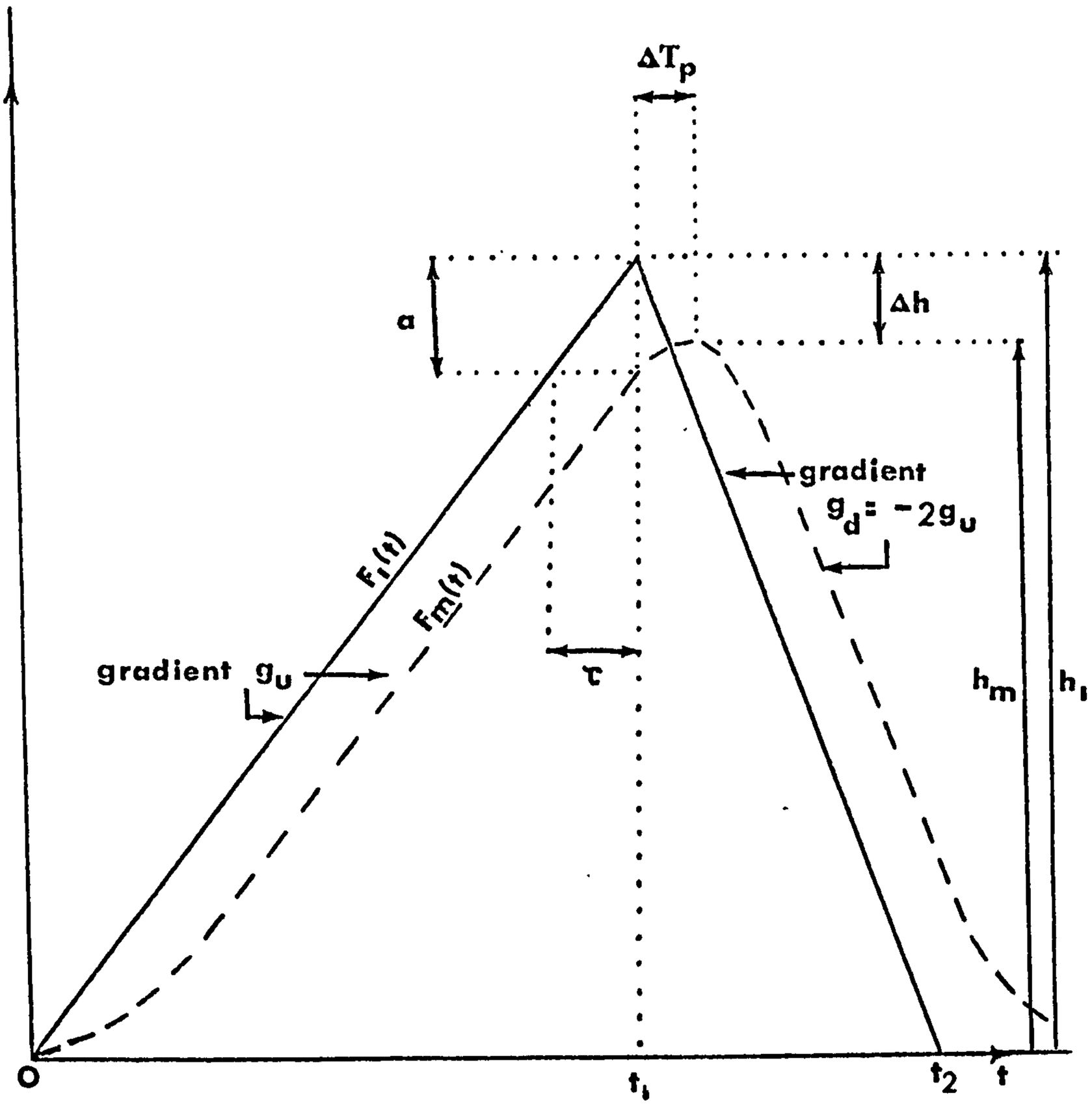

(b)

T (K)	β (K s^{-1})	$\Delta h/h_m$
40	0.017	2.95×10^{-3}
	0.4	7.70×10^{-2}
	1.7	5.26×10^{-1}
50	0.017	2.35×10^{-3}
	0.4	6.02×10^{-2}
	1.7	3.63×10^{-1}
60	0.017	1.96×10^{-3}
	0.4	4.94×10^{-2}
	1.7	2.77×10^{-1}

Fig. 3.6:

(a) time response curve for a peak in the flow rate

(b) change in peak height for different values of heating rate, β, and peak width at half height, $\Delta T_{½\,m}$

This can be expressed in terms of the peak width and height of the response curve, by observing that

$$h_m = h_1 - \Delta h$$

where the subscript m refers to the measured peak, and

$$\Delta t_{½_m} = \Delta t_{½_1} + 3\Delta h/8g^+ = \Delta t_{½_1} + 3.45 \qquad [3.15]$$

whence, equation [3.14] becomes

$$\Delta h/h_m = 6.9/(\Delta t_{½_m} - 10.4) \qquad [3.16]$$

So, the total fractional difference in peak height is a function of the peak width alone. Equation [3.16] can be restated in terms of temperature, when a linear temperature programme is used, observing that $T = T_0 + \beta t$, whence

$$\Delta h/h_m = 6.9\beta/(\Delta T_{½_m} - 10.4\beta)$$

The shift in peak height and peak position for various values of β and $\Delta T_{½_m}$ are tabulated in fig. (3.6b).

3.2 Technique and results

3.2.1 Interaction of oxygen with zinc oxide single crystals

The experiments described in this section concern the interaction of oxygen with single crystal zinc oxide at elevated temperatures. The zinc oxide, (sample 1, characterised in chapter 2) is in the form of hexagonal needles (ca. 50 diameter x 1 cm long) showing almost exclusively the $10\bar{1}0$ face. Their total surface area is 250 ± 30 cm^2.

The oxygen, obtained in litre flasks from B.O.C., is "Research Grade", 99.98% pure, with contaminants, quoted by B.O.C., as listed below:

Nitrogen	150 p.p.m.
Argon	50 p.p.m.
Water	1 p.p.m.
Hydrogen	< 1 p.p.m.
Carbon dioxide	< 1 p.p.m.
Hydrocarbons	< 1 p.p.m.

Above 800 K the behaviour of zinc oxide is markedly different from that at temperatures between 300 K and 800 K. Results of experiments in each temperature regime are treated in turn, and described below.

(a) Between 800 K and 1200 K

Above 800 K oxygen is found to adsorb on the zinc oxide $10\bar{1}0$ surface, with substantial interaction with the surface lattice layer, (see chapter 4). The extent of this interaction depends upon the pre-treatment. A set pre-treatment programme was closely adhered to throughout the course of these experiments. This is described below.

After the first clean up procedure to remove gross carbon contamination and out diffused material (see section 2.4), the zinc oxide is heated to a temperature between 1050 K and 1100 K, and left in vacuum for 10 to 15 minutes. Adsorbed contaminants, due to surface re-contamination by the residual gases in the vacuum system, are removed, and the surface is left fully depleted of oxygen (see later). The solid is then cooled to a temperature between 850 K and 1000 K, at which temperature it is treated with oxygen. On opening leak valve 1, oxygen flows into the reaction chamber with a flow rate, measured at steady state, that equals

$S_{O_2} P_a$ (torr cm^3 s^{-1}), S_{O_2} (cm^3 s^{-1}) being the ion pump speed for oxygen and P_a (torr) the mass spectrometer pressure. Adjustment of leak valve 2 to a conductance K_2 (cm^3 s^{-1}) gives a steady state pressure, P_{O_2}, oxygen over the zinc oxide given by

$$P_{O_2} = S_{O_2} P_a / K_2 \quad \text{torr}$$

The solid is treated for 1 hour in the temperature range 850 K to 1000 K in this pressure of oxygen, where 10^{-3} torr $< P_{O_2} <$ 0.5 torr. After this time the oxygen flow is turned off, the remaining gas phase oxygen is pumped away and the solid is quenched to a temperature of about 750 K in under a minute. At 750 K the zinc oxide has a surface coverage of oxygen unchanged from that obtained at the higher temperature oxygen treatment, because, during quenching, very little oxygen will have come off the surface, the rate of desorption being negligible below 850 K (see T.P.D. curves of fig. (3.7)). Now, by heating the solid at a rate linearly with time (β = 0.4 K s^{-1} was chosen to give maximum sensitivity with small time constant correction, and was used throughout), a peak in the measured oxygen flow rate occurs at about 1000 K. The total measured flow rate (which is the flow at the zinc oxide surface after time constant correction) in torr cm^3 s^{-1} can be converted to molecules s^{-1} by using the relation

$$1 \text{ torr } cm^3 = 3.54 \times 10^{16} \text{ molecules at } 300\,K$$

and this in turn gives the rate of change of fractional surface coverage of atomic oxygen, $d\theta_{oxy}/dt$, by

$$\frac{d\theta_{oxy}}{dt} = \frac{S_{O_2} P_a \times 2 \times 3.54 \times 10^{16}}{250 \times 6 \times 10^{14}}$$

for a surface area of 250 cm^2 containing 6 x 10^{14} surface oxygen atoms per square centimeter. Therefore,

$$\frac{d\theta_{oxy}}{dt} = 1180\, P_a$$

when S_{O_2} equals 1.25×10^3 cm^3 s^{-1} .

The T.P.D. peaks shown in fig. (3.7) are for pre-treatment in oxygen at various different pressures at 963 K. This series of peaks, which is entirely representative of all the experimentally obtained peaks, reveals several properties that are immediately recognisable. Firstly, the peaks are assymetrical, where the ratio of areas under the $d\theta_{oxy}/dt$ against t curve before and after the peak temperature is approximately 2:1 (1.83:1, see section 4.1.1). Secondly, the peak shifts to lower temperature for decreasing peak area, $\Delta\theta_{oxy}$. Thirdly, the total peak area increases with increasing oxygen pre-treatment pressure, and (see later) with decreasing pre-treatment temperature. Occasionally, a doublet appears in the T.P.D. spectrum (curve d of fig. (3.7)). An explanation of this behaviour is advanced in section 4.1.1. Curves a and c of fig. (3.7) are reproduced in fig. (3.8) (where subscripts 'm' refer to the experimentally measured flow rates) together with the curves corrected for the system response time, (as in section 3.1.2b); where the subscripts 'ZnO' refer to the actual flow rate at the zinc oxide surface. For a heating rate of 0.4 K s^{-1} (used throughout), the measured peak is shown to have shifted by 2.2 K to higher temperature, with about a 7% drop in peak height. The total peak area, $\Delta\theta_{oxy}$ is unchanged.

The change of peak temperature T_p , with peak area, $\Delta\theta_{oxy}$, for a series of experimentally obtained peaks, is shown in fig. (3.9). The total uncertainty in the peak temperature is shown as a bar (where the shift of T_p to lower temperature of 2.2 K due to the system time constant is in the opposite direction to the temperature gradient across the zinc oxide (ca. 3 K) due to the temperature lag of the reaction chamber furnace). A shift in T_p of over 100 K to lower temperature with decreasing $\Delta\theta_{oxy}$ cannot be explained by normal Polanyi-Wigner kinetics (see for example Petermann 1972, Ehrilch 1963). The variation in peak width at half

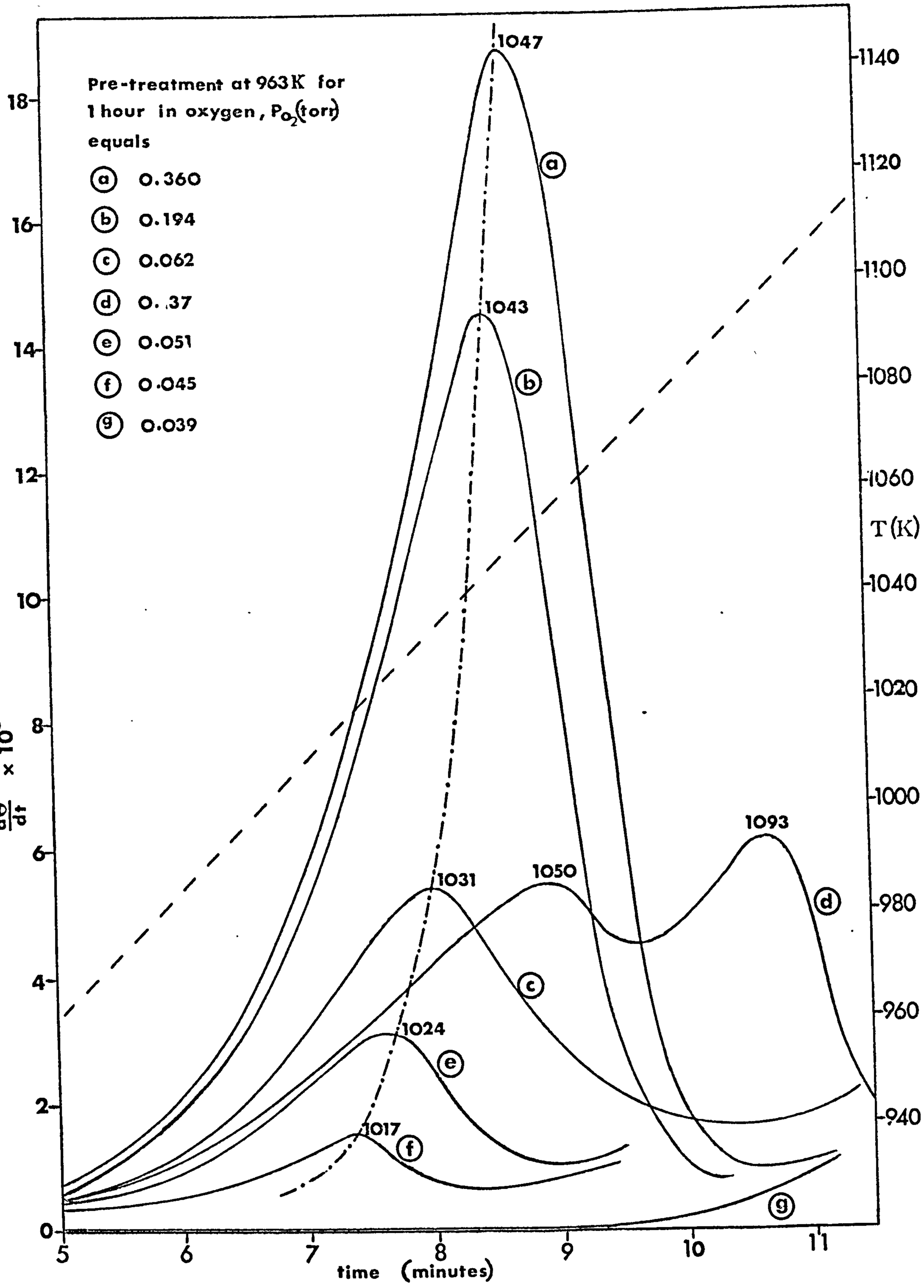

Fig. 3.7:

Oxygen T.P.D.'s from the $10\bar{1}0$ zinc oxide surface with various pre-treatments

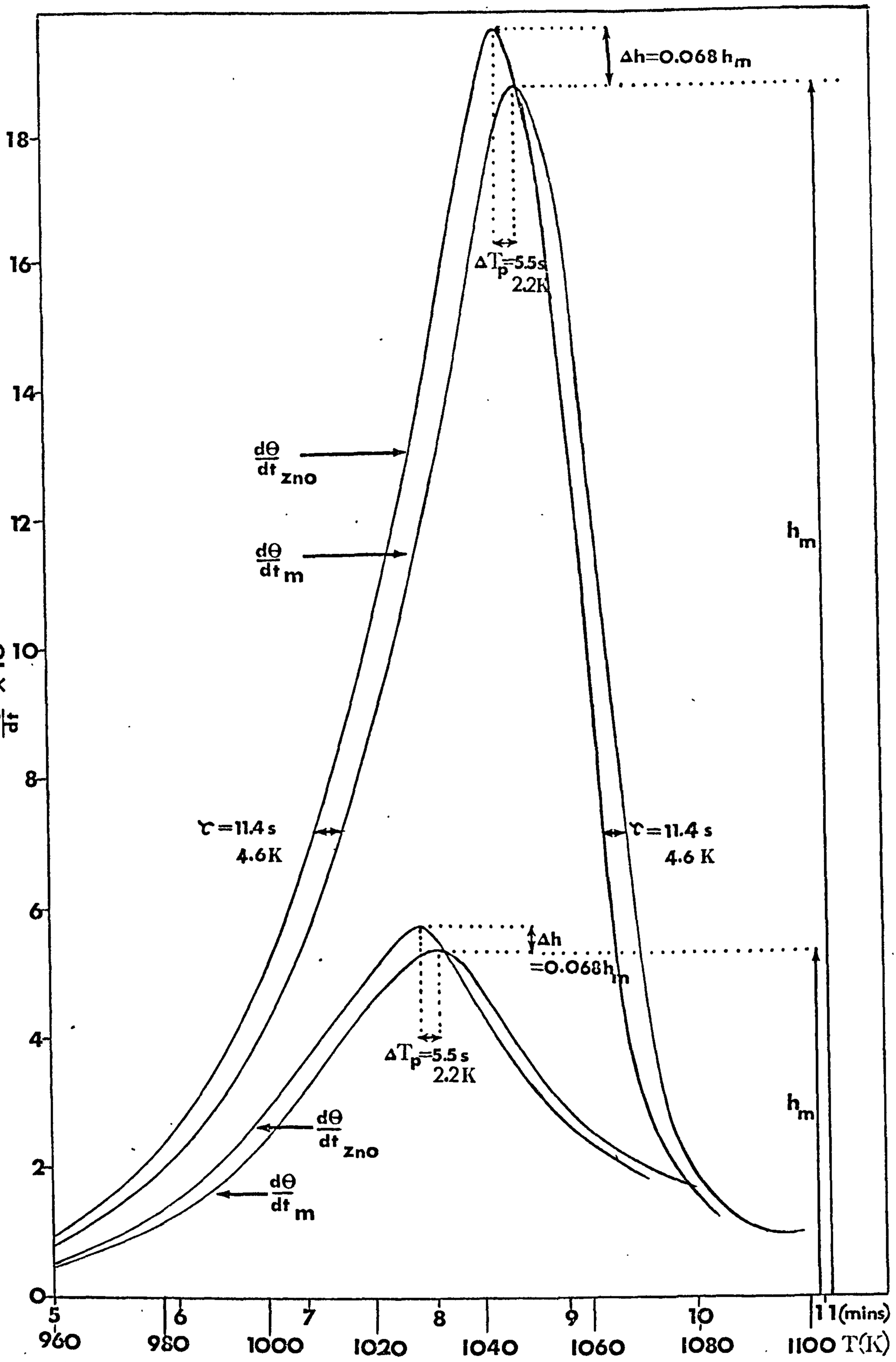

Fig. 3.8:

Oxygen T.P.D.'s from the $10\bar{1}0$ zinc oxide surface corrected for the time response of the system

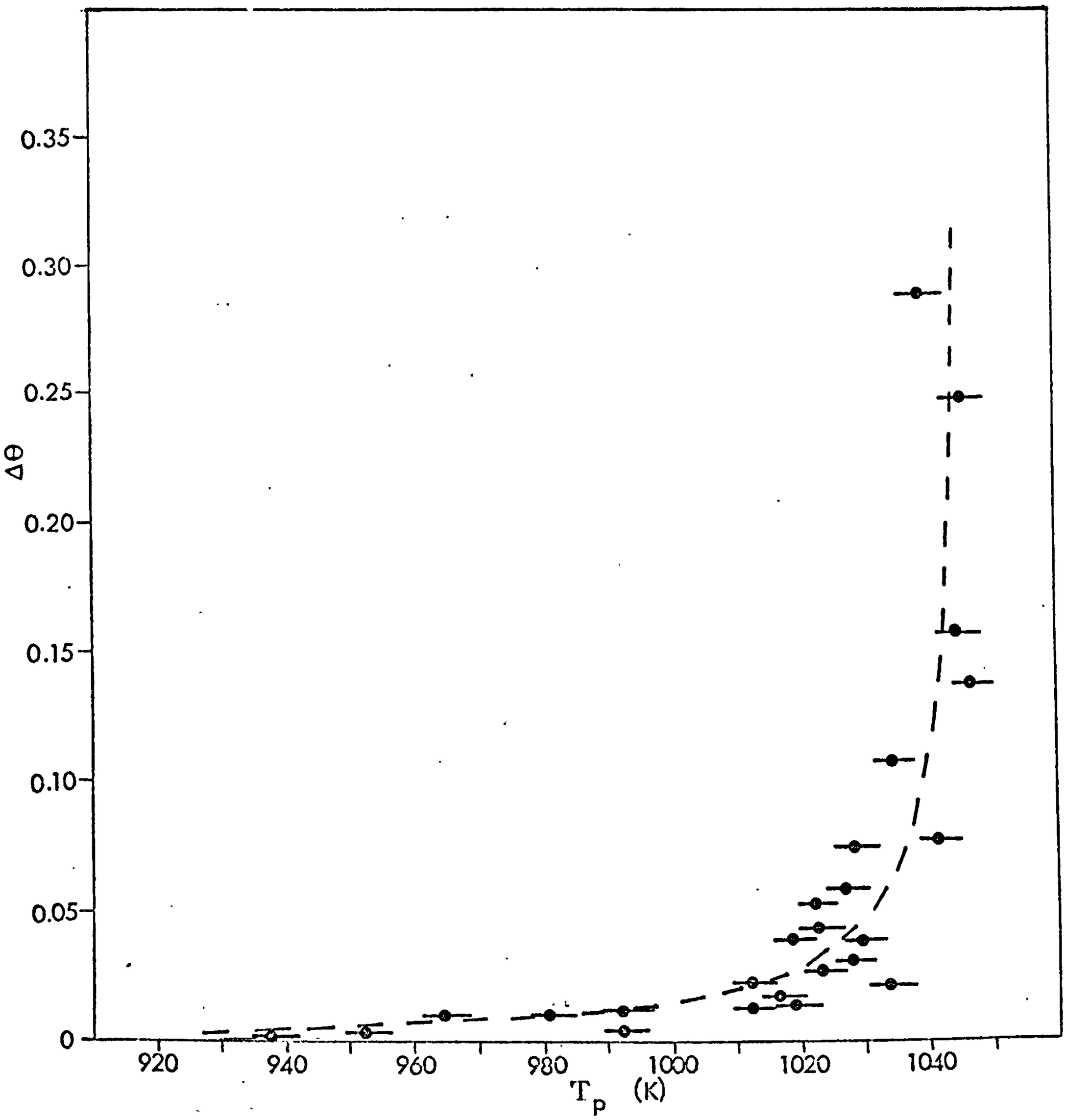

Fig. 3.9:

Variation of peak area $\Delta\theta$, with peak-maximum temperature, T_p

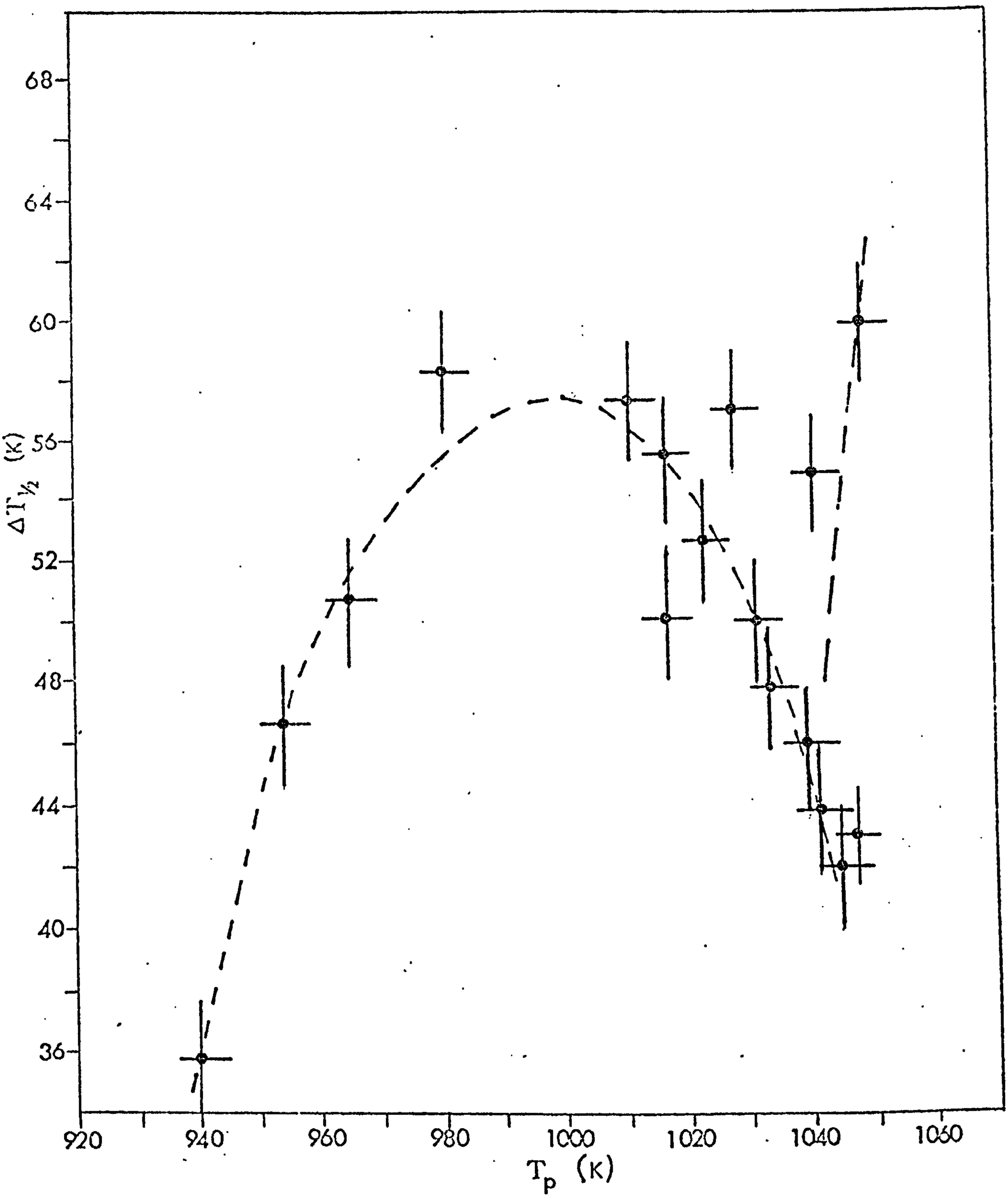

Fig. 3.10:

Variation of peak width at half height, $\Delta T_{1/2}$, with peak-maximum temperature, T_p

height, $\Delta T_{\frac{1}{2}}$, with peak temperature is shown in fig. (3.10). The error in measured peak width due to system response effects is given by equation [3.15] where, putting dT/dt = 0.4 for a heating rate of 0.4 K s^{-1}, then

$$\Delta T_{\frac{1}{2}m} = \Delta T_{\frac{1}{2}_1} + 1.4$$

which shows that the measured peak width, $\Delta T_{\frac{1}{2}m}$, is 1.4 K greater than the actual one. An explanation for the observed variation of peak width with peak temperature, together with the shift of peak temperature with peak size, will be advanced in section 4.1.1 .

The total peak area, $\Delta\theta_{oxy}$, can be plotted against the oxygen pre-treatment pressure, P_{O_2}, as a series of isotherms for different pre-treatment temperatures. However, it is observed that at high oxygen pressures and low temperatures the total amount of oxygen evolved during T.P.D. approaches a maximum that is equivalent to a fractional atomic coverage of 0.04. Thus, at this pressure and temperature of pre-treatment the surface is assumed to have its full quota of oxygen. At lower pre-treatment pressures and higher temperatures the total peak area, $\Delta\theta_{oxy}$, is less than 0.04 so, the total deficiency of oxygen from its full quota on the surface, at these new conditions of pre-treatment is given by

$$\theta = 0.04 - \Delta\theta_{oxy} \qquad [3.17]$$

where θ is the total oxygen deficiency (expressed as an atomic fraction). The above expression means that when $\Delta\theta_{oxy}$ is zero, i.e. when no oxygen peak is obtained (occurring at high pre-treatment temperatures and very low oxygen pressures, e.g. curve g of fig. (3.7)) there is a maximum concentration of oxygen deficiency corresponding to 4% of the total number of surface oxygen atoms. This will be justified in section 4.1.1 .

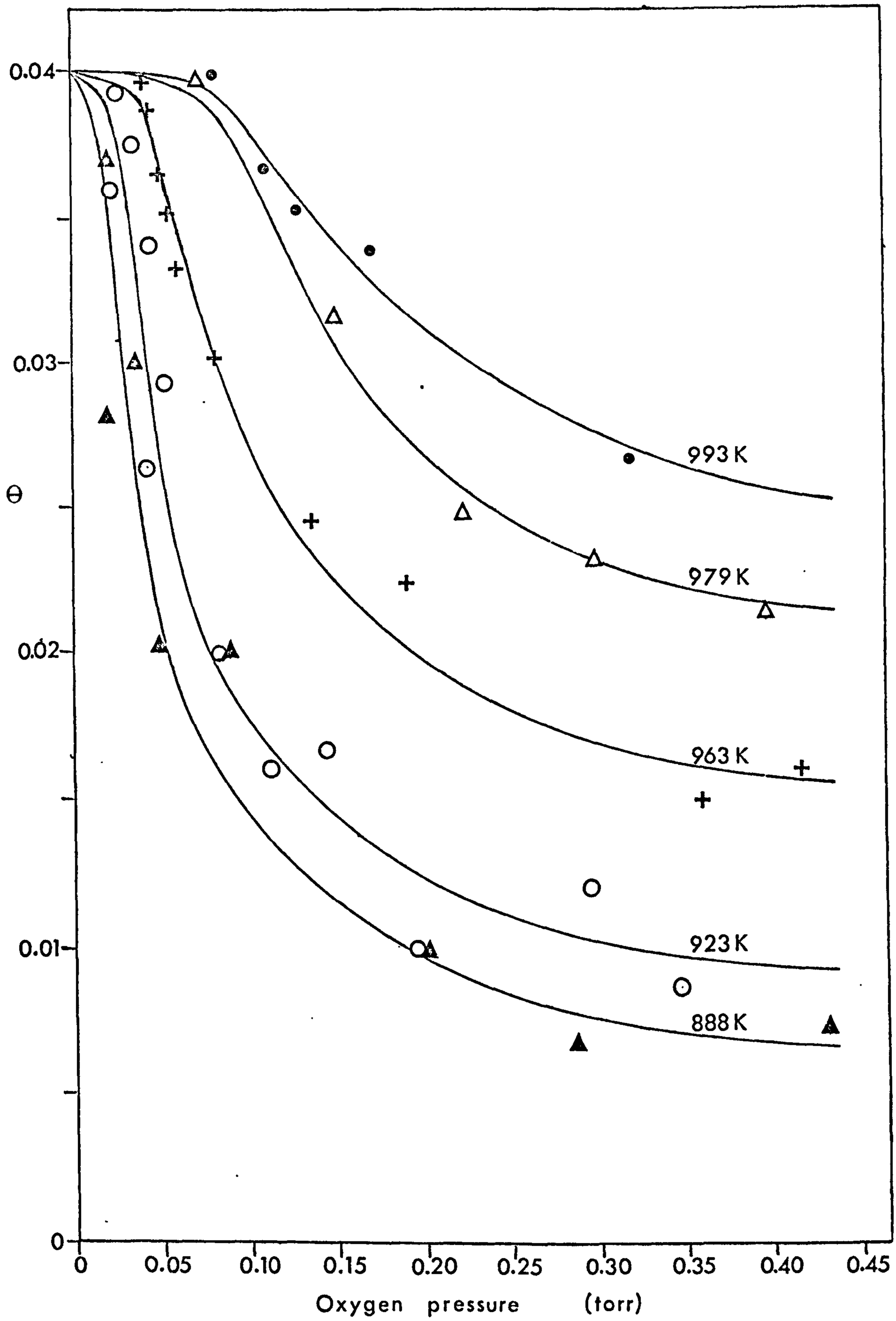

Fig. 3.11:

The fractional surface oxygen deficiency (vacancy concentration), θ, as a function of oxygen pressure, P_{O_2}, at various temperatures

Thus, the total fractional atomic deficiency defined by equation [3.17] can be plotted as a function of pre-treatment conditions (cf. fig. 3.11). In section 4.1.2 these isotherms, (θ vs. P_{O_2})$_T$, will be compared with those obtained theoretically, where it is shown that this fractional surface oxygen deficiency is merely the concentration of surface lattice oxygen vacancies.

So, the model tc be proposed later, (sections 4.1.1 and 4.1.2),is one in which oxygen in the gas phase interacts via an adsorbed phase with the surface lattice phase, producing a steady state concentration of surface lattice oxygen vacancies, dependent on the oxygen pressure and temperature of pre-treatment. Ensuring temperature programmed desorption allows the surface lattice phase to lose oxygen and increase the total vacancy concentration to a maximum of 4% of the surface. The total number of oxygen atoms lost from the lattice is given by the T.P.D. peak area, and is simply the difference between the maximum 4% vacancy concentration and the vacancy concentration obtaining at the steady state pre-treatment conditions.

(b) Below 800 K

After the initial clean up procedure described in section 2.4 three types of zinc oxide surface can be produced on which oxygen adsorption is to take place; these are: a contaminated surface, a vacancy rich uncontaminated surface and a vacancy deficient uncontaminated surface.

A surface that has been left at room temperature in vacuum for several hours will have been contaminated by residual gas impurities. Treatment of such a surface at low temperature in oxygen (for example, 450 K, P_{O_2} = 0.13 torr, for 1 hour as in fig. (3.12a)) followed by pump off of gas phase oxygen and temperature programmed desorption shows

reaction of surface adsorbed oxygen with adsorbed oxidiseable contaminants as in fig. (3.12a). Here, a fall in the total oxygen flow coincides with peaks in *m/e* 18 (H_2O), *m/e* 28 (CO) and *m/e* 44 (CO_2). Total peak areas indicate the extent of contamination, namely, the fractional coverage of water being 4.5×10^{-3} , and of oxidiseable hydrocarbons 3.7×10^{-3} .

A zinc oxide surface pre-treated at high temperature (> 800 K) in oxygen is rendered clean of surface contaminants. Such a surface can have a total concentration of surface oxygen vacancies between 0 and 4% dependent upon the pre-treatment conditions, as specified in the previous section (3.2.1a). Now, when this surface is cooled down to a temperature between 300 K and 750 K and treated for 1 hour with oxygen at pressures between 10^{-3} torr to 0.4 torr, followed by pump off of the gas phase oxygen, there are no low temperature peaks in the oxygen T.P.D. spectrum : the H_2O, CO_2 and CO backgrounds also remain unchanged. Curves b and c of fig.(3.12b) show this. Curve b shows a surface with very few vacancies, (pre-treatment at 293 K in $P_{O_2} = 0.4$ torr), where the rise in oxygen flow at the high temperature and of the T.P.D. spectrum is the beginning of the high temperature peak described in the previous section. Curve c shows a vacancy rich surface where there is no peak both at the low temperature and high temperature ends of the spectrum.

In the first few low temperature adsorption experiments performed, that is, immediately after the initial clean-up procedure, there appeared spasmodically a low temperature T.P.D. peak ($T_p \doteqdot 600$ K, curve a of fig. (3.12b)). This, however, completely disappears after several clean-up/adsorption/desorption cycles. It is tentatively attributed to remnant contaminating material. A full discussion is left to chapter 4.2.1 .

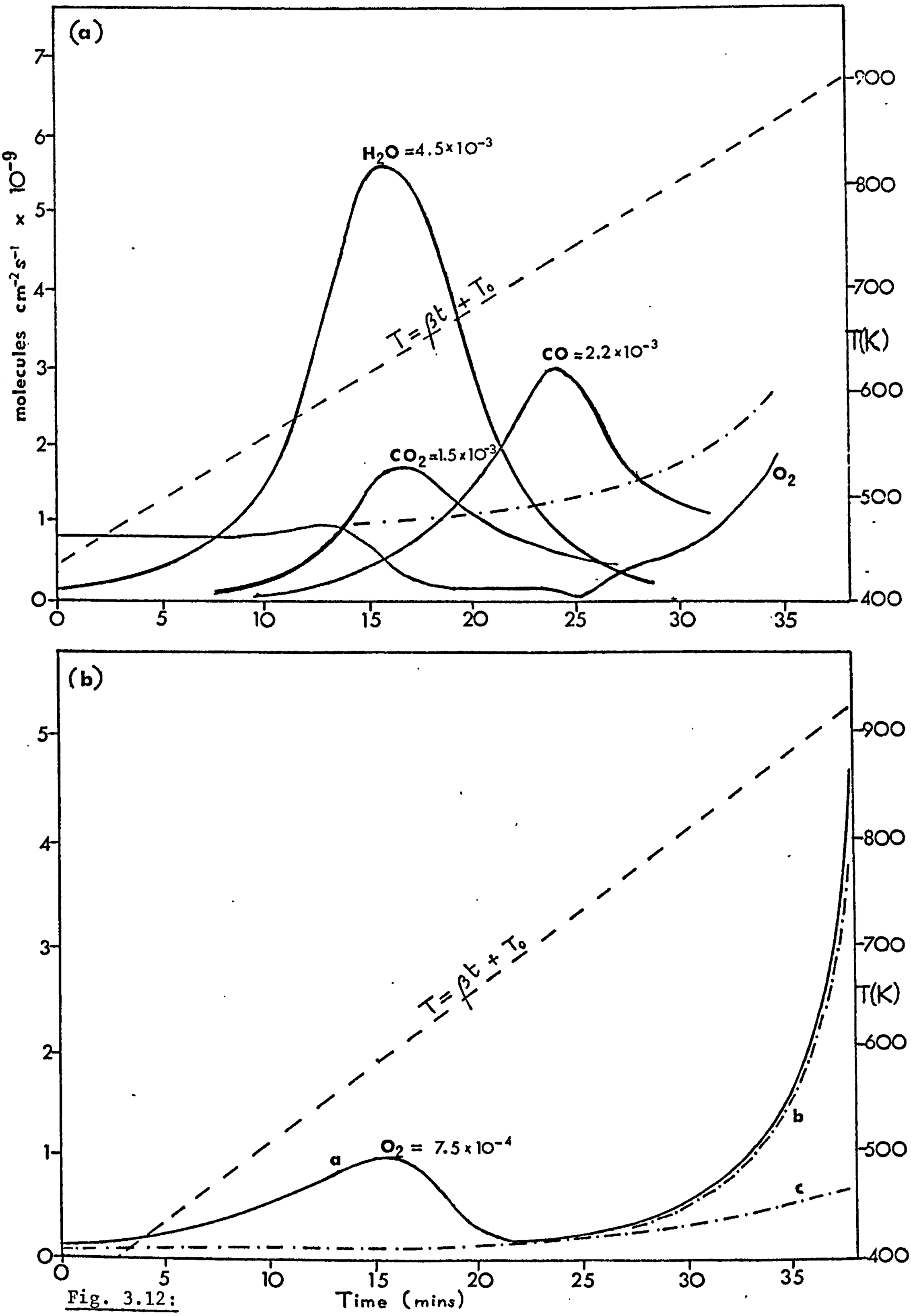

Fig. 3.12:

(a) T.P.D. spectra for H_2O, CO_2 , CO, and O_2 from a contaminated zinc oxide $10\bar{1}0$ surface pre-treated for 1 hour at 450 K in 0.13 torr oxygen

(b) T.P.D. spectra for O_2 from a cleaned zinc oxide $10\bar{1}0$ surface

The above experiments were repeated using O^{18} enriched oxygen (see next section) as the adsorbate and monitoring m/e 34 ($O^{16}O^{18}$) in the temperature programmed desorption. The background level of m/e 34 is ca. 100 times less than m/e 32, whereas the amount adsorbed would be only about 3 times less (isotopic oxygen gas mixture contains ca.25% $O^{16}O^{18}$ and 72% O_2^{16}). With this improved sensitivity it can be stated that there are no peaks in the low temperature T.P.D. spectrum, for all pre-treatment conditions that were employed, down to near the noise level of the mass spectrometers and, this corresponds to a sensitivity in the measurement of fractional atomic coverage down to $\theta \doteqdot 4 \times 10^{-6}$.

3.2.2 The interaction of isotopic oxygen with zinc oxide single crystals

In this section a series of experiments concerning the exchange of isotopic oxygen over zinc oxide single crystals are described. The zinc oxide sample is the same as used in the previous section (sample 1, characterised in chapter 2). The isotopic oxygen (B.O.C. "research grade"), with contaminants as listed in section 3.2.1 , was 15% enriched, that is a mixture of 72.25% O_2^{16} , 25.5% $O^{16}O^{18}$ and 2.25% O_2^{18} .

The exchange experiments are sub-divided into two groups. Firstly, high temperature exchange at low surface vacancy concentration. Secondly, temperature transient exchange experiments at high temperature.

(a) Isotopic oxygen exchange between 800 K and 1200 K at low surface vacancy concentration

When zinc oxide is treated in oxygen, at pressures between 0.1 and 0.4 torr and temperatures between 820 K and 920 K the steady state concentration of surface lattice oxygen vacancies will be low, as specified in section 3.2.1 . This means that the high temperature T.P.D.

peak (T ≒ 1040 K) will be large (up to $\Delta\theta_{Oxy} = 0.04$). By monitoring the thermodesorption peaks at m/e 32, 34 and 36, i.e. for O_2^{16} , $O^{16}O^{18}$ and O_2^{18} , and measuring their relative areas, the extent of surface lattice oxygen exchange can be followed. (It can be taken that no exchange takes place with sub-surface layer lattice oxygen : see chapter 4)). If after a certain pre-treatment schedule, that is, treatment in isotopic oxygen for a fixed time at a set temperature and pressure, the total fractional atomic concentration of O^{18} in the surface lattice layer is y^{18} , and of O^{16} it is y^{16} (which is $1 - y^{18}$), then, assuming all oxygens are at equivalent lattice sites on the surface, the ratio of peak areas (A_x is the area for gas x) in the T.P.D. spectra of m/e 32, 34 and 36 will be given by

$$A_{O_2^{18}} : A_{O^{16}O^{18}} : A_{O_2^{16}} = (y^{18})^2 : 2y^{18}y^{16} : (y^{16})^2 \qquad [3.18]$$

which is,

$$A_{O_2^{18}} : A_{O^{16}O^{18}} : A_{O_2^{16}} = (y^{18})^2 : 2y^{18}(1-y^{18}) : (1-y^{18})^2 \qquad [3.19]$$

where y^{16} is equal to $1 - y^{18}$. Normalising the above with respect to the area of the O^{18} peak gives

$$A_{O_2^{18}}/A_{O_2^{18}} : A_{O^{16}O^{18}}/A_{O_2^{18}} : A_{O_2^{16}}/A_{O_2^{18}} = 1 : 2\left(\tfrac{1}{y^{18}}-1\right) : \left(\tfrac{1}{y^{18}}-1\right)^2 \qquad [3.20]$$

Now, the total gas phase atomic fraction of O^{18} is obtained from the peak areas by

$$\text{Atomic fraction } O^{18} \text{ in gas phase} = \frac{2A_{O_2^{18}} + A_{O^{16}O^{18}}}{2(A_{O_2^{18}} + A_{O^{16}O^{18}} + A_{O_2^{16}})} \qquad [3.21]$$

which becomes, by using equation [3.19],

$$\text{Atomic fraction } O^{18} \text{ in gas phase} = \frac{2(y^{18})^2 + 2y^{18}(1-y^{18})}{2\left((y^{18})^2 + 2y^{18}(1-y^{18}) + (1-y^{18})^2\right)}$$

This simplifies to give

$$\text{Atomic fraction } O^{18} \text{ in gas phase} = y^{18} \qquad [3.22]$$

which is the same as the O^{18} atom fraction in the surface lattice layer. So, a plot of $2(1/y^{18} - 1)$ against y^{18} gives a curve (curve b of fig. (3.13)) of the ratio of the $O^{16}O^{18}$ peak size to the O_2^{18} peak size ($A_{O^{16}O^{18}}/A_{O_2^{18}}$) plotted against the total gas phase atom fraction of O^{18}, and a plot of $(1/y^{18} - 1)^2$ against y^{18}, (curve b of fig. (3.14)) gives the relative peak areas $A_{O_2^{16}}/A_{O_2^{18}}$ against the gas phase atom fraction of O^{18}, for this theoretical single lattice site model.

Now, for an experimental set of peaks in the m/e 32, 34 and 36 signals (monitored simultaneously during one T.P.D. run), plotting each of $A_{O^{16}O^{18}}/A_{O_2^{18}}$ (curve a of fig. (3.13)) and $A_{O_2^{16}}/A_{O_2^{18}}$ (curve a of fig. (3.14)) against the atom fraction of O^{18} in the gas phase, gives experimental points as shown in figs (3.13) and (3.14) corresponding to different extents of surface exchange (set by the pre-treatment). It is clear that these do not come close to the curve predicted by the simple single state model. A full analysis invoking two or more non-equivalent types of surface lattice oxygen site will be advanced in section 4.1.3 .

(b) <u>Temperature transient isotopic exchange at temperatures between 800 K and 1200 K</u>

After the preliminary clean-up procedure described in section 2.4 the zinc oxide crystals are heated to a temperature between 1050 K and 1100 K in vacuum for 10 minutes, leaving a clean surface with a maximum number

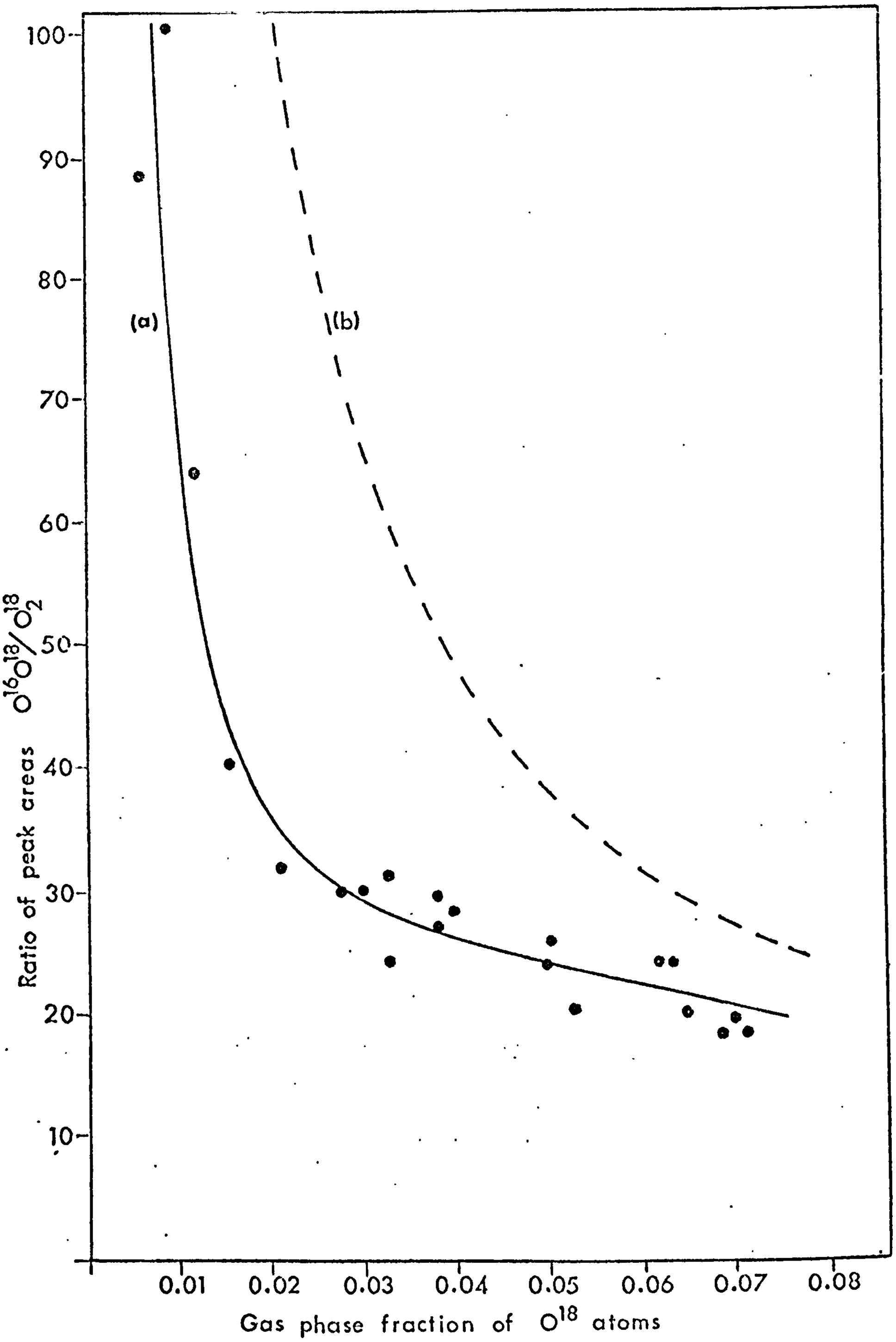

Fig. 3.13:

Ratio of the T.P.D. peak areas for $O^{16}O^{18}$ and O_2^{18}, i.e. $A_{O^{16}O^{18}}/A_{O_2^{18}}$ against the atom fraction of O^{18} in the gas phase

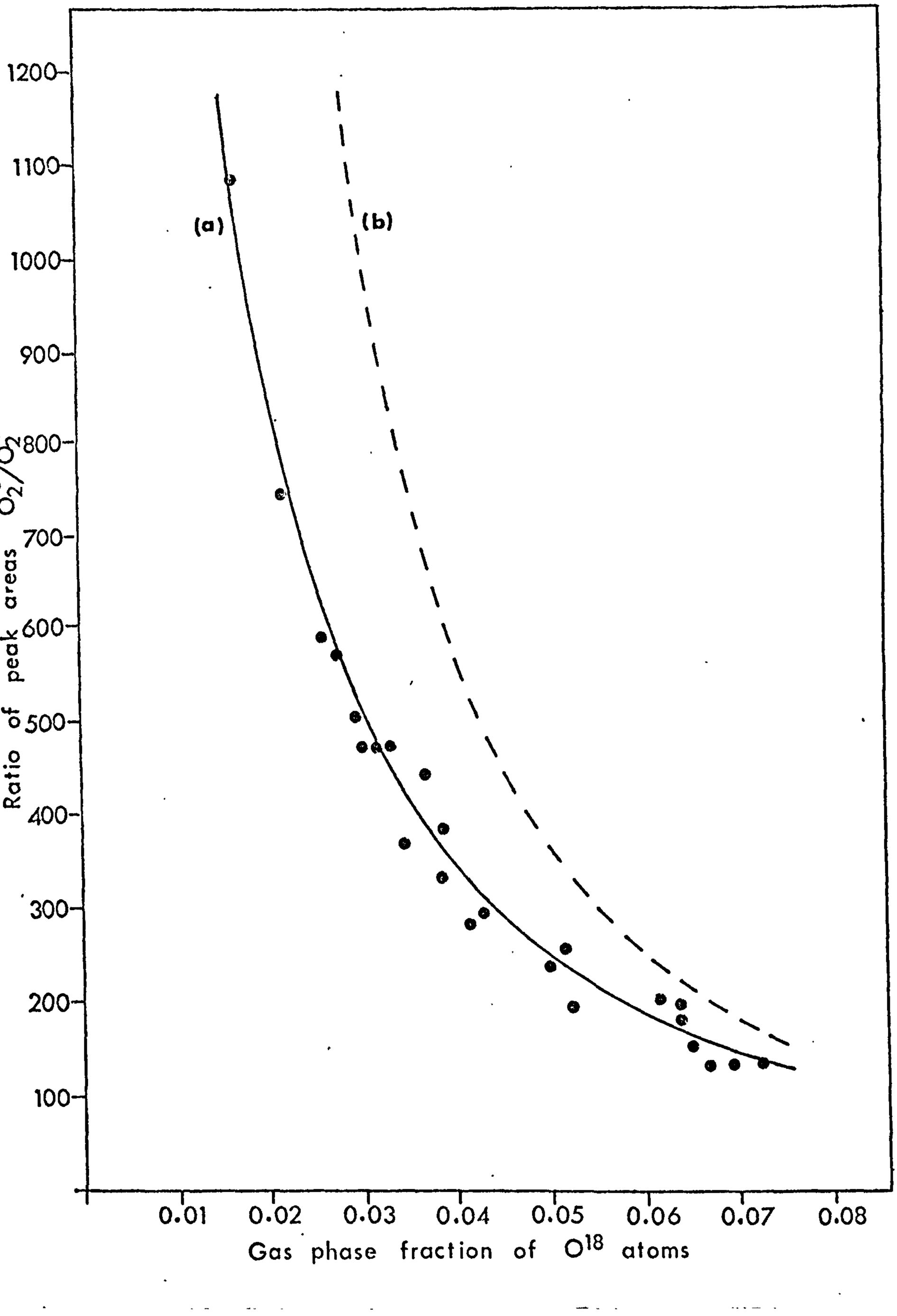

Fig. 3.14:

Ratio of the T.P.D. peak areas for O_2^{16} and O_2^{18}, i.e. $A_{O_2^{16}}/A_{O_2^{18}}$ against the atom fraction of O^{18} in the gas phase

(θ = 0.04) of surface oxygen vacancies. After cooling in vacuum to about 800 K, isotopic oxygen is passed over the solid at a flow rate ($F_{LV1}^{O^{16}O^{18}}$) determined by the setting of leak valve 1, (the superscript in $F_{LV1}^{O^{16}O^{18}}$ referring to the gas in question). Using equation [3.2], the total flow rate (ignoring, for the moment, system response corrections), $F_1^{O^{16}O^{18}}(t)$ at time t is given by

$$F_1^{O^{16}O^{18}}(t) = F_{LV1}^{O^{16}O^{18}} - F_{ZnO}^{O^{16}O^{18}}(t) \quad \text{torr cc s}^{-1} \qquad [3.23]$$

where $F_{ZnO}^{O^{16}O^{18}}$ is the total flow rate of O^{16} O^{18} onto the zinc oxide. Now, at t = 0 (T $\doteq$ 800 K) there is no exchange, and $F_{ZnO}^{O^{16}O^{18}}$ is zero. Hence

$$F_1^{O^{16}O^{18}}(t=0) = F_{LV1}^{O^{16}O^{18}} \quad \text{torr cc s}^{-1}$$

and this in equation [3.23] gives

$$F_{ZnO}^{O^{16}O^{18}}(t) = F_1^{O^{16}O^{18}}(t=0) - F_1^{O^{16}O^{18}}(t) \quad \text{torr cc s}^{-1} \qquad [3.24]$$

Now, when the zinc oxide is heated at a linear rate (β), the total flow $F_1^{O^{16}O^{18}}(t)$ at time t (and temperature T = T_o + βt) decreases as more O^{16} O^{18} goes onto the zinc oxide, i.e. as $F_{ZnO}^{O^{16}O^{18}}(t)$ increases. The total exchange rate is given by equation [3.24], and this in molecules per second per cm^2 ($dN_{O^{16}O^{18}}/dt$) is given by

$$dN_{O^{16}O^{18}}/dt = F_{ZnO}^{O^{16}O^{18}}(t) \times \frac{3.54 \times 10^{16}}{250}$$

for a surface area of 250 cm^2.

Since the total flow rate of $O^{16}\,O^{18}$ is decreasing, then also the pressure of this gas over the zinc oxide is changing in accordance with

$$P_{O^{16}O^{18}} = F_1^{O^{16}O^{18}}(t) / K_2 \quad \text{torr} \qquad [3.25]$$

So, in fig. (3.15) there are shown the results of such an experiment, where the pressure (for $K_2 = 3 \times 10^{-2}$ cm^3 s^{-1}) and exchange rate are as indicated. The total reaction chamber pressure (which is the sum of the partial pressures of O_2^{16} and $O^{16}\,O^{18}$) is constant at 7.3×10^{-2} torr (in the exchange process, when one molecule of $O^{16}\,O^{18}$ goes onto the zinc oxide surface one molecule of O_2^{16} is evolved, and the net number of molecules in the gas phase remains unchanged).

Curve a in fig. (3.15) shows the measured $O^{16}\,O^{18}$ flow versus time (and temperature). Curve b shows the curve corrected for system time constant, where, using equation [3.12] and the above value of $K_2 = 3 \times 10^{-2}$ cm^3 s^{-1} , then $\tau = 194$ s.

A whole set of such experiments were performed at different heating rates. The results will be discussed in section 4.1.4, and, in addition, it will be shown how the parameters obtained above are used to obtain the overall kinetics of the exchange process.

A set of experiments were run in conjunction with those described above. In these the zinc oxide was pre-treated at 1050 K to 1100 K in vacuum for 10 minutes, followed by cooling to 800 K, as before. Isotopic oxygen is allowed to flow over the zinc oxide and achieve a steady state flow rate at a particular setting of leak valve 2. Now, a step increase in temperature to a new value, (T_1 on fig. (3.16)), at which exchange takes place, is followd by an almost immediate drop in the $O^{16}\,O^{18}$ flow rate. The zinc oxide is kept at this temperature for 10 minutes.Fig. (3.16)

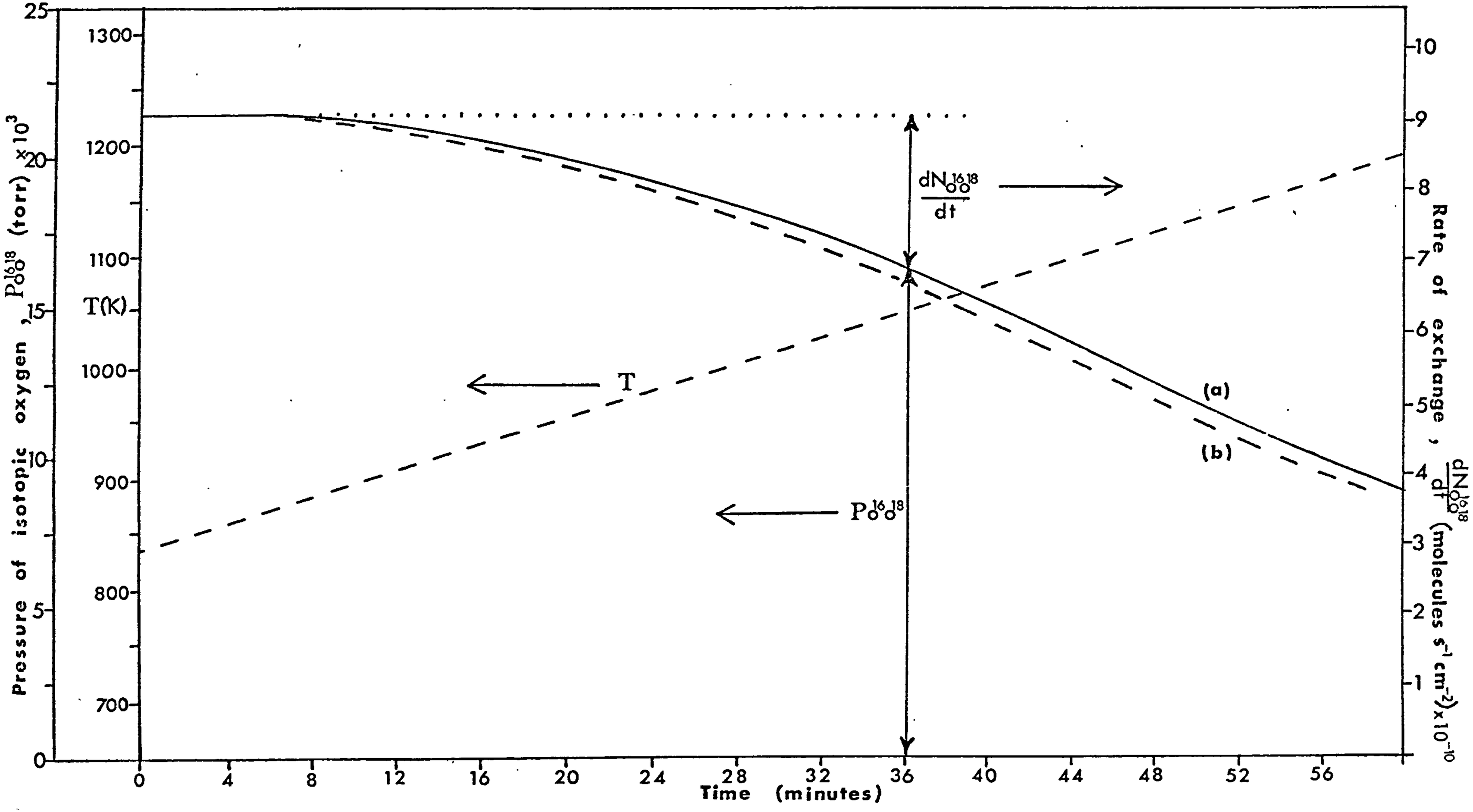

Fig. 3.15: Rate of O^{16} O^{18} exchange under temperature transient conditions and changing O^{16} O^{18} pressure

(a) the measured curve (b) the system time response corrected curve

shows the measured temperature and $O^{16}O^{18}$ flow rate versus time. This experiment is repeated for a series of different temperatures (T_2 , T_3 ... etc. in fig. (3.16)) at which the exchange takes place.

The total area, abcd, in fig. (3.16) gives the total amount of $O^{16}O^{18}$ exchanged in 10 minutes at that temperature. The total measured flow rate never drops by more than 20% of its initial low temperature value, so the pressure of $O^{16}O^{18}$, given by equation [3.25] remains approximately constant. Over the first 50 seconds of the experiment, both the temperature and the flow rate are changing. Thus there is an uncertainty in the total extent of exchange in this time. The total amount exchanged in 10 minutes is therefore assessed with an estimated error of ±10%. The pressure of $O^{16}O^{18}$ is 3.3×10^{-2} torr variable by ±10%, and the total oxygen pressure ($P_{O_2^{16}} + P_{O^{16}O^{18}}$) is constant at 0.12 torr. The results of the above experiments are given in section 4.1.4 together with a discussion of the exchange kinetics.

3.23 Decomposition of nitrous oxide on zinc oxide single crystals

The experiments described in this section are concerned with the decomposition of nitrous oxide over single crystals ($10\bar{1}0$ plane) of zinc oxide. The zinc oxide (sample 1, characterised in chapter 2) was that used in the previously described experiments. The nitrous oxide, obtained in litre flasks from B.O.C., is "Research Grade", 99.998% pure with contaminants as listed below,

Nitrogen	8 p.p.m.
Oxygen	2 p.p.m.
NO, NO_2	< 1 p.p.m.
Water	1 p.p.m.
Carbon dioxide	8 p.p.m.

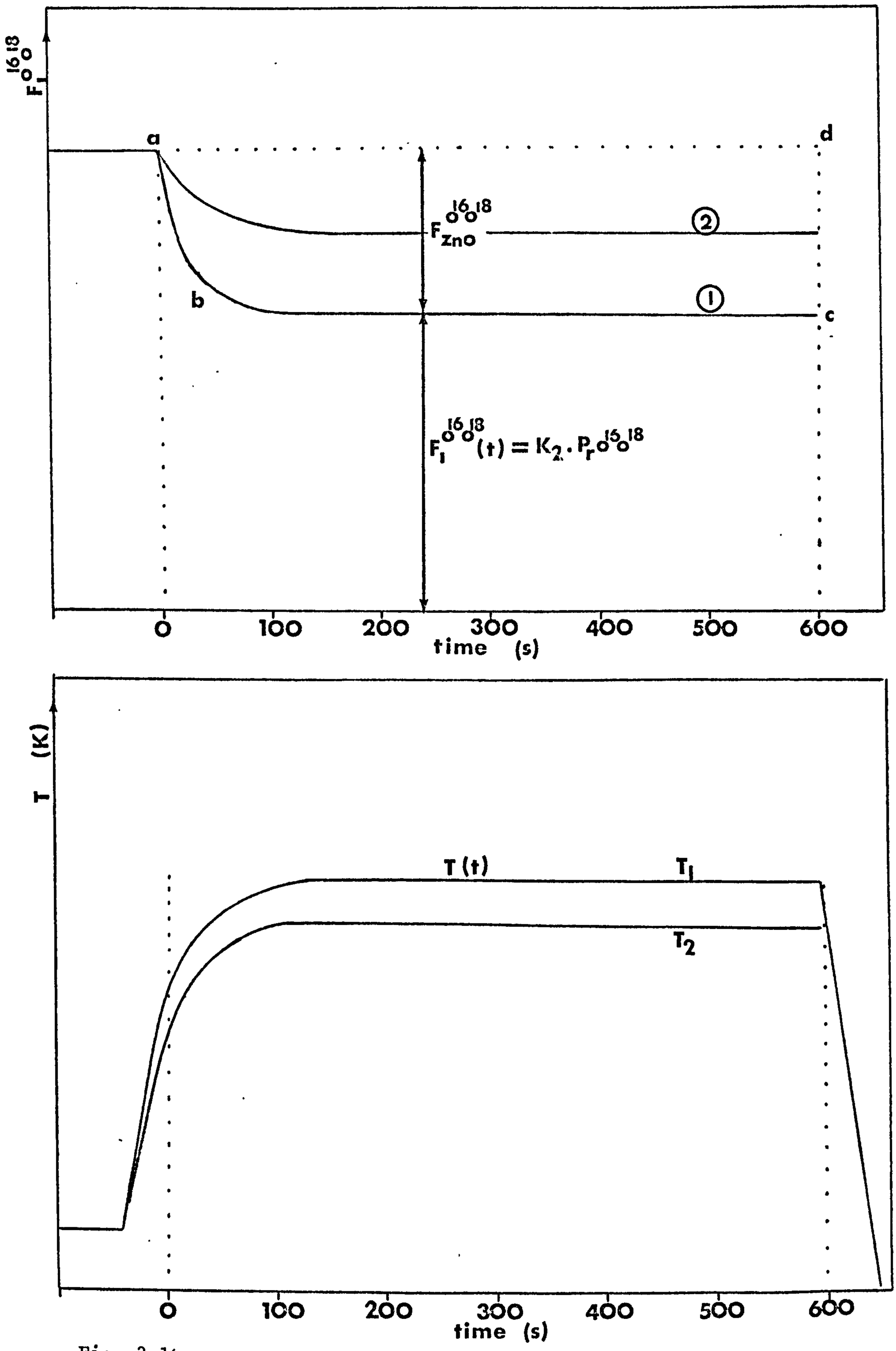

Fig. 3.16:

The change of O^{16} O^{18} gas flow onto the zinc oxide $10\bar{1}0$ surface, $F_{ZnO}^{O^{16}O^{18}}$, for the change in temperature versus time indicated

In these experiments nitrous oxide in the source chamber at a pressure, P_s , is allowed to flow through leak valve 1 at a rate $K_1 P_s$ into the reaction chamber. The pressure in the reaction chamber, P_{N_2O} , given by $K_1 P_s / K_2$, is controlled by leak valve 2 through which the gas exits. The cracking pattern (fig. 3.3b) indicates peaks at m/e 32 and 28 for oxygen and nitrogen at intensities of 5.2% and 55.3% of the parent peak. Because, typically, the extent of catalytic decomposition at the zinc oxide is of the order of 10^{-2}%, under our conditions,it is necessary that nitrous oxide be trapped out to a sufficiently low pressure before it reaches the mass spectrometer, in order to provide sufficient experimental sensitivity. At liquid nitrogen temperature (77.4 K) nitrous oxide is trapped out to a base pressure of 2.5×10^{-7} torr, and the corresponding effective pressures of oxygen and nitrogen produced at the mass spectrometer filament are 1.3×10^{-8} torr and 1.4×10^{-7} torr respectively, and are still too high. (Fig. 3.18 shows a total decomposition product gas flow rate of 1×10^{10} molecules s^{-1} cm^{-2} at 1000 K. This corresponds to a pressure of 5.65×10^{-8} torr at the mass spectrometers). At solid nitrogen temperature (obtained by pumping on liquid nitrogen to a pressure better than 40 torr, gives a trap temperature less than 59 K) the corresponding vapour pressure of nitrous oxide is 1.6×10^{-12} torr, at which pressure the oxygen and nitrogen fragments of the nitrous oxide cracking are negligibly low. So, nitrous oxide is removed at the solid nitrogen trap located as shown in fig.(3.1).

Both steady state and temperature transient experiments were performed and these are described in turn below.

3.2.3a Steady-state

The zinc oxide is pre-treated at a temperature between 1050 K and 1100 K for 10 minutes in vacuum at which temperature the surface has its maximum number of oxygen vacancies (θ = 0.04). The temperature is reduced in vacuum to one at which the decomposition reaction is to take place. At this temperature, nitrous oxide is allowed to flow over the zinc oxide. The gas flow is allowed to achieve steady state at a particular setting of leak valve 2. Monitoring of the decomposition products is at the mass psectrometer. When the mass spectrometer signals for m/e 32 and 28 are constant, (after about 10 mins) steady state decomposition is achieved. The total pressure of oxygen, (corrected for the background level, which is up to about 50% when the rate of decomposition is very low) gives the rate of decomposition in molecules s^{-1} cm^{-2} , dN_{O_2}/dt, by

$$dN_{O_2}/dt = \frac{P_{AO_2} \times S_{O_2} \times 3.54 \times 10^{16}}{250}$$

for a zinc oxide surface area of 250 cm^2 , at a reaction chamber pressure of nitrous oxide, P_{N_2O} , given by $K_1 P_s / K_2$. By changing the leak rate of either of leak valve 1 or 2 the reaction chamber pressure can be varied in the range 10^{-3} to 0.8 torr. (Since the extent of decomposition is so small, the pressures of nitrogen and oxygen do not contribute to the overall reaction chamber pressure:) When the gas flow has reached steady-state at this new pressure setting, the decomposition rate is again measured, as above. By varying the temperature of decomposition a set of isotherms can be evolved, as shown in fig.(3.17).

The total amount of oxygen incorporated onto the zinc oxide surface during nitrous oxide decomposition can be assessed by the following procedure: the nitrous oxide gas flow is turned off, the system evacuated

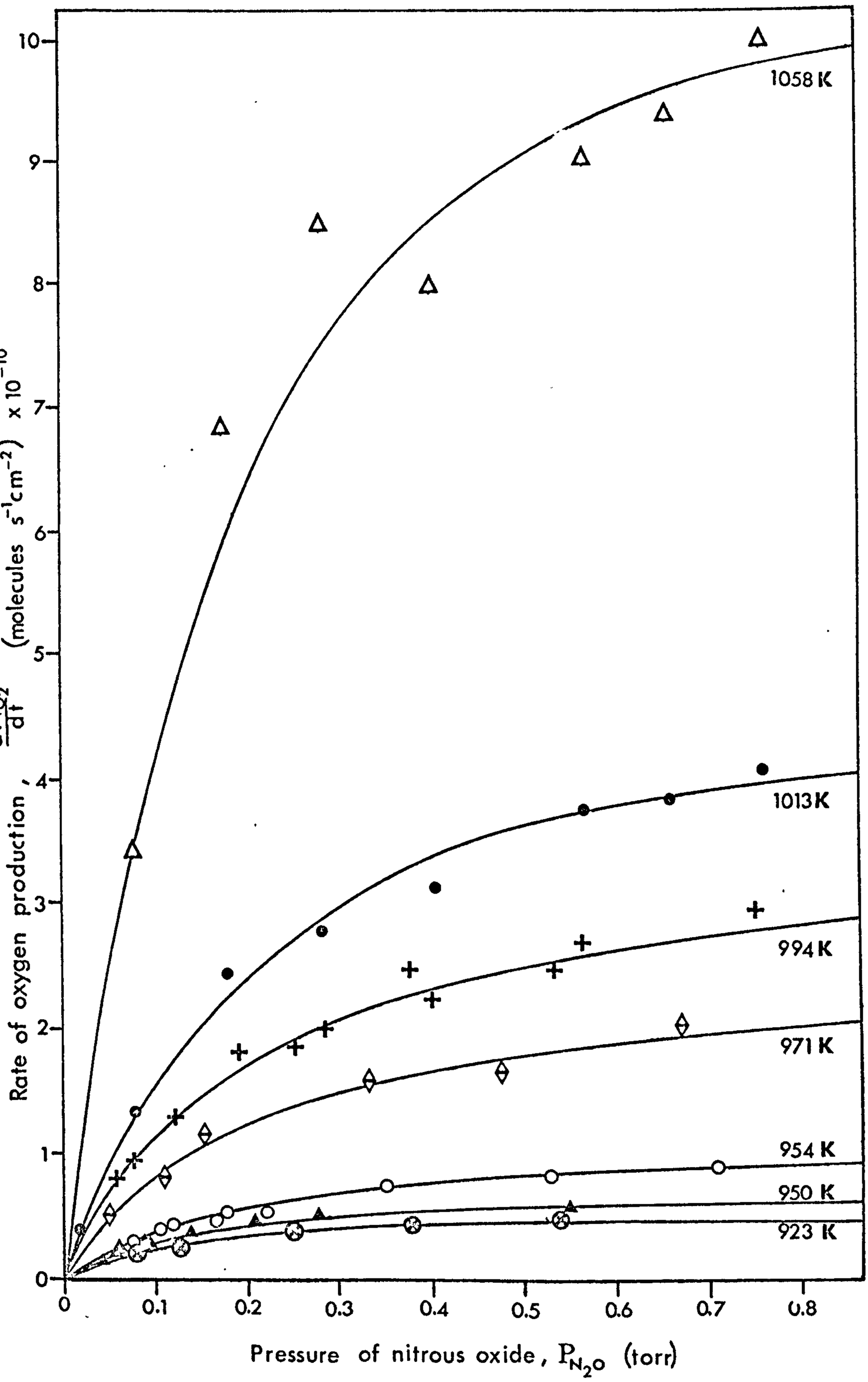

Fig. 3.17:

The rate of oxygen production in the steady-state decomposition of nitrous oxide at various temperatures, as a function of nitrous oxide pressure

and the zinc oxide quenched to a temperature of about 800 K. The high temperature T.P.D. spectrum (see section 3.2.1) shows no oxygen peak, for any of the pressure or temperature conditions used in the nitrous oxide decomposition reaction (indicated in fig. (3.17)). Thus, at all temperatures and pressures of nitrous oxide, in those ranges studied, the zinc oxide surface remains with its full quota of surface lattice oxygen vacancies as set by the pre-treatment conditions.

Theoretical analysis of these data will follow in section 4.1.5.

3.2.3b Temperature transient measurements

Nitrous oxide is passed over the zinc oxide surface at a constant flow rate and at constant pressure. A zinc oxide surface, that had been recontaminated by background system impurities over a period of several hours, is heated from room temperature at a linear heating rate ($\beta = 4.8 \times 10^{-2}$ K s^{-1}) in nitrous oxide. The flow of decomposition product gases as a function of time (and temperature) is shown in fig. (3.18). As the temperature increases the rate of oxygen production should increase exponentially. However, three distinct dips in this flow curve, (curve a, fig. (3.18)) are observed at 640 K, 720 K and 900 K. The overall product gas flow (measured by pressure change at the ion pump) exhibits three peaks at exactly these same temperatures (curve c, fig. (3.18)). It is thus concluded that there are three distinct oxidizeable impurity centres on this contaminated surface.

The peaks in the overall pressure curve correspond to an increased rate of reaction at site X, given by the general equation.

$$N_2O + X \longrightarrow N_2 + XO$$

When the surface has been heated to its maximum temperature in nitrous oxide, all contaminants have been removed. When now the surface is cooled at the same linear rate ($\beta = 4.8 \times 10^{-2}$ K s^{-1}) and same N_2O

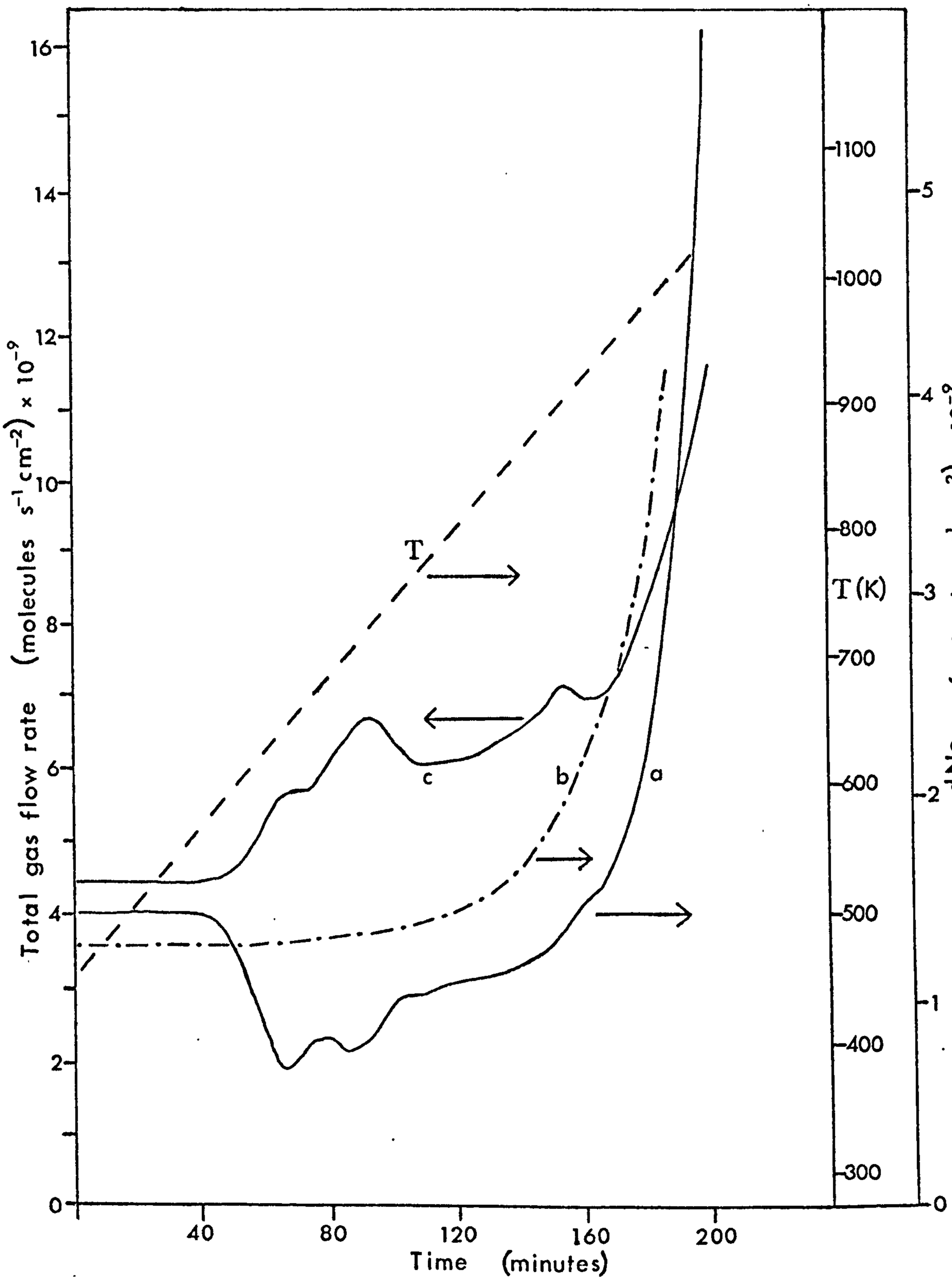

Fig. 3.18:

Nitrous oxide decomposition under temperature transient conditions on a contaminated zinc oxide $10\bar{1}0$ surface

pressure, an uninterrupted exponential fall in rate of oxygen production with decreasing temperature is observed (this is indicative of decomposition of nitrous oxide on a clean surface) (curve b, fig. (3.18)). The total area enclosed between the oxygen flow curves in the heating and cooling modes is a measure of the total number of oxygen molecules lost in oxidizing contaminants, which is about 4×10^{12} molecules cm^{-2}, i.e. about 8×10^{12} surface contaminant atoms per cm^2. This is a fractional coverage of 1.3×10^{-2}.

By repeating the above procedure of heating to a temperature of about 1000 K, then cooling at a linear rate in nitrous oxide at constant pressure, a series of curves for different pressures of nitrous oxide can be obtained. A representative sample of these, fig. (3.19), reveals the exponential fall in rate of oxygen production with falling temperature for three different pressures of nitrous oxide. The dashed lines indicate the correction for the time response of the system. At P_{N_2O} = 0.22 torr, leak valve 2 has a conductance $K_2 = 5 \times 10^{-2}$ cc s^{-1} and τ, given by equation [3.12] is 117 s : at P_{N_2O} = 0.036 torr, K_2 = 0.1 cc s^{-1} and τ is 59 s and at P_{N_2O} = 0.0081 torr K_2 is 0.25 and τ is 24 s.

A full discussion of these data is left until section 4.1.5 .

3.2.4 Miscellaneous gas reactions on zinc oxide single crystals

The zinc oxide single crystal sample used in these experiments was grown by the vapour phase oxidation of zinc iodide (sample 2, characterised in chapter 2) with a surface area of 450 ± 50 cm^2.

In these experiments gases produced in a microwave discharge were passed over the zinc oxide in the reaction chamber. Both carbon monoxide and oxygen gas were used to support the discharge. A microwave cavity

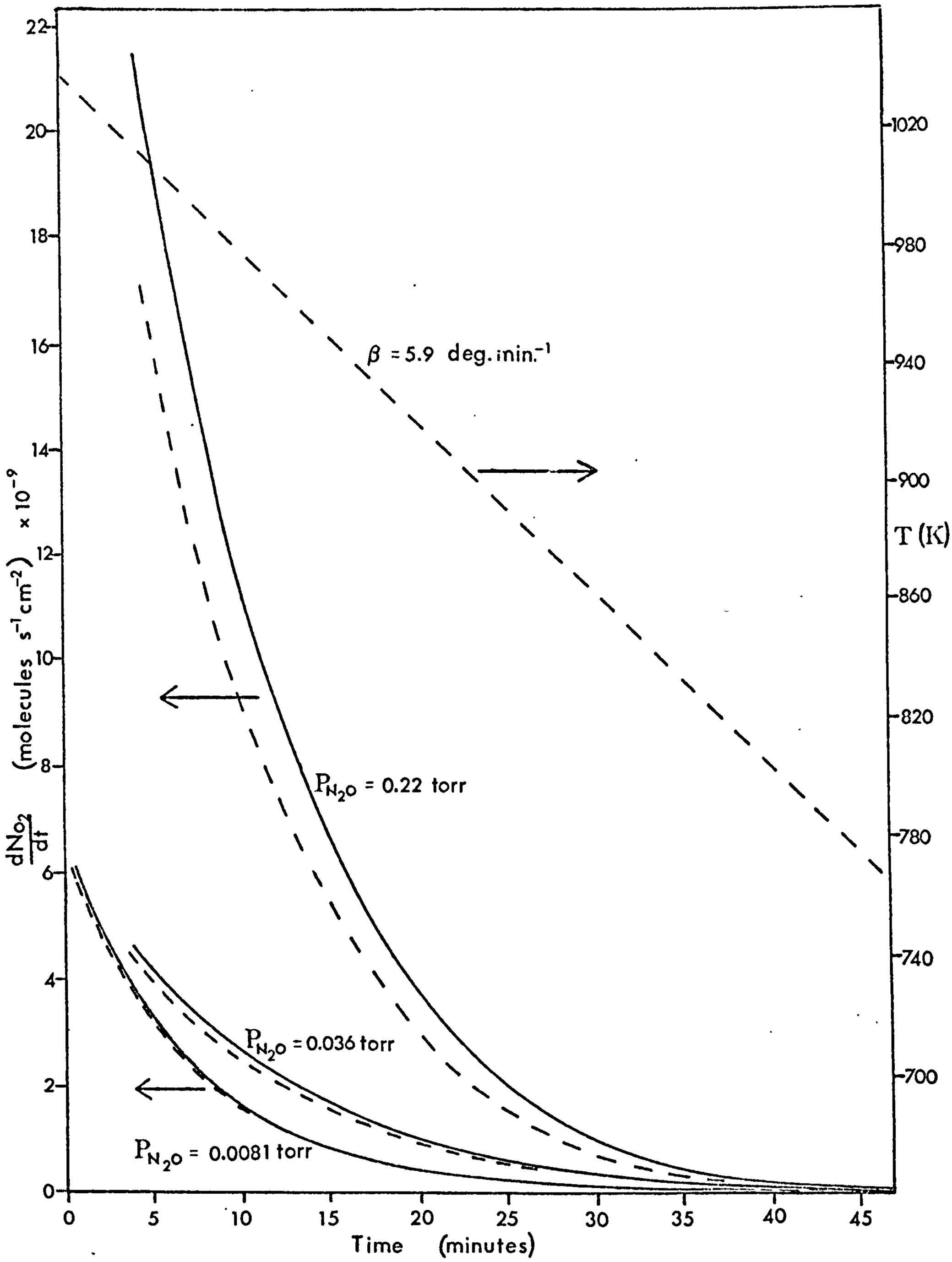

Fig. 3.19:

Nitrous oxide decomposition under temperature transient conditions, on a cleaned zinc oxide $10\bar{1}0$ surface

was placed around the inlet arm of the reaction chamber (cf. fig. 3.4) and activated when the gas pressure in the reaction chamber was ca. 0.1 torr (below 5×10^{-2} torr the gas pressure was toc low to maintain a discharge). When oxygen was passed through the microwave discharge, only m/e 28 (carbon monoxide) was monitored at the mass spectrometer (probably due to the formation of highly reactive atomic oxygen species in the discharge, and their subsequent immediate reaction with any carbon containing species on the apparatus walls). When carbon monoxide was used in the microwave discharge, a film of carbon formed on the reaction chamber walls in the cavity (probably due to the CO dissociation).

Both adsorptions and T.P.D. experiments were performed. In the adsorption experiments a constant flow of gas was allowed to pass over the zinc oxide surface (pre-treated at high temperature - ca. 850 K and high oxygen pressure ca. 0.2 torr, to give a surface with a low oxygen vacancy concentration - cf. section 4.1.2), at 850 K, with the microwave discharge activated. The flow rate decreased as the temperature was reduced, indicating adsorption of gas onto the surface. When the zinc oxide had been cooled to room temperature the gas flow rate returned to its original constant flow value. The integral of the $F_{ZnO}(t)$ (gas flow rate onto the zinc oxide surface which equals the initial constant flow rate minus the flow rate at time t) with respect to time gave the total amount adsorbed. The adsorbed species were identified in the subsequent T.P.D.

The results and discussion are left until section 4.2.3.

3.2.5 Oxygen adsorption on zinc oxide powder

In these experiments zinc oxide 'puratronic' powder was treated with oxygen ($10^{-3} < P_{O_2} < 0.4$) at temperatures between 300 K and 800 K. In all these experiments, the zinc oxide was pre-treated at ca. 850 K in

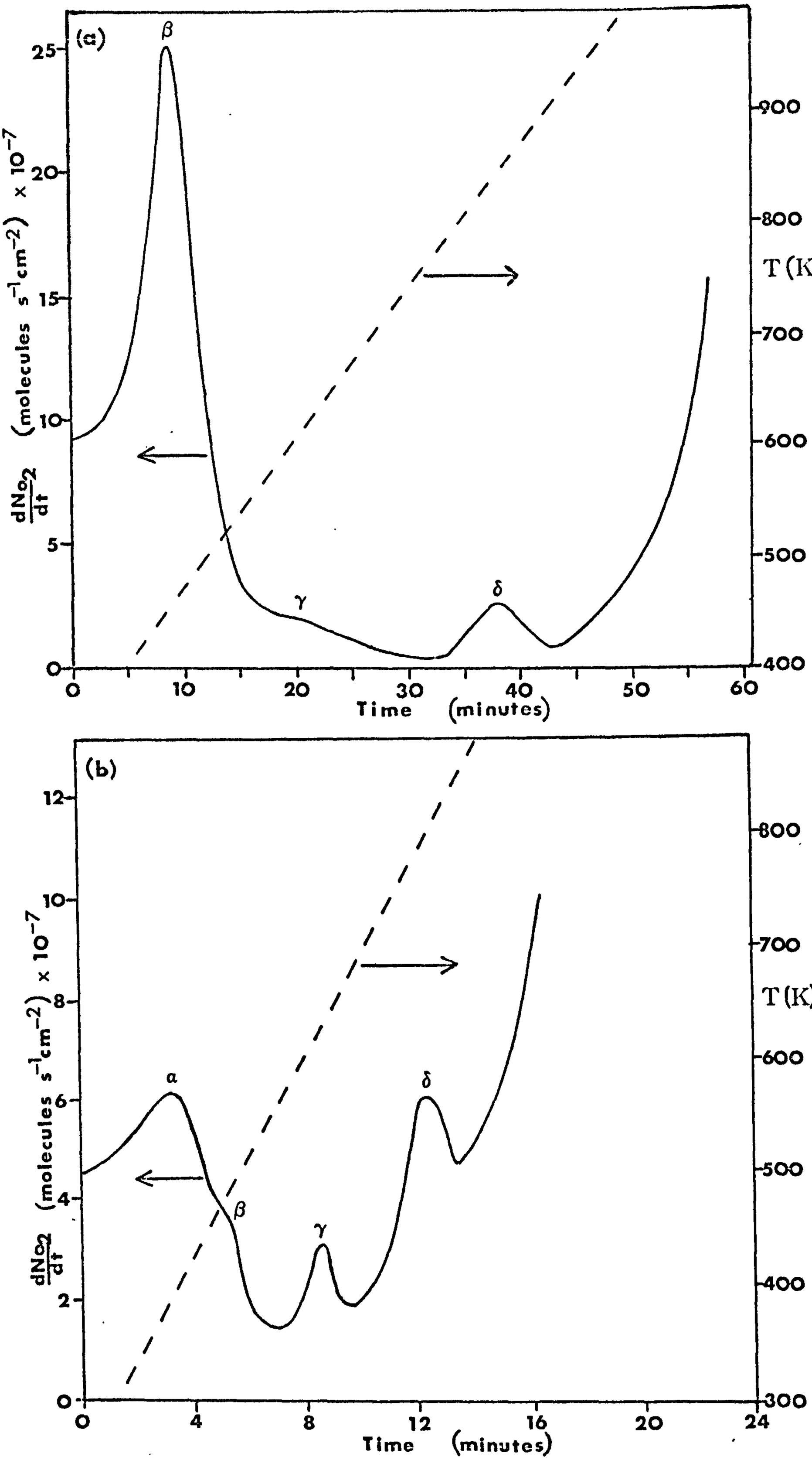

Fig. 3.20:

Oxygen T.P.D.'s from zinc oxide 'puratronic' powder.

oxygen (ca. 0.2 torr). Heating above 850 K resulted in the formation of a metallic film of zinc in the cooler parts of the reaction chamber.

The T.P.D. of these oxygen treated zinc oxide powder surfaces revealed up to four oxygen peaks. Fig. (3.20) shows two typical oxygen T.P.D.'s. Fig. (3.20a) is for a surface treated at 373 K in 0.19 torr oxygen; fig. (3.20b) is for a surface treated at 493 K in 0.23 torr oxygen.

The four different oxygen peaks are marked α, β, γ and δ.

The results of these experiments will be discussed in section 4.2.2.

Chapter 3 : References

Ehrlich, G., Adv. in Catalysis, 14, 255, (1963)

Green, M. and Lee, M.J., J. Scientific Inst. 43, 948, (1966)

Petermann, L.A., Prog. in Surf. Sci., 3, 1, (1972)

4. THEORY AND DISCUSSION

4.1 GAS INTERACTIONS WITH THE ZINC OXIDE SURFACE BETWEEN 800 K and 1200 K

When zinc oxide is heated in vacuum in the temperature range indicated above a quantity of molecular oxygen is evolved, which was shown (section 3.2.1) to be a maximum that corresponds to 4% of the total number of surface lattice oxygen sites. Two types of defect can be thus formed: zinc interstitials and oxygen vacancies.

Values of the maximum concentration of defects expressed as a fraction of the number of bulk atoms per cc., f_b, are given by Secco and Moore (1957) for zinc oxide under one atmosphere of zinc vapour,

$$f_b = 1.2 \times 10^2 \exp - \frac{1.39\,eV}{kT}$$

and by Kroger (1964) for zinc oxide under staurated vapour pressure of zinc,

$$f_b = 7.02 \times 10^{-3} \exp - \frac{0.635\,eV}{kT}$$

At 100 K, f_b is respectively 1.13×10^{-5} and 4.40×10^{-6}.

The self diffusion coefficient, $D_{s.d.}$, for zinc in zinc oxide crystals was measured by Secco and Moore (1957) between 1173 K and 1273 K and given by,

$$D_{s.d.} = 4.8 \exp - \frac{3.17\,eV}{kT} \qquad cm^2\,s^{-1}$$

while Linder (1952) found the relationship

$$D_{s.d.} = 1.3 \exp - \frac{3.20\,eV}{kT} \qquad cm^2\,s^{-1}$$

for sintered material between 1073 K and 1673 K. At 1000 K, these give for the diffusion coefficient, respectively, 4.7×10^{-16} and $9.0 \times 10^{-17}\,cm^2\,s^{-1}$.

In a typical experiment (section 3.2.1) the equivalent of up to 4% of the surface lattice oxygen atoms are lost to the gas phase at ca. 1000 K in a time of about 100 seconds. Were the defects so produced allowed to

move into the bulk they would diffuse a characteristic distance, l, given approximately by, $l = \sqrt{D_{1000K}\, t}$ cm. Using the higher value of the diffusion coefficient at 1000 K, l is 22 Å. This means that the defects are confined to a shell ca. 22 Å in depth and with an average density expressed as a fraction of the number of the bulk atoms per cc., f_b, of 2.6×10^{-3}, which is more than 200 times their saturation solubility ($f_b = 1.13 \times 10^{-6}$). Thus since the 4% of the surface defects cannot be nearly accommodated in the diffusion depth it is highly reasonable to suppose that they are confined to the outermost surface of the crystal.

The zinc interstitial defect at the surface would be in an interstice just beneath the surface plane, and, being therefore in an energetically similar environment to the bulk species, for it the above solubility restriction would apply. A surface oxygen vacancy, however, is markedly different in bonding configuration to one in the bulk. It is thus highly probable that the bulk saturation concentration can be exceeded in the outermost surface layer. It is concluced therefore, that between 800 K and 1200 K the major surface defects are surface oxygen vacancies.

Diffusion of anion vacancies, D_{V_o}, (Hoffman and Lauder, 1970) in single crystal zinc oxide between 1423 K and 1673 K is given by,

$$D_{V_o} = 1.05 \times 10^{3} \exp - \frac{4.08\,eV}{kT} \qquad cm^2\, s^{-1}$$

Their diffusion depth at 1000 K in 100 seconds is then $\sqrt{D_{V_o,1000K}\, t}$, which is 1.62 Å, and this being less than the interionic distance (1.98 Å) means that anion vacancies are immobile perpendicular to the surface lattice plane.

In the remainder of this section a model of the oxygen deficient $10\bar{1}0$ surface will be used, described by anion vacancies in the uppermost layer. These may be mobile within the surface plane, but, in the temperature range

studied, they cannot move into the bulk.

4.1.1 Kinetics of the decomposition of the surface lattice layer

Two mechanisms which give very similar overall rate expressions are formulated below. These are as follows:-

A. Vacancy-pair mechanism

In this mechanism there are three stages leading to oxygen desorption and formation of surface oxygen vacancies. Using the Kroger-Vink notation they are as follows:- a pre rate determining step pseudo-equilibrium between lattice oxygen and an adsorbed species,

$$^{s}O_{x}^{x} \underset{}{\overset{K_1}{\rightleftharpoons}} {}^{s}V_{o}^{+}\cdots O^{-} \qquad \text{.....step 1A}$$

where the left-hand superscript refers to the surface phase, followed by the rate determining abstraction of the nearest neighbour lattice oxygen,

$$^{s}O_{x\ n.n.}^{x} + {}^{s}V_{o}^{+}\cdots O^{-} \xrightarrow[r.d.s.]{k_{2A}} O_2(g) + {}^{s}V_{o}^{+}\cdots{}^{s}V_{o}^{+} + 2{}^{s}e^{-} \qquad \text{.....2A}$$

with evolution of molecular oxygen and formation of a doubly charged vacancy pair (with compensating electrons in the space charge region); this quickly dissociates into two separate vacancies, viz.:

$$^{s}V_{o}^{+}\cdots{}^{s}V_{o}^{+} \xrightarrow{k_{3A}} 2\,{}^{s}V_{o}^{+} \qquad \text{.....3A}$$

A parallel zinc loss reaction, with vacancy destruction and step site formation (see later)

$$^{s}V_{o}^{+} + {}^{s}e^{-} \xrightarrow[r.d.s.]{k_4} Zn(g) + {}^{s}O_{x}^{x} \qquad \text{.....4A}$$

is followed by immediate oxidation of the zinc

$$2\,Zn(s) + O_2(g) \xrightarrow{k_5} 2\,ZnO(s) \qquad \text{.....5A}$$

condensed on the surface of the cooler parts of the reaction chamber, where it takes no further part in the reaction. Step 5A is also the overall zinc oxide formation reaction.

Material balance for the gas phase gives,

$$dP_{O_2}/dt = k_{2A}\,[{}^{s}V_O^{+}\cdots O^{-}][{}^{s}O_{x\ n.n}^{x}] - k_5\,P_{O_2}.P_{Zn}^{2} \qquad [4.1]$$

and, for the rapidly removed zinc

$$dP_{Zn}/dt = k_4\,[{}^{s}V_O^{+}]\,[{}^{s}e^{-}] - 2k_5\,P_{O_2}.P_{Zn}^{2} \qquad [4.2]$$

whence,

$$dP_{O_2}/dt = k_{2A}\,[{}^{s}V_O^{+}\cdots O^{-}][{}^{s}O_{x\ n.n}^{x}] - \frac{k_4}{2}\,[{}^{s}V_O^{+}][{}^{s}e^{-}] \qquad [4.3]$$

Material balance for the surface phase gives for the pre rate determining step pseudo-equilibrium,

$$K_1 = \frac{[{}^{s}V_O^{+}\cdots O^{-}]}{[{}^{s}O_x^{x}]} \qquad [4.4]$$

in addition,

$$d[{}^{s}V_O^{+}]/dt = 2k_{3A}\,[{}^{s}V_O^{+}\cdots{}^{s}V_O^{+}] - k_4[{}^{s}V_O^{+}][{}^{s}e^{-}] \qquad [4.5]$$

and for the rapidly decomposing divacancy

$$\frac{d[V_O^{+}\cdots V_O^{+}]}{dt} = k_{2A}[{}^{s}V_O^{+}\cdots O^{-}][{}^{s}O_{x\ n.n}^{x}] - k_{3A}[{}^{s}V_O^{+}\cdots{}^{s}V_O^{+}] \qquad [4.6]$$

whence, [4.6] into [4.5] gives

$$d[{}^{s}V_o^{\cdot\cdot}]/dt = 2k_{2A}[{}^{s}V_o^{\cdot\cdot}\cdots O^{-}][{}^{s}O_x^x{}_{n.n.}] - k_4[{}^{s}V_o^{\cdot\cdot}][{}^{s}e^{-}] \quad [4.7]$$

which with [4.4] yields,

$$d[{}^{s}V_o^{\cdot\cdot}]/dt = 2K_1k_{2A}[{}^{s}O_x^x][{}^{s}O_x^x{}_{n.n.}] - k_4[{}^{s}V_o^{\cdot\cdot}][{}^{s}e^{-}] = 2dP_{O_2}/dt \quad [4.8]$$

Since the vacancy density reaches a maximum of only 4% of the total number of surface lattice oxygen sites, $[{}^{s}O_x^x]$ is very nearly constant, and equal to the number cm^{-2} of oxygen atoms in a perfect $10\bar{1}0$ surface. The fractional vacancy concentration may now be written,

$$\theta = \frac{[{}^{s}V_o^{\cdot\cdot}]}{[{}^{s}O_x^x]}$$

With this definition [4.8] can be rewritten as

$$d\theta/dt_A = 2K_1k_{2A}[{}^{s}O_x^x{}_{nn}] - k_4\theta[{}^{s}e^{-}] \quad [4.9]$$

where subscripts 'A' refer to mechanism A.

B. Mobile atom mechanism

This is so called because the pseudo-equilibrium between lattice oxygen and an adsorbed species, viz.,

$${}^{s}O_x^x \rightleftharpoons {}^{s}V_o^{\cdot\cdot}\cdots O^{-} \quad \text{.....step 1B}$$

is followed by the rate determining dissociation of the adsorbed oxygen complex to give an ionized vacancy and a reactive and mobile oxygen atom on the surface,

$$ {}^{s}V_o^{+}\cdots O^{-} \xrightarrow[r.d.s.]{k_{2B}} {}^{s}V_o^{+} + {}^{s}e^{-} + O \qquad \text{.....step 2B} $$

which immediately interacts with another adsorbed oxygen complex with evolution of molecular oxygen and formation of a second vacancy,

$$ {}^{s}V_o^{+}\cdots O^{-} + O \xrightarrow{k_{3B}} O_2(g) + {}^{s}V_o^{+} + {}^{s}e^{-} \qquad \text{.....3B} $$

Steps 4 and 5, entered here for completeness, are the same as in the vacancy pair mechanism, namely,

$$ {}^{s}V_o^{+} + {}^{s}e^{-} \xrightarrow[r.d.s.]{k_4} Zn(g) + {}^{s}O_x^{x} \qquad \text{.....4B} $$

$$ 2Zn(s) + O_2(g) \xrightarrow{k_5} 2ZnO(s) \qquad \text{.....5B} $$

Material balance for the gas phase gives,

$$ dP_{O_2}/dt = k_{3B}[{}^{s}V_o^{+}\cdots O^{-}][O] - k_5 P_{O_2} P_{Zn}^2 \qquad [4.10] $$

and,

$$ dP_{Zn}/dt = k_4[{}^{s}V_o^{+}][{}^{s}e^{-}] - 2k_5 P_{O_2} P_{Zn}^2 = 0 \qquad [4.11] $$

Whence,

$$ dP_{O_2}/dt = k_{3B}[{}^{s}V_o^{+}\cdots O^{-}][O] - \frac{k_4}{2}[{}^{s}V_o^{+}][{}^{s}e^{-}] \qquad [4.12] $$

Material balance for the surface phase gives,

$$ K_1 = \frac{[{}^{s}V_o^{+}\cdots O^{-}]}{[{}^{s}O_x^{x}]} \qquad [4.13] $$

and,

$$d[V_o^+]/dt = k_{2B}[{}^sV_o^+\cdots O^-] + k_{3B}[{}^sV_o^+\cdots O^-][O] - k_4[{}^sV_o^+][{}^se^-] \quad [4.14]$$

and,

$$d[O]/dt = k_{2B}[{}^sV_o^+\cdots O^-] - k_{3B}[{}^sV_o^+\cdots O^-][O] = 0 \quad [4.15]$$

whence, [4.15] in [4.14] yields

$$d[{}^sV_o^+]/dt = 2k_{2B}[{}^sV_o^+\cdots O^-] - k_4[{}^sV_o^+][{}^se^-] \quad [4.16]$$

which with [4.13] gives

$$d[{}^sV_o^+]/dt = 2K_1k_{2B}[{}^sO_x^x] - k_4[{}^sV_o^+][{}^se^-] = 2\,dP_{O_2}/dt \quad [4.17]$$

which can, as before, be expressed in the terms of , viz.,

$$d\theta/dt_B = 2K_1k_{2B} - k_4\theta[{}^se^-] \quad [4.18]$$

where subscript 'B' refers to mechanism B.

The overall rate equations thus equate the rate of vacancy concentration change to the difference in rate between two parallel but opposing reactions, one that increases θ, whose rate is $\vec{J}_{2A}$ and $\vec{J}_{2B}$ of the two reaction schemes (the forward direction of the arrows indicating the direction of increasing θ), and the other that reduces θ, whose rate is $\overleftarrow{J}_4$ for both mechanisms.

The detailed structure of equations [4.9] and [4.18] involving the influence of the space charge and decomposition at step sites will now be considered.

4.1.1a The space charge potential

Equations [4.9] and [4.18] can be written in the general form

$$d\theta/dt = \vec{J}_2 - \overleftarrow{J}_4 \qquad [4.19]$$

Considering first $\overleftarrow{J}_4$, there is the relationship

$$\overleftarrow{J}_4 = k_4 \alpha^s_{V_o^+} \cdot \alpha^s_{e^-} \qquad [4.20]$$

where α_i^α is the activity of species i in the phase α. Therefore, using the usual absolute rate expression, there is,

$$\overleftarrow{J}_4 = \frac{kT}{h} \alpha^s_{V_o^+} \cdot \alpha^s_{e^-} \exp - \frac{\Delta F_4^{o\neq}}{kT} \qquad [4.21]$$

where k, T and h have their usual meanings and $\Delta F_4^{o\neq}$ is the standard molecular free energy of formation of the activated complex in step 4 of both mechanisms.

Now, for electrons at the surface

$$\bar{\mu}_e = \mu_e^o + kT \ln \alpha^s_{e^-} + e\phi_s \qquad [4.22]$$

where $\bar{\mu}_e$ is the electrochemical potential and μ_e^o the standard chemical potential of the electrons, taking the standard state as corresponding to the Fermi level at the bottom of the conduction band (see fig. 4.2), ϕ_s is the surface potential and e is the charge on the electron (i.e.

$- 1.6 \times 10^{-19}$ Coulombs). Since the Fermi level is uniform throughout the zinc oxide phase (no electric current is flowing), then also,

$$\bar{\mu}_e = \mu^{\circ}_e + kT \ln a^{b}_{e^-} + e\phi_b \qquad [4.23]$$

where b refers to the charge free bulk. Taking $\phi_b = 0$ and equating [4.22] and [4.23] then gives,

$$kT \ln a^{b}_{e^-} = kT \ln a^{s}_{e^-} + e\phi_s \qquad [4.24]$$

and this with [4.21] gives

$$\overleftarrow{J_4} = \frac{kT}{h} a^{s}_{V_o^+} \cdot a^{b}_{e^-} \exp - \left[\frac{\Delta F_4^{\circ\ddagger} + e\phi_s}{kT}\right] \qquad [4.25]$$

Now, the change in standard free energy ΔF° for a reversible reaction at constant temperature and pressure is

$$\Delta F^{\circ} = \sum F^{\circ}(final) - \sum F^{\circ}(initial) \qquad [4.26]$$

Now for the reaction

$$^{s}V_o^+ + {}^{s}e^- \underset{}{\overset{K_4^{\ddagger}}{\rightleftharpoons}} \text{transition state}$$

where the transition state is in equilibrium with reactants, the total standard free energy of activation is given by the difference between the standard free energy of the activated complex and of the reactants as given by equation [4.26]. Thus,

$$\Delta F_4^{o\ddagger} = \{\mu_{\ddagger}^{o} + \beta_4 z\phi_s\} - \{\mu_{sV_o^+}^{o} + z\phi_s + \mu_{se^-}^{o} + e\phi_s\}$$

Which simplifies to

$$\Delta F_4^{o\ddagger} = \Delta F_4^{o\ddagger}(\phi_s=0) + (\beta_4 - 1) z\phi_s - e\phi_s \qquad [4.27]$$

Where $\beta_4 (0<\beta_4<1)$ is related to the fractional charge on the transition state, $z=-e$ and $\Delta F_4^{o\ddagger}(\phi_s=0)$ is the standard free energy change when the surface space charge potential is zero. Substituting equation [4.27] in [4.25] gives,

$$\overleftarrow{J_4} = \frac{kT}{h} \alpha_{V_o^+}^{s} . \alpha_{e^-}^{b} \exp - \left[\frac{\Delta F_4^{o\ddagger}(\phi_s=0) + (\beta_4 - 1) z\phi_s}{kT}\right] \qquad [4.28]$$

The physical meaning of this equation is that the effect of electron activity on the rate of the reaction is determined by bulk activity (which is constant during the surface decomposition) and not by variations in the surface activity which are compensated for by changes in the surface potential. But the surface potential does affect the free energy of charged species, e.g. surface vacancies, which are not in equilibrium with the bulk.

The rate, $\vec{J}_2$, of step 2 in the reaction schemes is similarly affected by surface potential, but the resultant equations differ for each mechanism. For the vacancy pair mechanism the forward rate, $\vec{J}_{2A}$ is given by,

$$\vec{J}_{2A} = 2 k_{2A} \alpha_{V_o^{\cdot\cdot}-O^-}^{s} \alpha_{O_x^x\ n.n.}^{s}$$

and since the activity of the nearest neighbour site is unity the above, expressed in the absolute rate equation, becomes

$$\vec{J}_{2A} = \frac{2kT}{h} \alpha_{V_o^{\cdot\cdot}-O^-}^{s} \exp - \frac{\Delta F_{2A}^{o\ddagger}}{kT} \qquad [4.29]$$

where $\Delta F^{o\ddagger}_{2A}$ is the standard free energy of formation of the transition state in the forward step 2 of mechanism A. In the reverse step 2A the reaction

$$ {}^{s}V_o^{+} \ldots {}^{s}V_o^{+} + 2{}^{s}e^{-} + O_2(g) \rightleftharpoons \text{transition state A} $$

gives for its standard free energy of activation, $\overleftarrow{\Delta F}^{o\ddagger}_{2A}$,

$$ \overleftarrow{\Delta F}^{o\ddagger}_{2A} = \left\{\mu^{o}_{\ddagger} + 2\beta_{2A} z\phi_s\right\} - \left\{2\mu^{o}_{{}^{s}e^{-}} + 2e\phi_s + \mu^{o}_{{}^{s}V_o^{+}\ldots{}^{s}V_o^{+}} + 2z\phi_s + \mu^{o}_{O_2}\right\} $$

where the factor 2 in front of the term $z\phi_s$ indicates that the vacancy pair species is doubly charged, and $2\beta_{2A} z\phi_s$ $(0<\beta_{2A}<1)$ is the total increase in potential energy of the transition state. The rate of the forward step 2A, (equation [4.29]), is modified accordingly. Hence,

$$ \vec{J}_{2A} = \frac{2kT}{h}\, a^{s}_{V_o^{+}\ldots O^{-}} \exp - \left[\frac{\Delta F^{o\ddagger}_{2A}(\phi_s=0) + 2\beta_{2A} z\phi_s}{kT}\right] \qquad [4.31] $$

Similarly, for the mobile atom mechanism, the forward rate, $\vec{J}_{2B}$, is given by

$$ \vec{J}_{2B} = 2k_{2B}\, a^{s}_{V_o^{+}\ldots O^{-}} $$

and expressed in the form of the absolute rate equation, this is

$$ \vec{J}_{2B} = \frac{2kT}{h}\, a^{s}_{V_o^{+}\ldots O^{-}} \exp - \frac{\Delta F^{o\ddagger}_{2B}}{kT} \qquad [4.32] $$

In the equation for the formation of the transition state in the reverse step 2B, namely,

$$ {}^{s}V_o^{+} + {}^{s}e^{-} + O \rightleftharpoons \text{transition state B} $$

the standard free energy of activation $\overleftarrow{\Delta F}^{o\ddagger}_{2B}$ is given by

$$\overleftarrow{\Delta F}^{o\ddagger}_{2B} = \{\mu^{o}_{\ddagger} + \beta_{2B} z\phi_s\} - \{\mu^{o}_{s_{V_o^{\cdot\cdot}}} + z\phi_s + \mu^{o}_{s_{e^-}} + e\phi_s + \mu^{o}_{o}\} \quad [4.33]$$

and, since the transition state energy is increased by $\beta_{2B} z\phi_s$ $(0<\beta_{2B}<1)$ the forward reaction rate of equation [4.32] is modified, viz.,

$$\vec{J}_{2B} = \frac{2kT}{h} a^{s}_{V_o^{\cdot\cdot}\cdots O^-} \exp - \left[\frac{\Delta F^{o\ddagger}_{2B}(\phi_s=0) + \beta_{2B} z\phi_s}{kT}\right] \quad [4.34]$$

Assuming ideal behaviour of the surface species, where activities can be replaced by concentrations, the overall rate expression, including space charge effects, are for mechanisms A and B respectively

$$d\theta/dt_A = XK_1 \exp - \left[\frac{\Delta F^{o\ddagger}_{2A}(\phi_s=0) + 2\beta_{2A} z\phi_s}{kT}\right] - Y\theta \exp - \left[\frac{\Delta F^{o\ddagger}_{4}(\phi_s=0) + (\beta_4 - 1) z\phi_s}{kT}\right] \quad [4.35]$$

and

$$d\theta/dt_B = XK_1 \exp - \left[\frac{\Delta F^{o\ddagger}_{2B}(\phi_s=0) + \beta_{2B} z\phi_s}{kT}\right] - Y\theta \exp - \left[\frac{\Delta F^{o\ddagger}_{4}(\phi_s=0) + (\beta_4 - 1) z\phi_s}{kT}\right] \quad [4.36]$$

The effect of the space charge is shown schematically in fig. (4.1). The potential energies of all charged species are altered, while uncharged species remain constant.

It is observed that, for symmetrical activation peaks, a shift in either of the reactant or product potential energies of ΔE produces a

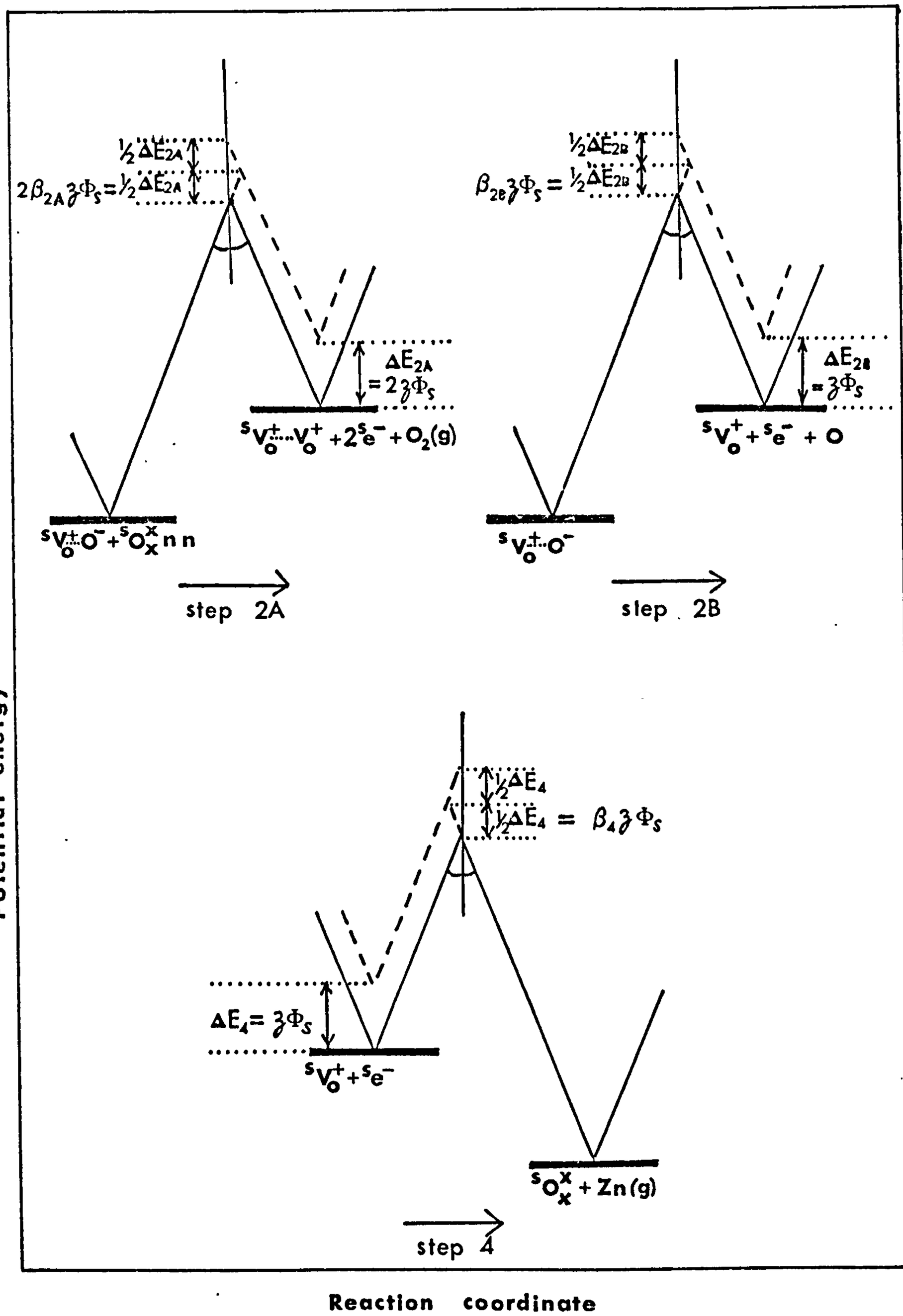

Fig. 4.1:

Relationship between potential energy changes of ground states and activated states using a "symmetrical activation peak" model

change in the transition state potential energy of $\Delta E/2$. It is clear, then, that for this case $\beta_{2A} = \beta_{2B} = \beta_4 = 1/2$. This will be used in the remainder of the analysis.

4.1.1b. Variation of the space charge potential with θ

As the reaction proceeds the concentration of surface vacancies builds up (with corresponding counter charge of electrons in the space charge region). The surface density of $^sV_o^+$ centres is eventually so high that while $^sV_o^+$ may start as a surface state a few tenths of an eV below the conduction band edge, it is assumed that the band broadens and overlaps the conduction band edge at the higher concentration levels. In this case $^sV_o^+$ is a fully ionised donor state with a compensating electron in the space charge region.

As the concentration of ionised vacancies builds up the energy levels of the zinc oxide become progressively bent down. In other words, the surface becomes increasingly positive, (fig. 4.2). The creation of such a surface requires the expenditure of energy. This is $e\phi_s$ in eV, where ϕ_s is the space charge potential (fig. 4.2). Now, $e\phi_s$ is required in terms of θ .

The net space charge per unit area of surface, Q_s , is given by Gauss's law, i.e.

$$Q_s = -\left\{\frac{\varepsilon\varepsilon_o kT}{q}\right\}\left\{\frac{du}{dx}\right\}_s \qquad [4.37]$$

Q_s is in Coulombs per square centimeter, ε is the relative permittivity of zinc oxide, which is 8.5 (as in Heiland et al. 1959), ε_o is the permittivity of free space, which is 8.85×10^{-14} Farads per centimeter. $(du/dx)_s$ is the electric field at the surface in reduced units,

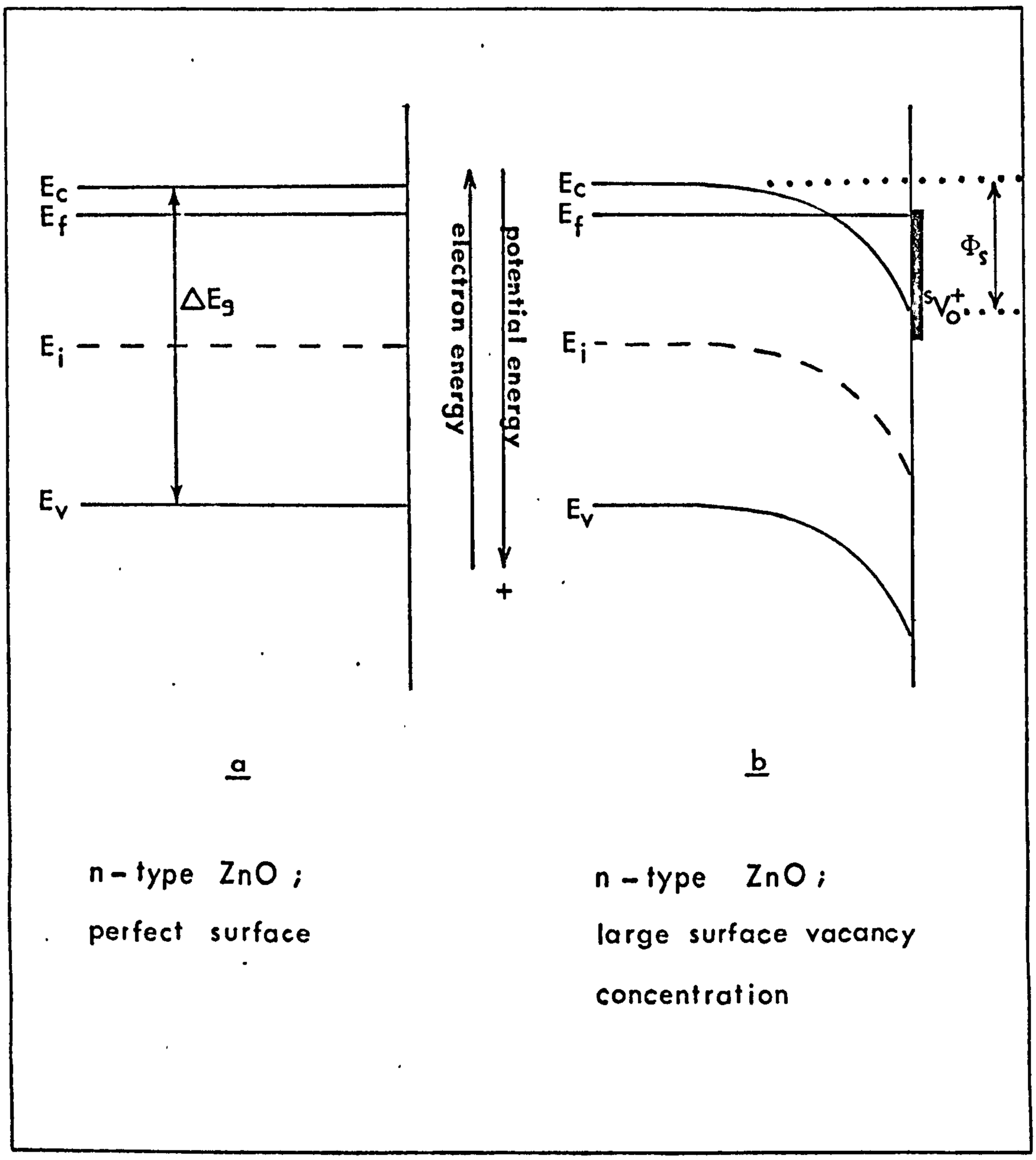

Fig. 4.2:

The zinc oxide surface energy band diagram

where u is defined

$$u = \frac{E_F - E_I}{kT} \qquad [4.38]$$

and, in general,

$$\omega_{p,q} = \frac{E_p - E_q}{kT}$$

The surface is highly degenerate from about $\Theta = 0.01$ onwards, so, the space charge equation is cast entirely in the degenerate form, (Stratton 1955, Seiwatz and Green 1958), namely,

$$\left\{du/dx\right\}_s = -\frac{1}{L_D}\left[\frac{4}{15}\left\{u_s - \omega_{c,I}\right\}^{5/2} F_{1/2}\left\{\omega_{I,c}\right\}\right]^{1/2} \qquad [4.39]$$

noting that,

$$u_s = \left\{\frac{E_F - E_I}{kT}\right\}_s \quad \text{and} \quad \omega_{c,I} = \left\{\frac{E_c - E_I}{kT}\right\}_{anywhere}$$

So, therefore,

$$u_s - \omega_{c,I} = \left\{\frac{E_F - E_c}{kT}\right\}_s \doteq \frac{q\phi_s}{kT} \qquad [4.40]$$

because the term $\left[(E_F - E_c)/kT\right]_{bulk}$ is small, and can with no significant loss in accuracy (for this degenerate case) be taken as zero.

The Fermi integral, $F_{1/2}(\eta)$, is given by

$$\lim_{\eta \to -\infty} F_{1/2}(\eta) = 1/2\,\pi^{1/2} e^{\eta}$$

so in this case

$$F_{1/2}(\omega_{I,c}) = 1/2\,\pi^{1/2} \exp - \left\{\frac{E_c - E_I}{kT}\right\}$$

which is,

$$F_{1/2}(\omega_{r,c}) = \tfrac{1}{2}\pi^{1/2} \exp - \frac{\Delta E_g}{kT}$$

where ΔE_g is the energy gap, as shown in fig. (4.2).

Also, the intrinsic Debye length, L_D , is given by

$$L_D = \left\{\frac{\varepsilon \varepsilon_o kT}{2q^2 n_i}\right\}^{1/2} \qquad [4.41]$$

where n_i is the intrinsic carrier concentration of zinc oxide, and is given by

$$n_i = \{N_v N_c\}^{1/2} \exp - \frac{\Delta E_g}{2kT} \qquad [4.42]$$

Now, let the geometric mean effective density of states be given by

$$\{N_v N_c\}^{1/2} = N = 4\pi \left\{\frac{2m_e kT}{h^2}\right\}^{3/2} \qquad [4.43]$$

where m_e is the effective mass of the electron, then

$$n_i = N \exp - \frac{\Delta E_g}{2kT} \qquad [4.44]$$

where N is calculated in equation [4.43] as $5.44 \times 10^{15}\ T^{3/2}\ cm^{-3}$ (This takes the effective mass ratio of holes and electrons to be unity, which is a reasonable approximation.)

Substituting [4.44] into [4.41] gives

$$L_D = \left\{ \frac{\varepsilon\varepsilon_0 kT}{(2q^2)(5.44\times10^{15})\, T^{3/2} \exp -(\Delta E_g/2kT)} \right\}^{1/2} \qquad [4.45]$$

and substituting [4.40] and [4.45] into [4.39] gives

$$\left\{ du/dx \right\}_s = \left\{ \frac{3.27\times10^{15}\, q^2\, T^{3/2} (q\phi_s/kT)^{5/2}}{\varepsilon\varepsilon_0 k} \right\}^{1/2}$$

Now, by substituting this back into the Gauss's law, equation [4.37], Q_s can be obtained, which is

$$Q_s = - \left\{ \frac{\varepsilon\varepsilon_0 kT}{q} \right\} \left\{ \frac{3.27\times10^{15}\, q^2\, T^{3/2} (q\phi_s/kT)^{5/2}}{\varepsilon\varepsilon_0 kT} \right\}^{1/2}$$

which gives

$$Q_s = - 1.78 \times 10^{-10}\, T^{5/4} \left\{ \frac{q\phi_s}{kT} \right\}^{5/4} \qquad [4.46]$$

But, the total vacancy concentration per cm^2 is merely the electron charge concentration, Q_s, divided by the charge on the electron, viz.,

$$[{}^{s}V_o^{+}] = - Q_s/q \quad \text{per } cm^2$$

and, the total fractional vacancy concentration is given by

$$\theta = - Q_s/q[{}^{s}O_x^{x}]$$

where $[{}^{s}O_x^{x}]$ is the number of surface oxygen atoms per cm^2, and equals 6×10^{14} (see Chapter 1.1.2). Thus

$$\theta = 1.90 \times 10^{-6} \left\{ \frac{q\phi_s}{k} \right\}^{5/4}$$

which when rearranged gives finally

$$e\phi_s = -3.25\theta^{0.8}, \quad eV$$

which is,

$$z\phi_s = 3.25\theta^{0.8}, \quad eV$$

The overall rate, equations [4.35] and [4.36], can now be restated using this θ dependence of surface potential and are, for the vacancy-pair mechanism

$$d\theta/dt_A = XK_1 \exp-\left\{\frac{\Delta F_{2A}^{0\ddagger}(\phi_s=0) + 3.25\theta^{0.8}}{kT}\right\} - Y\theta \exp-\left\{\frac{\Delta F_4^{0\ddagger}(\phi_s=0) - 1.62\theta^{0.8}}{kT}\right\} \quad [4.47]$$

and for the mobile atom mechanism

$$d\theta/dt_B = XK_1 \exp-\left\{\frac{\Delta F_{2B}^{0\ddagger}(\phi_s=0) + 1.62\theta^{0.8}}{kT}\right\} - Y\theta \exp-\left\{\frac{\Delta F_4^{0\ddagger}(\phi_s=0) - 1.62\theta^{0.8}}{kT}\right\} \quad [4.48]$$

4.1.1c. The step site potential

The production of surface lattice oxygen at step sites, via step 4 of the proposed reaction sequence, is written precisely as,

$$^sV_O^+ + {}^se^- \xrightarrow{k_4} Zn(g) + {}^sO_{x\,s.s.}^x \quad [4.49]$$

where $^sO_{x\,s.s.}^x$ refers to a surface lattice oxygen at a step site, and the reaction is shown schematically in fig. (4.3). Here it is shown how, when a zinc atom on a surface site next to a vacancy evaporates from

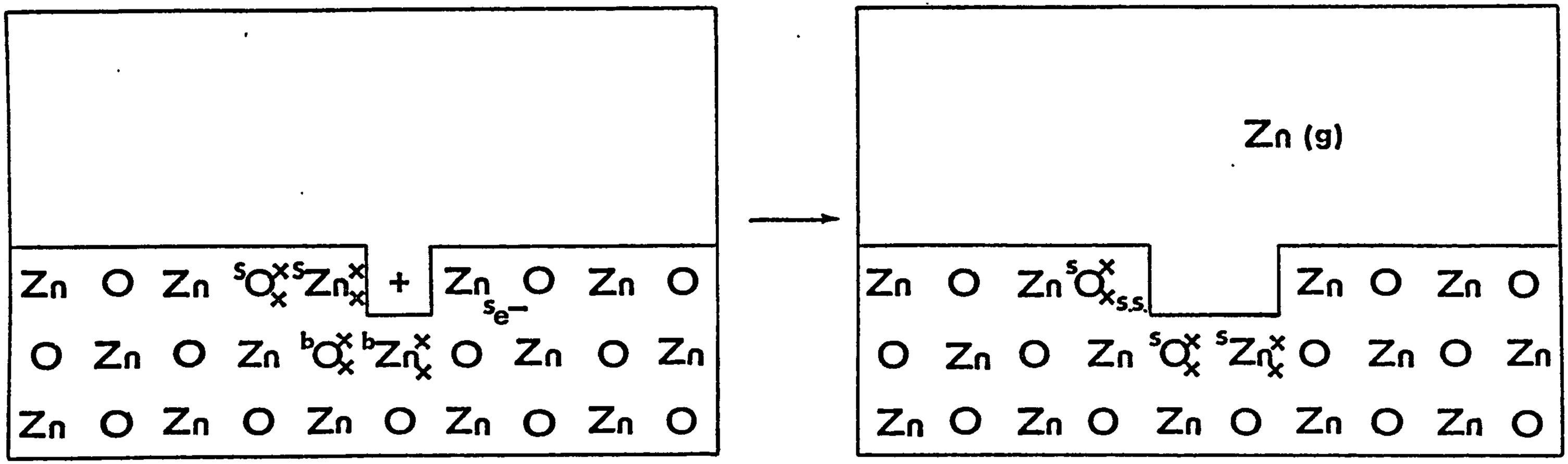

$$ {}^{s}V_{o}^{+} + {}^{s}e^{-} + {}^{s}Zn_{x}^{x} + {}^{s}O_{x}^{x} \longrightarrow Zn(g) + {}^{s}O_{x\,s.s.}^{x} + {}^{s}O_{x}^{x} + {}^{s}Zn_{x}^{x} $$

Fig. 4.3:

Schematic diagram of the formation of a step on a zinc oxide prism surface by loss of a zinc atom from a site neighbouring a surface lattice oxygen vacancy

the surface, a zinc and an oxygen atom that were at bulk sites, marked in the diagram as $^{b}Zn_{x}^{x}$ and $^{b}O_{x}^{x}$, are now revealed to the surface. Furthermore, an oxygen atom that was at a perfect lattice surface site, $^{s}O_{x}^{x}$, is now in a different bonding configuration, namely at a step site, $^{s}O_{x\,s.s.}^{x}$. The overall reaction is then

$$^{s}V_{o}^{+} + {}^{s}e^{-} + {}^{s}Zn_{x}^{x} + {}^{s}O_{x}^{x} \xrightarrow{k_4} Zn(g) + {}^{s}O_{x\,s.s.}^{x} + {}^{s}O_{x}^{x} + {}^{s}Zn_{x}^{x}$$

which, when like terms on both sides of this equation are cancelled, gives equation [4.49] above.

It is proposed that there is an increased vacancy formation rate, by loss of an oxygen atom from a step site, which is due solely to an increased equilibrium constant for $^{s}V_{o}^{+}\cdots O^{-}$ formation at such a site, namely K_1 in step 1 of both reaction schemes. Therefore, in the equilibrium of step 1, namely

$$^{s}O_{x}^{x} \rightleftharpoons^{K_1'} {}^{s}V_{o}^{+}\cdots O^{-}$$

and,

$$^{s}O_{x\,s.s.}^{x} \rightleftharpoons^{K_1''} {}^{s}V_{o}^{+}\cdots O^{-}$$

the total concentration of the $^{s}V_{o}^{+}\cdots O^{-}$ surface complex is given by

$$[^{s}V_{o}^{+}\cdots O^{-}] = K_1'[^{s}O_{x}^{x}] + K_1''[^{s}O_{x\,s.s.}^{x}] \qquad [4.50]$$

Now, if a fraction, $\theta_{s.s.}$ of all surface lattice oxygen sites are at steps, i.e. $1-\theta_{s.s.}$ perfect lattice sites, then equation [4.50] can be expressed

$$[{}^{s}V_o^{+}\cdots O^{-}] = N\left[(1-\theta_{s.s.})\exp-\left\{\frac{\Delta F_i^{\circ}}{kT}\right\} + \theta_{s.s.}\exp-\left\{\frac{\Delta F_i^{\circ}-\Delta E}{kT}\right\}\right] \quad [4.51]$$

where $N = [{}^{s}O_x^x] + [{}^{s}O_{x\,s.s}^x]$ is a constant equal to the number cm^{-2} of oxygen atoms in a perfect $10\bar{1}0$ surface, and ΔF_i° is the free energy of formation of the ${}^{s}V_o^{+}\cdots O^{-}$ species from a perfect lattice oxygen site, and, ΔE is the extent to which this energy is reduced, that is, the increase in chemical potential of a step site oxygen over one at a perfect surface lattice site. Equation [4.51], when rearranged, gives

$$\frac{[{}^{s}V_o^{+}\cdots O^{-}]}{N} = K_i = \exp-\left\{\frac{\Delta F_i^{\circ} - kT\ln(1+\theta_{s.s.}\{\exp\Delta E/kT - 1\})}{kT}\right\} \quad [4.52]$$

and this in equations [4.47] and [4.48] gives for the overall rate equations, of the vacancy-pair mechanism

$$d\theta/dt_A = X\exp-\left\{\frac{\Delta F_{i,2A}^{o\ddagger} + 3.25\theta^{0.8} - kT\ln(1+\theta_{s.s.}\{\exp\Delta E/kT - 1\})}{kT}\right\} - Y\theta\exp-\left\{\frac{\Delta F_4^{o\ddagger}(\phi_s=0) - 1.62\theta^{0.8}}{kT}\right\} \quad [4.53]$$

and, of the mobile atom mechanism

$$d\theta/dt_B = X\exp-\left\{\frac{\Delta F_{i,2B}^{o\ddagger} + 1.62\theta^{0.8} - kT\ln(1+\theta_{s.s}\{\exp\Delta E/kT - 1\})}{kT}\right\} - Y\theta\exp-\left\{\frac{\Delta F_4^{o\ddagger}(\phi_s=0) - 1.62\theta^{0.8}}{kT}\right\} \quad [4.54]$$

where $\Delta F^{o\ddagger}_{1,2A}$ and $\Delta F^{o\ddagger}_{1,2B}$ are the total activation free energies of steps 1 and 2 of the reaction sequence, i.e. $\Delta F^{o\ddagger}_{1,2} = \Delta F^{o\ddagger}_{2} + \Delta F^{o}_{1}$

Equations [4.53] and [4.54] can be recast in terms of enthalpies, with a corresponding change in the pre-exponential factors (incorporating the $exp(\Delta S/k)$ term), namely

$$d\theta/dt_A = X' \exp-\left\{\frac{\Delta H^{o\ddagger}_{1,2A} + 3.25\theta^{0.8} - kT \ln(1+\theta_{s.s}\{\exp \Delta E/kT - 1\})}{kT}\right\} - Y'\theta \exp-\left\{\frac{\Delta H^{o\ddagger}_{4} - 1.62\theta^{0.8}}{kT}\right\} \qquad [4.53a]$$

and

$$d\theta/dt_B = X' \exp-\left\{\frac{\Delta H^{o\ddagger}_{1,2B} + 1.62\theta^{0.8} - kT \ln(1+\theta_{s.s}\{\exp \Delta E/kT - 1\})}{kT}\right\} - Y'\theta \exp-\left\{\frac{\Delta H^{o\ddagger}_{4} - 1.62\theta^{0.8}}{kT}\right\} \qquad [4.54b]$$

The overall potential energy diagrams for these mechanisms are shown in fig. (4.4). It must be mentioned here that the energy changes due to step formation, as shown in the exponentials of equations [4.53a] and [4.53b], and drawn schematically in fig. (4.4) are a simplification of what is believed to be the real case.

Firstly, in fig. (4.4), the potentials of the species $^{s}V_o^{+}\cdots O^{-}$, $^{s}V_o^{+}\cdots {}^{s}V_o^{+}$ and $^{s}V_o^{+}$ are all shown to be constant irrespective of whether they are formed at a step (the potentials of the latter two species, however, are space charge varying). Secondly, in the vacancy-pair mechanism, only the first of the oxygen atoms coming out of the surface lattice layer is shown to change in potential at a step, we assume that the lattice configuration of the nearest neighbour atom (i.e. whether it is at a step site or

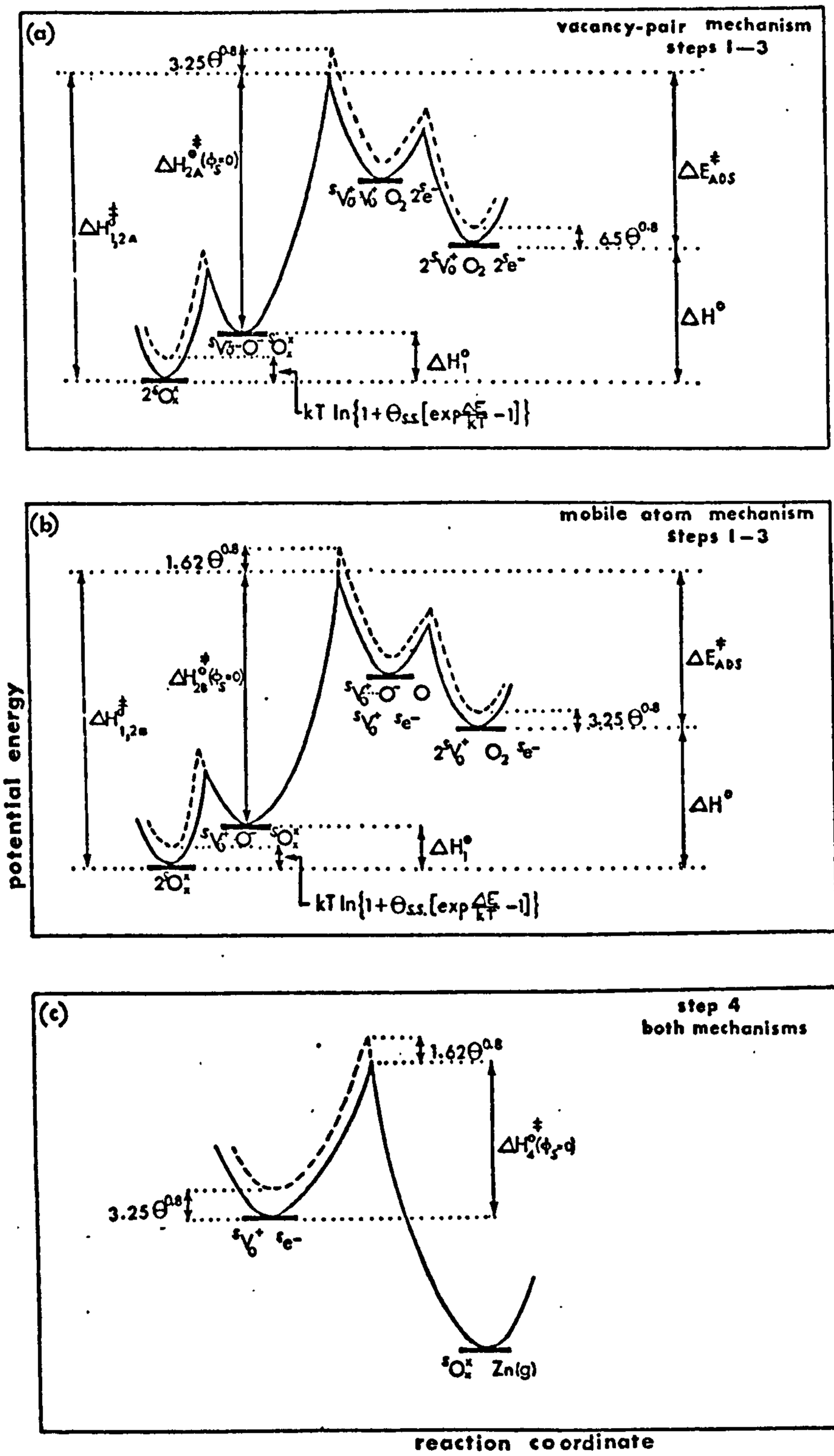

Fig. 4.4:

Overall potential energy diagram of the various steps in the zinc oxide surface decomposition reaction for:

(a) surface lattice oxygen loss via the vacancy-pair mechanism

(b) surface lattice oxygen loss via the mobile atom mechanism

(c) surface lattice zinc loss

a perfect lattice site) will not influence the overall kinetics. Finally, in step 4 of the reaction sequence as depicted in the potential energy diagram, fig. (4.4c), no account is taken of the fact that a lattice zinc atom at a step site is produced as well as a step site oxygen (see fig. (4.3)). It is tacitly assumed that the activation energy for zinc loss from such a step site will not be much different from the activation energy for zinc loss from a perfect lattice site. Intuitively this appears a considerable simplification, but the inclusion of this term in the mechanism would make the mathematics intractable, and in any event the zinc atoms in the two kinds of site are much more similar to each other than are the corresponding two kinds of oxygen atom.

4.1.1d Numerical Analysis of the rate equation

The overall rate expressions, equations [4.53a] and [4.54a] can be put in terms of θ and T alone.Since θ is a function of T and t, there is the relation

$$d\theta = (\partial\theta/\partial t)_T\, dt + (\partial\theta/\partial T)_t\, dT$$

which can be restated, using $dT/dt = \beta$, a constant heating rate of 0.4 K s^{-1} , as follows

$$d\theta/dT = \beta^{-1} (\partial\theta/\partial t)_T + (\partial\theta/\partial T)_t \qquad [4.55]$$

The condition for quasi-steady-state, which we assume in our case, is that if the vacancy formation rate, $d\theta/dt$ is at steady-state at a temperature T_1 , when a step change in temperature is applied, $T_2 - T_1$, the new value of the vacancy formation rate at T_2 is realised almost immediately. This requires a comparatively large value for $(\partial\theta/\partial t)_T$ in equation [4.55], and necessitates the condition for quasi-steady-state

that,

$$\beta^{-1}\,(\partial\theta/\partial t)_T \gg (\partial\theta/\partial T)_t \qquad [4.56]$$

Note that this condition is dependent on the value of β. For very large heating rates $\beta^{-1}(\partial\theta/\partial t)_T$ becomes small, and quasi-steady-state no longer exists. We have tested the quasi-steady-state condition by observing the effect of a change of heating rate on kinetic parameters (e.g. linearity and gradient of the Arrhenius plot) of the rate equation; there was no noticeable difference between those for very small heating rates (e.g. $\beta = 0.017\ K\,s^{-1}$, when quasi-steady-state is almost certain, and those for a heating rate of $\beta = 0.4\ K\,s^{-1}$. At this heating rate then, using the condition of equation [4.56] in equation [4.55], (and writing now the partial differential as a total differential) we obtain the relationship

$$d\theta/dT = \beta^{-1}\, d\theta/dt$$

and $d\theta/dt$ can be replaced by $\beta\, d\theta/dT$ in the overall rate equations.

The activation energy change due to step sites, namely $kT\ln(1+\theta_{s.s.}\{\exp\Delta E/kT - 1\})$ in the overall rate expressions, is a function of $\theta_{s.s}$ and T, i.e. $f(\theta_{s.s.},T)$. It can be shown (see appendix 4.1) that this function is relatively insensitive to temperature change and can be approximated to a function variable in $\theta_{s.s.}$ alone, i.e. $f(\theta_{s.s.})$. In addition, we assert that there is a close correspondence between the vacancy concentration and the step site concentration prevailing at any particular temperature, such that the function $f(\theta_{s.s.})$ can be approximated by one variable in θ, i.e. $g(\theta)$. That this is a good approximation is shown later.

The method of procedure for solving for the various parameters in the rate equation is given below, using the vacancy-pair mechanism as the 'worked example'. The recast rate equation (cf. [4.53a] is, using the approximations listed above,

$$d\theta/dT = (X'/\beta)\ exp-\left\{\frac{\Delta H^{0\ddagger}_{1,2A} + 3.25\theta^{0.8} - g(\theta)}{kT}\right\} - (Y'\theta/\beta)\ exp-\left\{\frac{\Delta H^{0\ddagger}_{4} - 1.62\,\theta^{0.8}}{kT}\right\} \qquad [4.57]$$

(i) *Evaluation of X' and* $\Delta H^{0\ddagger}_{1,2A}$: At low temperatures and at low values of θ the second term on the right-hand side of equation [4.57] is essentially zero. Furthermore, since θ is close to zero, $g(\theta)$ is very small and negligible and so is $\theta^{0.8}$, whence

$$d\theta/dT \doteq (X'/\beta)\ exp-\frac{\Delta H^{0\ddagger}_{1,2A}}{kT}$$

From the experimental variation of $ln\,(d\theta/dT)$ with $1/T$, for the initial portion of the T.P.D. curve, one obtains X' and $\Delta H^{0\ddagger}_{1,2A}$, as for a normal Arrhenius plot. Low values of θ are ensured by using those T.P.D. data obtained from zinc oxide which had been oxygen pre-treated at high pressure (cf. section 3.2.1).

The resulting values were: $X' = 5.2 \times 10^{13}\ s^{-1}$; $\Delta H^{0\ddagger}_{1,2A} = 3.47\ eV$

(ii) *Evaluation of Y' and* $\Delta H^{0\ddagger}_{4}$ *by iterative solution of the approximate form of the rate equation:* At low to intermediate value of θ, $g(\theta)$ will be very near to zero, whence an evaluation of and Y' assuming $g(\theta) = 0$ will be fairly near to the correct value.

Furthermore if, as we do, use T.P.D. data from fully oxygenated surfaces, the effect of $g(\theta)$ on the curve is small. We now solve equation [4.57], knowing X' and $\Delta H^{0\neq}_{1,2A}$, assuming $g(\theta) = 0$. The method is as follows.

We select an experimental T.P.D. curve of $d\theta/dt$ versus T for which the initial θ value is close to zero, i.e. high pressure oxygen pre-treatment (e.g. curve "a" of fig. (3.7)). We note the temperature on this curve at which $d\theta/dt$ is close to zero, i.e. when $\theta \doteqdot 0.04$; that is the temperature past the peak maximum at which the vacancy concentration is no longer increasing and we are in steady state. We call this temperature $T_{max.}$. Then, substituting the known values we have,

$$5.2 \times 10^{13} \exp - \left\{ \frac{3.47 + 3.25(0.04)^{0.8}}{kT_{max}} \right\}$$

$$= 0.04\, Y' \exp - \left\{ \frac{\Delta H_4^{0\neq} - 1.62(0.04)^{0.8}}{kT_{max}} \right\}$$

or the known quantity

$$Z = Y' \exp - \frac{\Delta H_4^{0\neq}}{kT_{max}}$$

We must now separate Y' and $\Delta H_4^{0\neq}$ which is done by the following iterative method. We arbitrarily select a value of Y', which then fixes $\Delta H_4^{0\neq}$, and then proceed to attempt to generate the T.P.D. curve. Starting from a low temperature, T_0, (ca. 850 K) at which $\theta = \theta_0$ and $(d\theta/dT)_{\theta_0, T_0}$ is small. With all our parameters set (and taking $g(\theta) = 0$) we select a small temperature increment, δT $(= T_1 - T_0)$ of, say, 10 K; we assume that $(d\theta/dT)_{\theta_0, T_0}$ is constant

over this increment and we compute its value from the relation (with selected Y' and $\Delta H_4^{o\ddagger}$ values inserted),

$$(d\theta/dT)_{\theta_o,T_o} = \frac{5.2\times10^{13}}{0.4}\exp-\left\{\frac{3.47+3.25\,\theta_o^{0.8}}{kT_o}\right\} - \frac{8\times10^{15}}{0.4}\exp-\left\{\frac{3.83-1.62\theta_o^{0.8}}{kT_o}\right\} \qquad [4.58]$$

The next value of θ, namely θ_1, at $T_1 = T_o + \delta T$ is obtained from

$$\theta_1 = \theta_o + \delta\theta_o \qquad [4.59]$$

where

$$\delta\theta_o = (d\theta/dT)_{\theta_o,T_o} \cdot \delta T \qquad [4.60]$$

The new pair of θ_1 and T_1 are now used in equation [4.58] to calculate $(d\theta/dT)_{\theta_1,T_1}$, whence at $T_2 = T_1 + \delta T$, θ_2, given by

$$\theta_2 = \theta_1 + \delta\theta_1 \qquad [4.59a]$$

is obtained using the value for $\delta\theta_1$ obtained from

$$\delta\theta_1 = (d\theta/dT)_{\theta_1,T_1} \cdot \delta T \qquad [4.60a]$$

and so on for all values of $d\theta/dT$ versus T up to $\theta \doteq 0.04$, namely the full curve. The total area under the generated curve, $\Delta\theta$,

is given by $\sum_i \delta\theta_i$ and is equal to $0.04 - \theta_0$.

For the case of $\theta_0 = 0$, i.e. for the fully oxygenated surface, the generated curve of $d\theta/dT$ versus T is compared with the experimental T.P.D. curve. If the comparison is poor a new pair of Y' and $\Delta H_4^{0\neq}$ values are selected and the above iterative procedure is repeated to generate a new curve. This is done until the fit is really good (see later for goodness-of-fit).

For the case described above, i.e. for the fully oxygenerated surface, a good fit with the experimental T.P.D. curve is obtained and all the parameters can be generated with precision without the use of the $g(\theta)$ function. It is only when we come to compare experimental T.P.D. curves from partially oxygenated surfaces with those curves generated using the above iterative method where θ_0 does not equal 0 that the fit is no longer good and a $g(\theta)$ function must be invoked. The physical reason for this observation is that step sites can only result from zinc loss. Thus, starting from a fully oxygenated surface most of our oxygen is lost from perfect surface lattice oxygen sites and only the end of the T.P.D. curve, where zinc loss becomes appreciable, does oxygen loss occur from step sites. But, starting from a partially oxygenated surface, i.e. one starting with step sites, oxygen loss from these sites occurs early in the T.P.D. curve and so, for these curves, the $g(\theta)$ "correction" is necessary.

(iii) *Evaluation of $g(\theta)$:* Now, the $g(\theta)$ term accounts for the change in activation energy for oxygen loss resulting in the formation of step sites: as indicated in equation [4.57] it is written as a function of θ alone. Our task then is to generate a function $g(\theta)$ versus θ,

which with slightly adjusted (if necessary) Y' and $\Delta H_4^{0\ddagger}$ values, gives an accurate description of ALL our T.P.D. data.

The initial $g(\theta)$ functions were guessed at on the basis that no step sites are formed until zinc loss has occurred (i.e. only for substantial θ values, where the zinc loss becomes appreciable, will step sites occur). Hence $g(\theta) \doteqdot 0$ over a substantial range of θ. At high θ the levelling out of $g(\theta)$ was guessed at because new step sites will not go on being generated without limit.

With a $g(\theta)$ function and Y' and $\Delta H_4^{0\ddagger}$ the iterative procedure was used to generate a T.P.D. curve. The resulting generated curve was compared with the experimental curve and $g(\theta)$ adjusted until the fit was good. A single set of $g(\theta)$, X' and Y', and, $\Delta H_{1,2A}^{0\ddagger}$ and $\Delta H_4^{0\ddagger}$ parameters must fit all the T.P.D. curves for all values of the initial surface vacancy concentration, i.e. for all θ_0 values. This very tedious operation yielded highly satisfactory fits when the parameters in equation [4.57] were as follows:-

$X' = 5.2 \times 10^{13}\ s^{-1}$; $Y' = 8 \times 10^{15}\ s^{-1}$; $\Delta H_{1,2A}^{0\ddagger} = 3.47$ eV; $\Delta H_4^{0\ddagger} = 3.83$ eV

The final $g(\theta)$ function for mechanism A, $g_A(\theta)$, is shown in fig. (4.5b).

A family of curves of $d\theta/dT$ versus T is generated for different values of the initial surface vacancy concentration, θ_0 (established by the oxygen pre-treatment conditions), using the above parameters. This is shown in fig. (4.6). Fitting of these curves to the experimentally obtained T.P.D. curves (c.f. fig. (3.7)) is achieved by comparison of the characteristic parameters that uniquely define such curves, these are: the temperature of the peak maximum (T_p); the peak width at half height ($\Delta T_{1/2}$); and, the peak shape, i.e. relative areas on either side of the peak vertical. Fig. (4.7) shows the theoretical variation of peak

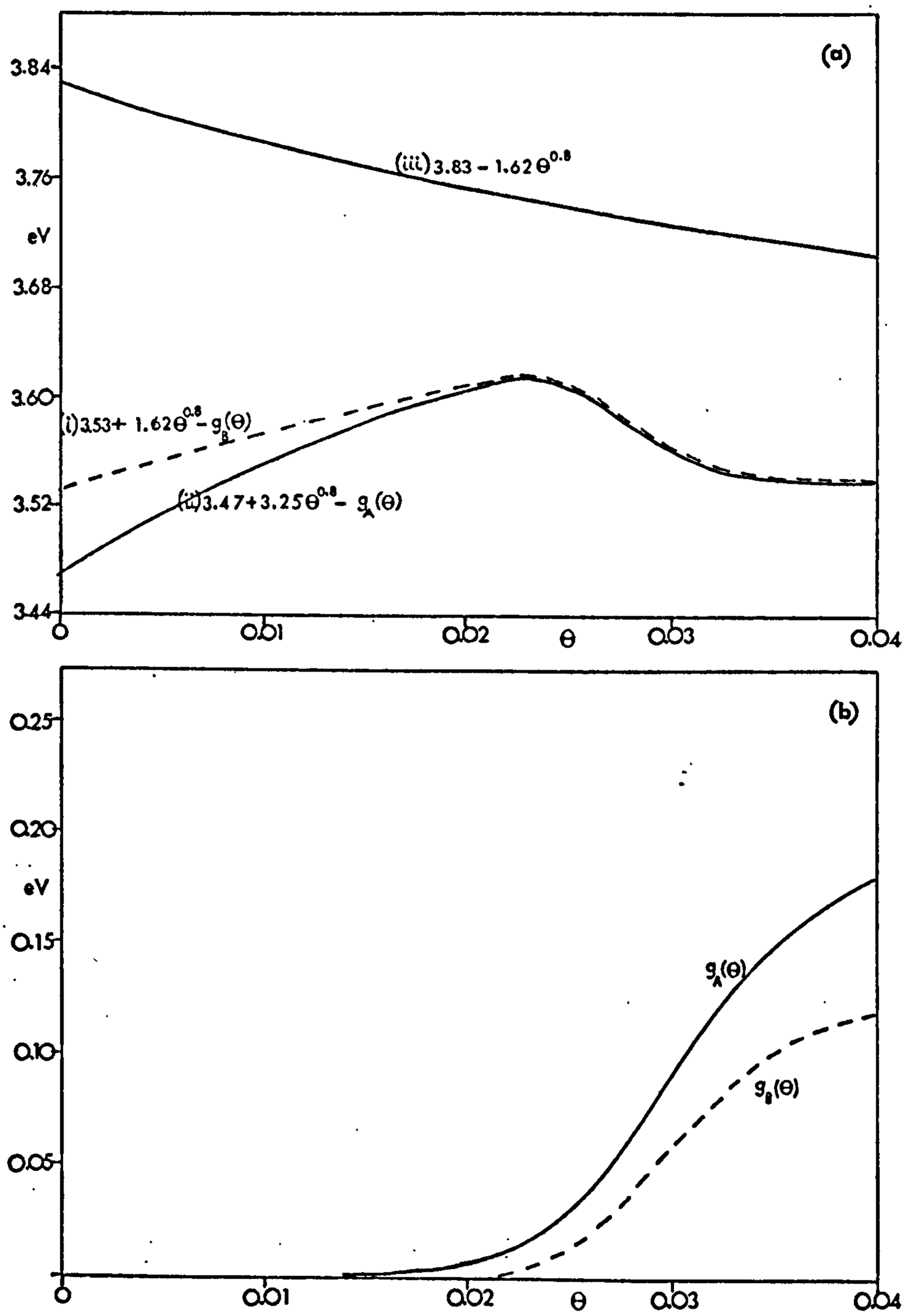

Fig. 4.5:

(a) overall activation energies, in eV, versus θ for:

(i) surface oxygen loss reaction of the mobile atom mechanism

(ii) surface oxygen loss reaction of the vacancy-pair mechanism

(iii) surface zinc loss reaction

(b) the $g(\theta)$ functions, in eV, versus θ for the vacancy-pair mechanism ($g_A(\theta)$) and for the mobile atom mechanism ($g_B(\theta)$)

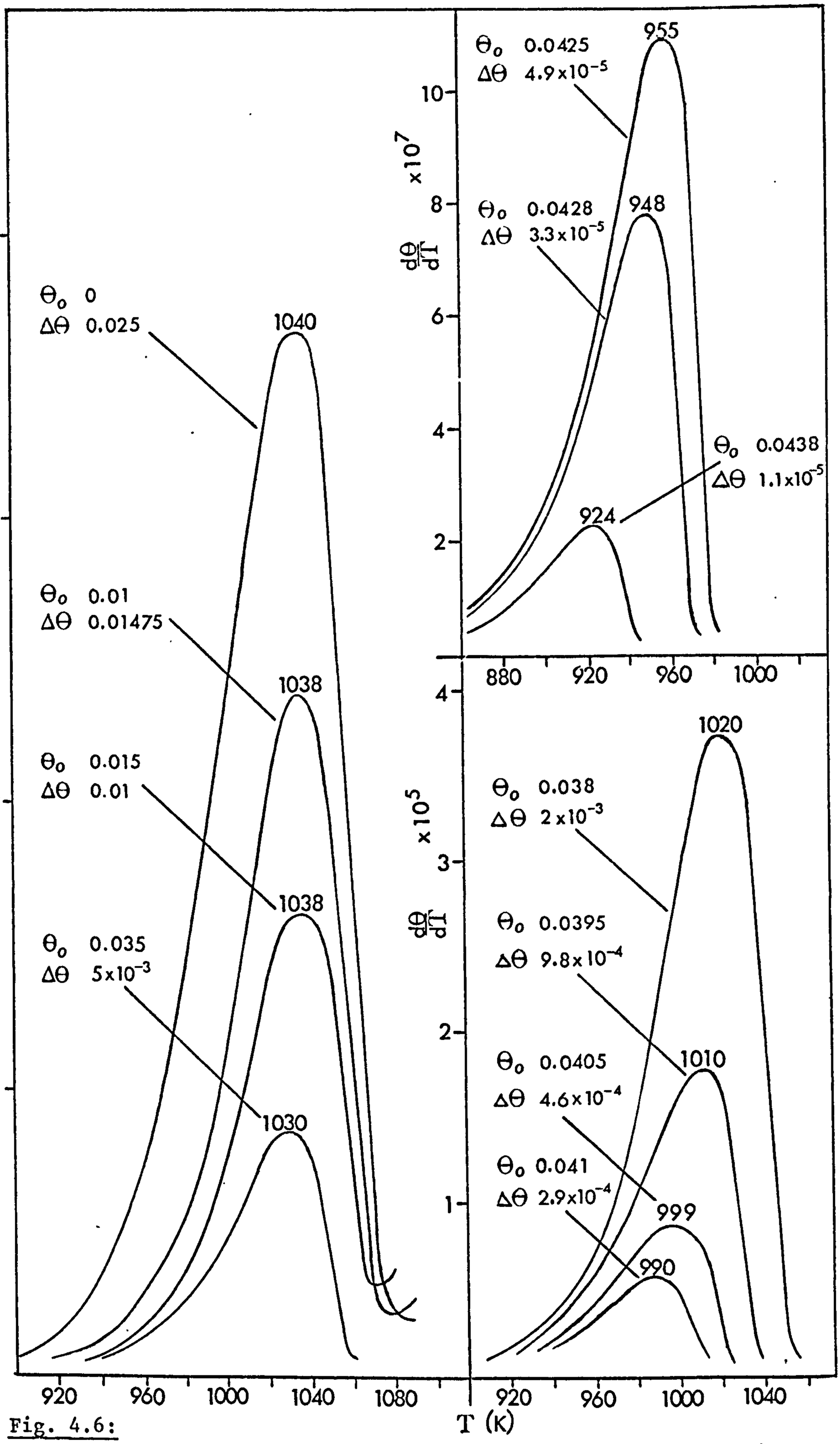

Fig. 4.6:

Generated curves of $d\Theta/dT$ versus T for various values of Θ_o obtained using the iterative solution of the approximate form of the overall rate equation for the vacancy-pair mechanism

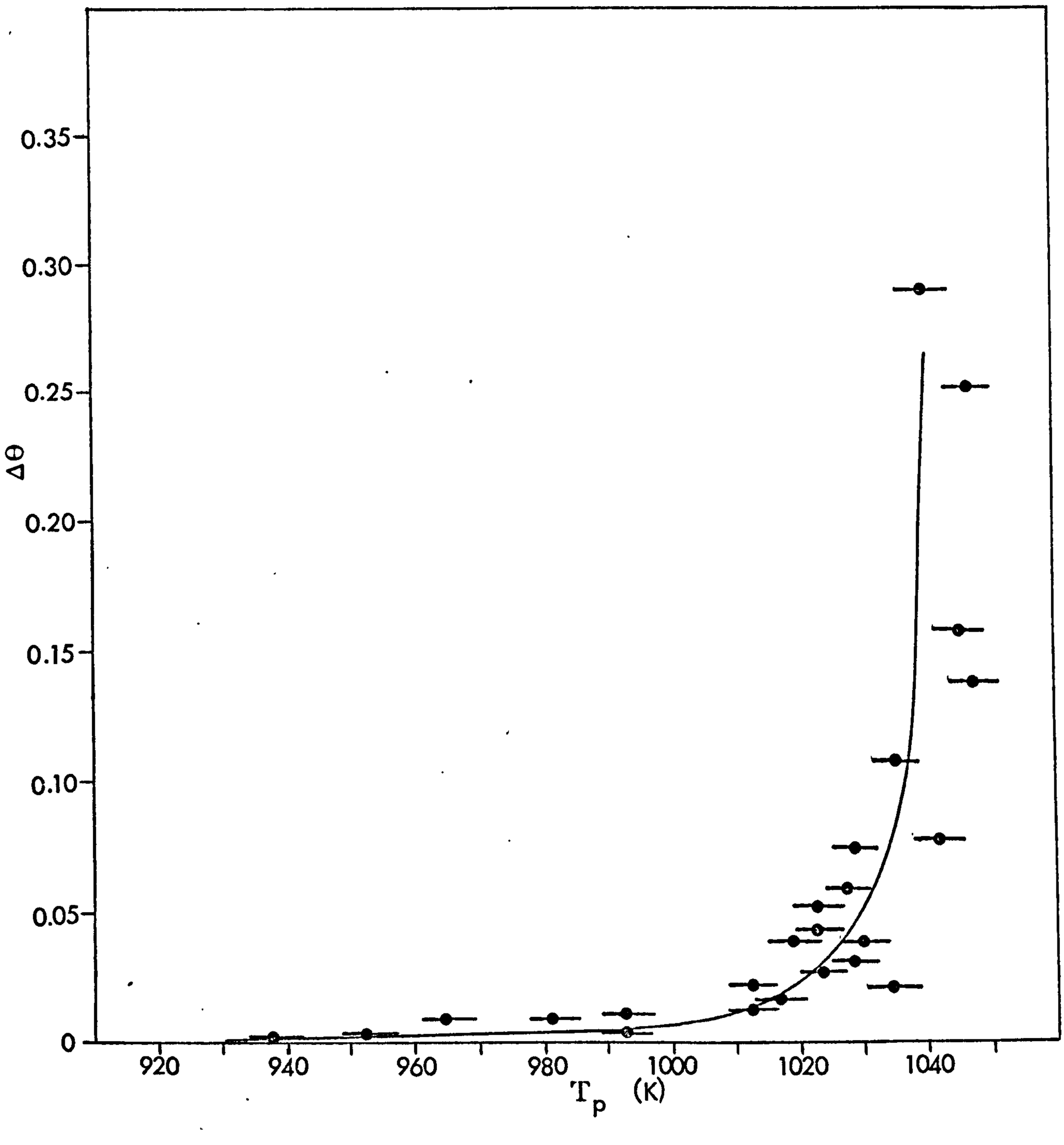

Fig. 4.7:

——— ····variation of peak area, $\Delta\theta$, with peak-maximum temperature, T_P , obtained from fig. (4.6)

—●— ·····experimental variation of peak area with peak-maximum temperature, reproduced from fig. (3.9)

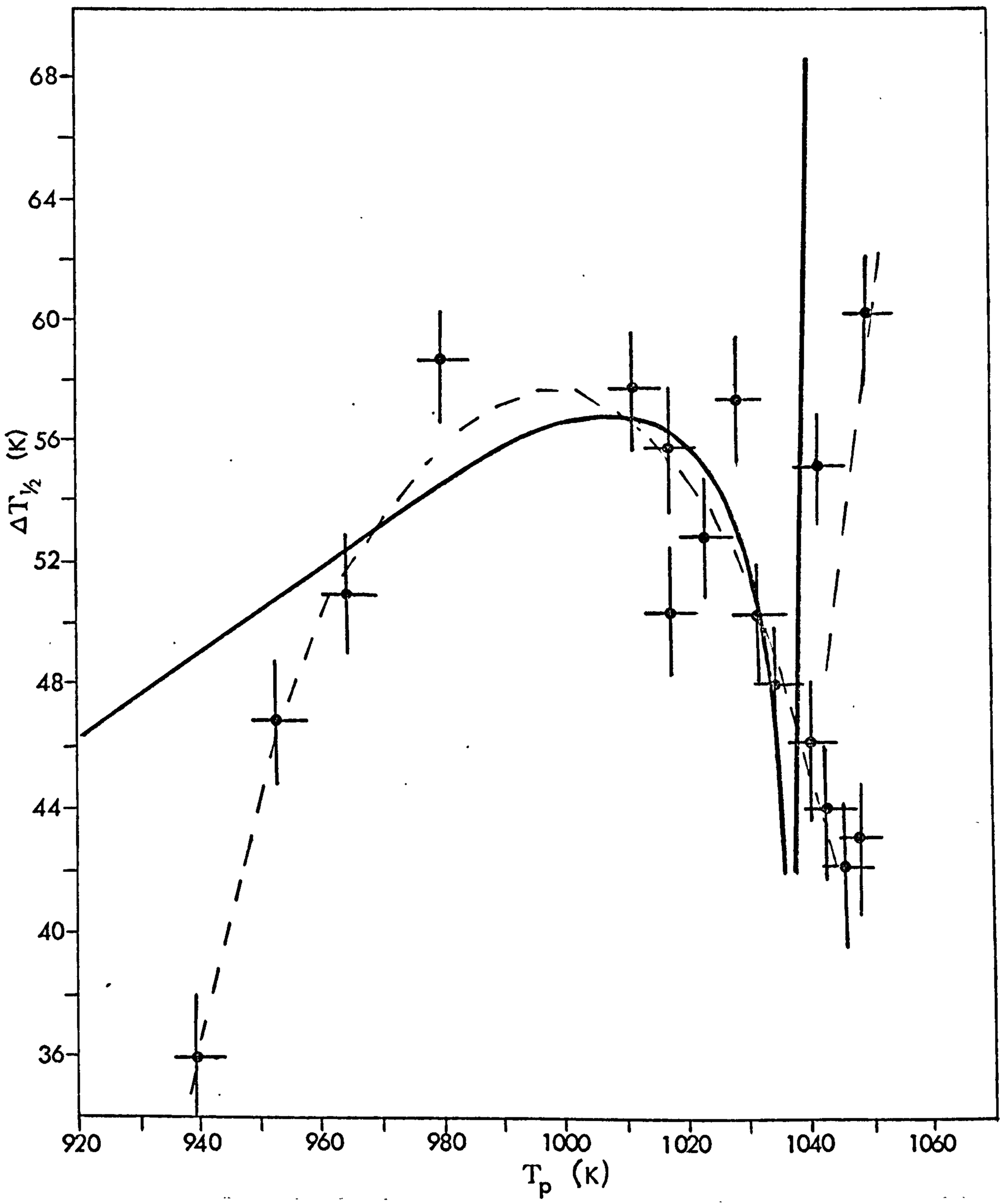

Fig. 4.8:

—— .... variation of peak width at half height, $\Delta T_{1/2}$, with peak-maximum temperature, T_p , obtained from fig. (4.6)

-+- .... experimental variation of peak width at half height with peak-maximum temperature, reproduced from fig. (3.10)

temperature, T_P , with peak area, $\Delta\theta$, obtained from fig. (4.6) (solid line) compared with experimental values reproduced from fig. (3.9): this indicates a peak temperature varying by over 100 K with peak area.

Fig. (4.8) shows the variation of peak width at half height, $\Delta T_{\frac{1}{2}}$, with peak temperature (solid line) compared with experimental values of these parameters (cf. fig. 3.10). The peak shape is analysed in terms of the symmetry of the peak with respect to the vertical axis, and can be evaluated numerically by measuring the fractional areas under the curve before and after the peak-maximum temperature. For ten theoretically generated curves the fractions are 0.676 ± 0.03 before the peak-maximum temperature and 0.324 ± 0.03 after. For a sample of ten experimental T.P.D. curves these fractions are 0.647 ± 0.03 and 0.353 ± 0.03, which agree with the theoretical within sample error.

A similar analysis for mechanism B yields parameters either very similar to or identical with those obtained for mechanism A. Thus $g(\theta)$ for mechanism B, i.e. $g_B(\theta)$, and $\Delta H^{o\ddagger}_{1,2B}$ are slightly changed, as shown in fig. (4.5a) and (4.5b), while the other parameters are unchanged. Thus since the two mechanisms give very similar parameters we have no method of distinguishing between them.

(iv) *Iterative solution of the full form of the rate equation:* With the parameters obtained by solution of the approximate form of the rate equation the full form of the rate equation, using the vacancy-pair mechanism as the 'worked example', becomes

$$d\theta/dT = \frac{5.2\times10^{13}}{\beta}\exp-\left\{\frac{3.47+3.25\theta^{0.8}-kT\ln(1+\theta_{s.s.}\{\exp\Delta E/kT-1\})}{kT}\right\} - \frac{8\times10^{15}\theta}{\beta}\exp-\left\{\frac{3.83-1.62\theta^{0.8}}{kT}\right\} \quad [4.61]$$

To solve this equation the following iterative method is used. Starting from a low temperature, T_0 , (ca. 850 K) at which $\Theta = \Theta_0$ and $\theta_{s.s.} = \theta_{s.s._0}$ (and $(d\Theta/dT)_{\theta_0, T_0}$, $\theta_{s.s._0}$ is small)) we select a small temperature increment, $\delta T\ (= T_1 - T_0)$ over which we assume $(d\Theta/dT)_{\theta_0\, T_0\, \theta_{s.s._0}}$ to be constant. We compute its value by inserting $\Theta = \Theta_0$ and $\theta_{s.s.} = \theta_{s.s._0}$ at T_0 into equation [4.61], whence

$$(d\Theta/dT)_{\theta_0, T_0, \theta_{s.s._0}} = \frac{5.2 \times 10^{13}}{\beta} \exp -\left\{\frac{3.47 + 3.25\Theta_0^{0.8} - kT_0 \ln(1 + \theta_{s.s._0}\{\exp 0.25/kT_0 - 1\})}{kT_0}\right\}$$

$$- \frac{8 \times 10^{15}\Theta_0}{\beta} \exp -\left\{\frac{3.83 - 1.62\Theta_0^{0.8}}{kT_0}\right\} \qquad [4.62]$$

where a trial value of $\Delta E = 0.25 eV$ has been chosen to be used. The next value of Θ, namely Θ_1 , at $T_1 = T_0 + \delta T$ is obtained from

$$\Theta_1 = \Theta_0 + \delta\Theta_0 \qquad [4.63]$$

where

$$\delta\Theta_0 = (d\Theta/dT)_{\Theta_0, T_0, \theta_{s.s._0}} \cdot \delta T \qquad [4.64]$$

The next value of $\theta_{s.s.}$, namely, $\theta_{s.s._1}$ is obtained from

$$\theta_{s.s._1} = \theta_{s.s_0} + \delta\theta_{s.s._0} \qquad [4.65]$$

where

$$\delta\theta_{s.s._0} = (d\theta_{s.s.}/dT)_{\theta_0, T_0, \theta_{s.s._0}} \cdot \delta T \qquad [4.66]$$

Now, the rate of step site formation at these values of θ_0 , T_0 and $\theta_{s.s_0}$ is simply given by the rate at which zinc evaporates from the surface, i.e. by the second part of the right-hand side of equation [4.62], whence this in equation [4.66] gives

$$\delta\theta_{s.s._0} = \left[\frac{8\times10^{15}\theta_0}{\beta}\, exp-\left\{\frac{3.83-1.62\,\theta_0^{0.8}}{kT_0}\right\}\right]\delta T \qquad [4.67]$$

so , $\theta_{s.s._1}$ can be computed using equation [4.67] to obtain $\delta\theta_{s.s._0}$, and this in equation [4.65] to obtain $\theta_{s.s._1}$.

The new set of θ_1 , $\theta_{s.s._1}$ and T_1 are used in equation [4.62] to calculate $(d\theta/dT)_{\theta_1, T_1, \theta_{s.s._1}}$, whence at T_2 $(= T_1 + \delta T)$

$$\theta_2 = \theta_1 + \delta\theta_1 \qquad [4.63a]$$

where

$$\delta\theta_1 = (d\theta/dT)_{\theta_1, T_1, \theta_{s.s._1}} \cdot \delta T \qquad [4.64a]$$

and they are used again in equation [4.67] to calculate $\delta\theta_{s.s._1}$ and hence $\theta_{s.s._2}$ where

$$\theta_{s.s._2} = \theta_{s.s._1} + \delta\theta_{s.s._1} \qquad [4.65a]$$

And so on and so on .....

Continuing this analysis over the full temperature range of the T.P.D. curve, i.e. ca. 850 K to 1100 K one obtains values of θ, $\theta_{s.s.}$, $d\theta/dT$ and $d\theta_{s.s.}/dT$ versus temperature. Fig. (4.9) shows a family of $d\theta/dT$ versus T curves generated using the above procedure, for different values of the initial surface oxygen vacancy concentration, θ_o, and for differing intial step site concentrations, $\theta_{s.s._o}$. The set of three curves generated using the initial condition that $\theta_o = 0$ shows how the values of T_p and $\Delta\theta$ obtained depend upon the value of $\theta_{s.s._o}$. When $\theta_0=0$ and $\theta_{s.s._o}=0$ the generated curve, fig. (4.9), yields the parameters $\Delta\theta \doteqdot 0.025$ and $T_p = 1040K$ (this is very nearly the same as the curve generated using the solution of the approximate form of the rate equation, with $g(\theta)$, and $\theta_o = 0$, cf. fig. (4.6)). When $\theta_o=0$ and $\theta_{s.s._o}= 0.05$ the generated curve yields the parameters $\Delta\theta \doteqdot 0.04$ and $T_p = 1024\,K$. This behaviour can be explained qualitatively by observing how the activation energy of the oxygen loss reaction changes with $\theta_{s.s._o}$. For $\theta_{ss._o} = 0$, the curve of fig. (4.5a) shows how this activation energy changes with θ. The position of the maximum in this activation energy at $\theta \doteqdot 0.025$ means that for the curve generated with the initial conditions that $\theta_o=0$ and $\theta_{s.s._o}=0$ the difference in the rates of the oxygen and the zinc loss reactions will be small, i.e. $d\theta/dT \doteqdot 0$, when θ is about 0.025, and the generated curve will terminate at this value of θ. However, for the case when $\theta_{s.s._o}$ is not zero the maximum in the activation energy is displaced to lower energy, at $\theta \doteqdot 0.025$ $d\theta/dT$ no longer equals zero, and the generated curve continues past this value of $\theta = 0.025$ and terminates at $\theta \doteqdot 0.04$.

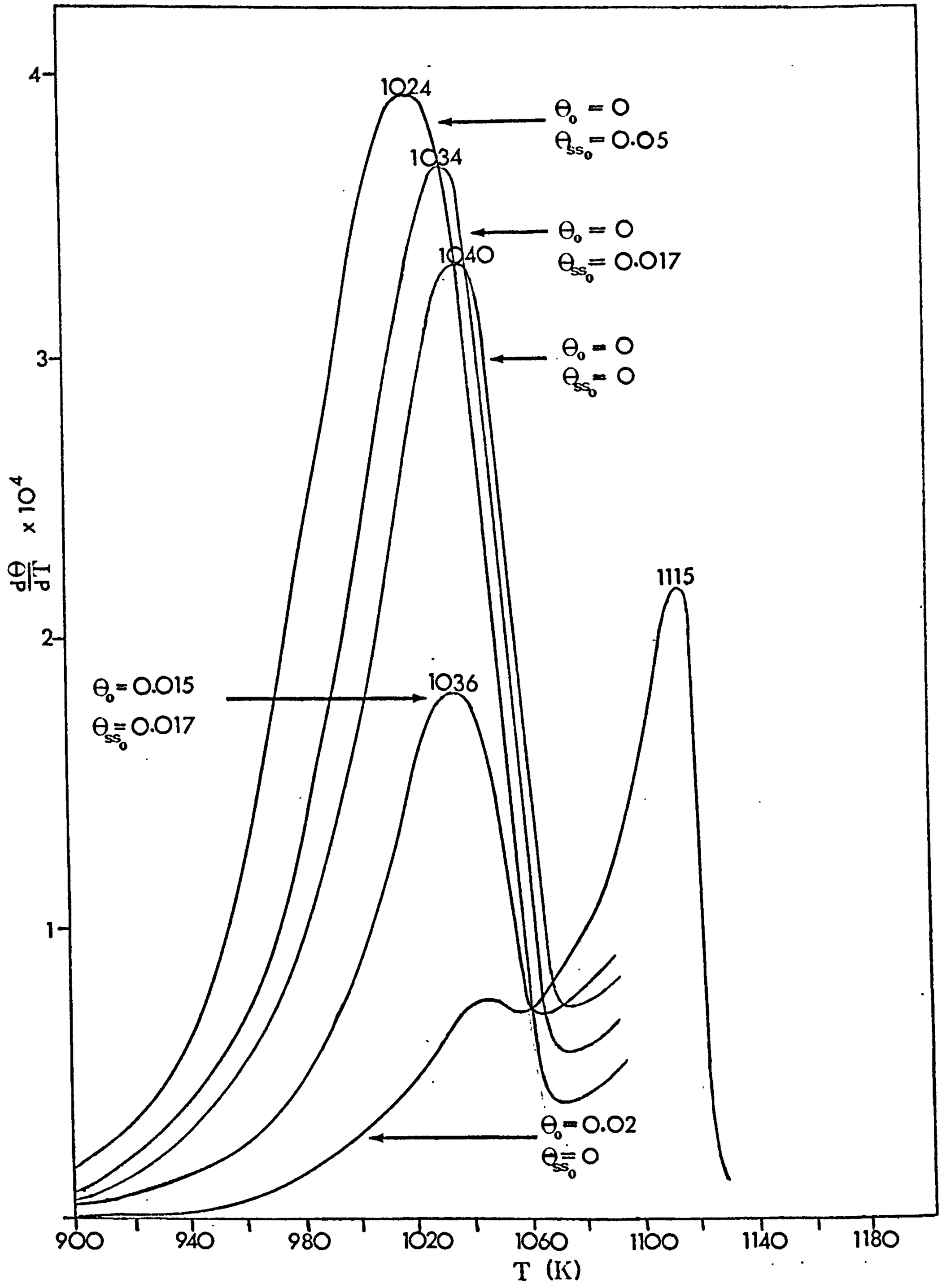

Fig. 4.9:

Generated curves of $d\theta/dT$ versus T for various values of θ_o and θ_{ss_o} obtained using the iterative solution of the full form of the overall rate equation for the vacancy-pair mechanism

The position of the maximum in the activation energy for the case of $\theta_{s.s._0} = 0$ also explains the discontinuity in the $\Delta T_{1/2}$ versus T_p relationship (cf. fig. (4.8)). For the curves generated using the initial condition of $\theta_{s.s._0} = 0$ and $\theta_0 = 0$ the value of $d\theta/dT$ goes to zero at $\theta \doteqdot 0.025$ and the curve terminates at this value of θ. The $\Delta T_{1/2}$ versus T_p relationship for this case is represented by the portion of the $\Delta T_{1/2}$ versus T_p curve (fig. (4.8)) at high T_p. For the curves generated using the initial condition of $\theta_0 \neq 0$, i.e. a partially oxygenated surface, at $\theta \doteqdot 0.025$ $d\theta/dT \neq 0$ and the curve now terminates at $\theta \doteqdot 0.04$. For this case the $\Delta T_{1/2}$ versus T_p relationship is represented by the low T_p portion of the $\Delta T_{1/2}$ versus T_p curve.

The scatter on the $\Delta T_{1/2}$ versus T_p curve and on the $\Delta\theta$ versus T_p curve can be explained by variations in the initial step site concentration from its value of $\theta_{s.s._0} = 0$ at $\theta = 0$, that had been assumed throughout this analysis, since the values of all of these parameters have been shown to be sensitive to the value of $\theta_{s.s._0}$. In fact, for fully oxygenated surfaces, in most cases the step site concentration is small (see section 4.1.3). The physical reasoning behind this occurrence is that in most cases, during the oxygen pre-treatment at high pressure, oxygen vacancies are destroyed and steps are annealed out to give an essentially near perfect surface lattice, i.e. low θ_0, low $\theta_{s.s._0}$. If, however, during such a pre-treatment the vacancies are destroyed and there has been insufficient annealing time to destroy all step sites, then the condition $\theta_0 \doteqdot 0$ but $\theta_{s.s._0} \neq 0$ will prevail.

There are shown in fig. (4.9) two curves generated using our iterative method, for the case of initially partially oxygenated surfaces. When $\theta_0 = 0.015$ and with a high initial step site concentration, $\theta_{s.s._0}=0.017$, a single peak is observed. When, however, with a similar initial surface vacancy concentration, $\theta_0 = 0.02$, the initial step site concentration is zero, a doublet structure is observed. A doublet is occasionally observed in experimental T.P.D. curves (cf. fig.(3.7d)). The qualitative explanation of this behaviour is that it again arises due to the maximum in the activation energy (fig. (4.5a)). Starting at $\theta_{s.s._0}=0$ and $\theta_0=0.02$, θ and $d\theta/dT$ increase as T increases, but when θ approaches 0.025 $d\theta/dT$ becomes small (but not zero). Beyond $\theta \doteqdot 0.025$ the activation energy for the oxygen loss reaction decreases and $d\theta/dT$ rises rapidly with T, and again returns to zero when $\theta \doteqdot 0.04$, hence the doublet structure is observed.

Fig. (4.10) shows values of the activation energy change due to step sites, i.e. $kT\ln(1+\theta_{s.s}\{\exp\Delta E/kT-1\})$, evaluated using our full iterative analysis. Curve "b" is for $\theta_0=0$, $\theta_{s.s_0}=0$ and with $\Delta E = 0.25\,eV$: curve "a" is for $\theta_0=0$, $\theta_{s.s._0}=0$ and with $\Delta E=0.35\,eV$. Also shown for comparison is the $g_A(\theta)$ term which was chosen for the approximate solution of the rate equation. There is an obvious close correspondence between these curves, lending confidence to the proposed mechanism and indicating that the ΔE value, which is the difference in free energy between formation of a $^{s}V_o^{\cdot}\cdots O^{-}$ species at a step site and at a perfect lattice site, lies somewhere between 0.25 and 0.35eV. In addition, this shows that, in the approximate solution of the rate equation, it is valid to make the assumption that the term $kT\ln(1+\theta_{ss}\{\exp\Delta E/kT-1\})$ can be

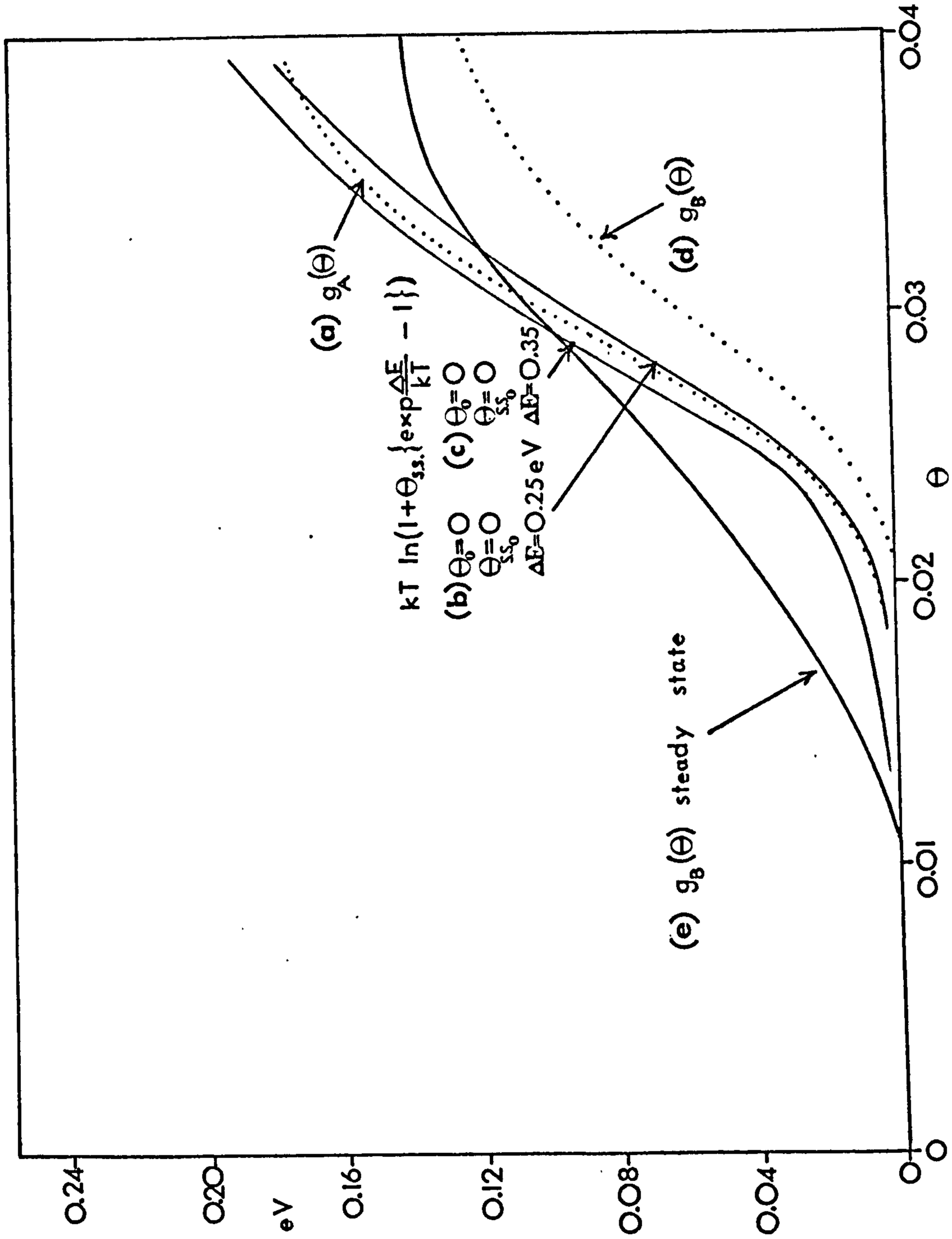

Fig. 4.10:

The change in activation energy of the oxygen loss reaction (in eV) with Θ - various $g(\Theta)$ functions

closely approximated by a function variable in θ alone, i.e. $g(\theta)$, and indeed that our choice of $g(\theta)$ was a good one.

4.1.1e Summary

Halpern and Germain (1975) observed a high temperature peak on an oxygen T.P.D. of zinc oxide powder. They analysed their peak using a Polanyi-Wigner kinetic model (see below) and obtained a desorption with an activation energy of 3.61eV.

The first order Polanyi-Wigner equation (see, for example, Petermann 1972, and Ehrlich 1963) can be written

$$-dc/dt = \nu C \exp - \Delta E^{\ddagger}/kT \qquad [4.68]$$

where $\Delta E^{\ddagger}$ is the activation energy of the desorption process and C is the surface coverage. Such an equation would described a peak in the T.P.D. spectrum identical to one which is obtained in these experiments; that is, a desorption peak non-symmetrical with respect to the vertical axis with areas before and after the peak maximum temperature in the ratio ca. 2:1. However, using these authors' model one cannot explain the marked shift in peak maximum temperature, T_p , to lower temperatures with decreasing peak area, and the peak width at half height would be insensitive to peak temperature and peak area. This model was therefore rejected as an alternative.

Accepting that the model proposed here of opposing oxygen loss and zinc loss reactions is the correct one, several important observations concerning the detailed nature of the overall reaction kinetics can be made. These are listed below.

(i) Two important results emerge from our preceding analysis. The formation of charged surface oxygen vacancies and the formation of step sites must be invoked in order to explain all of our experimental observations, as described in the previous section.

There is evidence (Eger, Goldstein and Many 1975, by photodesorption of surface oxygen) that accumulation layers due to more than 5×10^{13} cm^{-2} excess surface positive charges can exist on the surface of zinc oxide, where such strong accumulation layers have not been reported on other semiconductors. Therefore, the 2.4×10^{13} cm^{-2} surface excess charges ($\theta = 0.04$) that we obtain, is not unlikely.

(ii) Göpel(1)(1976) has reported the formation of step arrays perpendicular to the c-axis, on the $10\bar{1}0$ zinc oxide surface when heated at 1100 K in ca. 2×10^{-7} torr oxygen, by using the observation of the splitting of LEED reflections, (Henzler 1973, observed similar step arrays on vacuum cleaved prism, $11\bar{2}0$ faces). A mean step height of 2.6×10^{-8} cm, corresponding to the depth of one lattice layer, was observed occurring every 41×10^{-8} cm, which is 8 lattice constants parallel to the c-axis. This gives a fractional surface concentration of step sites of 0.125, which is not too dissimilar to the maximum value of $\theta_{s.s} \doteqdot 0.2$ (see next section) that we obtain.

(iii) The frequency factor of the zinc loss reaction which has a value of 8×10^{15} s^{-1} is much higher than the value of 10^{13} s^{-1} which is a typical value of the molecular vibration frequency. Using the most generalised form of the absolute reaction rate equation, the frequency factor, A, is given by

$$A = \bar{r}\{kT/h\}\{F^{\ddagger}/F_{init.}\}$$

where $\bar{r}$ is the average transmission coefficient, $F^{\ddagger}$ is the partition function of the activated state and $F_{init.}$ is the partition function of the initial state. Now, when the activated complex is less strongly bound to the surface than the molecule or atom in its initial state, $\{F^{\ddagger}/F_{init.}\}$ can become greater than unity and the value of A be larger than 10^{13} s^{-1}. When the activated complex has both translational and rotational freedom $\{F^{\ddagger}/F_{init.}\}$ can become as large as 10^{3} to 10^{4}. In our case we assume that the large value of the frequency factor arises out of these considerations. That the activated complex in the zinc loss reaction has more degrees of freedom than the ground state seems consistent with the fact that in its initial state the zinc atom is in the perfect surface lattice, having no translational freedom, but the activated complex, which is a surface adsorbed species will be much more loosely bound.

(iv) In the rate determining step of the oxygen loss reaction the initial state has an oxygen atom on the surface next to a vacancy, i.e. with more degrees of freedom than an oxygen atom in the perfect surface lattice. In this case it is not unlikely that $\{F^{\ddagger}/F_{init.}\}$ is close to unity and quite reasonable to observe a frequency factor of 5.2×10^{13} s^{-1}.

4.1.2 <u>The interaction of oxygen with the zinc oxide surface at steady-state</u>

Two reaction schemes that correspond to the vacancy-pair and the mobile atom mechanisms of the previous section are formulated below. In each case the most simplified scheme is shown. Other, more complicated mechanisms involving the formation of various hypothetical intermediates can be written, but their overall steady-state equations are similar in form to the simpler reaction schemes described below, and, in any event, the experimental data does not differentiate between them.

A. Vacancy-pair mechanism

The first two steps are the reversible adsorption/desorption of oxygen gas onto vacancy sites and its incorporation into the surface lattice so destroying the vacancies, viz.,

$$^{s}O_{x}^{x} \underset{k_{-1}}{\overset{k_1}{\rightleftharpoons}} {}^{s}V_{o}^{+}\cdots O^{-} \qquad \text{..... step 1}$$

and

$$^{s}O_{x\ n.n.}^{x} + {}^{s}V_{o}^{+}\cdots O^{-} \underset{k_{-2A}}{\overset{k_{2A}}{\rightleftharpoons}} 2\,{}^{s}V_{o}^{+} + O_2(g) + 2\,{}^{s}e^{-} \qquad \text{.... step 2}$$

where, for simplicity, steps 2A and 3A of the vacancy-pair surface lattice decomposition mechanism (cf. section 4.1.1) are shown as one. Accompanying the foregoing reactions is the parallel, but non-reversible, surface zinc loss reaction,

$$^{s}V_{o}^{+} + {}^{s}e^{-} \xrightarrow{k_3} Zn(g) + {}^{s}O_{x}^{x} \qquad \text{.... step 3}$$

and the oxidation of the zinc condensed on the walls of the reaction chamber, viz.,

$$2\,Zn(s) + O_2(g) \xrightarrow{k_4} ZnO(s) \qquad \text{.... step 4}$$

Now, at steady-state, the rate of concentration change with time is zero for all the species concerned in the reaction scheme. So, for material balance in the gas phase

$$dP_{O_2}/dt = 0$$

whence,

$$k_{-2A}[^{s}V_{o}^{+}]^2 P_{O_2} + k_4 P_{O_2} P_{Zn}^2 = k_{2A}[^{s}V_{o}^{+}\cdots O^{-}][^{s}O_{x\ n.n}^{x}] \qquad [4.69]$$

and since,

$$dP_{Zn}/dt = 0$$

it follows that,

$$k_3[{}^{s}V_0^{+}] = 2k_4 P_{O_2} P_{Zn}^2 \qquad [4.70]$$

In equations [4.69] and [4.70] the activity of surface electrons is not included for the reasons set out in the previous section (4.1.1a). Combining [4.69] and [4.70] gives,

$$[{}^{s}V_0^{+}\cdots O^{-}] = \frac{k_{-2A}[{}^{s}V_0^{+}]^2 P_{O_2}}{k_{2A}[{}^{s}O_x^{x}\ n.n.]} + \frac{k_3[{}^{s}V_0^{+}]}{2k_{2A}[O_x^{x}\ n.n]} \qquad [4.71]$$

Now for the zinc oxide surface phase, material balance gives

$$d[{}^{s}O_x^{x}]/dt = 0$$

whence,

$$k_1[{}^{s}O_x^{x}] + k_{2A}[{}^{s}V_0^{+}\cdots O^{-}][{}^{s}O_x^{x}\ n.n] = k_{-1}[{}^{s}V_0^{+}\cdots O^{-}] + k_{-2A}[{}^{s}V_0^{+}]^2 P_{O_2} + k_3[{}^{s}V_0^{+}] \qquad [4.72]$$

and substituting for $[{}^{s}V_0^{+}\cdots O^{-}]$ from equation [4.71] into [4.72] gives,

$$k_1[{}^{s}O_x^{x}] = \frac{k_{-1}k_{-2A}[{}^{s}V_0^{+}]^2 P_{O_2}}{k_{2A}[{}^{s}O_x^{x}\ n.n]} + \frac{k_3[{}^{s}V_0^{+}]}{2}\left(1 + \frac{k_{-1}}{k_{2A}[{}^{s}O_x^{x}\ n.n]}\right) \qquad [4.73]$$

Now, with the condition that

$$\frac{k_{-1}}{k_{2A}[{}^{s}O_x^{x}\ n.n]} \gg 1$$

k_{-1} being a fast, pre-rate determining step rate constant, and, k_{2A} the rate constant in the rate determining step of the decomposition process described in the previous section, equation [4.73] becomes, after rearrangement,

$$P_{O_2} = \frac{k_1 k_{2A}[{}^{s}O_x^x][{}^{s}O_{x\,n.n.}^x]}{k_{-1}k_{-2A}[{}^{s}V_o^+]^2} - \frac{k_3}{2k_{-2A}[{}^{s}V_o^+]} \qquad [4.74]$$

This equation must now be stated in a form that relates P_{O_2} directly to θ and T, since these are the experimentally measured quantities. If the θ and $\theta_{s.s.}$ variations of all the rate constants are isolated, using those surface potential variations indicated in the potential energy diagram (cf. fig. (4.4)) then equation [4.74] becomes

$$P_{O_2} = \frac{A}{\theta^2}\exp-\left(\frac{6.5\theta^{0.8} - kT\ln\left(1+\theta_{s.s.}\{\exp \Delta E/kT - 1\}\right)}{kT}\right) - \frac{B\exp-(1.62\theta^{0.8}/kT)}{2\theta\exp-(3.25\theta^{0.8}/kT)} \qquad [4.75]$$

where A and B are constants at constant temperature. When θ (and $\theta_{s.s.}$) are small equation [4.75] becomes

$$P_{O_2} = A/\theta^2 \qquad [4.75a]$$

where A is the overall equilibrium constant, at zero θ and zero $\theta_{s.s.}$, for the reaction

$$2{}^{s}O_x^x \rightleftharpoons 2{}^{s}V_o^+ + O_2(g) + 2{}^{s}e^-$$

Rearranging [4.75] gives

$$P_{O_2} = \left[\frac{A}{\theta}\exp-\left(\frac{1.62\theta^{0.8}}{kT}\right)\right]\left[\frac{1}{\theta}\exp-\left(\frac{4.87\theta^{0.8} - kT\ln\left(1+\theta_{ss.}\{\exp \Delta E/kT - 1\}\right)}{kT}\right) - \frac{B}{2A}\right] \qquad [4.76]$$

B. Mobile atom mechanism

This mechanism which parallels the non-steady-state decomposition reaction of the previous section involves three steps in which the surface lattice oxygen is in equilibrium with oxygen in the gas phase. Firstly, an equilibrium between oxygen in a lattice site and a surface adsorbed oxygen complex, namely

$$ {}^{s}O_{x}^{x} \underset{k_{-1}}{\overset{k_1}{\rightleftharpoons}} {}^{s}V_{o}^{+}\cdots O^{-} \qquad \text{.... step 1} $$

followed by a quasi-reversible decomposition of this species to give a positively charged oxygen vacancy, with corresponding space charge electron, and a mobile surface oxygen atom, viz.,

$$ {}^{s}V_{o}^{+}\cdots O^{-} \underset{k_{-2B}}{\overset{k_{2B}}{\rightleftharpoons}} {}^{s}V_{o}^{+} + {}^{s}e^{-} + O \qquad \text{.... step 2} $$

This is followed by the rate determining adsorption/desorption of gas phase oxygen, namely

$$ {}^{s}V_{o}^{+}\cdots O^{-} + O \underset{k_{-3B}}{\overset{k_{3B}}{\rightleftharpoons}} {}^{s}V_{o}^{+} + O_2(g) + {}^{s}e^{-} \qquad \text{.... step 3} $$

The parallel, non-reversible, zinc loss reactions are as before, namely

$$ {}^{s}V_{o}^{+} + {}^{s}e^{-} \xrightarrow{k_4} Zn(g) + {}^{s}O_{x}^{x} \qquad \text{.... step 4} $$

and,

$$ 2Zn(s) + O_2(g) \xrightarrow{k_5} 2ZnO(s) \qquad \text{.... step 5} $$

Now, with mass balance for the gas phase, at steady-state,

$$dP_{O_2}/dt = 0$$

whence from steps 3 and 5,

$$k_{3B}[{}^{s}V_O^{\cdot\cdot}\cdots O^{-}][O] = k_{-3B}[{}^{s}V_O^{\cdot\cdot}]P_{O_2} + k_5 P_{Zn}^2 P_{O_2} \qquad [4.77]$$

and with

$$dP_{Zn}/dt = 0$$

it follows that

$$k_4[{}^{s}V_O^{\cdot\cdot}] = 2P_{Zn}^2 P_{O_2} \qquad [4.78]$$

which in equation [4.77] gives

$$k_{3B}[{}^{s}V_O^{\cdot\cdot}\cdots O^{-}][O] = k_{-3B}[{}^{s}V_O^{\cdot\cdot}]P_{O_2} + \frac{k_4}{2}[{}^{s}V_O^{\cdot\cdot}] \qquad [4.79]$$

Material balance for the surface phase, at steady-state, gives

$$d[{}^{s}O_X^X]/dt = 0$$

whence,

$$k_1[{}^{s}O_X^X] = k_4[{}^{s}V_O^{\cdot\cdot}] \quad k_{-1}[{}^{s}V_O^{\cdot\cdot}\cdots O^{-}] \qquad [4.80]$$

and with

$$d[O]/dt = 0$$

it follows that

$$k_{2B}[{}^{S}V_O^{+}\cdots O^{-}] + k_{-3B}[{}^{S}V_O^{+}]P_{O_2} = k_{-2B}[{}^{S}V_O^{+}] + k_{3B}[{}^{S}V_O^{+}\cdots O^{-}][O] \quad [4.81]$$

Substrating [4.79] from [4.81] and rearranging gives

$$\frac{k_{2B}[{}^{S}V_O^{+}\cdots O^{-}]}{k_{-2B}[{}^{S}V_O^{+}]} - \frac{k_4}{2k_{-2B}} = [O] \quad [4.82]$$

Putting this value for [O] and the value of $[{}^{S}V_O^{+}\text{-}O]$ from equation [4.80] into equation [4.79] gives, after rearrangement

$$P_{O_2} = \frac{k_{3B}}{k_{-3B}[{}^{S}V_O^{+}]}\left[\frac{k_1[{}^{S}O_X^{x}] - k_4[{}^{S}V_O^{+}]}{k_{-1}}\right]\left[\frac{k_1 k_{2B}[{}^{S}O_X^{x}]}{k_{-1}k_{-2B}[{}^{S}V_O^{+}]} - \frac{k_4}{k_{-2B}}\left(\frac{k_{2B}}{k_{-1}} + \frac{1}{2}\right)\right] - \frac{k_4}{2k_{-3B}} \quad [4.83]$$

and since $k_1[{}^{S}O_X^{x}] \gg k_4[{}^{S}V_O^{+}]$ and $k_{-1} \gg k_{2B}$, equation [4.83] can be rewritten as

$$P_{O_2} = \frac{k_1 k_{3B}[{}^{S}O_X^{x}]}{k_{-1}k_{-2B}[{}^{S}V_O^{+}]}\left[\frac{k_1 k_{2B}\,{}^{S}O_X^{x}}{k_{-1}k_{-2B}\,{}^{S}V_O^{+}} - \frac{k_4}{2k_{-2B}}\right] - \frac{k_4}{2k_{-3B}} \quad [4.84]$$

This can be reduced further by consideration of the term $k_4/2k_{-3B}$.

The magnitudes of both these rate constants are known. From section 4.1.1

$$k_4 = 8 \times 10^{15} \exp-\left(\frac{3.83\,eV}{kT}\right)$$

and section 4.1.4

$$k_{-3B} = (1.0 \pm 0.6) \times 10^{5} \exp-\left(\frac{1.22\,eV}{kT}\right)$$

whence, at 1000 K

$$k_4/2k_{-3B} = 4 \times 10^{-3} \quad \text{torr}$$

which is small compared with P_{O_2} over the range of experimental pressures employed in this study. So, equation [4.84] when reduced further, can be written

$$P_{O_2} = \frac{k_1 k_{3B} [{}^{s}O_x^x]}{k_{-1} k_{-3B} [{}^{s}V_o^+]} \left[\frac{k_{2B} k_1 [{}^{s}O_x^x]}{k_{-2B} k_{-1} [{}^{s}V_o^+]} - \frac{k_4}{2k_{-2B}} \right] \qquad [4.85]$$

Now, using the θ and $\theta_{s.s.}$ dependencies of the rate constants, shown in the potential energy diagram of fig. (4.4), equation [4.85] becomes

$$P_{O_2} = \left[\frac{K}{\theta} \exp - \left\{ \frac{3.25\,\theta^{0.8} - kT \ln(1+\theta_{s.s}\{\exp \Delta E/kT - 1\})}{kT} \right\} \right] \times \left[\frac{1}{\theta} \exp - \left\{ \frac{3.25\theta^{0.8} - kT \ln(1+\theta_{s.s}\{\exp \Delta E/kT - 1\})}{kT} \right\} - C \right] \qquad [4.86]$$

whence K and C are temperature dependent constants. When θ (and $\theta_{s.s.}$) are small, equation [4.86] becomes

$$P_{O_2} = K/\theta^2 \qquad [4.86a]$$

where K is the overall equilibrium constant for the reaction

$$2\,{}^{s}O_x^x \rightleftharpoons 2\,{}^{s}V_o^+ + O_2(g) + 2\,{}^{s}e^-$$

Equations [4.76] and [4.86] describe the relationship between the surface oxygen vacancy concentration, θ, at a temperature T, and with an oxygen gas pressure of P_{O_2}, at steady-state. When θ is small both equations reduce to the form $P_{O_2} = K/\theta^2$. When θ is large (approaching 0.04) there is a marked deviation from the isotherm described by the equation $P_{O_2} = K/\theta^2$, due to the θ dependence

of the exponentials in equations [4.76] and [4.86]. We can choose arbitrary functions $g(\theta)$, as an approximation to the terms $kT\ln(1+\theta_{s.s}\{\exp\Delta E/kT-1\})$ (cf. section 4.1.1d). Equations [4.76] and [4.86] become very similar when suitable values of $g(\theta)$ are chosen. The value of $g(\theta)$ used in equation [4.70] for the vacancy pair mechanism is virtually identical to that for the mobile atom mechanism ($g(\theta)$ versus θ in fig. (4.13b)) used in equation [4.86]. Thus since the two mechanisms give very similar parameters we have no method of distinguishing between them.

The method of solution of these equations is described below, taking equation [4.86] for the mobile atom mechanism as the 'worked example'.

Replacing $kT\ln(1+\theta_{s.s.}\{\exp\Delta E/kT-1\})$ by $g(\theta)$ in equation [4.86], where $g(\theta)$ is shown in fig. (4.13b), there is the relation

$$P_{O_2} = \left[\frac{K}{\theta}\exp-\left\{\frac{3.25\theta^{0.8}-g(\theta)}{kT}\right\}\right]\left[\frac{1}{\theta}\exp-\left\{\frac{3.25\theta^{0.8}-g(\theta)}{kT}\right\} - C\right] \qquad [4.87]$$

which can be rewritten

$$P_{O_2} = \left[\frac{K}{\theta}f(\theta,T)\right]\left[\frac{1}{\theta}f(\theta,T) - C\right] \qquad [4.88]$$

where $f(\theta,T)$ describes the θ and T dependent exponential terms in equation [4.87]. Now, at T, the steady-state isothermal temperature in question, when $P_{O_2}=0$, $\theta_0 \doteq 0.04$. These values in equation [4.88] gives

$$C = \frac{1}{\theta_0}f(\theta_0,T)$$

whence C can be evaluated. Putting this in equation [4.88] and dividing by K gives

$$\frac{P_{O_2}}{K} = \frac{f(\theta,T)}{\theta}\left(\frac{f(\theta,T)}{\theta} - \frac{f(\theta_o,T)}{\theta_o}\right) \qquad [4.89]$$

The right-hand side of equation [4.89] is a function of θ alone at a known constant temperature. By insetting values of θ from 0 to 0.04 the corresponding values of P_{O_2}/K can be obtained. Now, when plotting P_{O_2} against θ for trial value of K, a comparison can be made between the generated isotherms and the experimental value of P_{O_2} versus θ (cf. fig. (3.11)). Figs (4.11) to (4.13a) show such isotherms compared with experimental values. The solid lines correspond to the best K values and the broken lines indicate extreme values of K envelopping all experimental points.

It is immediately obvious that this treatment yields the correct s-shape of the experimentally obtained isotherm. The reason for this s-shape is that at high θ (and low P_{O_2}) there is an increased rate of oxygen loss due to step sites (cf. section 4.1.1d) and the steady-state value of θ at these low oxygen pressures is greater than that predicted by the equation $P_{O_2} = K/\theta^2$.

Plotting the log of the K values obtained in these isotherms against $1/T$ (fig. 4.14) should give a straight line whose gradient gives the enthalpy of the reaction

$$2^{s}O_x^x \rightleftharpoons 2^{s}V_o^+ + O_2(g) + 2^{s}e^-$$

using the relation

$$\frac{d\ln K_p}{d(1/T)} = -\frac{\Delta H^\circ}{k}$$

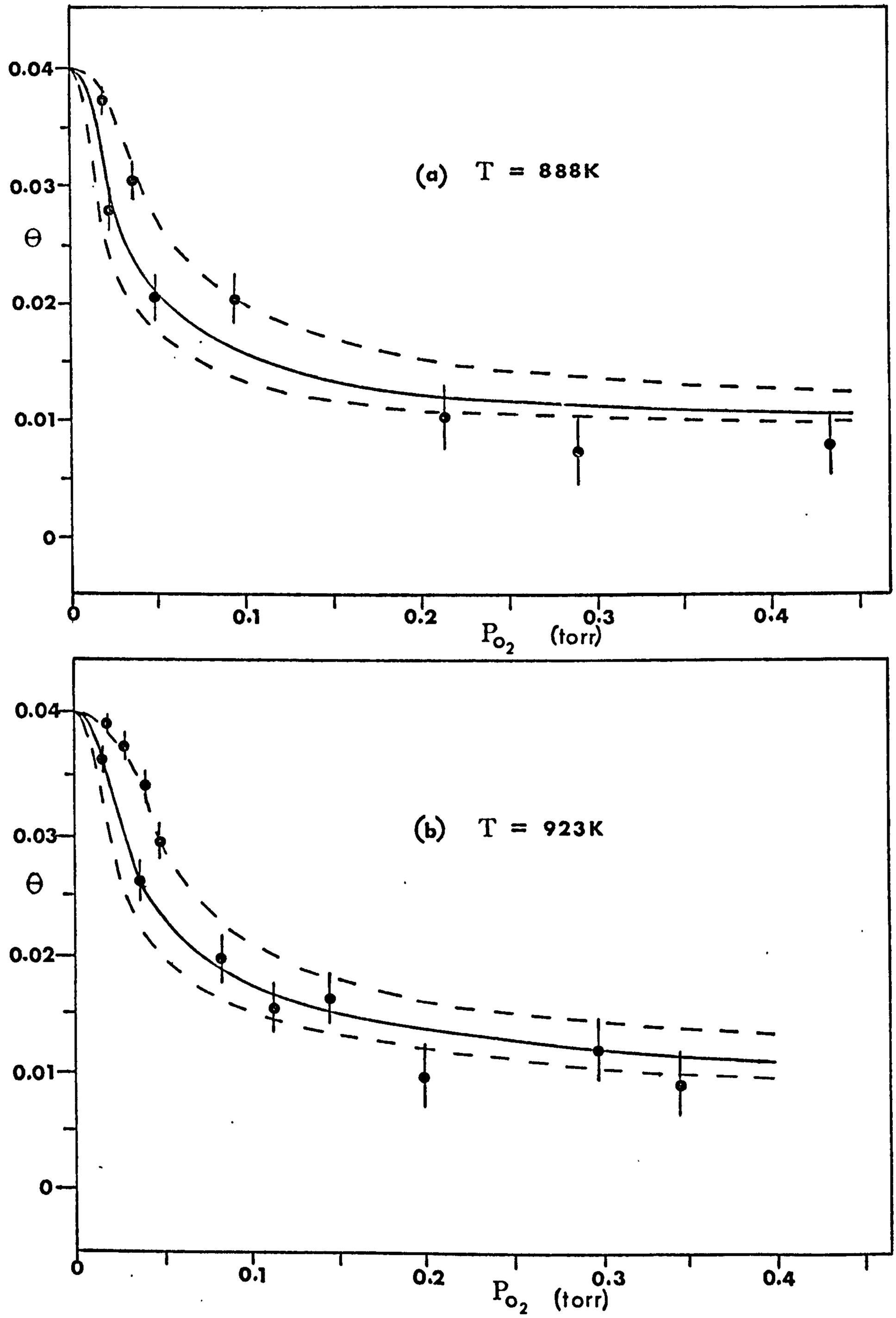

Fig. 4.11:

Theoretical variation of surface oxygen vacancy concentration, θ, with oxygen pressure, P_{O_2}, at steady-state isothermal conditions, compared with experimental values reproduced from fig. (3.11) (a) at T = 888 K, (b) at T = 923 K

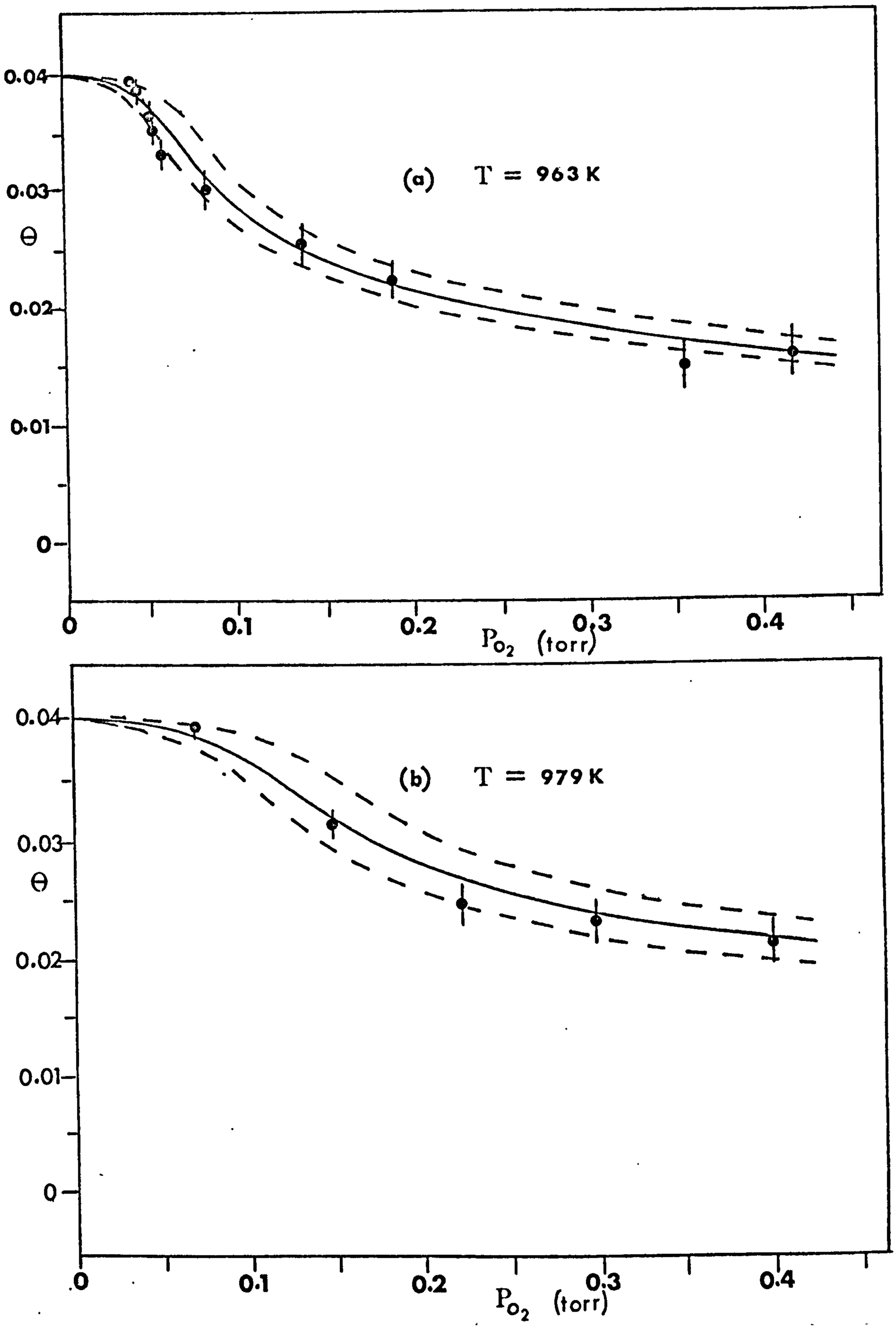

Fig. 4.12:

Theoretical variation of surface oxygen vacancy concentration, θ, with oxygen pressure, P_{O_2}, at steady-state isothermal conditions, compared with experimental values reproduced from fig. (3.11)

(a) at T = 963 K (b) at T = 979 K

Text cut off in original

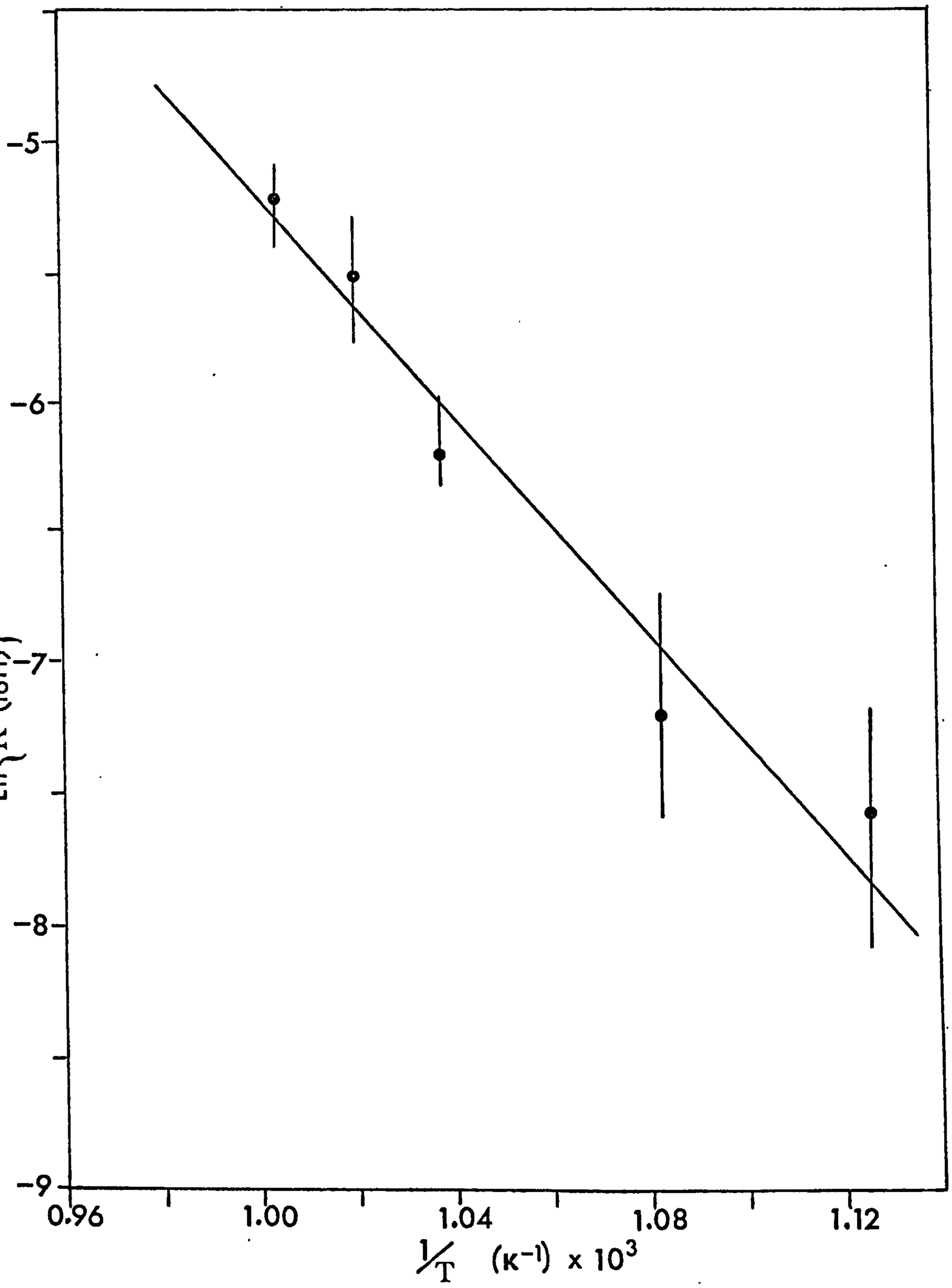

Fig. 4.14:

Temperature variation of the equilibrium constant for the reaction

$$2^{s}O_{x}^{x} \rightleftharpoons 2^{s}V_{o}^{\cdot\cdot} + 2^{s}e^{-} + O_{2}(g)$$

where K_p is the equilibrium constant in terms of pressure and ΔH° is the standard enthalpy of the reaction. The points in fig. (4.14) correspond to the best K values of figs (4.11) to (4.13a) and the error bars indicate the extreme values of K. The gradient gives an enthalpy of 1.83 ± 0.26 eV.

In fig. (4.13b) there is shown the approximate variation of the step site concentration versus θ corresponding to the chosen function $g(\theta)$ using the relation

$$g(\theta) = kT \ln(1 + \theta_{s.s.}\{\exp \Delta E/kT - 1\})$$

at T = 1000 K and with ΔE = 0.25 eV. This indicates an increasing surface step site concentration with increasing θ, flattening off at high θ. This suggests that the step site concentration reaches a maximum value of ca. 0.2. The shape of the function $g(\theta)$ required to give the best fit to the steady-state experimental data can be compared with those $g(\theta)$ functions used in the previous section for the T.P.D. data (cf. fig. (4.10)). The same general form for this function is observed; a steady increase in $g(\theta)$ commencing at θ = 0.01 to 0.02 when its value is $g(\theta) \doteqdot 0$ eV, up to θ = 0.04 when it reaches a maximum value of between $g(\theta) \doteqdot 0.12$ and $g(\theta) \doteqdot 0.18$ eV.

A summary of the role of surface step sites in the proposed steady-state reaction scheme, and the assumptions made in order to obtain a quantitative kinetic analysis is as follows. It is reasonable to assume that at constant temperature the total number of surface step sites is set by the relative rate of their formation (due to the zinc loss reaction of section 4.1.1c) and their destruction (when they are annealed out by movement of surface lattice atoms). Now, the rate of zinc loss at constant temperature is proportional to the surface oxygen

vacancy concentration. So, at constant temperature, the step site concentration should also be approximately proportional to the surface oxygen vacancy concentration. In addition, it is assumed that this proportionality is temperature insensitive, so that at temperatures between ca. 850 and 1100 K, $\theta_{s.s.}$ is approximately proportional to θ . Since this relation is assumed to be temperature insensitive then $g(\theta)$ is a function of θ alone as indicated.

4.1.3 Isotopic oxygen exchange: rate determining vacancy formation

O^{18} atoms are incorporated into the zinc oxide surface lattice by treating the surface with O^{18} enriched oxygen gas, as described in section 3.2.2. The gas was 15% O^{18} enriched, which means that at a total pressure, P_T , it contained $0.7225 P_T$ of O_2^{16} , $0.255 P_T$ of $O^{16}O^{18}$ and $0.0225 P_T$ of O_2^{18} .

Two equations describing the incorporation of O^{18} into the surface lattice can be written as follows

$$ {}^{s}O^{16}_{x} + O_2^{18}(g) \xrightarrow{k_{ex.}} {}^{s}O^{18}_{x} + O^{16}O^{18}(g) \qquad [4.90] $$

where the rate of incorporation of O^{18} , $(d[{}^{s}O^{18}_{x}]/dt)_1$ is given by

$$ (d[{}^{s}O^{18}_{x}]/dt)_1 = -dP_{O_2^{18}}/dt = k_{ex.}[{}^{s}O^{16}_{x}]\, P_{O_2^{18}} \qquad [4.91] $$

where k_{ex} is the exchange rate constant, and,

$$ {}^{s}O^{16}_{x} + O^{16}O^{18}(g) \xrightarrow{k_{ex}} {}^{s}O^{18}_{x} + O_2^{16}(g) \qquad [4.92] $$

where the rate of incorporation, $(d[{}^{s}O^{18}_{x}]/dt)_2$, is given by

$$\left(d[{}^{s}O^{18}_{x}]/dt\right)_2 = -\, dP_{O^{16}O^{18}}/dt = \tfrac{1}{2} k_{ex.}[{}^{s}O^{16}_{x}]\; P_{O^{16}O^{18}} \qquad [4.93]$$

where the factor ½ is included in the above equation to account for the fact that there is an equal chance of an O^{16} atom in O^{16} O^{18} (g) exchanging with the surface lattice ${}^{s}O^{16}_{x}$ with no net change in [${}^{s}O^{18}_{x}$]. The total rate of O^{18} incorporation is now given by

$$d[{}^{s}O^{18}_{x}]/dt = \left(d[{}^{s}O^{18}_{x}]/dt\right)_1 + \left(d[{}^{s}O^{18}_{x}]/dt\right)_2 = k_{ex.}[{}^{s}O^{16}_{x}]\left(P_{O_2^{18}} + \tfrac{1}{2}P_{O^{16}O^{18}}\right) \qquad [4.94]$$

Two equations describing the loss of O^{18} from the surface lattice can be written as follows

$${}^{s}O^{18}_{x} + O_2^{16}(g) \xrightarrow{k_{ex}} {}^{s}O^{16}_{x} + O^{16}O^{18}(g) \qquad [4.95]$$

where the rate of O^{18} loss from the surface lattice, $-\left(d[{}^{s}O^{18}_{x}]/dt\right)_1$ is given by

$$-\left(d[{}^{s}O^{18}_{x}]/dt\right)_1 = dP_{O^{16}O^{18}}/dt = k_{ex.}[{}^{s}O^{18}_{x}]\; P_{O_2^{16}} \qquad [4.96]$$

and,

$${}^{s}O^{18}_{x} + O^{16}O^{18}(g) \xrightarrow{k_{ex}} {}^{s}O^{16}_{x} + O_2^{18}(g) \qquad [4.97]$$

where the rate of O^{18} loss, $-\left(d[{}^{s}O^{18}_{x}]/dt\right)_2$, is given by

$$-\left(d[{}^{s}O^{18}_{x}]/dt\right)_2 = \tfrac{1}{2} k_{ex.}[{}^{s}O^{18}_{x}]\; P_{O^{16}O^{18}} \qquad [4.98]$$

where the factor ½ accounts for the equal chance that a gaseous O^{18} will exchange with the lattice $^sO^{18}_x$ with no net change in $[\ ^sO^{18}_x\ ]$. The total rate of O^{18} loss from the surface lattice is now given by

$$-d[^sO^{18}_x]/dt = k_{ex.}[^sO^{18}_x](P_{O_2^{16}} + \tfrac{1}{2}P_{O^{16}O^{18}}) \qquad [4.99]$$

At equilibrium, the rate of O^{18} incorporation into the surface lattice equals the rate at which it is lost from the surface lattice, and, combining equations [4.94] and [4.99] gives

$$\frac{[^sO^{18}_x]}{[^sO^{16}_x]} = \frac{P_{O_2^{18}} + \tfrac{1}{2}P_{O^{16}O^{18}}}{P_{O_2^{16}} + \tfrac{1}{2}P_{O^{16}O^{18}}} \qquad [4.100]$$

which gives

$$\frac{[^sO^{18}_x]}{[^sO^{16}_x]} = \frac{0.15}{0.85}$$

i.e. the same fraction of O^{18} in the surface lattice as in the gas phase.

Let us now consider the situation at low extent of exchange, i.e. far away from equilibrium when $[\ ^sO^{18}_x\ ] \ll 0.15N$, where N is the number of oxygen atoms per cm^2 on a $10\bar{1}0$ zinc oxide surface. In this case the rate of incorporation of O^{18} into the surface lattice, as given by equation [4.94], is much greater than its loss, as given by equation [4.99]. We consider the O^{18} incorporation reaction as the adsorption and incorporation into the lattice at surface oxygen vacancies. The rate of production of vacancies by oxygen loss from the surface lattice is, written in its simplest form,

$$2\,^sO^{16}_x \xrightarrow{k_1} 2\,^sV_o^+ + 2\,^se^- + O_2^{16}(g) \qquad [4.101]$$

where the loss of O^{18} from the surface lattice is not considered, since we are at the condition of $[\,{}^{s}O^{18}_{x}\,] \ll 0.15N$. The parallel zinc loss reaction is given by

$$ {}^{s}V_{o}^{+} + {}^{s}e^{-} \xrightarrow{k_2} {}^{s}O^{16}_{x} + Zn(g) \qquad [4.102] $$

Oxygen adsorption at vacancies, from a gas mixture containing O_2^{16} (g), $O^{16}\,O^{18}$ (g) and O_2^{18} (g) is given by the following three equations; for O_2^{16} (g) adsorption there is

$$ O_2^{16}(g) + 2\,{}^{s}V_{o}^{+} + 2\,{}^{s}e^{-} \xrightarrow{k_{-1}} 2\,{}^{s}O^{16}_{x} \qquad [4.103] $$

for $O^{16}\,O^{18}$ (g) adsorption there is

$$ O^{16}O^{18}(g) + 2\,{}^{s}V_{o}^{+} + 2\,{}^{s}e^{-} \xrightarrow{k_{-1}} {}^{s}O^{16}_{x} + {}^{s}O^{18}_{x} \qquad [4.104] $$

and O_2^{18} (g) adsorption there is

$$ O_2^{18}(g) + 2\,{}^{s}V_{o}^{+} + 2\,{}^{s}e^{-} \xrightarrow{k_{-1}} 2\,{}^{s}O^{18}_{x} \qquad [4.105] $$

whence from equations [4.104] and [4.105] the total rate of O^{18} surface incorporation is given by

$$ d[{}^{s}O^{18}_{x}]/dt = k_{-1}[{}^{s}V_{o}^{+}]^{2}\left(2P_{O_2^{18}} + P_{O^{16}O^{18}}\right) \qquad [4.106] $$

Now, at steady state in oxygen (but not steady state with respect to O^{18}/O^{16}) there is the condition

$$ d[{}^{s}V_{o}^{+}]/dt = 0 $$

whence, equating the rate of vacancy formation, as given by equation [4.101], with the rate of vacancy destruction, as given by equations [4.102] to [4.105] there is the relation

$$2k_1[{}^{s}O^{16}_{x}] = k_2[{}^{s}V_o^{+}] + 2k_{-1}[{}^{s}V_o^{+}]^2(P_{O_2^{16}} + P_{O^{16}O^{18}} + P_{O_2^{18}}) \qquad [4.107]$$

which is

$$2k_1[{}^{s}O^{16}_{x}] = k_2[{}^{s}V_o^{+}] + 2k_{-1}[{}^{s}V_o^{+}]^2 P_T \qquad [4.108]$$

Now, at low temperature (ca. 850 K to 1000 K) and high pressure of oxygen (above 0.1 torr) $k_2[{}^{s}V_o^{+}]$ is much smaller than $2k_1[{}^{s}O^{16}_{x}]$ and $2k_{-1}[{}^{s}V_o^{+}]^2P_T$ (cf. sections 4.1.1 and 4.1.2). Under these conditions equation [4.108] becomes

$$2k_1[{}^{s}O^{16}_{x}] = 2k_{-1}[{}^{s}V_o^{+}]^2 P_T \qquad [4.109]$$

which is the same as the equation $P_{O_2} = K/\theta^2$ where $K = k_1/k_{-1}$ (cf. equations [4.75a] and [4.86a] of section 4.1.2). Putting $k_{-1}[{}^{s}V_o^{+}]^2$ from equation [4.109] into equation [4.106] gives for the rate of O^{18} incorporation

$$d[{}^{s}O^{18}_{x}]/dt = k_1[{}^{s}O^{16}_{x}](2P_{O_2^{18}} + P_{O^{16}O^{18}})/P_T \qquad [4.110]$$

and comparison of this with equation [4.94] shows that

$$k_{ex.} = 2k_1/P_T \qquad [4.111]$$

i.e. that the overall exchange kinetics, for these conditions of low $[{}^{s}O^{18}_{x}]$ and low $[{}^{s}V_{O}^{+}]$ (low T and high P_{O_2}), are governed by the rate of vacancy formation and surface oxygen loss, whose rate constant is k_1.

At high temperature (above ca. 1000 K) and low oxygen pressure (less than 0.1 torr), $2k_1[{}^{s}O^{16}_{x}]$ and $k_2[{}^{s}V_{O}^{+}]$ are much larger than $k_{-1}[{}^{s}V_{O}^{+}]^2 P_T$ and equation [4.108], under these conditions, becomes

$$2k_1[{}^{s}O^{16}_{x}] = k_2[{}^{s}V_{O}^{+}] \qquad [4.112]$$

It has been shown (sections 4.1.1 and 4.1.2) that for these conditions of temperature and oxygen pressure the steady state concentration of surface lattice oxygen vacancies is close to its maximum value of $\theta = 0.04$ (cf. fig. (3.11)), that is

$$\theta = \frac{[{}^{s}V_{O}^{+}]}{[{}^{s}O^{16}_{x}]} = \frac{2k_1}{k_2} = 0.04 \qquad [4.113]$$

and the rate of O^{18} incorporation into the surface lattice, equation [4.106], is now determined by the adsorption rate, whence equation [4.106] becomes

$$d[{}^{s}O^{18}_{x}]/dt = k_{-1}\,(0.04)^2\,[{}^{s}O^{16}_{x}]^2\,(2P_{O_2^{18}} + P_{O^{16}O^{18}}) \qquad [4.114]$$

where the exchange rate constant $k_{ex.}$ of equation [4.94], for these conditions of low $[{}^{s}O^{18}_{x}]$ and $\theta = 0.04$ is given by

$$k_{ex.} = 2k_{-1}\,(0.04)^2[{}^{s}O^{16}_{x}] \qquad [4.115]$$

In the experiments described in section 3.2.2a the zinc oxide $10\bar{1}0$ surface is heated at a temperature between 820 K and 920 K in oxygen containing 15% O^{18} , at a total pressure between 0.1 and 0.4 torr. After evacuation of the system the oxygen T.P.D.'s at m/e 32, 34 and 36 are monitored simultaneously on the mass spectrometer and the area under each peak is measured. For the above pre-treatment conditions the steady state surface lattice oxygen vacancy concentration is low (cf. fig. (3.11)) and the exchange kinetics for $[\,^{s}O^{18}_{x}\,] \ll 0.15N$, are described by equation [4.111], i.e. determined by the vacancy formation rate.

For the homogeneous surface (single state) model described in section 3.2.2a, the ratio of peak areas for O_2^{18} , O^{16} O^{18} and O_2^{16} is given by equation [3.20], namely

$$A_{O_2^{18}}/A_{O_2^{18}} : A_{O^{16}O^{18}}/A_{O_2^{18}} : A_{O_2^{16}}/A_{O_2^{18}} = 1 : 2(1/y^{18}-1) : (1/y^{18}-1)^2 \qquad [4.116]$$

where y^{18} is the fractional atomic concentration of O^{18} in the surface lattice layer. This model assumes the free movement of atoms along the surface in the desorption process, where the probability of getting a molecule XY to form on the surface and be desorbed is proportional to the concentration of X times the concentration of Y in this mobile surface. This, then, is for the mobile atom mechanism of sections 4.1.1 and 4.1.2. That the same, above result is obtained for the vacancy-pair mechanism, where there is no free movement of atoms along the surface is shown in the appendix 4.2 of this chapter.

When the experimental peak area ratios $A_{O^{16}O^{18}}/A_{O_2^{18}}$ and $A_{O_2^{16}}/A_{O_2^{18}}$ are plotted against the gas phase fraction of O^{18} (from equation [3.21]) it was shown in section 3.2.2a that these experimental values do not agree with those predicted by this simple single state model.

Consider a heterogeneous surface made up of many types of surface lattice oxygen atom,each of different 'reactivity'. These surface lattice oxygen atom states can be numbered 1 to i. A term x_i of state i can be defined, which we call the 'reactivity' of state i, which gives the rate of vacancy formation, and hence oxygen evolution, from the surface lattice oxygen state i, relative to state i = 1 when the reactivity $x_1 = 1$. The reactivity of state i, x_i, relative to state j, x_j, is then given by the ratio of the rate constants for vacancy formation from these states by the relation

$$x_i/x_j = k_{1_i}/k_{1_j} \qquad [4.117]$$

which can be related to the difference in activation energy of vacancy formation by the relation

$$x_i/x_j = \exp -(E^{\ddagger}_i - E^{\ddagger}_j)/kT \qquad [4.118]$$

Let the fraction of the surface occupied by oxygen atoms in state i be P_i (noting that the total occupancy of these atom states is $P_i N$ per cm^2), where

$$\sum_i P_i = 1 \qquad [4.119]$$

Let the fractional atom concentration of O^{18} in state i be y_i^{18}, where $1 - y_i^{18}$ gives the fractional atom concentration of O^{16} in the same state.

In a model where all state 1 to i are randomly distributed on the surface, and, where free surface movement of atoms is allowed, (i.e. the mobile atom mechanism) we can evaluate the relative yields of .

desorbed O_2^{18} (g), $O^{16}\ O^{18}$ (g) and O_2^{16} (g) by the following 'counting procedure'.

(i) *Relative yield of O_2^{18} gas:* The relative probability that an O^{18} atom comes out of the surface lattice oxygen state i, and enters the mobile surface phase, is given by

$$P_i x_i y_i^{18}$$

This atom can now combine with an O^{18} atom in another state, j, where $j \neq i$, where the relative probability of this event is given by the relative probability of finding a state j with an O^{18} atom, $P_j y_j^{18}$. Hence the total relative probability of this 'cross-state' combination is $P_j y_j^{18} (P_i x_i y_i^{18})$.

Whence for all such 'cross-state' combinations the total relative probability is given by

$$\sum_{j \neq i} \left(P_j y_j^{18} \sum_i P_i x_i y_i^{18} \right) \qquad [4.120]$$

Equally, the O^{18} atom coming out of lattice state i can combine with another O^{18} atom in the same state i elsewhere on the surface, the relative probability of this event being given by

$$P_i y_i^{18} (P_i x_i y_i^{18})$$

and the otal relative probability of all such 'intra-state' combinations is then

$$\sum_i P_i^2 x_i (y_i^{18})^2 \qquad [4.121]$$

The total relative probability for all combinations, both 'cross-state' and 'intra-state' is then

$$\left[\sum_{j\neq i}\left(P_j\, y_j^{18}\ \sum_i P_i\, x_i\, y_i^{18}\right)\ +\ \sum_i P_i^2\, x_i\,(y_i^{18})^2\right]\ \propto\ A_{O_2^{18}}$$

which is proportional to the desorbed yield of O_2^{18} gas, i.e. $A_{O_2^{18}}$

(ii) *Relative yield of O^{16} O^{18} gas:* The relative probability that an O^{18} atom comes out of lattice state i and enters the mobile surface phase is given by

$$P_i\, x_i\, y_i^{18}$$

and that it now combines with an O^{16} atom in another state j, where $j \neq i$, is given by,

$$P_j(1-y_j^{18})(P_i\, x_i\, y_i^{18})$$

The total relative probability for all such 'cross-state' combinations is given by

$$\sum_{j\neq i}\left(P_j(1-y_j^{18})\ \sum_i P_i\, x_i\, y_i^{18}\right) \qquad [4.122]$$

Equally this O^{18} atom coming out of lattice state i can combine with an O^{16} atom in the same state i elsewhere on the surface. The total relative probability for all such'intra-state' combinations is

$$\sum_i P_i^2\, x_i\,(1-y_i^{18})\, y_i^{18} \qquad [4.123]$$

Also, an O^{16} atom can come out of lattice state i and enter the mobile surface phase, the relative probability of this being

$$P_i\, x_i\,(1-y_i^{18})$$

This O^{16} atom can combine with an O^{18} atom in another state j, where $j \neq i$, and the relative probability of this combination is

$$P_j\, y_j^{18}\,(P_i\, x_i(1-y_i^{18}))$$

and for all such 'cross-state' combinations it is

$$\sum_{j\neq i}\left(P_j\, y_j^{18} \sum_i P_i\, x_i\,(1-y_i^{18})\right) \qquad [4.124]$$

Equally, this O^{16} atom coming out of lattice state i can combine with an O^{18} atom in the same state i elsewhere on the surface. The total relative probability of all such 'intra-state' combinations is

$$\sum_i P_i^2\, x_i\,(1-y_i^{18})\, y_i^{18} \qquad [4.125]$$

Therefore, for both 'cross-state' and 'intra-state' combinations the total relative probability is given by

$$\left[\sum_{j\neq i}\left(P_j\,(1-y_j^{18})\sum_i P_i\, x_i\, y_i^{18}\right) + \sum_{j\neq i}\left(P_j\, y_j \sum_i P_i\, x_i\,(1-y_i^{18})\right) + 2\sum_i P_i^2\, x_i\,(1-y_i^{18})\, y_i^{18}\right] \propto A_{O^{16}O^{18}} \qquad [4.126]$$

which is proportional to the desorbed yield of $O^{16}\,O^{18}$ gas, i.e. $A_{O^{16}O^{18}}$

(iii) *Relative yield of O_2^{16} gas:* The relative probability that an O^{16} atom comes out of the surface lattice oxygen state i, and enters the mobile surface phase is given by

$$P_i\, x_i\,(1-y_i^{18})$$

and that it combines with another O^{16} atom in state j, where $j \neq i$, is

$$P_j\,(1-y_j^{18})\; P_i\, x_i\,(1-y_i^{18})$$

whence for all such 'cross-state' combinations the total relative probability is

$$\sum_{j\neq i}\left(P_j\,(1-y_j^{18})\sum_i P_i\, x_i\,(1-y_i^{18})\right) \qquad [4.127]$$

Equally, this O^{16} atom coming out of lattice state i can combine with another O^{16} atom in the same state i elsewhere on the surface, the relative probability of this event being given by

$$P_i^2 x_i (1-y_i^{18})^2$$

and for all such 'intra-state' combinations the total relative probability is given by

$$\sum_i P_i^2 x_i (1-y_i^{18})^2 \qquad [4.128]$$

The total relative probability for all combinations, both 'cross-state' and 'intra-state' is then

$$\left[\sum_{j \neq i} \left(P_j (1-y_j^{18}) \sum_i P_i x_i (1-y_i^{18}) \right) + \sum_i P_i^2 x_i (1-y_i^{18})^2 \right] \propto A_{O_2^{16}} \qquad [4.129]$$

which is proportional to the desorbed yield of O_2^{16} gas, i.e. $A_{O_2^{16}}$

(iv) '*Random distribution of States' model:* So, the desorbed yields of $O^{16}O^{18}$ and O_2^{16} can be expressed relative to the yield of O_2^{18} by the following relation

$$\frac{A_{O_2^{18}}}{A_{O_2^{18}}} : \frac{A_{O^{16}O^{18}}}{A_{O_2^{18}}} : \frac{A_{O_2^{16}}}{A_{O_2^{18}}} = 1 : \frac{\sum_{j \neq i} \left(P_j y_j^{18} \sum_i P_i x_i (1-y_i^{18}) \right) + \sum_{j \neq i} \left(P_j (1-y_j^{18}) \sum_i P_i x_i y_i^{18} \right) + 2 \sum_i P_i^2 x_i y_i^{18} (1-y_i^{18})}{\sum_{j \neq i} \left(P_j y_j^{18} \sum_i P_i x_i y_i^{18} \right) + \sum_i P_i^2 x_i (y_i^{18})^2} : \frac{\sum_{j \neq i} \left(P_j (1-y_j^{18}) \sum_i P_i x_i (1-y_i^{18}) \right) + \sum_i P_i^2 x_i (1-y_i^{18})^2}{\sum_{j \neq i} \left(P_j y_j^{18} \sum_i P_i x_i y_i^{18} \right) + \sum_i P_i^2 x_i (y_i^{18})^2} \qquad [4.130]$$

which can be simplified to give

$$\frac{A_{O_2^{18}}}{A_{O_2^{18}}} : \frac{A_{O^{16}O^{18}}}{A_{O_2^{18}}} : \frac{A_{O_2^{16}}}{A_{O_2^{18}}} = 1 : (\alpha - 2) : (1 + \beta - \alpha) \qquad [4.131]$$

where

$$\alpha = \frac{\sum_{j\neq i}\left(P_j y_j'^{8} \sum_i P_i x_i\right) + \sum_{j\neq i}\left(P_j \sum_i P_i x_i y_i'^{8}\right) + 2\sum_i P_i^2 x_i y_i'^{8}}{\sum_{j\neq i}\left(P_j y_j'^{8} \sum_i P_i x_i y_i'^{8}\right) + \sum_i P_i^2 x_i (y_i'^{8})^2} \qquad [4.132]$$

and

$$\beta = \frac{\sum_{j\neq i}\left(P_j \sum_i P_i x_i\right) + \sum_i P_i^2 x_i}{\sum_{j\neq i}\left(P_j y_j'^{8} \sum_i P_i x_i y_i'^{8}\right) + \sum_i P_i^2 x_i (y_i'^{8})^2} \qquad [4.133]$$

and where the fractional concentration of O^{18} in the desorbed gas, as given by equation [3.21], is

$$\frac{2A_{O_2}^{18} + A_{O^{16}O^{18}}}{2(A_{O_2}^{18} + A_{O^{16}O^{18}} + A_{O_2}^{16})} = \frac{\alpha}{2\beta} \qquad [4.134]$$

Equations [4.131] to [4.133] then describe the total relative desorbed gas yields using a model of the heterogeneous surface where there is a random distribution of atom states and where long range interatomic combinations are operative.

We can test this model by using, as a first approximation, a two-state surface configuration. In actual fact this is likely to closely resemble the real situation, since state 1 will be the oxygen atom at a perfect surface lattice site and state 2 will be a more reactive surface lattice oxygen atom (e.g. at a step site) occupying a small fraction of the surface. So, we can define state 1, occupying a fraction P_1 (where $P_1 \doteq 1$) of the surface, having a reactivity x_1 and a fractional concentration of O^{18} given by $y_1'^{8}$. State 2, the more reactive state, occupies a fraction P_2 of the surface and has a reactivity x_2. For the purpose of testing this model we consider the situation where state 2 is fully equilibrated with O^{16} , i.e. $y_2'^{8} = 0.15$. Putting these values of

P, α and y^{18} into equation [4.132] and [4.133] for the 'randomly-distributed states' model there is after rearrangement

$$\alpha = \frac{y_1^{18}(1+2P_1/P_2) + 0.15(x_2/x_1)(1+2P_2/P_1) + (x_2/x_1)\,y_1^{18} + 0.15}{y_1^{18}(0.15 + y_1^{18}(P_1/P_2)) + 0.15(x_2/x_1)(y_1^{18} + 0.15P_2/P_1)} \qquad [4.135]$$

and

$$\beta = \frac{1 + (P_1/P_2) + (x_2/x_1)(1 + P_2/P_1)}{y_1^{18}(0.15 + y_1^{18}(P_1/P_2)) + 0.15(x_2/x_1)(y_1^{18} + 0.15\,P_2/P_1)} \qquad [4.136]$$

Now, we can plot $A_{O^{16}O^{18}}/A_{O_2^{18}}$, given by $\alpha - 2$ in equation [4.131] versus gas phase atom fraction of O^{18}, given by $\alpha/2\beta$ in equation [4.134] for trial values of P_2/P_1 and x_2/x_1 and selected values of y_1^{18}. Four such plots are shown in fig. (4.15), curves 1 to 4. It can be seen that in all cases the ratio of $A_{O^{16}O^{18}}/A_{O_2^{18}}$ is greater than that predicted by the single state model (broken line) whereas the experimental points fall beneath the 'single state curve'. As the fractional occupancy of the more reactive state goes up, or as its relative reactivity increases the curve of $A_{O^{16}O^{18}}/A_{O_2^{18}}$ versus gas phase fraction of O^{18} moves further above the 'single-state curve'. As P_2/P_1 and x_2/x_1 get smaller and smaller the curve approaches the single state curve, until when P_2 and x_2 = 0 they meet the single state curve. These curves, however, never go below the single state curve, where the experimental values occur. This model is therefore rejected.

(v) *'Grouped states' model:* A model of a heterogeneous surface can be postulated where the different states are not randomly distributed, but where states of a like kind occur in groups, and, where only short range

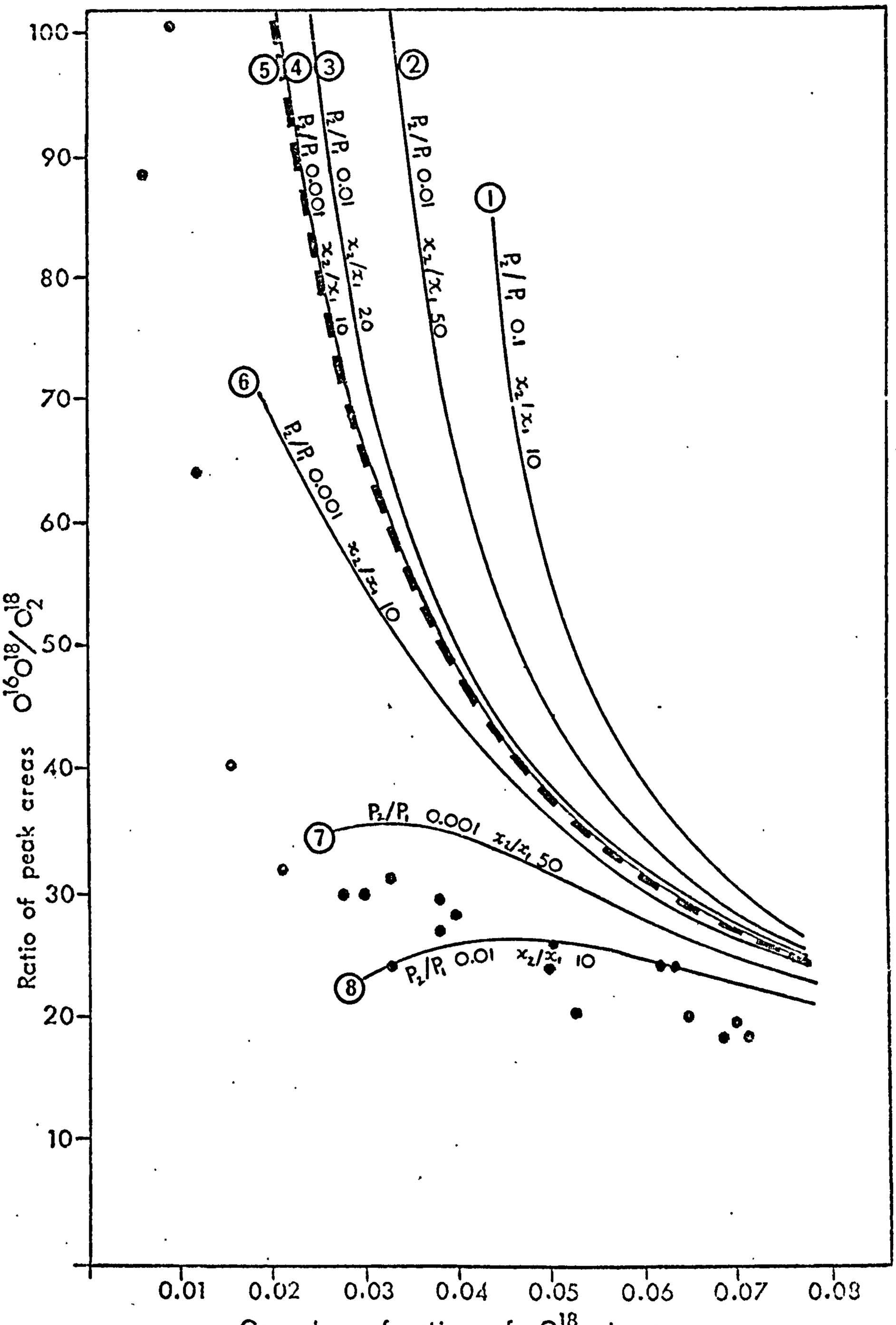

Fig. 4.15:

Theoretical variation of $A_{O^{16}O^{18}}/A_{O_2^{18}}$ with gas phase fraction of O^{18} atoms for:-

Curves 1 to 4 : 'randomly distributed states' model

Curves 6 to 8 : 'grouped states' model

Broken line : 'single state' model

- compared with experimental values reproduced from fig. (3.13)

inter-atomic combinations are allowed (in the limit this becomes surface lattice oxygen loss via the vacancy-pair mechanism). In this case the 'cross-state' combination terms in equation [4.130] become unimportant and can be neglected. In addition, the probability that, when an atom comes out of the lattice from state i, it combines with another atom in state i, is unity (since all like states are grouped together and only 'intra-state' combinations are considered); hence in equation [4.130] P_i^2 can be replaced by P_i for the 'intra-state' combination terms. In equation [4.131] we now have, therefore,

$$\alpha = \frac{2\sum P_i x_i y_i''}{\sum_i P_i x_i (y_i'^{8})^2} \qquad [4.137]$$

and

$$\beta = \frac{\sum P_i x_i}{\sum_i P_i x_i (y_i'^{8})^2} \qquad [4.138]$$

Again, we can test this model using the two states approximation. Putting for state 1, P_1, x_1 and $y_1'^{8}$ and for state 2, P_2, x_2 and $y_2'^{8}$ = 0.15 (for fully O^{18} equilibrated state 2), into equations [4.137] and [4.138] for α and β, we get after rearrangement

$$\alpha = \frac{2(y_1'^{8} + 0.15(P_2x_2/P_1x_1))}{((y_1'^{8})^2 + 0.15^2(P_2x_2/P_1x_1))} \qquad [4.139]$$

and

$$\beta = \frac{(1 + (P_2x_2/P_1x_1))}{((y_1'^{8})^2 + 0.15^2(P_2x_2/P_1x_1))} \qquad [4.140]$$

Now, a plot of $A_{O^{16}O^{18}}/A_{O_2^{18}}$, given by $\alpha-2$ in equation [4.131], versus gas phase atom fraction of O^{18}, given by $\alpha/2\beta$ in equation [4.134], can be made for trial values of P_2/P_1 and x_2/x_1 for selected values of y_1^{18}. Three such plots are shown in fig. (4.15), curves 6 to 8. It can be seen that in all cases the ratio of $A_{O^{16}O^{18}}/A_{O_2^{18}}$ is less than that predicted by the single state model, as indeed are the experimental values. As P_2/P_1 and x_2/x_1 tend towards zero so these values of $A_{O^{16}O^{18}}/A_{O_2^{18}}$ versus gas atom fraction of O^{18} tend to the single state curve. The best fit to the experimental values, using this two state model, is for P_2/P_1 = 0.01 and x_2/x_1 = 10 (curve 8, fig. (4.15)).

We are thus forced to the conclusion that our zinc oxide surface consists of groups or regions of reactive states occupying ca. 1% of the surface under these conditions of oxygen pre-treatment. This is consistent with arrays of steps on the surface. Furthermore, we conclude that surface lattice atom combinations yielding adsorbed molecules are extremely short range (in the limit - the vacancy-pair mechanism).

A full theoretical analysis using this model for the case when more than two types of state occur and for the case when the reactive states are not fully equilibrated with O^{18} follows below.

(vi) *'Grouped states' model - full analysis:* When the values for α and β of equations [4.137] and [4.138] are put into equation [4.131] the relation

$$\frac{A_{O_2^{18}}}{A_{O_2^{18}}} : \frac{A_{O^{16}O^{18}}}{A_{O_2^{18}}} : \frac{A_{O_2^{16}}}{A_{O_2^{18}}} = 1 : 2\left[\frac{\sum_i P_i x_i y_i^{18}}{\sum_i P_i x_i (y_i^{18})^2} - 1\right] : \left[\frac{\sum_i P_i x_i}{\sum_i P_i x_i (y_i^{18})^2} - 2\frac{\sum_i P_i x_i y_i^{18}}{\sum_i P_i x_i (y_i^{18})^2} + 1\right] \quad [4.141]$$

is obtained.

For a set pre-treatment in isotopic oxygen, the fractional concentration of O^{18} in state i, y_i^{18} , relative to the fractional concentration of O^{18} in state k, y_k^{18} , (when neither of these states is fully equilibrated with the gas phase, i.e. $y^{18} < 0.15$; see below) is given by

$$\frac{y_i^{18}}{y_k^{18}} = \frac{k_{1i}}{k_{1_k}} = \frac{x_i}{x_k} \qquad [4.142]$$

since the total amount of exchange into state i, in a fixed time is set by the exchange rate constant (equation [4.94]), which is proportional to the vacancy formation rate k_1 , (equation [4.111]).

The relative reactivities of all states i, x_i , can be referred to a defined standard state, $x_1 = 1$, when y^{18} is y_1^{18} . So, when $x_i = x_2$ the corresponding fractional atomic concentration of O^{18} in state 2, y_2^{18} , is equal to $x_2 y_1^{18}$: when $x_i = x_3$, $y_3^{18} = x_3 y_1^{18}$, and so on. Hence, equation [4.141] can be re-stated,using the relation $y_i^{18} = x_i y_1^{18}$, as

$$\frac{A_{O_2^{18}}}{A_{O_2^{18}}} : \frac{A_{O^{16}O^{18}}}{A_{O_2^{18}}} : \frac{A_{O_2^{16}}}{A_{O_2^{18}}} = 1 : 2\left[\frac{\sum_i P_i x_i^2}{y_1^{18}\sum_i P_i x_i^3} - 1\right] : \left[\frac{\sum_i P_i x_i}{(y_1^{18})^2\sum_i P_i x_i^3} - 2\frac{\sum_i P_i x_i^2}{y_1^{18}\sum_i P_i x_i^3} + 1\right] \qquad [4.143]$$

and the atom fraction of O^{18} in the gas phase is then given, using equation [3.21], by

$$\frac{y_1^{18}\sum_i P_i x_i^2}{\sum_i P_i x_i} \qquad [4.144]$$

Equation [4.143] defines the relative areas of the O_2^{18} , $O^{16}O^{18}$ and O_2^{16} peaks for all values of y_i^{18} where the state i is not yet fully exchanged, that is where $y_i^{18} < 0.15$. However, as more and more exchange takes place, the states of high reactivity (where i is large)

will become fully exchanged. Let us now re-define y_i^{18} from i = 1 to i = $\ell - 1$ where $x_i\, y_1^{18} = y_i^{18}$ is less than 0.15, and, y_ℓ^{18} for all ℓ ,(where $x_\ell\, y_1^{18} \geqslant 0.15$,) is equal to 0.15. Equation [4.143] can now be re-stated as follows

$$\frac{A_{O_2}^{19}}{A_{O_2}^{18}} : \frac{A_{O^{16}O^{18}}}{A_{O_2}^{18}} : \frac{A_{O_2}^{16}}{A_{O_2}^{18}} = 1 : 2\left[\frac{y_1^{18}\sum_i P_i x_i^2 + 0.15\sum_\ell P_\ell x_\ell}{(y_1^{18})^2\sum_i P_i x_i^3 + (0.15)^2\sum_\ell P_\ell x_\ell} - 1\right] : \left[\frac{\sum_i P_i x_i - 2y_1^{18}\sum_i P_i x_i^2 - 2(0.15)\sum_\ell P_\ell x_\ell}{(y_1^{18})^2\sum_i P_i x_i^3 + (0.15)^2\sum_\ell P_\ell x_\ell} + 1\right] \qquad [4.145]$$

where the atom fraction of O^{18} in the gas phase is now given by

$$\frac{y_1^{18}\sum_i P_i x_i^2 + 0.15\sum_\ell P_\ell x_\ell}{\sum_i P_i x_i} \qquad [4.146]$$

The histogram shown in fig. (4.16a) shows values of P_i at selected integral values of x_i . Using this histogram all the summations $\sum_i P_i x_i$, $\sum_i P_i x_i^2$ and $\sum_i P_i x_i^3$ can be evaluated. By putting a range of values of y_1^{18} into equations [4.143] and [4.144] curves of $A_{O^{16}O^{18}}/A_{O_2^{19}}$ and $A_{O_2^{16}}/A_{O_2^{18}}$ versus atom fraction of O^{18} in the gas phase can be obtained for the case when the states are not fully exchanged with O^{18} , and, putting values of y_1^{18} into equations [4.145] and [4.146] for the situation when the high reactivity states become fully exchanged. Curves of $A_{O^{16}O^{18}}/A_{O_2^{18}}$ and $A_{O_2^{16}}/A_{O_2^{18}}$ versus gas phase atom fraction of O^{18} are plotted in figs (4.17) and (4.18) together with experimental points reproduced from figs (3.13) and (3.14). These curves show a behaviour defined by equations [4.143] and [4.144], when none of the states are fully exchanged, below a value of 0.025 of the O^{18} gas phase atom fraction. At this value there is a marked inflexion when the high reactivity states are becoming fully exchanged, and above 0.025

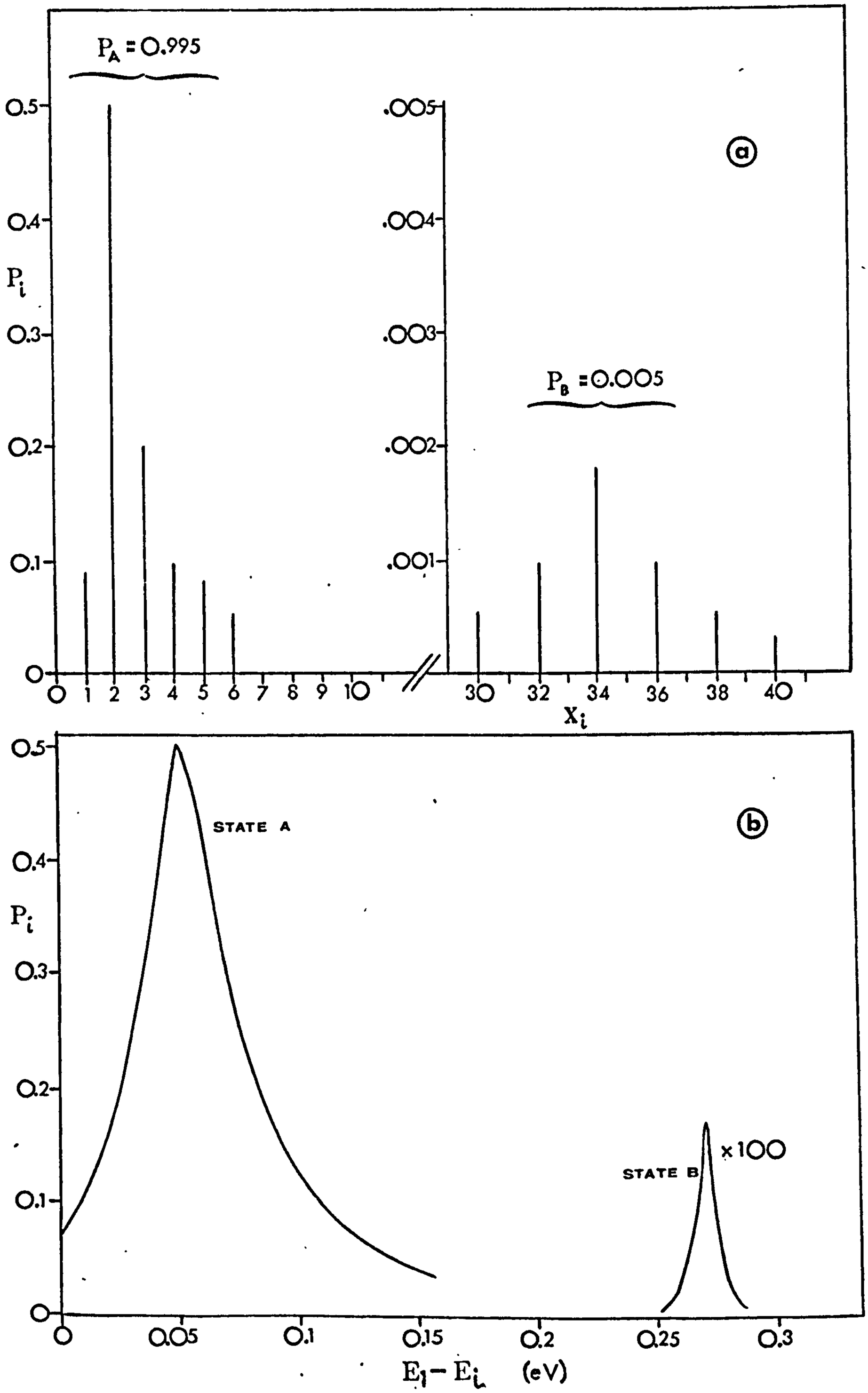

Fig. 4.16:

(a) Histogram of surface lattice oxygen atom states; reactivity against fractional surface population

(b) Density of surface lattice oxygen atom states.

equations [4.145] and [4.146] are used. At high values of O^{18} atom fraction the curves tend towards the single state curve, and, at a value of 0.15 they should meet it.

The histogram indicates that the states occur in two groups; group 'A' from $\mathcal{X}_i$ = 1 to 6 with a total surface fraction, P_A = 0.995, and, group 'B' from $\mathcal{X}_i$ = 30 to 40 with a total surface fraction P_B = 0.005. Similar histograms with P_B = 0.0075 and P_B = 0.003 were also used. The resulting $A_{O^{16}d^8}/A_{O_2^{18}}$ and $A_{O_2^{16}}/A_{O_2^{18}}$ versus O^{18} gas phase atom fraction curves are indicated by the dotted lines in figs (4.17) and (4.18). The histogram with P_B = 0.005 (solid line of figs (4.17) and (4.18) gives the best fit to experimental points, whilst the scatter of experimental values is approximately contained within the curves for P_B = 0.003 and 0.0075.

The histogram can be re-stated in terms of a density of states diagram by using the relationship between reactivity x_i and activation energy $E_i^{\neq}$ found in equation [4.118]. Fig. (4.16b) is such a diagram. Here the activation energy of state i, $E_i^{\neq}$, is compared to the activation energy of the defined standard state 1, $E_1^{\neq}$, by using equation [4.118], and putting k = 1 and $x_1 = 1$ then

$$kT \ln x_i = E_1^{\neq} - E_i^{\neq}$$

This shows that the activation energy for oxygen loss and vacancy formation from the two states differs by 0.225eV. If it is assumed that state A describes an oxygen at a normal surface lattice site then state B shows that a fraction of the surface oxygen atoms, 0.005 ± 0.002, are at sites where the activation energy for vacancy formation is 0.225eV less than the activation energy for vacancy formation from perfect surface lattice oxygen sites. This fits in well with the theory proposed in the previous sections (4.1.1 and 4.1.2) where it was shown that the activation energy for vacancy formation at a step site oxygen atom is

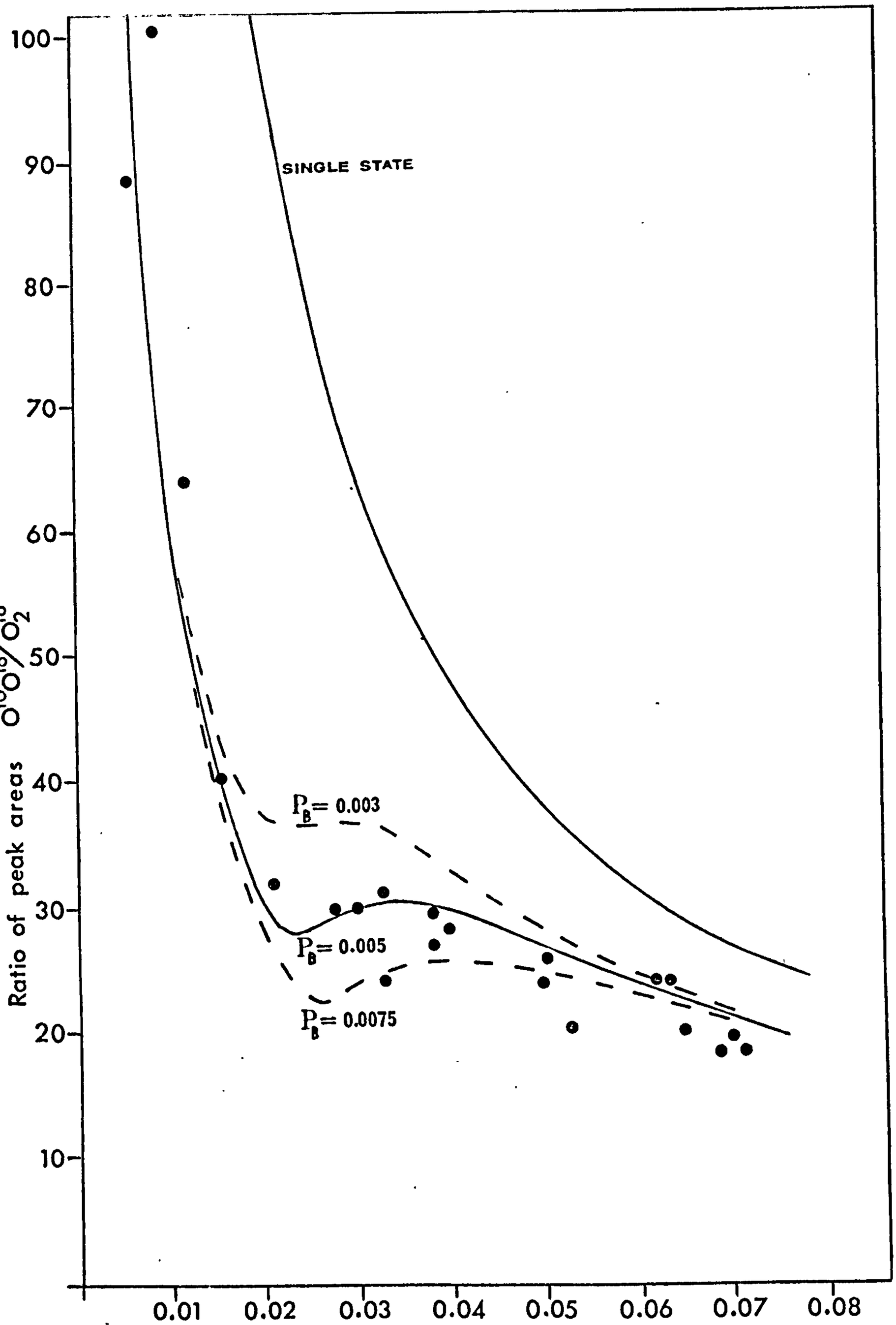

Fig. 4.17:

Theoretical variation of $A_{O^{16}O^{18}}/A_{O_2^{18}}$ with gas phase fraction of O^{18} atoms for 'grouped states' model evaluated using a histogram - distribution of states, compared with experimental values reproduced from fig. (3.13).

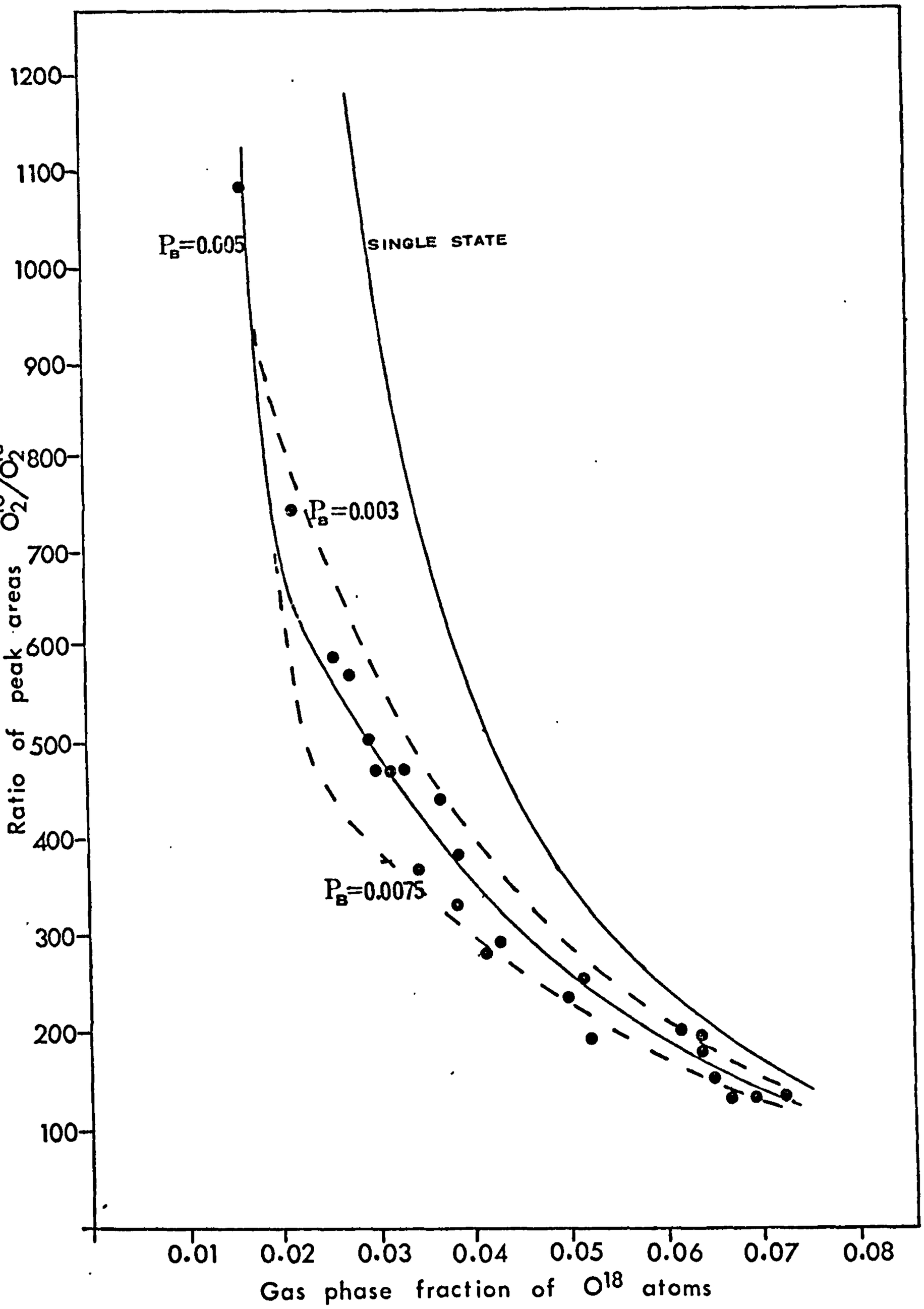

Fig. 4.18:

Theoretical variation of $A_{O_2^{16}}/A_{O_2^{18}}$ with gas phase fraction of O^{18} atoms for 'grouped states' model evaluated using a histogram distribution of states, compared with experimental values reproduced from fig. (3.14).

0.25 - 0.35eV less than the activation energy for vacancy formation at a perfect lattice oxygen site.

Many other distributions of α_i were tried but none was found to fit the experimental points of figs (4.17) and (4.18). Indeed, even when the distribution in fig. (4.16a) is approximated by one of two discreet states occurring at $\alpha_1 = 1$ and $\alpha_2 = 10$, the fit is not as good as for the 'many states' distribution (cf. fig. (4.19)). This would indicate that the spectrum of activation energies, shown in fig. (4.15b) is better than the discreet activation energies model, which one would intuitively expect to be the case.

Similar histograms to that shown in fig. (4.15a), but using more values of α_i were shown hardly to affect the results obtained, and it is sufficient to use histograms as indicated, with 12 integral values of α_i.

(vii) *Summary:* It has been shown in this section that, for an oxygen T.P.D. spectrum where only one peak, and hence one activation energy state, can be resolved, by pre-treatment in isotopic oxygen followed by taking T.P.D. spectra of O_2^{18}, $O^{16}O^{18}$ and O_2^{16}, a second state, with a very small fractional concentration and only a slightly different activation energy, can be resolved.

This technique and analysis can, in principle, be applied generally to any surface-gas adsorption problem, where it is suspected that two or more states may occur, but which cannot be resolved by a standard T.P.D. procedure.

In addition we have been able to differentiate between two entirely different surface state configurations, one where reactive surface oxygen states are randomly distributed on the surface, and the other where the reactive surface oxygen states are grouped together. If the reactive oxygen surface atoms identified in this analysis are indeed step site

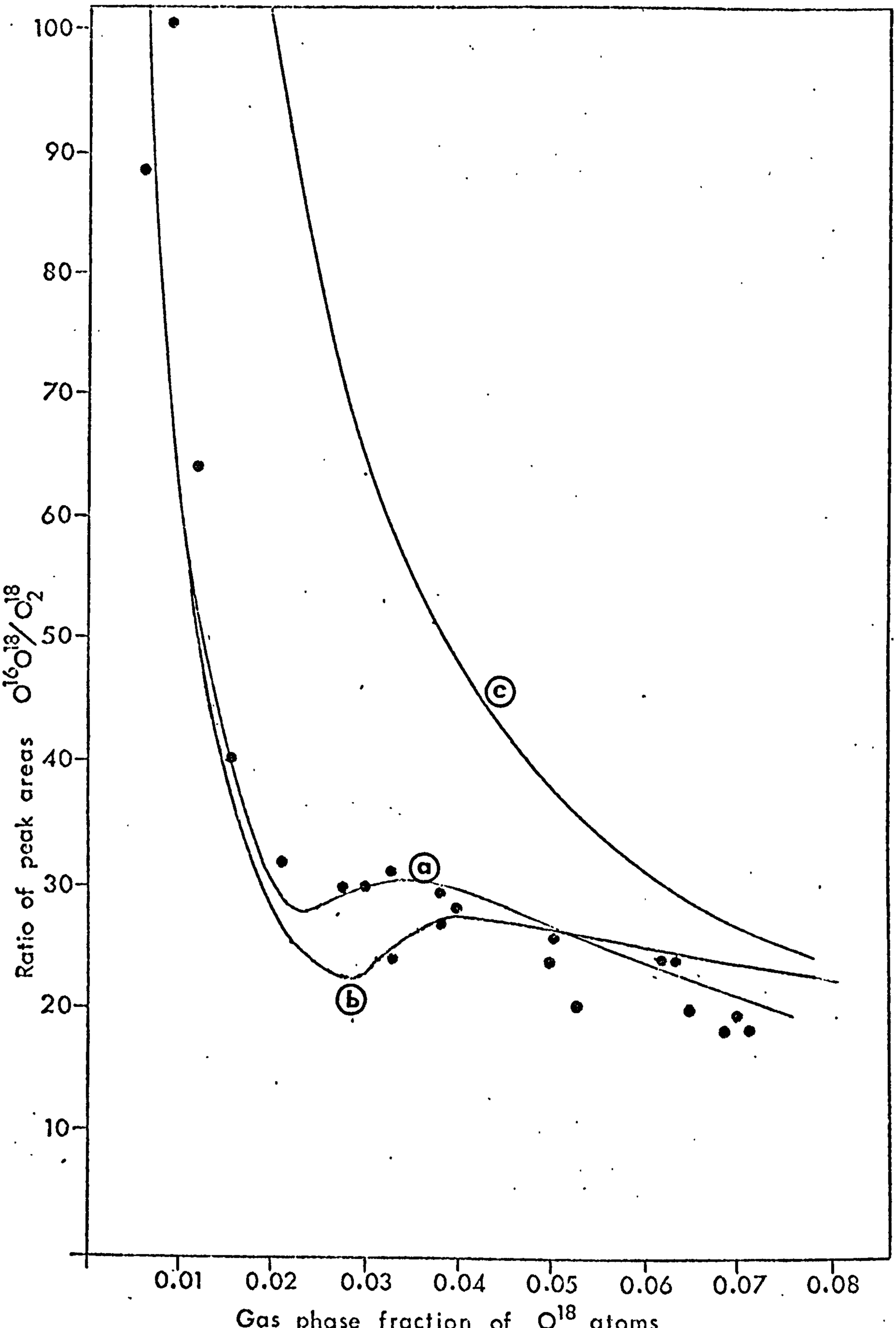

Fig. 4.19:

Theoretical variation of $A_{O^{16}O^{18}}/A_{O_2^{18}}$ with gas phase fraction of O^{18} atoms for 'grouped states' model,

(a) using histogram distribution of states

(b) using two state model

(c) using single state model

- compared with experimental values reproduced from fig. (3.13).

oxygen atoms, then it has been shown that these steps occur in groups or arrays on the $10\bar{1}0$ zinc oxide surface. We can also infer from this treatment that interatomic combinations arise from short range interactions, and that, of the two mechanisms described in sections 4.1.1 and 4.1.2, the vacancy-pair mechanism is preferred.

4.1.4 Isotopic oxygen exchange: rate determining oxygen adsorption

In the previous section it was shown how, at different pre-treatment conditions of temperature and isotopic oxygen pressure, the kinetics of the exchange process can change.

In section 3.2.2b there are described temperature transient isotopic exchange experiments at temperatures between 800 K and 1200 K, and oxygen pressures below ca. 0.1 torr. It has been shown (sections 4.1.1 and 4.1.2) that the surface lattice oxygen vacancy concentration is constant at a value of $\theta = 0.04$, and that the exchange kinetics are determined by the rate of oxygen adsorption onto the surface (section 4.1.3), under these conditions of temperature and pressure. Equation [4.104] describes the adsorption of $O^{16}O^{18}$ gas over surface oxygen vacancies and subsequent incorporation into the lattice destroying the vacancies. This gives for the rate of adsorption of $O^{16}O^{18}$

$$dP_{O^{16}O^{18}}/dt = k_{-1}\,[{}^{s}V_O^{+}]^2\,P_{O^{16}O^{18}} \qquad [4.147]$$

when the total extent of surface exchange is small, i.e. when $[{}^{s}O_x^{18}] \ll 0.15N$

This is very approximately equal to the rate of incorporation of O^{18} into the surface lattice described by equation [4.106], since $P_{O^{16}O^{18}} > 2P_{O_2^{18}}$

Using equation [4.147] and a constant value of $\theta = [{}^{s}V_O^{+}]/N = 0.04$, the rate of adsorption of $O^{16}O^{18}$ is given by

$$dP_{O^{16}O^{18}}/dt = k_{-1}\,(0.04)^2\,N^2\,P_{O^{16}O^{18}} \qquad [4.148]$$

Equation [4.148] describing the adsorption rate limiting exchange kinetics can be expressed in a more general form, namely

$$dN_{O^{16}O^{18}}/dt = \left(\frac{\sigma}{\sqrt{2\pi m k T}}\right) P_{O^{16}O^{18}}\ f(\theta)\ exp-\frac{\Delta E^{\ddagger}_{ads}(eV)}{kT} \qquad [4.149]$$

(the general equation for direct activated adsorption as in Hayward and Trapnell, 1964) where $dN_{O^{16}O^{18}}/dt$, molecules $cm^{-2}\ s^{-1}$ is the exchange rate, σ the sticking coefficient, m the mass of $O^{16}O^{18}$, $P_{O^{16}O^{18}}$ the pressure of $O^{16}O^{18}$ $f(\theta)$ is a function of the number of available adsorption sites, in our case $f(\theta) = \theta^2 = (0.04)^2$, $\Delta E^{\ddagger}_{ads}$ is the activation energy to adsorption. All other symbols have their usual meaning. This can be rearranged to give

$$ln\left(\frac{dN_{O^{16}O^{18}}}{dt}.\ P^{-1}_{O^{16}O^{18}}\right) = ln C\theta^2 - \frac{\Delta E^{\ddagger}_{ads}(eV)}{kT} \qquad [4.150]$$

where all constant terms are collected into constant C. ($\sqrt{2\pi m k T}$ is very slowly varying in T compared to the exponential, and is approximately constant over our temperature range.)

The data in fig. (3.15) shows values of $dN_{O^{16}O^{18}}/dt$ and $P_{O^{16}O^{18}}$ changing under temperature transient conditions. Assuming that the rate of change of temperature with time is sufficiently slow, then the exchange rate can be said to be at pseudo-steady-state at all times and equation [4.111] can be applied. Both C and $\Delta E^{\ddagger}_{ads}$ can be obtained from a plot of $ln(\ dN_{O^{16}O^{18}}/dt\ .\ P^{-1}_{O^{16}O^{18}}\ )$ versus $1/T$. Such a plot is shown in fig. (4.20) using the data shown in fig. (3.15). The gradient gives a value for $\Delta E^{\ddagger}_{ads}$ of 1.21 ± 0.04eV, and the intercept at $1/T = 0$ gives for C a value of (1.6 ± 1.0) x 10^{20} molecules $cm^{-2}\ s^{-1}$ $torr^{-1}$ (since θ is constant at 0.04).

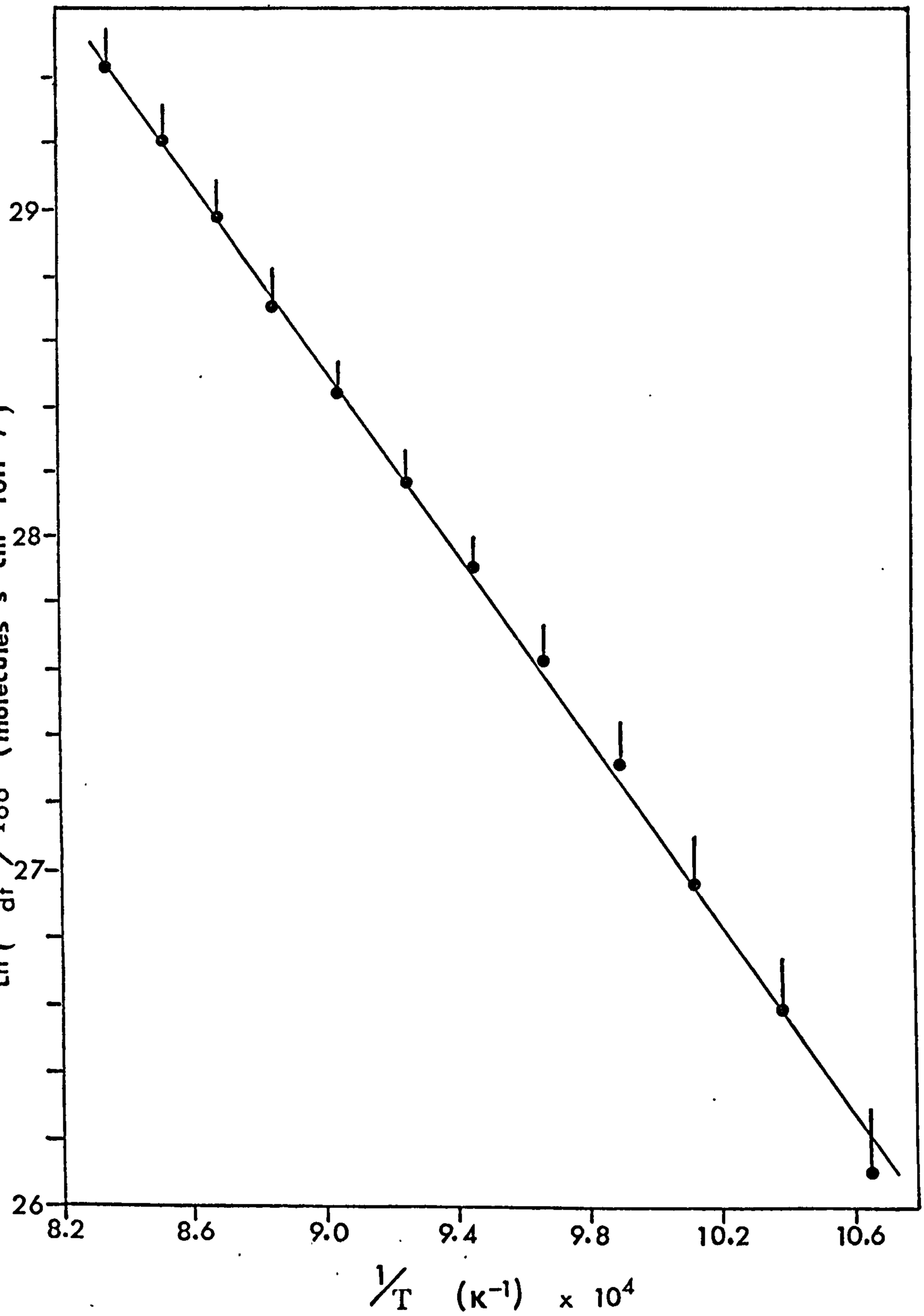

Fig. 4.20:

Arrhenius plot of the log of the rate of $O^{16}O^{18}$ incorporation normalised to constant O^{16} O^{18} pressure, versus 1/T

That the reaction is in fact under pseudo-steady-state conditions has been shown by performing several temperature transient experiments using different heating rates from 0.02 K s^{-1} to 0.2 K. s^{-1} . Using these heating rates the experimental data gave a straight line Arrhenius plot (equation [4.150]) with an activation energy very close to 1.17eV, in all cases. Were the exchange reaction not at steady state for these heating rates one would expect a non-linear Arrhenius plot with an activation energy changing with changing heating rate. As a check of the pseudo-steady-state condition a second type of exchange experiment was performed, as described in section 3.2.2b. In this experiment, the amount of $O^{16}O^{18}$ exchanged was monitored for a fixed time at a set temperature and constant $P_{O^{16}O^{18}}$. By plotting the amount exchanged in this fixed period of time and at constant pressure of $O^{16}O^{18}$ against $1/T$, a straight line, whose gradient gives $\Delta E^{\ddagger}_{ad}$, should be obtained. Such a plot is shown in fig. (4.21). The large error bars occur because of the uncertainty in the value of the number of molecules $O^{16}O^{18}$ exchanged - see section 3.2.2b. The gradient gives a value for $\Delta E^{\ddagger}_{ads}$ of 1.18 ± 0.08eV which is very close to the value obtained earlier.

The equation relating the rate of adsorption with pressure, P, torr , can be written

$$dN/dt = \frac{(1.6 \pm 1.0)\times 10^{20}}{6 \times 10^{14}} \theta^2 P \exp - \frac{(1.21 \pm 0.04)\ eV}{kT} \qquad [4.151]$$

where dN/dt is the rate of adsorption in molecules s^{-1} per surface atom. This can be compared with the rate of vacancy formation given in section 4.1.1

$$d\theta/dt = 5.2 \times 10^{13} \exp - \frac{3.5(eV)}{kT} \qquad [4.152]$$

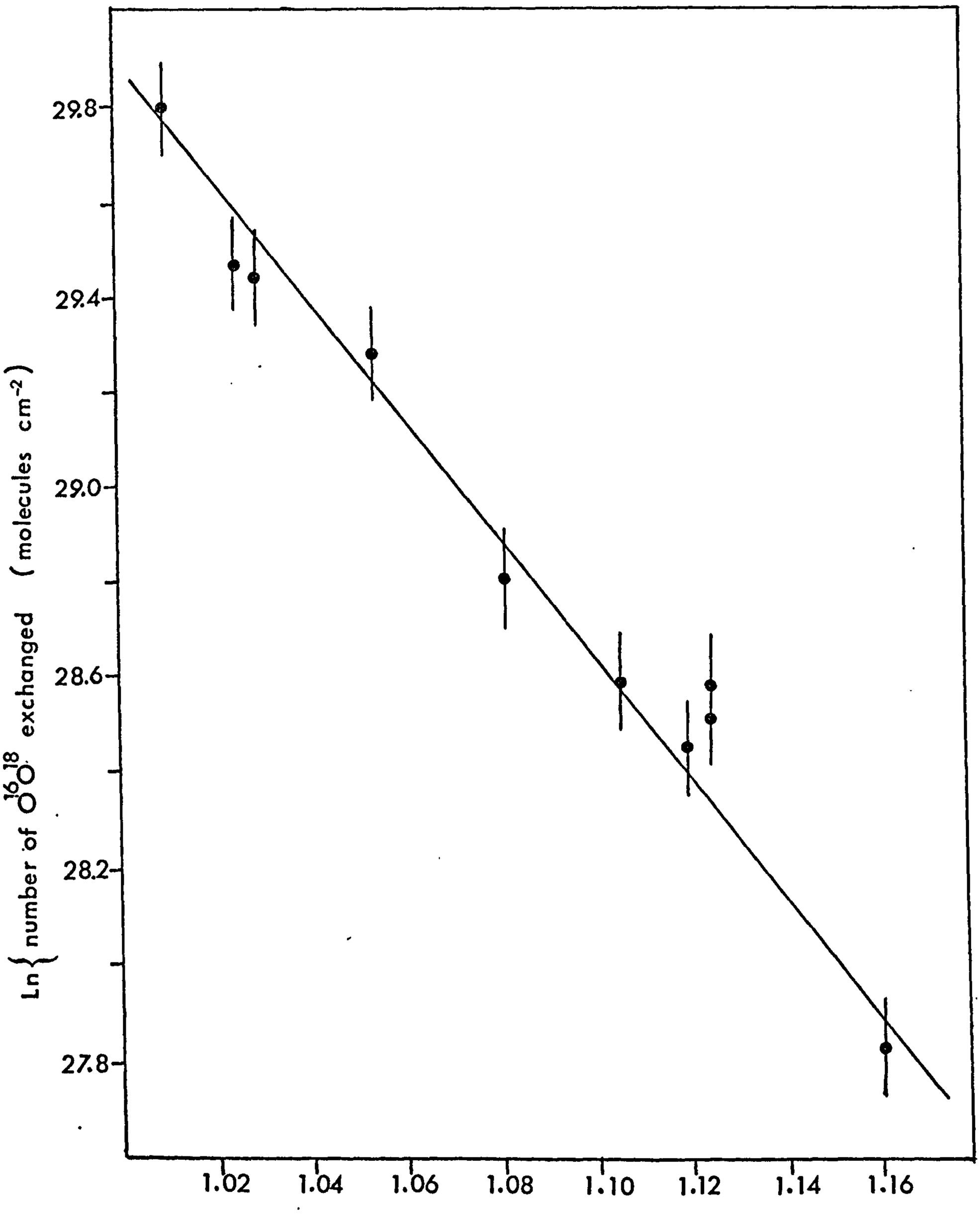

Fig. 4.21:

Log of the amount of O^{16} O^{18} incorporated in a fixed time and constant pressure, versus 1/T

where the activation energy is given as approximately 3.5eV, neglecting its Θ variation which is not important for this comparison.

At P = 0.1 torr and T = 900 K, the adsorption rate is 6.9×10^{-6} molecules s^{-2} (surface atom)$^{-1}$ and the vacancy formation rate is 1.2×10^{-6} s^{-1} . Under these conditions the vacancy formation rate is slower and the exchange kinetics are determined by the vacancy formation rate - see section 4.1.3. At P = 10^{-2} torr and T = 900 K the adsorption rate is 6.9×10^{-7} molecules s^{-1} (surface atom)$^{-1}$ and the vacancy formation rate is 1.2×10^{-6} s^{-1} . Now the exchange kinetics are determined by the adsorption rate. At P = 0.1 torr but T = 1000 K the adsorption rate is 3.31×10^{-5} molecules s^{-1} (surface atom)$^{-1}$ and the vacancy formation rate is 1.10×10^{-4} . Once again exchange kinetics are determined by the adsorption kinetics. So, the criterion for the assumptions made in section 4.1.3, that at high temperature and low oxygen pressure the exchange kinetics are determined by adsorption rate, and, that at lower temperatures and high oxygen pressure vacancy formation is the rate determining step, appears by the above analysis to be substantiated.

The value of $\Delta E^{\neq}_{ads}$, marked on fig. (4.4) should be given by the difference between the total activation energy for vacancy formation ($\Delta H^{0\neq}_{1,2A}$ for the vacancy-pair mechanism and $\Delta H^{0\neq}_{1,2B}$ for the mobile atom mechanism) and the overall enthalpy of the gaseous oxygen/surface vacancy interaction, ΔH^{0}.

$\Delta H^{0\neq}_{1,2A}$ is 3.47eV and $\Delta H^{0\neq}_{1,2B}$ is 3.53eV, from section 4.1.1 and ΔH^{0} 1.83 ± 0.26eV from section 4.1.2. All these values are at zero Θ, i.e. when there are no surface vacancies. Using a value of 3.5eV for the activation energy of vacancy formation this gives, for $\Delta E^{\neq}_{ads}$, a value given by the relation

$$\Delta E^{\neq}_{ads} = \Delta H^{0\neq}_{1,2} - \Delta H^{0} \qquad [4.153]$$

of 1.67 ± 0.26eV, at $\Theta = 0$. The value obtained in this section, $\Delta E^{\neq}_{ads} = (1.21 \pm 0.04)$eV is for $\Theta = 0.04$. Now, fig. (4.4) indicates that the adsorption activation energy $\Delta E^{\neq}_{ads}$ is Θ dependent, decreasing with increasing Θ. So, to obtain a value for $\Delta E^{\neq}_{ads}$ at $\Theta = 0$ one must use the relation

$$\Delta E^{\neq}_{ads}(\Theta=0) = \Delta E^{\neq}_{ads}(\Theta=0.04) + 3.25\,\Theta^{0.8}$$

for the vacancy-pair mechanism, and

$$\Delta E^{\neq}_{ads}(\Theta=0) = \Delta E^{\neq}_{ads}(\Theta=0.04) + 1.62\,\Theta^{0.8}$$

for the mobile atom mechanism. This gives values for $\Delta E^{\neq}_{ads}(\Theta=0)$ of 1.46 ± 0.04eV and 1.33 ± 0.04eV respectively. These compare well with the value of 1.67 ± 0.26eV obtained from the difference between vacancy formation activation energy and overall enthalpy.

4.1.5 Nitrous oxide decomposition over zinc oxide single crystals

It is shown that the mechanism for nitrous oxide decomposition is consistent with a charge transfer adsorption of nitrous oxide onto a surface oxygen vacancy site at which it decomposes. So, the rate of vacancy formation, as discussed in section 4.1.1, must be included in the reaction mechanism. Hence, the first step is the formation of an adsorbed oxygen/vacancy complex

$$^{s}O_{x}^{x} \quad \underset{}{\overset{K_1}{\rightleftharpoons}} \quad ^{s}V_{o}^{+}\ldots\ldots O^{-} \qquad \ldots\ldots\ldots\ldots\ldots\ldots \text{step 1}$$

followed by its disassociation to form oxygen and a bare vacancy. The detailed mechanism of this process, as discussed in section 4.1.1, is not required here, and for simplicity the overall step is used, namely

$$^{s}V_{o}^{+}\ldots\ldots O^{-} \xrightarrow{k_2} \tfrac{1}{2}O_2(g) + {}^{s}V_{o}^{+} + {}^{s}e^{-} \qquad \ldots\ldots\ldots \text{step 2}$$

The parallel surface zinc loss reaction is as before, viz.,

$$^{s}V_{o}^{+} + {}^{s}e^{-} \xrightarrow{k_3} {}^{s}O_{x}^{x} + Zn(g) \qquad \ldots\ldots\ldots\ldots \text{step 3}$$

and the zinc condensed in a cooler part of the reaction chamber is oxidised by nitrous oxide according to the following reaction

$$Zn(s) + N_2O(g) \xrightarrow{k_4} ZnO(s) + N_2(g) \qquad \ldots\ldots\ldots \text{step 4}$$

whence the zinc oxide so produced takes no further part in the reaction.

The mechanism of nitrous oxide decomposition at surface oxygen vacancy sites can now be formulated as a pseudo-equilibrium between gas phase nitrous oxide and an adsorbed nitrous oxide complex, viz.,

$$^{s}V_o^{+} + {}^{s}e^{-} + N_2O(g) \underset{k_{-5}}{\overset{k_5}{\rightleftharpoons}} {}^{s}V_o^{+}\cdots N_2O^{-} \qquad \text{.....step 5}$$

followed by decomposition of this adsorbed complex, which is given by the equation below, namely

$$^{s}V_o^{+}\cdots N_2O^{-} \xrightarrow{k_6} {}^{s}V_o^{+}\cdots O^{-} + N_2(g) \qquad \text{.....step 6}$$

leaving an oxygen/vacancy surface complex; whereupon this oxygen can either go back into the surface lattice via step 1, or go into the gas phase via step 2 of this reaction mechanism.

Material balance for the gas phase gives

$$2\, dP_{O_2}/dt = k_2[{}^{s}V_o^{+}\cdots O^{-}] \qquad [4.154]$$

and

$$dP_{N_2}/dt = k_6[{}^{s}V_o^{+}\cdots N_2O^{-}] + k_4 P_{Zn} P_{N_2O} \qquad [4.155]$$

also,

$$dP_{Zn}/dt = k_3[{}^{s}V_o^{+}] - k_4 P_{Zn} P_{N_2O} = 0 \qquad [4.156]$$

where, as before, the surface electron activity is taken as constant.

Combining equations [4.155] and [4.156] yields

$$dP_{N_2}/dt = k_6[{}^{s}V_o^{\cdot\cdot}\cdots N_2O^-] + k_3[{}^{s}V_o^{\cdot\cdot}] \qquad [4.157]$$

Material balance for the surface phase gives

$$d[{}^{s}V_o^{\cdot\cdot}\cdots O^-]/dt = k_1[{}^{s}O_x^x] + k_6[{}^{s}V_o^{\cdot\cdot}\cdots N_2O^-] - k_{-1}[{}^{s}V_o^{\cdot\cdot}\cdots O^-] - k_2[{}^{s}V_o^{\cdot\cdot}\cdots O^-] = 0 \qquad [4.158]$$

and, at steady state

$$d[{}^{s}O_x^x]/dt = k_3[{}^{s}V_o^{\cdot\cdot}] + k_{-1}[{}^{s}V_o^{\cdot\cdot}\cdots O^-] - k_1[{}^{s}O_x^x] = 0 \qquad [4.159]$$

Putting equation [4.154] and [4.159] into [4.158] gives

$$2\,dP_{O_2}/dt = k_6[{}^{s}V_o^{\cdot\cdot}\cdots N_2O^-] + k_3[{}^{s}V_o^{\cdot\cdot}] \qquad [4.160]$$

which when compared with [4.157] yields

$$2\,dP_{O_2}/dt = dP_{N_2}/dt = k_6[{}^{s}V_o^{\cdot\cdot}\cdots N_2O^-] + k_3[{}^{s}V_o^{\cdot\cdot}] \qquad [4.161]$$

Also, at steady state

$$d[{}^{s}V_o^{\cdot\cdot}\cdots N_2O^-]/dt = k_5[{}^{s}V_o^{\cdot\cdot}]\,P_{N_2O} - k_{-5}[{}^{s}V_o^{\cdot\cdot}\cdots N_2O^-] - k_6[{}^{s}V_o^{\cdot\cdot}\cdots N_2O^-] = 0 \qquad [4.162]$$

whence this in equation [4.161] yields

$$2\,dP_{O_2}/dt = dP_{N_2}/dt = \frac{k_6 k_5[{}^{s}V_o^{\cdot\cdot}]\,P_{N_2O}}{k_6 + k_{-5}} + k_3[{}^{s}V_o^{\cdot\cdot}] \qquad [4.163]$$

Now, the equation for site conservation gives the total number of surface sites, C, which is a constant, by

$$C = [{}^{s}O_X^X] + [{}^{s}V_O^+ \cdots O^-] + [{}^{s}V_O^+] + [{}^{s}V_O^+ \cdots N_2O^-] \qquad [4.164]$$

which with equation [4.162] gives

$$C - [{}^{s}O_X^X] - [{}^{s}V_O^+ \cdots O^-] = [{}^{s}V_O^+]\left(1 + \frac{k_5 P_{N_2O}}{k_{-5} + k_6}\right) \qquad [4.165]$$

The term on the left-hand side of equation [4.165] is the total maximum number of bare vacancies on the zinc oxide surface, N ($P_{N_2O} = 0$, this is a constant $\theta = 0.04$, cf. section 4.1.1). So the total number of bare vacancies at which nitrous oxide can adsorb at pressure P_{N_2O} is given by

$${}^{s}V_O^+ = \frac{N}{\left(1 + \frac{k_5 P_{N_2O}}{k_{-5} + k_6}\right)} \qquad [4.166]$$

which in equation [4.163] gives

$$2\,dP_{O_2}/dt = dP_{N_2}/dt = \frac{N\left(\frac{k_6 k_5 P_{N_2O}}{k_{-5} + k_6} + k_3\right)}{\left(1 + \frac{k_5 P_{N_2O}}{k_{-5} + k_6}\right)} \qquad [4.167]$$

Equation [4.167] is the most general form of the rate equation, but its form can be simplified in a manner dependent on the relative values of its constituent rate constants and of nitrous oxide pressure.

When $k_{-5} \gg k_6$, that is rate determining adsorbed complex decomposition, equation [4.167] simplifies to

$$2\,dP_{O_2}/dt = dP_{N_2}/dt = \frac{N(k_6 K_5 P_{N_2O} + k_3)}{1 + K_5 P_{N_2O}} \qquad [4.168]$$

which at high nitrous oxide pressure, i.e. when $k_6 K_5 P_{N_2O} \gg k_3$ gives

$$2\,dP_{O_2}/dt = dP_{N_2}/dt = \frac{N k_6 K_5 P_{N_2O}}{1 + K_5 P_{N_2O}} \qquad [4.169]$$

When $k_6 \gg k_{-5}$ equation [4.163] shows that the rate of decomposition is controlled by the now, rate determining nitrous oxide adsorption. The total concentration of adsorbed complex will be low since as soon as a nitrous oxide molecule adsorbs, it dissociates. Hence $k_5 P_{N_2O} \ll k_6$ and equation [4.167] can be modified accordingly to give

$$2\,dP_{O_2}/dt = dP_{N_2}/dt = N(k_5 P_{N_2O} + k_3) \qquad [4.170]$$

which when $k_5 P_{N_2O} \gg k_3$ gives

$$2\,dP_{O_2}/dt = dP_{N_2}/dt = N k_5 P_{N_2O} \qquad [4.171]$$

Equations [4.168] to [4.171] which describe specific cases of the overall rate equation can now be compared with experimental results obtained as described in section 3.2.3.

(i) *Steady state N_2O decomposition:* The data for the steady state decomposition of nitrous oxide, given in fig. (3.17) shows a non-linear increase in decomposition rate with increasing nitrous oxide pressure. This is indicative of increasing saturation of available adsorption sites, i.e. bare surface lattice oxygen vacancies, with increasing pressure, as described by equation [4.169]. Rearrangement of equation [4.169] yields the following

$$P_{N_2O}\left(dP_{O_2}/dt\right)^{-1} = P_{N_2O}\left(\tfrac{1}{2} N k_6\right)^{-1} + \left(\tfrac{1}{2} N k_6 K_5\right)^{-1} \qquad [4.172]$$

and

$$\left(dP_{O_2}/dt\right)^{-1} = P_{N_2O}^{-1}\left(\tfrac{1}{2}Nk_6K_5\right)^{-1} + \left(\tfrac{1}{2}Nk_6\right)^{-1} \qquad [4.173]$$

So, in fig. (4.22) there is plotted $P_{N_2O}\left(dN_{O_2}/dt\right)^{-1}$ (where dN_{O_2}/dt is simply dP_{O_2}/dt normalised to the units of molecules s^{-1} cm^{-2}) versus P_{N_2O} (in torr), for the data of fig. (3.17). Within experimental scatter, straight lines are indeed obtained as predicted by equation [4.172]. The gradient as a function of temperature is $\left(\tfrac{1}{2}Nk_6\right)^{-1}$. In fig. (4.23) there is plotted $\left(dN_{O_2}/dt\right)^{-1}$ versus $P_{N_2O}^{-1}$ giving, again, straight lines whose gradients as a function of temperature are, by equation [4.173], $\left(\tfrac{1}{2}Nk_6K_5\right)^{-1}$. When, at a particular temperature, the gradient obtained in fig. (4.22), i.e. $\left(\tfrac{1}{2}Nk_6\right)^{-1}$ is divided by the gradient obtained in fig. (4.23), i.e. $\left(\tfrac{1}{2}Nk_6K_5\right)^{-1}$, K_5 , the equilibrium constant for adsorption of nitrous oxide is obtained. So, values for both $\tfrac{1}{2}Nk_6$ and K_5 as a function of temperature are easily obtained from these plots.

The term $\tfrac{1}{2}Nk_6$ involves N, the total maximum concentration of available adsorption sites and k_6 the rate constant of adsorbed complex decomposition, both of which can potentially vary with temperature. In section 3.2.3 it was shown that for all conditions of nitrous oxide pressure and temperature the total initial oxygen vacancy concentration ($\theta =$ 0.04, as set by the pre-treatment of section 4.1.1) remained throughout. That is to say, there was no net incorporation of oxygen into the surface lattice during nitrous oxide decomposition. Thus N is a constant at all experimental temperatures and pressures of nitrous oxide, given by the 4% vacancy concentration established in the pre-treatment. An Arrhenius plot of $\ln\left(\tfrac{1}{2}Nk_6\right)$ versus $1/T$ should therefore give a straight line whose

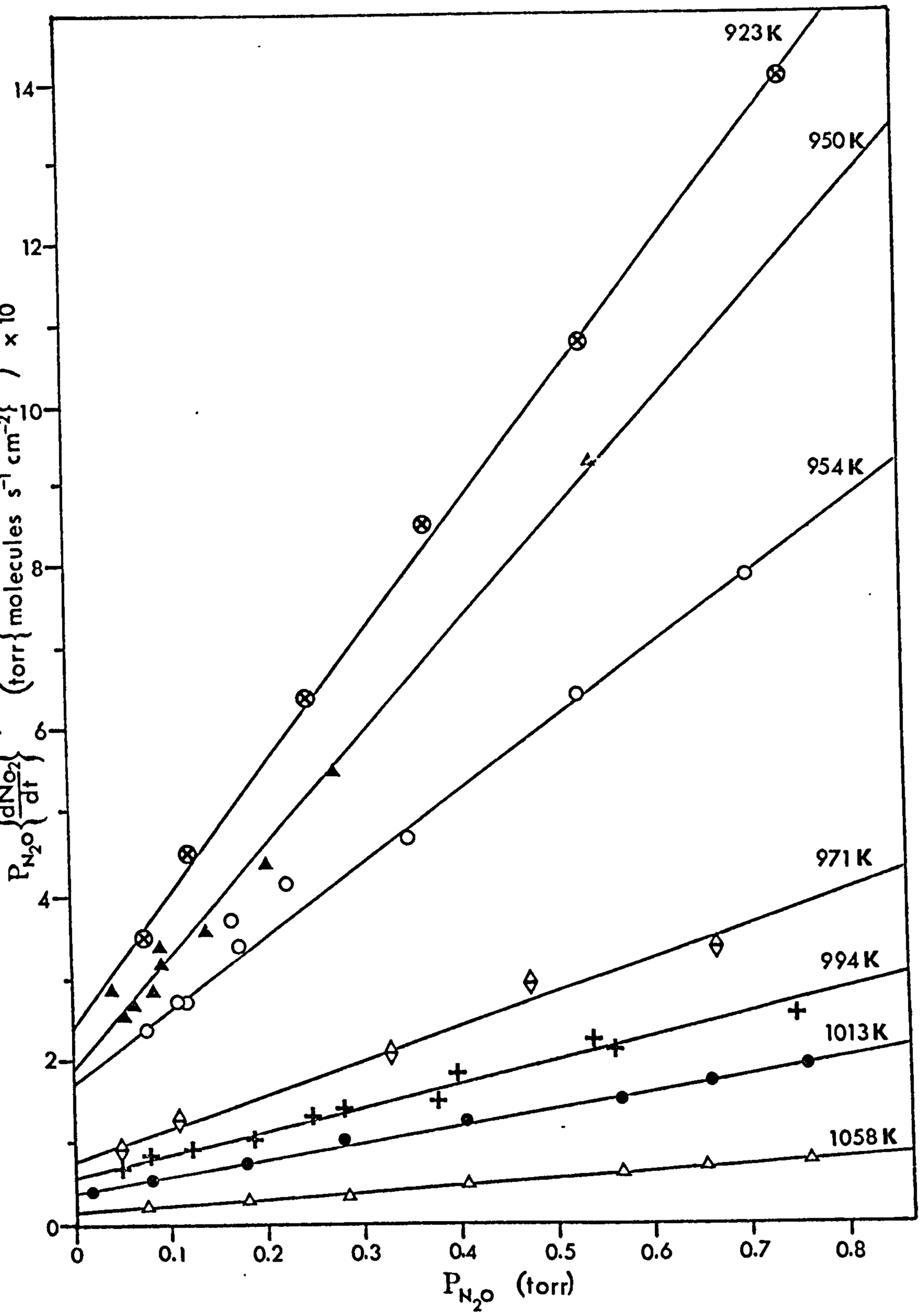

Fig. 4.22:

Nitrous oxide pressure divided by the rate of decomposition plotted against nitrous oxide pressure for the steady-state decomposition of nitrous oxide.

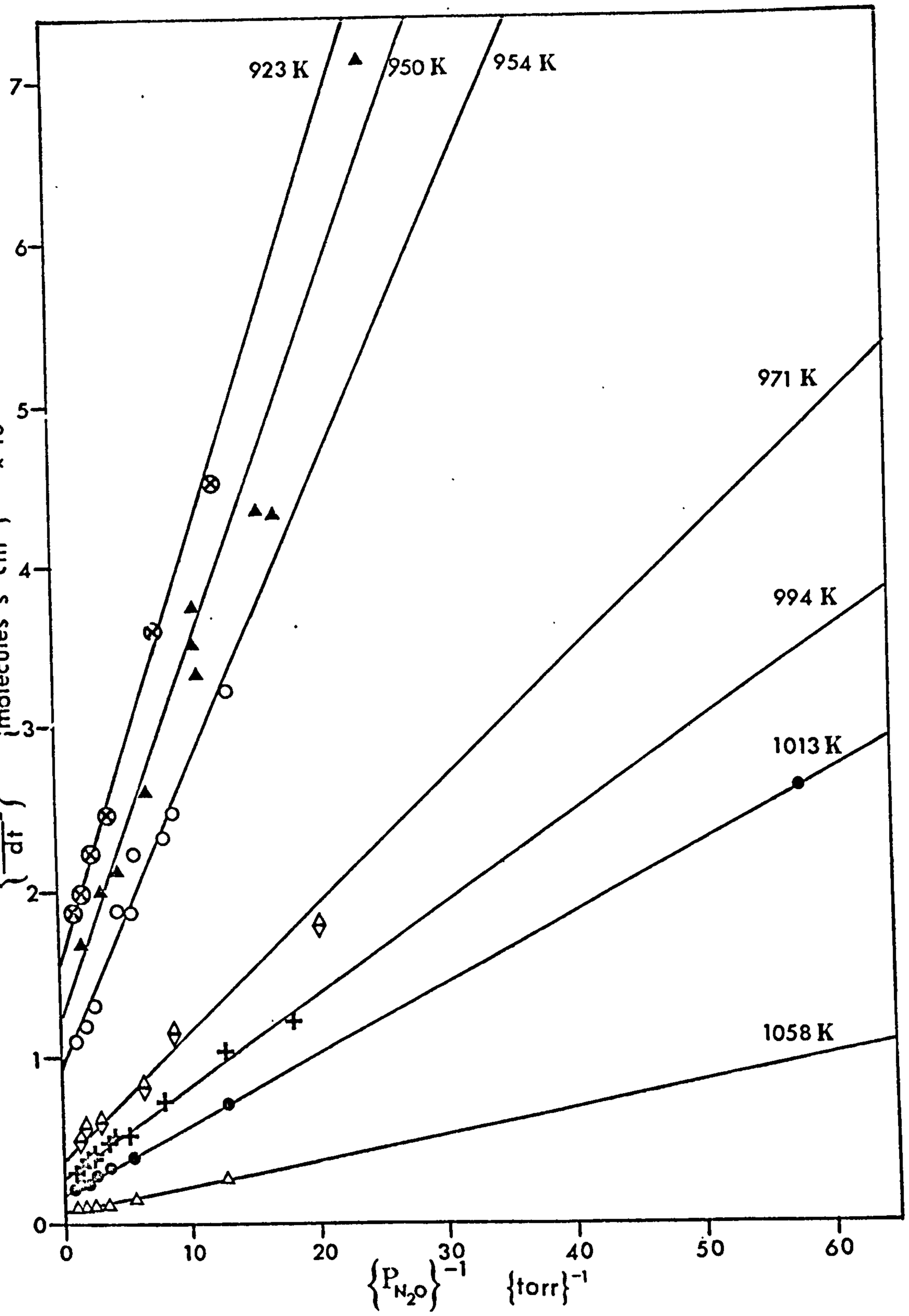

Fig. 4.23:

Reciprocal of the rate of decomposition plotted against the reciprocal of the nitrous oxide pressure for the steady-state decomposition of nitrous oxide.

gradient gives the activation energy of the decomposition of the adsorbed complex. Such a plot is shown in fig. (4.24). The intercept at $1/T = 0$ gives the pre-exponential factor of the rate constant, when divided by $\frac{1}{2}N$ ($\frac{1}{2} \times 0.04 \times 6 \times 10^{14}$ molecules cm^{-2}). Therefore, fig. (4.24) gives for k_6

$$k_6 = (9 \pm 7) \times 10^7 \exp - \frac{(2.04 \pm 0.08)\,eV}{kT} \qquad [4.174]$$

By using the equation

$$\frac{d \ln K_p}{d(1/T)} = - \frac{\Delta H^\circ}{k}$$

where K_p is the equilibrium constant of a gas reaction expressed in pressures, and ΔH° the standard enthalpy of the reaction, a plot of $\ln K_5$ against $1/T$, as shown in fig. (4.25) gives a straight line, slope $-\Delta H^\circ/k$. The intercept at $1/T = 0$ gives the pre-exponential factor. Therefore, fig. (4.25) gives for K_5

$$K_5 = (4 \pm 2) \times 10^{-2} \exp + \frac{(0.42 \pm 0.06)\,eV}{kT} \quad torr^{-1} \qquad [4.175]$$

This shows an exothermic heat of charge transfer adsorption of nitrous oxide over a surface oxygen vacancy of ca. 0.42eV.

The large uncertainty in K_5 values arises because the quotient of 2 experimentally obtained gradients gives K_5 .

(ii) *Temperature transient N_2O decomposition:* The temperature transient data, a representative sample of which is shown in fig. (3.19), indicate the variation of decomposition rate with temperature for various constant pressures of nitrous oxide. If we assume pseudo-equilibrium at all times during temperature transient, i.e. slowly changing temperature

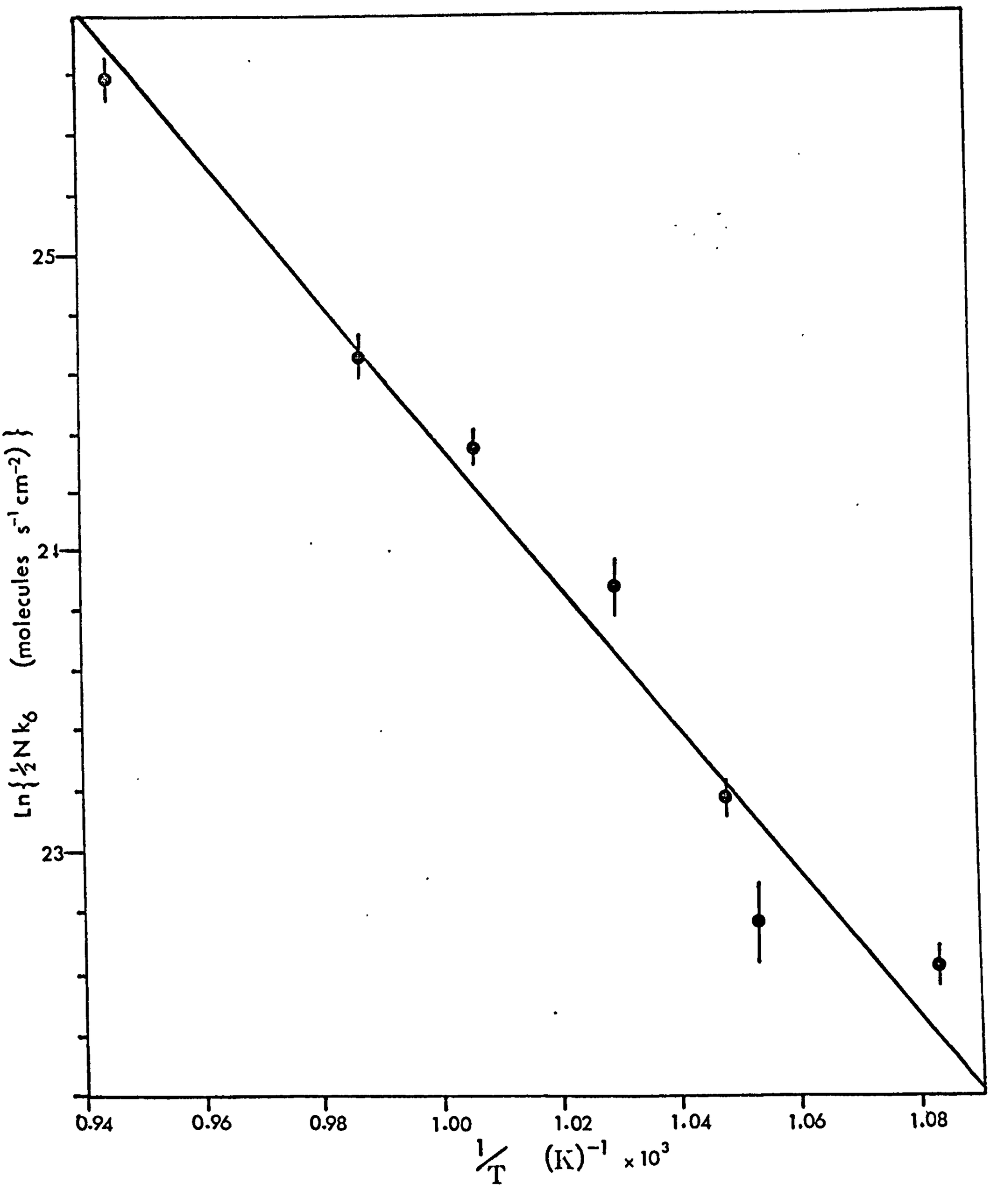

Fig. 4.24:

Arrhenius plot for the steady-state decomposition of nitrous oxide.

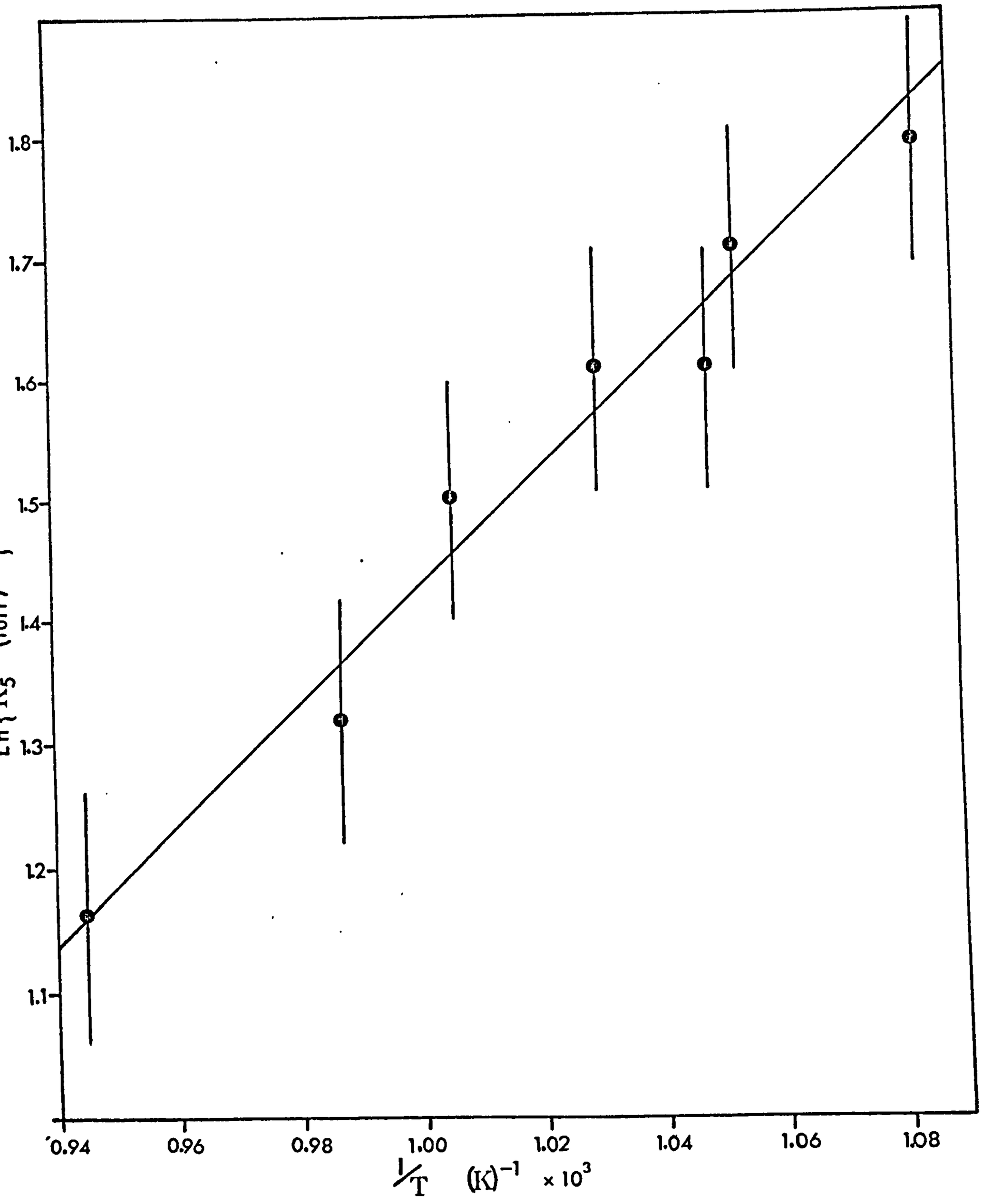

Fig. 4.25:

Temperature dependence of the equilibrium constant for nitrous oxide adsorption.

(cf. change of heating rate). Plotting the logerithm of the rate against $1/T$ for curve (a), (fig. (3.19)) gives a straight line (curve (a) of fig. (4.26)), whose gradient gives a total apparent activation energy of (1.60 ± 0.05)eV. The intercept at $1/T = 0$ gives for the pre-exponential factor $(2 \pm 1) \times 10^{19}$ molecules O cm^{-2} s^{-1}. This, when multiplied by 2 (rate of N_2O decomposition is twice the rate of O_2 formation) and divided by N, the total number of sites at which decomposition can take place gives, for the pre-exponential factor, a value $(1.6 \pm 0.8) \times 10^5$ s^{-1}; and at unit pressure (divide by P_{N_2O} = 0.22 torr) the total apparent rate constant of nitrous oxide decomposition becomes

$$(7.3 \pm 3.6) \times 10^5 \exp - \frac{(1.60 \pm 0.05)eV}{kT} \quad torr^{-1} s^{-1} \qquad [4.176]$$

Equation [4.169] shows that the total apparent rate constant for nitrous oxide decomposition is $k_6 K_5$ $torr^{-1}$ s^{-1} (divided by a term $(1 + K_5 P_{N_2O} \simeq 2)$ describing the saturation of available adsorption sites. $K_5 P_{N_2O}$ at P_{N_2O} = 0.22 torr is of the order of 1 for the temperature range under consideration. Hence, the Arrhenius plot (fig. (4.26(a))) would not be expected to diverge much from linearity over this temperature range, as indeed it does not. So,

$$\frac{k_6 K_5}{2} \doteqdot (7.3 \pm 3.6) \times 10^5 \exp - \frac{(1.60 \pm 0.05)eV}{kT} \quad torr^{-1} s^{-1} \qquad [4.177]$$

Using the value of the steady state decomposition rate k_6 of equation [4.174], equation [4.177] becomes

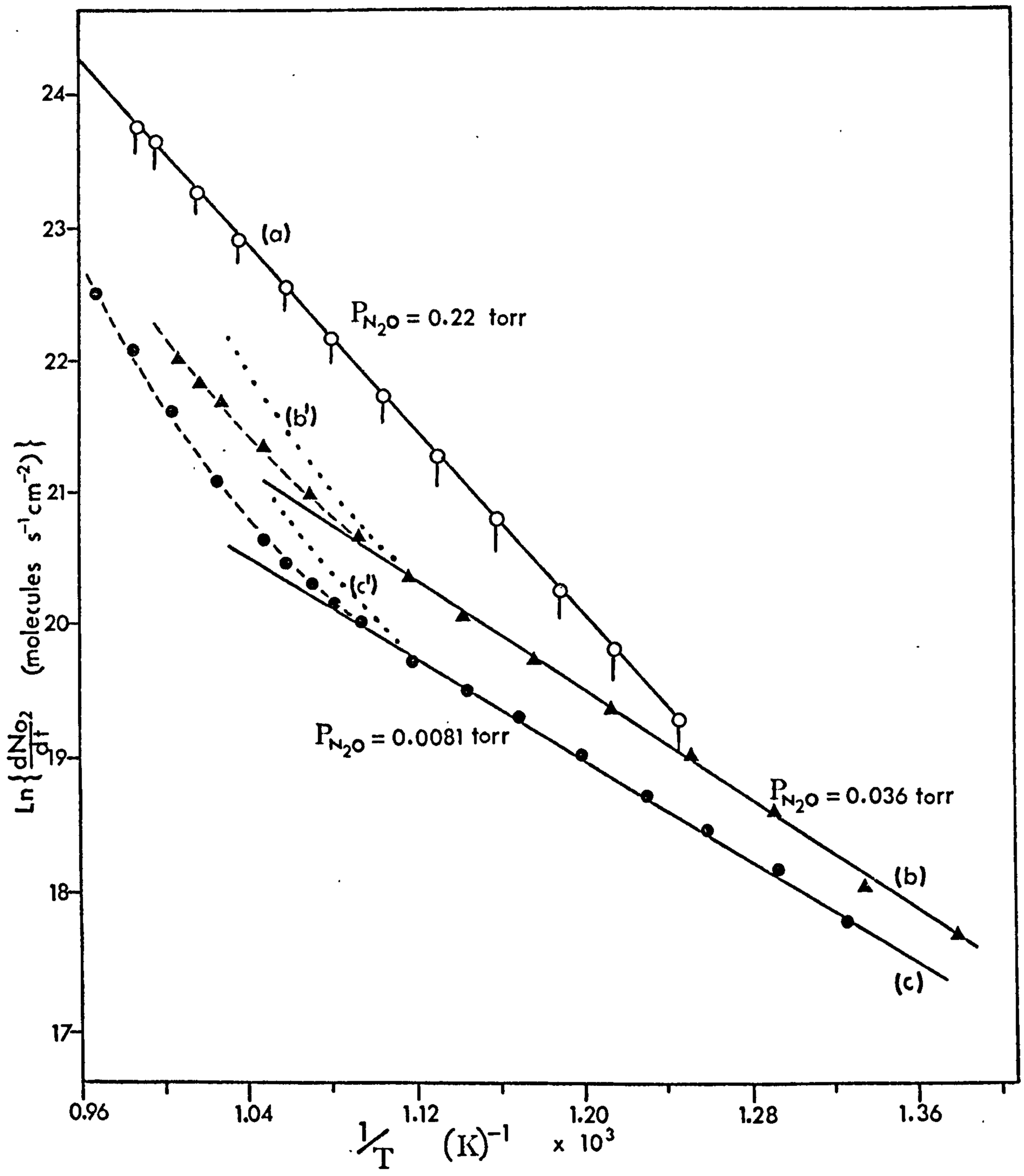

Fig. 4.26:

Arrhenius plots for the temperature transient decomposition of nitrous oxide at various pressures of nitrous oxide.

$$K_5 = (1.6 \pm 1.3) \times 10^{-2} \exp + \frac{(0.44 \pm 0.13)eV}{kT} \qquad [4.178]$$

which, within experimental error is very close to the value of K_5 (equation [4.175]) obtained at steady state.

The temperature transient change of reaction rate at low pressure (curve (c) of fig. (3.19) where P_{N_2O} = 0.0081 torr) yields on the Arrhenius plot (fig. (4.26 (c)) a straight line over the temperature range 740 K to 940 K. The gradient gives an activation energy of 0.87 ± 0.03eV with an intercept at $1/T = 0$ of $(2.4 \pm 0.8) \times 10^{13}$ molecules O_2 cm^{-2} s^{-1} . This gives for the rate constant of nitrous oxide decomposition, when normalised for unit site concentration and pressure,

$$(2.5 \pm 0.8) \times 10^{2} \exp - \frac{(0.87 \pm 0.03)eV}{kT} \qquad torr^{-1}s^{-1} \qquad [4.179]$$

and for curve (b) of fig. (3.19) at P_{N_2O} = 0.036 torr the straight line Arrhenius plot (fig. 4.26 (b)) gives for the rate constant

$$(1.7 \pm 0.5) \times 10^{2} \exp - \frac{(0.87 \pm 0.03)eV}{kT} \qquad torr^{-1}s^{-1} \qquad [4.180]$$

It is assumed that this different activation energy at low nitrous oxide pressure corresponds to the activation energy for nitrous oxide adsorption. That is to say, that the overall kinetics can now be described by equation [4.171], which gives from equations [4.179] and [4.180]

$$k_5 = (2.10 \pm 0.65) \times 10^{2} \exp - \frac{(0.87 \pm 0.03)eV}{kT} \qquad torr^{-1}s^{-1} \qquad [4.181]$$

Using this value of k_5 and observing that $k_{-5} = k_5 / K_5$ this gives, combining equations [4.175] and [4.181] for k_{-5}

$$k_{-5} = (5.2 \pm 4.2) \times 10^3 \exp - \frac{(1.31 \pm 0.09)eV}{kT} \quad s^{-1} \qquad [4.182]$$

Comparing the magnitude of k_{-5} and k_6 at 1000K in equations [4.174] and [4.182] gives:- At 1000 K k_{-5} is of the order of 1×10^{-3} s^{-1} and k_6 is 3×10^{-3} s^{-1}. These are very close, well within experimental error. Thus a change in observed kinetics from rate determining adsorbed complex decomposition, where $k_{-5} \gg k_6$, to rate determining gas adsorption, where $k_6 \gg k_{-5}$, is quite consistent with that observed experimentally when either of k_6 of k_{-5} varies with nitrous oxide pressure. Step 5 of the reaction mechanism shows that when a nitrous oxide molecule desorbs one electron is released, with its corresponding contribution to the space charge potential. The potential energy of the transition state is increased as the nitrous oxide adsorbed state coverage gets smaller. The term increasing the activation energy of desorption is thus $1.67\theta^{0.8}$, where θ is the total fraction of bare vacancies, cf. section 4.1.1. This predicts a five-fold decrease in k_{-5} when the coverage is small over that when coverage is large, at 1000 K. So, using this, it is quite reasonable to suggest that when P_{N_2O} is small, coverage of adsorbed nitrous oxide is small, k_{-5} is less than k_6 and rate determining adsorption prevails. When P_{N_2O} is large, coverage is large, k_{-5} is larger than k_6 and there is rate determining adsorbed complex decomposition.

At low nitrous oxide pressure and high temperature the value of k_3 in equation [4.170] is comparable with the value of $k_5 P_{N_2O}$; that is, at these conditions of temperature and nitrous oxide pressure, the

loss of zinc from the zinc oxide surface, k_3 being the rate constant for this reaction, causes an increase in the overall rate of nitrous oxide decomposition (via step 4 of the reaction mechanism). Using a value of k_3 obtained in section 4.1.1, (cf. k_4 of section 4.1.1) that is

$$k_3 = 8 \times 10^{15} \exp - \frac{3.70\,eV}{kT} \qquad s^{-1}$$

at $\theta = 0.04$, and k_5 obtained from equation [4.181] in equation [4.170], new values of the log of the decomposition rate against $1/T$ can be obtained; curve b' at $P_{N_2O} = 0.036$ torr and curve c' at $P_{N_2O} = 0.081$ torr. The increased rate at high temperature shows the same general trend as that observed experimentally.

(iii) *Summary:* The potential energy diagram of the various steps in the decomposition of nitrous oxide is shown in fig. (4.27).

In this analysis we use the model of charge transfer adsorption of nitrous oxide molecules over oxygen vacancies. The change in space charge potential as a function of the amount adsorbed allows us to explain the changing kinetics, i.e. from rate determining adsorbed complex decomposition to rate determining nitrous oxide adsorption. Thus we are forced to employ a charge transfer model. Our data, however, do not give us direct evidence that the adsorption sites are vacancies. Although the observation that the adsorption sites become saturated (cf. the steady-state decomposition data), would suggest that adsorption takes place on special sites, and, that using oxygen vacancies as these special sites seems sensible and, indeed, gives a consistent kinetic model, we would like a direct correlation between oxygen vacancy concentration and nitrous oxide adsorption and decomposition. Therefore, we would suggest for future experiments, the following:

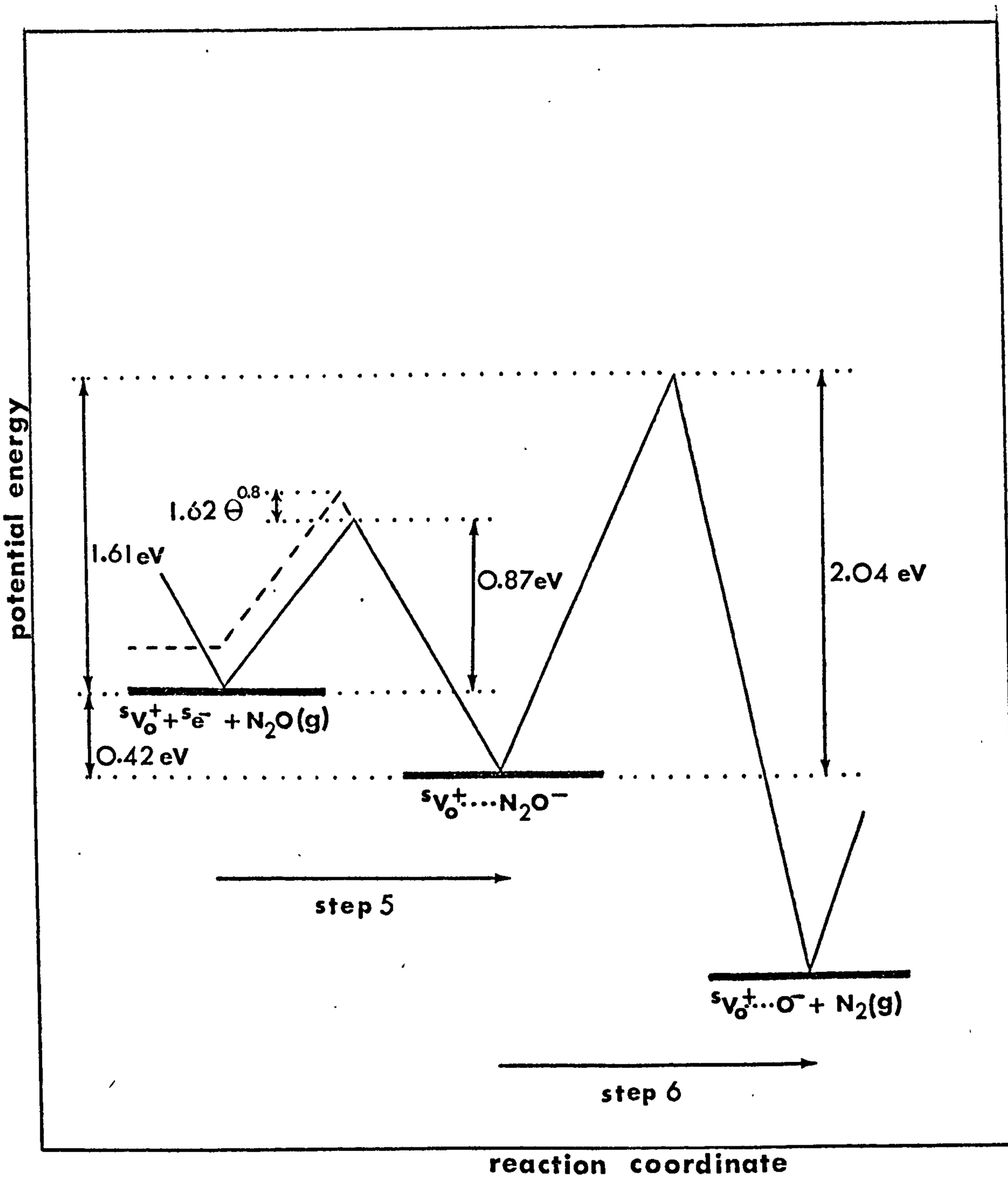

Fig. 4.27:

Potential energy diagram of the various steps in the decomposition of nitrous oxide on a $10\bar{1}0$ oxide surface.

(a) Since, in all the above experiments, we have been working with a zinc oxide surface with a constant surface oxygen vacancy density, namely θ = 0.04, both steady state and temperature transient decomposition reactions ought to be performed on zinc oxide surfaces with different oxygen pre-treatments, i.e. θ values varying from 0 to 0.04.

(b) Performing T.P.D. experiments on the adsorption of nitrous oxide over zinc oxide with various different surface oxygen vacancy concentrations, to obtain a correlation between the size of the N_2O T.P.D. peak and the value of θ set by the oxygen pre-treatment.

(c) 'Thermally programmed reaction' of nitrous oxide over the zinc oxide surface: this requires the simultaneous monitoring of N_2, O_2 and N_2O during the T.P.D. of adsorbed nitrous oxide. The position of peaks in these gas flows as a function of θ (oxygen pre-treatment) should be very diagnostic of the detailed nature of the reaction mechanism.

The value of the pre-exponential factors, namely $(9 \pm 7) \times 10^7$ s^{-1} for the decomposition of the $^sV_O^+ \cdots N_2O^-$ complex and $(5.2 \pm 4.2) \times 10^3$ s^{-1} for the desorption of the $^sV_O^+ \cdots N_2O^-$ complex, are much smaller than the value of 10^{13} s which is a typical value of the molecular vioration frequency. Using the most generalised form of the reaction rate equation, the frequency factor, A, is given by

$$A = \bar{\tau} (kT/h)(F^{\ddagger}/F_{init.})$$

where $\bar{\tau}$ is the average transmission coefficuent, $F^{\ddagger}$ is the partition function of the activated state and $F_{init.}$ is the partition function of the initial state. These low values of the pre-exponential factor

arise from a low value of $\bar{r}$. So, 'slow reactions' where $A \ll kT/h$ are due to the value of $\bar{r}(F^{\ddagger}/F_{init.})$ where $\bar{r}$ can have values, in the extreme case, as low as 10^{-13}. (Petermann, 1972).

4.2 GAS INTERACTIONS WITH THE ZINC OXIDE SURFACE BETWEEN 300 K AND 1200 K

The results of experiments on the interaction of oxygen with the zinc oxide surface in the temperature range 300 K to 800 K are discussed in this section. The results for both clean and contaminated surfaces of zinc oxide single crystals and powder are discussed. In this temperature range the surface lattice defect structure does not change during oxygen treatment, and the surface oxygen vacancy concentration is as set by the high temperature (above 800 K) oxygen pre-treatment (cf. section 4.1.1 and 4.1.2).

4.2.1 The interaction of oxygen with the $10\bar{1}0$ zinc oxide single crystal surface

The results of these experiments are described in section 3.2.1b.

Three kinds of adsorbing surface have been identified for the zinc oxide $10\bar{1}0$ surface, these are: a contaminated surface; a clean,vacancy-rich surface; a clean,vacancy deficient surface.

A contaminated surface treated with oxygen showed, typically, peaks in the T.P.D. spectra for H_2O, CO and CO_2 , but no oxygen T.P.D. peak (cf. fig. (3.12a). Two sources of contamination can be identified, they are either contamination by background gas impurities or by the surface diffusion of impurity atoms or molecules along the walls of the reaction chamber. The peak in the CO T.P.D. at 720 K (total fractional coverage equals 2.2×10^{-3}) suggests the result of oxidation of surface elemental carbon contaminant (since there is no corresponding peak in the H_2O T.P.D.) This impurity probably arises by diffusion along the walls of the reaction chamber. Peaks at 620 K in the CO_2 and H_2O T.P.D.'s are possibly due to the oxidation of surface hydrogen and hydrocarbons (total fractional coverage equals 4.5×10^{-3} for H_2O and 1.5×10^{-3} for CO_2). These impurities probably contaminate the surface from the gas phase.

In the oxygen T.P.D. of a cleaned surface no peaks are obtained for both vacancy rich and vacancy deficient surfaces. We conclude that there is no oxygen adsorption on clean $10\bar{1}0$ zinc oxide surfaces down to a resolution of 4×10^{-6} fractional surface coverage (cf. adsorption of isotopic oxygen in section 3.2.1b).

Occasionally, particularly just after the zinc oxide sample had been introduced into the reaction chamber, a peak at 580 K was observed in the oxygen T.P.D. (cf. fig. 3.12b). After many adsorption/desorption cycles this peak was no longer observed. We tentatively assign this peak to adsorbed oxygen on remnant out-diffused impurity atom sites (e.g. sodium or potassium - cf. ESCA work in section 2.4.1). The assymetrical peak shape suggests a first order desorption, probably of a molecular oxygen adsorbed species. That this peak disappears after many adsorption/desorption cycles is consistent with the removal into the gas phase of the impurities at high temperature.

4.2.2 The interaction of oxygen with the zinc oxide powder surface

In section 3.2.5 it was shown that an oxygen treated ($10^{-3} < P_{O_2} < 0.4$ torr; $300\ K < T < 800\ K$) zinc oxide surface yielded several peaks in the oxygen T.P.D. The behaviour of these desorption peaks with pre-treatment, and the desorption kinetics is discussed below.

(i) The kinetics of the oxygen desorption process can be described by the standard Polanyi-Wigner rate equation (see, for example, Petermann 1972, Ehrlich 1963), namely

$$-dc/dt = \nu c^n \exp-(\Delta E^{\ddagger}/kT) \qquad [4.183]$$

where $\Delta E^{\ddagger}$ is the activation energy of the desorption process, ν is the pre-exponential frequency-factor and n is the order of the reaction. At the peak-maximum temperature, T_p , the desorption flow rate is constant, i.e. $d^2c/dt^2 = 0$. Differentiating equation [4.183] with respect to time gives

$$-d^2c/dt^2 = \nu\beta c^n(\Delta E^{\ddagger}/kT^2)\exp-(\Delta E^{\ddagger}/kT) + \nu c^{n-1}(dc/dt)\exp-(\Delta E^{\ddagger}/kT) \quad [4.184]$$

where $dT/dt = \beta$, the heating rate.

Now, putting $d^2c/dt^2 = 0$ at T_p equation [4.184] becomes

$$\beta c^n (\Delta E^{\ddagger}/kT_p^2) = - c^{n-1} (dc/dt)_{T_p} \quad [4.185]$$

and substituting for dc/dt from equation [4.183] gives

$$\beta (\Delta E^{\ddagger}/kT_p) = \nu c^{n-1} \exp-(\Delta E^{\ddagger}/kT_p)$$

or

$$\ln\left(\frac{\beta}{T_p^2 c^{n-1}}\right) + \ln\left(\frac{\Delta E^{\ddagger}}{k\nu}\right) = -\left(\frac{\Delta E^{\ddagger}}{k}\right)\left(\frac{1}{T_p}\right) \quad [4.186]$$

(ii) For a first order desorption, n = 1, and equation [4.186] becomes

$$\ln\left(\frac{\beta}{T_p^2}\right) + C = -\left(\frac{\Delta E^{\ddagger}}{k}\right)\left(\frac{1}{T_p}\right) \quad [4.187]$$

where the constant C is $\ln\left(\frac{\Delta E^{\ddagger}}{k\nu}\right)$, i.e. the peak-maximum temperature varies with the heating rate but is independent of surface coverage, i.e. independent of peak area. Peak "β" of fig. (3.20) exhibited this

behaviour. By measuring the peak-maximum temperature for a series of heating rates ($0.017 \leqslant \beta \leqslant 1.7$ K s^{-1}), plotting $\ln(\beta/T_p^2)$ versus $1/T_p$ gave a straight line whose gradient gave an activation energy of $\Delta E^{\ddagger} = 1.05 \pm 0.1$eV.

(iii) For a second order desorption, n = 2, and equation [4.186] becomes

$$\ln\left(\frac{\beta}{CT_p^2}\right) + C = -\left(\frac{\Delta E^{\ddagger}}{k}\right)\left(\frac{1}{T_p}\right) \qquad [4.188]$$

i.e. the peak-maximum temperature varies with heating rate and with coverage (i.e. peak area). Peak "δ" of fig. (3.20) exhibited this behaviour. By measuring the peak-maximum temperature and peak area for a series of heating rates ($0.17 \leqslant \beta \leqslant 1.7$ K s^{-1}), and plotting $\ln(\beta/CT_p^2)$ versus $1/T_p$ a straight line was obtained whose gradient gave an activation energy for desorption of $\Delta E^{\ddagger} = 1.90 \pm 0.1$eV.

(iv) The peaks labelled "α" and "γ" were not analysed by this technique. They only appeared sporadically on the oxygen T.P.D.'s, often poorly resolved, and there was insufficient data to obtain a variation of peak-maximum temperature with heating rate.

(v) The size of all peaks decreased dramatically after the first few adsorption/desorption cycles. We attribute this behaviour to a decreasing surface area due to sintering, which is appreciable at 900 K.

(vi) The increasing flow rate at the high temperature end of the oxygen T.P.D. (cf. fig. 3.20) is probably loss of oxygen from the lattice (cf. section 4.1.1), however, we did not heat our samples above ca. 900 K, because at higher temperatures, there was appreciable zinc loss from the zinc oxide (zinc film in cooler part of reaction chamber). That zinc oxide powder is less stable at these temperatures than the $10\bar{1}0$ surface

of the single crystals is consistent with the lower thermal stability of the polar faces constituting a large part of the powder surface.

(viii) The multiplicity of peaks in the oxygen T.P.D. can be explained in two ways. Firstly, in the powder form, zinc oxide reveals all its crystallographic surfaces, i.e. both prism and polar type, and the different peaks then correspond to different adsorption sites on these different faces. Secondly, our zinc oxide surface was not characterised by E.S.C.A. We could not use the same cleaning procedure as adopted for the single crystals since we could not heat our powder above 900 K. It is then quite likely that our surfaces are gorssly contaminated with out-diffused material. Typically, the surface coverage on oxygen adsorption is low, for peak "β" (cf. fig. (3.20a) the fractional surface coverage is $\theta = 1.7 \times 10^{-4}$ (pre-treated in 0.19 torr O_2 at 373 K) for peak "δ" (cf. fig. (3.20b) the fractional surface coverage is $= 3 \times 10^{-5}$. This is very small compared with the probable amount of surface contamination. We therefore do not propose to make any firm conclusions about the nature of the adsorption reaction or of the adsorption site.

(ix) The first order desorption peak, activation energy 1.05 ± 0.1eV, corresponds very closely to a value obtained by Göpel (2) (1976) of 1.14eV. His first order desorption from the single crystal prism surface was attributed to desorption of adsorbed molecular oxygen (as O_2^-.).

(x) The second order desorption peak activation energy 1.90 ± 0.1eV could then be postulated to arise from desorption of adsorbed disocciated oxygen, say O^- or $O^=$.

4.2.3 Miscellaneous gas reactions on zinc oxide single crystals

In the experiments described in section 3.2.4, the zinc oxide $10\bar{1}0$ surface was treated with gas produced in a microwave discharge. The following conclusions can be drawn.

(i) When oxygen gas was used, only CO was monitored at the mass spectrometer (cf. section 3.2.4). By measuring the change in CO flow rate, as the temperature was reduced from 850 K to room temperature the total amount of gas adsorbed was found to be 5.6×10^{13} molecules cm^{-2} which is a fractional coverage of ca. 0.1. (Pre-treatment pressure of CO = 0.126 torr.) Upon desorption there were no peaks in the oxygen T.P.D. but four peaks in the CO T.P.D. at ca. 420 K, 520 K, 690 K and 900 K. The total area under these peaks gave a surface coverage of ca. 0.05, i.e. about half of that originally adsorbed. The T.P.D. of CO_2 gave peaks at exactly equivalent positions, also giving a surface coverage of ca. 0.05. We attribute this behaviour to the adsorption of CO and atomic oxygen (produced in the microwave discharge), some of the adsorbed CO reacting with the oxygen to give CO_2 in the desorption stage.

(ii) When CO gas was used as the adsorbate (no microwave discharge) the ensuing T.P.D. showed no peaks, i.e. CO does not adsorb on a $10\bar{1}0$ zinc oxide surface in the temperature range studied (room temperature to 850 K). When CO gas in a microwave discharge was used as the adsorbate, the ensuing T.P.D. showed two peaks at 520 K and at 910 K. Thus, the microwave CO is 'activated" (e.g. CO radical or ion) and <u>can</u> adsorb on zinc oxide.

These experiments do not give information about the nature of the adsorbing 'activated' gas species, since none will reach the mass spectrometer head. However, it is quite clear that adsorption of these species occurs when it does not for the 'unactivated' gases.

Appendix 4.1

In the overall rate expressions of equations [4.53a] and [4.54a] the term $kT\ln(1+\theta_{s.s}\{\exp \Delta E/kT - 1\})$ describing the change in activation energy of the oxygen loss reaction due to step sites, is a function of the step site concentration, $\theta_{s.s.}$, and temperature, T, i.e.

$$f(\theta_{s.s.}, T) = kT \ln(1 + \theta_{s.s.}\{\exp \Delta E/kT - 1\}) \qquad [A4.1]$$

The function, $f(\theta_{s.s.}, T)$, can be written in the differential form, namely

$$df = (\partial f/\partial \theta_{s.s.})_T \, d\theta_{s.s.} + (\partial f/\partial T)_{\theta_{s.s.}} dT \qquad [A4.2]$$

This equation means that the total change in the value of the function $f(\theta_{s.s.}, T)$, i.e. df , arises from the sum of two parts: one due to a change in $\theta_{s.s.}$ alone, i.e. $(\partial f/\partial \theta_{s.s.})_T d\theta_{ss}$ the other due to temperature change alone, i.e. $(\partial f/\partial T)_{\theta_{s.s}} dT$

In order that the temperature variation of $f(\theta_{s.s.}, T)$ be neglected, it is required that

$$(\partial f/\partial \theta_{s.s.})_T d\theta_{s.s.} \gg (\partial f/\partial T)_{\theta_{s.s.}} dT$$

or,

$$d\theta_{s.s.}/dT \gg \left|(\partial f/\partial T)_{\theta_{s.s.}}/(\partial f/\partial \theta_{s.s.})_T\right| \qquad [A4.3]$$

where the modulus of the quotient of the two partial differentials is taken, since either of $(\partial f/\partial T)_{\theta_{s.s.}}$ or $(\partial f/\partial \theta_{s.s})_T$ can be negative.

The partial differentials are obtained by differentiating equation [A4.1]; that is, $(\partial f/\partial \theta_{s.s.})_T$ is the partial differential of $f(\theta_{s.s.}, T)$ with respect to $\theta_{s.s.}$ when T is kept constant and is given by

$$(\partial f/\partial \theta_{s.s.})_T = \frac{kT(e^{\Delta E/kT} - 1)}{1 + \theta_{s.s.}(e^{\Delta E/kT} - 1)} \qquad [A4.4]$$

and $(\partial f/\partial T)_{\theta_{s.s.}}$ is the partial differential of $f(\theta_{s.s.}, T)$ with respect to T when $\theta_{s.s.}$ is kept constant and is given by

$$(\partial f/\partial T)_{\theta_{s.s.}} = k\ln(1+\theta_{s.s.}(e^{\Delta E/kT}-1)) - \frac{\Delta E.\theta_{s.s.}\, e^{\Delta E/kT}}{T(1+\theta_{s.s.}(e^{\Delta E/kT}-1))} \qquad [A4.5]$$

Values of $\theta_{s.s.}$ and $d\theta_{s.s.}/dT$ at temperatures T, can be obtained from the iterative analysis of the full rate expression, as outlined in section 4.1.1d . For $\theta_0 = 0$, $\theta_{s.s._0} = 0$ and $\Delta E = 0.25$ the full solution gives the curve of $d\theta/dT$ versus T shown in fig. (4.9). Values of $\theta_{s.s.}$ and $d\theta_{s.s.}/dT$ at various T have been obtained in this solution and are shown below.

T	$\theta_{s.s.}$	$d\theta_{s.s.}/dT$
1000	1.0×10^{-5}	5.4×10^{-6}
1050	2.6×10^{-3}	3.1×10^{-4}
1100	6.8×10^{-2}	3.8×10^{-3}
1125	2.4×10^{-1}	1.4×10^{-2}

Values of $(\partial f/\partial\theta_{s.s})_T$ and $(\partial f/\partial T)_{\theta_{s.s.}}$ can be obtained by substituting values of $\Theta_{s.s.}$ and T, shown above, into equations [A4.4] and [A4.5] and these are shown below

T	$(\partial f/\partial\theta_{s.s})_T$	$(\partial f/\partial T)_{\theta_{s.s.}}$	$\left\lvert(\partial f/\partial T)_{\theta_{s.s.}}/(\partial f/\partial\theta_{s.s.})_T\right\rvert$
1000	1.49	-3.09×10^{-8}	2.07×10^{-8}
1050	1.30	-6.55×10^{-6}	5.04×10^{-6}
1100	0.65	-6.09×10^{-5}	9.37×10^{-5}
1125	0.30	-6.15×10^{-5}	2.05×10^{-4}

The quotient $\left\lvert(\partial f/\partial T)_{\theta_{s.s.}}/(\partial f/\partial\theta_{s.s})_T\right\rvert$ is about two orders of magnitude smaller than $d\theta_{s.s}/dT$ over the temperature range of interest, i.e. over the temperature range of the entire T.P.D. curve. Since the inequality of equation [A4.3] is observed, the function $f(\theta_{s.s.},T)$ can be closely approximated to a function varying with $\theta_{s.s.}$ alone, i.e.

$$f(\theta_{s.s.},T) \doteqdot f(\theta_{s.s.})$$

Appendix 4.2

Exchange of O^{18} with the surface lattice layer : vacancy-pair mechanism

We assume that there is no free movement of atoms along the surface during the T.P.D. since in this model all desorbed molecules are formed by producing a vacancy-pair in the surface lattice. Thus, the amount of O_2^{18} evolved is proportional to the number of O^{18} - O^{18} pairs, the amount of O^{16} O^{18} proportional to the number of O^{16} - O^{18} pairs and the amount of O_2^{16} is proportional to the number of O^{16} - O^{16} pairs in the surface lattice layer.

We assume the surface lattice is a square mesh (approximately true for the oxygen atoms in the zinc oxide $10\bar{1}0$ surface plane: but, the same result is obtained for other mesh arrangements, e.g. hexagonal or linear.

In the square mesh, we have assembled a 'counting method' for summation of these pair-wise positions. We consider O^{18} atoms in a sea of O^{16} atoms and take each O^{18} atom in turn as a reference point and look at what it is surrounded by.

When an O^{18} atom is chosen as the reference atom in the square mesh, atoms can be arranged around the central reference atom in five different ways, these are:-

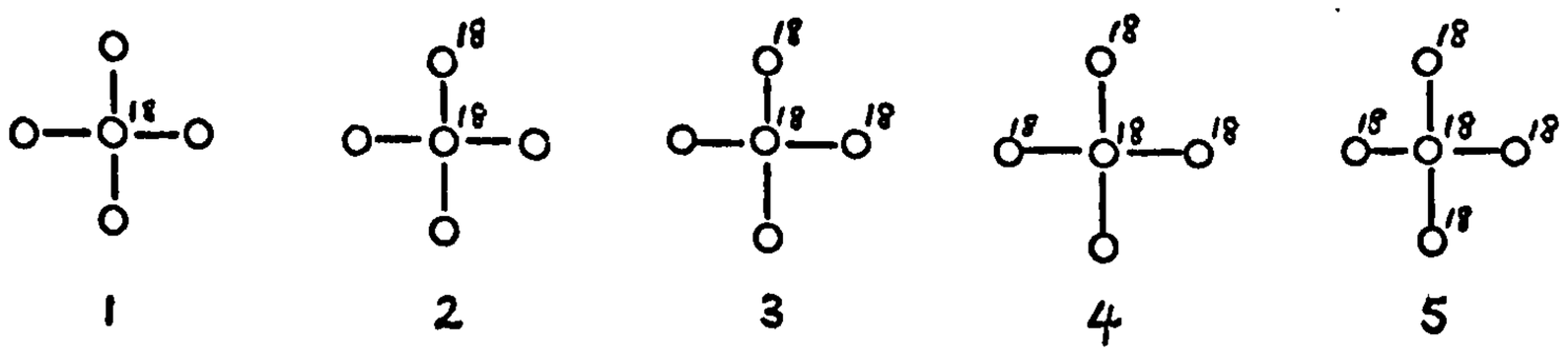

where, for clarity the superscript of O^{16} is omitted. We consider each arrangement in turn, and count the number of ways in which these atoms can be combined pair-wise.

If the first arrangement appears exclusively in the surface lattice, there will be n^{18} such groupings, where n^{18} is the number of O^{18} atoms in the surface containing N lattice points ($n^{16} = N - n^{18}$, where n^{16} is the number of O^{16} atoms). In this first arrangement, there are four ways of making an $O^{18} - O^{16}$ pair-wise combination, but no way of making an $O^{18} - O^{18}$ pair. So, the total number of $O^{18} - O^{16}$ pairs over the whole lattice is $4n^{18}$. The total number of pair-wise combinations of all atoms in the square mesh is 2N, whence the number of $O^{16} - O^{16}$ pairs is $2N - 4n^{18} - 0 = 2n^{16} - 2n^{18}$.

For the second arrangement, the total number of $O^{18} - O^{16}$ pair-wise combinations in the surface lattice is $3n^{18}$ and the total number of $O^{18} - O^{18}$ pairs is $\frac{1}{2}n^{18}$ (not n^{18} since the outer O^{18} atom could be made the reference point and the $O^{18} - O^{18}$ pair would have been counted twice), whence the number of $O^{16} - O^{16}$ pair-wise combinations is $2N - 3n^{18} - \frac{1}{2}n^{18}$, which is $2n^{16} - 3\frac{1}{2}n^{18}$.

The same procedure adopted for all five arrangements gives the total number of pair-wise combinations as indicated below:-

	O^{18}-O^{18}	O^{16}-O^{18}	O^{16}-O^{16}	total
1	0	$4n^{18}$	$2n^{16} - 2n^{18}$	2N
2	$\frac{1}{2}n^{18}$	$3n^{18}$	$2n^{16} - 3\frac{1}{2}n^{18}$	2N
3	$1n^{18}$	$2n^{18}$	$2n^{16} - 1n^{18}$	2N
4	$3\frac{1}{2}n^{18}$	$1n^{18}$	$2n^{16} - \frac{1}{2}n^{18}$	2N
5	$2n^{18}$	0	$2n^{16}$	2N

Now, we must consider the relative probabilities of finding such arrangements in the surface lattice.

For the first arrangement, the probability of one O^{16} atom next to the reference atom is n^{16}/N . The probability of four O^{16} atoms surrounding the reference atom is hence $(n^{16}/N)^4$. This grouping can only be arranged in one way.

For the second grouping the probability of having three O^{16} atoms and one O^{18} atom surrounding the reference atom is $(n^{16})^3 n^{18}/N4$. But this grouping can be arranged in four ways, as indicated below,

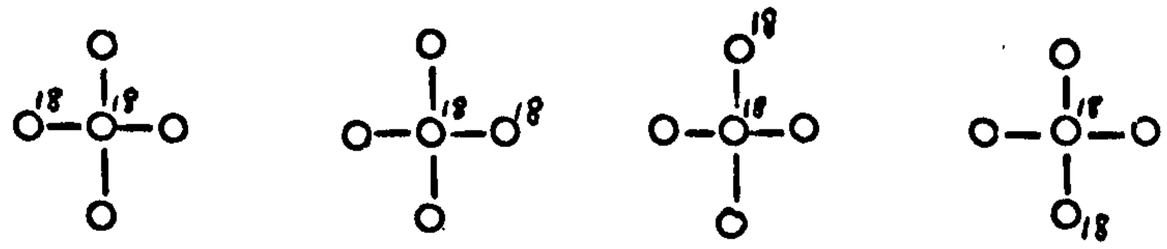

Hence the total probability of finding such arrangements is $4(n^{16})^3 n^{18}/N4$.

The probabilities for all five groupings can be obtained from the expansion of $(n^{16}+n^{18})^4/N^4$, namely

$$\frac{(n^{16}+n^{18})^4}{N4} = 1 = \left(\frac{n^{16}}{N}\right)4 + \frac{4(n^{16})^3 n^{18}}{N4} + \frac{6(n^{16})^2(n^{18})^2}{N4} + \frac{4n^{16}(n^{18})^3}{N4} + \left(\frac{n^{18}}{N}\right)4$$

where the sum of all probabilities, $\sum P = 1$, as required. The first term on the right-hand side gives the probability of arrangement 1, the second the probability of arrangement 2.... , and so on.

Now, when all such groupings are considered together, the total number of O^{18} - O^{18} pairs in the surface lattice, $N_{O^{18}-O^{18}}$, is the sum of the number of these pairs in each grouping times the probability of occurrence of that grouping; similarly for $N_{O^{16}-O^{18}}$ and $N_{O^{16}-O^{16}}$. This then gives for $N_{O^{18}-O^{18}}$,

$$N_{O^{18}-O^{18}} = \frac{2(n^{16})^3(n^{18})^2}{N^4} + \frac{6(n^{16})^2(n^{18})^3}{N^4} + \frac{6(n^{16})(n^{18})^4}{N^4} + \frac{2(n^{18})^5}{N^4} = \frac{2(n^{18})^2(n^{16}+n^{18})^3}{N^4}$$

and, using the relation $N = n^{16} + n^{18}$, there is

$$N_{O^{18}-O^{18}} = \frac{2(n^{18})^2}{N}$$

For $N_{O^{16}-O^{18}}$ there is the expression

$$N_{O^{16}-O^{18}} = \frac{4(n^{16})^4(n^{18})}{N^4} + \frac{12(n^{16})^3(n^{18})^2}{N^4} + \frac{12(n^{16})^2(n^{18})^3}{N^4} + \frac{4(n^{16})(n^{18})^4}{N^4} = \frac{4(n^{16})(n^{18})(n^{16}+n^{18})^3}{N^4}$$

which becomes

$$N_{O^{16}-O^{18}} = \frac{4(n^{16})(n^{18})}{N}$$

and for $N_{O^{16}-O^{16}}$ there is the expression

$$N_{O^{16}-O^{16}} = \frac{2(n^{16})^5}{N^4} - \frac{2(n^{16})^4(n^{18})}{N^4} + \frac{8(n^{16})^4(n^{18})}{N^4} - \frac{6(n^{16})^3(n^{18})^2}{N^4} + \frac{12(n^{16})^3(n^{18})^2}{N^4} - \frac{6(n^{16})^2(n^{18})^3}{N^4}$$
$$+ \frac{8(n^{16})^2(n^{18})^3}{N^4} - \frac{2(n^{16})(n^{18})^4}{N^4} + \frac{2(n^{16})(n^{18})^4}{N^4} = \frac{2(n^{16})^2(n^{16}+n^{18})^3}{N^4}$$

which becomes

$$N_{O^{16}-O^{18}} = \frac{2(n^{16})^2}{N}$$

Hence there is the relation

$$\frac{N_{O^{18}-O^{18}}}{N_{O^{18}-O^{18}}} : \frac{N_{O^{18}-O^{16}}}{N_{O^{18}-O^{18}}} : \frac{N_{O^{16}-O^{16}}}{N_{O^{18}-O^{18}}} = 1 : 2\left(\frac{N}{n^{18}} - 1\right) : \left(\frac{N}{n^{18}} - 1\right)^2$$

and using the relation that the total amount of each species AB evolved, A_{AB}, is proportional to the number of atom pairs in the surface lattice, N_{A-B}, and observing that $y^{18} = n^{18}/N$, there is

$$\frac{A_{O_2^{18}}}{A_{O_2^{18}}} : \frac{A_{O^{16}O^{18}}}{A_{O_2^{18}}} : \frac{A_{O_2^{16}}}{A_{O_2^{18}}} = 1 : 2\left(\frac{1}{y^{18}} - 1\right) : \left(\frac{1}{y^{18}} - 1\right)^2$$

which is the same as the relationship obtained using a mobile atom desorption model (section 4.1.3).

Chapter 4 : References

Eger, D., Goldstein, Y. and Many, A., R.C.A. Review 36, 508, (1975)

Ehrlich, G., Adv. in Catalysis 14, 255, (1963)

Göpel, W., (1) Surface Sci., 55, 362, (1976)

Göpel, W., (2) Ber. Bun. Ges. 80, 481, (1976)

Halpern, B. and Germain, J.E., J. Catalysis, 37, 44, (1975)

Hayward, D.O. and Trapnell, D.M.W., "Chemisorption", Butterworths, London, (1964)

Heiland, G., Mollwo, E. and Stockmann, F., "Solid State Physics", eds. Seitz, F. and Turnbull, D., Academic Press, New York, 8, 193, (1959)

Henzler, M., Surface Sci., 36, 109, (1973)

Hoffman, J.W. and Lauder, I., Trans. Faraday Soc., 66, no. 573, 2346, (1970)

Kröger, F.A., "The Chemistry of Imperfect Crystals", North-Holland Amsterdam, (1964)

Lindner, R., Acta Chem. Scand., 6, 457 (1952)

Petermann, L.A., Prog. in Surf. Sci. 3, 1, (1972)

Secco, E.A. and Moore, W.J., J. Chem. Phys., 26, 942, (1957)

Seiwatz, R. and Green, M., J. Appl. Phys., 29, 1034, (1958)

Stratton, R., Proc. Phys. Soc. (London), B68, 746, (1955)